# INVESTIGATION OF FLUX ACTIVATED TUNGSTEN INERT GAS WELDING & HYBRID PROCESS

A thesis submitted in fulfilment

of the requirement for the award of the degree of

## DOCTOR OF PHILOSOPHY

**Submitted by**


## SURINDER KUMAR TATHGIR

**(Regd. No. 951608001)**


Under the Supervision of


**Dr Ajay Batish**

(Professor, M.E.D.)

T.I.E.T, Patiala

**Dr Dinesh W. Rathod**

(Assistant Professor, M.E.D.)

N.I.T., Srinagar




**MECHANICAL ENGINEERING DEPARTMENT**

**THAPAR INSTITUTE OF ENGINEERING AND TECHNOLOGY,**

**PATIALA-147001**


**September 2021**

*Dedicated*
*To*
*My Parents and Family*

# CERTIFICATE

I, Surinder Kr. Tathgir, at this moment, declare that the thesis entitled "**Investigation of Flux Activated Tungsten Inert Gas Welding & Hybrid Process**" is an authentic and bonafide record of my research work. This research work has been submitted to **Thapar Institute of Engineering and Technology, Patiala,** as a requirement for the award of the degree of **Doctor of Philosophy** under the supervision of **Dr Ajay Batish**, Professor, Mechanical Engineering Department, T.I.E.T. Patiala and **Dr Dinesh W. Rathod,** Assistant Professor, Mechanical Engineering Department, N.I.T. Srinagar. However, no part of the matter embodied in this thesis has been present and submitted to any other university or institute to award any degree or diploma.

Date: 31/08/2021

**Surinder Kumar Tathgir**
(Reg. no. 951608001)

It is certified that the above statement made by the student is correct to the best of our knowledge and belief.

**Dr Ajay Batish**
Professor
Mechanical Engineering Department
T.I.E.T., Patiala

**Dr Dinesh W. Rathod**
Assistant Professor
Department of Mechanical Engineering
N.I.T. Srinagar

# PREFACE

This basis for this research stems from my passion for developing a better method to improve the microstructure and mechanical properties of the weldment by hybrid arc welding (H.A.W.) and to explore the use of A – T.I.G. welding. All of the studies presented henceforward was conducted at Thapar Institute of Engineering and Technology (T.I.E.T., Deemed to be University), Patiala. An elaborated part of stationary A – T.I.G. welding with Ar and $H_2$ mixed shielding environment is mentioned in Chapter 4 and Chapter 5 (Published). I was the principal investigator, responsible for the idea formation, data collection and analysis, and the study mentioned in the manuscript. Some of the destructive tests were performed at the I.I.T. Ropar campus and UCE, Punjabi University. I completed all experiments under the supervision of my supervisors (**Dr Ajay Batish** and **Dr Dinesh W. Rathod**). I wrote both the manuscript of the published research papers (DOI: 10.1080/10426914.2019.1666990 and DOI: 10.1080/10426914.2020.1765251) used in this dissertation with the permission of the permission co-ordinator of the journal (Materials and Manufacturing Processes of Taylor & Francis).

# ACKNOWLEDGEMENT

I am highly grateful and indebted to the authorities of Thapar Institute of Engineering and Technology, Patiala, for allowing me to do such informative research and financial support.

I express my profound gratitude towards my supervisors, **Dr Ajay Batish** (Deputy Director/Professor, Mechanical Engineering Department, Thapar University) and **Dr Dinesh W. Rathod** (Assistant Professor, Department of Mechanical Engineering, N.I.T. Srinagar) for inspiring me incessantly. I was lucky enough to receive thoughtful guidance, motivation, encouragement and endless support during my research work. They have always been cooperative and supportive. My success and the completion of my thesis would not have been possible without the supervisors' support and guidance. Their wide experience, professional advice, and willingness to offer valuable suggestions have made this work possible.

I would also like to extend my deepest gratitude to Dr T. P. Singh (Professor/Ex-Head, Mechanical Engineering Department, T.I.E.T) and Dr T. K. Bera (Professor/Present Head, Mechanical Engineering Department) for providing the Departmental facilities and for allowing me to work at odd hours in the Advanced Measurement Lab.

I would like to express my core appreciation towards my Doctoral Committee Members for believing in my integrity.

I would also wish to express my sincere regard to Dr Tarun Nanda, Dr T. K. Bera, Dr Atul Sharma, Dr Deepa Mudgal, Dr Gautam Setia, Dr Satish Sharma, Dr Ratnesh Kumar, Dr Harish Garg and Dr P. Kalyan for their constant support and encouragement during this research work.

I am also grateful to Dr Dhiraj K. Mahajan (Associate Professor, I.I.T. Ropar) and Mr Rupinder Singh (S.L.A., I.I.T. Ropar) for their co-operation and to use their campus facility. I must also thank Dr Vinay Gupta (Professor, U.C.O.E., Punjabi University) to use their lab facility.

Some colleagues were never too busy to extend me a helping hand whenever needed. I am extremely grateful to my colleagues Mr Lalit Kumar, Mr Manoj kumar, Mr Gagandeep Singh, Mr Binu Kumar, Mr M.suri, Mr A.K.Rath, and Mr Rajinder Kumar of the Central Workshop (CW) and all other staff members of the Mechanical Engineering Department (M.E.D.) who helped me throughout. I'd like to acknowledge the assistance of Mr Narinder Singh (Technician, T.I.E.T.) and Mr Babban (Technician, T.I.E.T.).

I also want to thank my friends who always encouraged me to achieve this goal, and I will be indebted to all those friends.

I want to express my deepest gratitude to my parents and family for always being beside me and for their moral support. Above all, I raise my hands to pay my best regards to that Almighty

for always being blissful and bestowing his blessings on me for accomplishing my task without any impediments.

# TABLE OF CONTENTS

# LIST OF FIGURES

## Chapter 1



## Chapter 2



## Chapter 3

# Chapter 4

# Chapter 5

# Chapter 6

## Chapter 7



## Chapter 8

# LIST OF TABLES

## Chapter 1



## Chapter 3



## Chapter 4



## Chapter 5



## Chapter 6



## Chapter 7

## Chapter 8

# LIST OF ABBREVIATIONS

| | |
|---|---|
| A | Ampere |
| AA – TIG | Automated Activated TIG Welding |
| ADAS | Austenite Dendrite Arm Spacing |
| *AF* | Acicular Ferrite |
| AGS | Austenite Grain Size |
| AISI | American Iron and Steel Institute |
| ANOVA | Analysis of Variance |
| A-TIG | Activated TIG Welding |
| AF | Austenite – ferrite solidification mode |
| ASS | Austenitic Stainless Steel |
| ASTM | American Society of Testing and Materials |
| BCC | Body Centre Cubic |
| DoF | Degree of Freedom |
| DWR | Depth to Width Ratio |
| DSS | Duplex Stainless Steel |
| EDM | Electric Discharge Machining |
| FA | Ferrite – Austenite solidification mode |
| FB-TIG | Face Bound Tungsten Inert Gas Welding |
| FDAS | Ferrite Dendrite Arm Spacing |
| FGS | Ferrite Grain Size |
| FZ | Fusion Zone |
| FSS | Ferritic Stainless Steel |
| GTAW | Gas Tungsten Arc Welding |
| HAW | Hybrid Arc Welding |
| HEE | Hydrogen Embrittlement Environment |
| HAZ | Heat Affected Zone |
| HI | Heat Input |
| K-TIG | Key Hole TIG |
| *L* | Characteristic Length of the Weld Pool |
| LF | Lorentz Force |
| MSS | Martensitic Stainless Steel |

| | |
|---|---|
| NG-GTAW | Narrow Gap Gas Tungsten Arc Welding |
| OA | Orthogonal Array |
| *Pe* | Peclet Number |
| P | Penetration |
| $P_a$ | Penetration Area |
| PAW | Plasma Arc Welding |
| PWHT | Post Weld Heat Treatment |
| SAW | Submerged Arc Welding |
| SCC | Stress Corrosion Cracking |
| SEM | Scanning Electron Microscope |
| SD | Schaeffler Diagram |
| SMAW | Shielded Metal Arc Welding |
| SS | Stainless Steel |
| STF | Surface Tension Force |
| TIG | Tungsten Inert Gas Welding |
| UTS | Ultimate Tensile Strength |
| U-TIG | Ultrasonic Tungsten Inert Gas Welding |
| v/v | Volume Concentration |
| VHN | Vickers's Hardness Number |
| WA | Widmanstatten austenite |
| XRD | X-RAY Diffraction |
| YS | Yield Strength |

# LIST OF SYMBOLS

| | |
|---|---|
| $\alpha l$ | Thermal diffusivity of liquid |
| $\alpha$-Fe | Alpha Ferrite |
| CO | Carbon Monoxide |
| $CO_2$ | Carbon Dioxide |
| $CrO_3$ | Chromium Trioxide |
| $Cr_{eq}$ | Chromium equivalent |
| $Cr_3C_2$ | Chromium Carbide |
| $\delta$ | Delta |
| $d\sigma/dT$ | Surface Tension Gradient |
| $MoS_2$ | Molybdenum Disulfide |
| $MoO_3$ | Molybdenum Trioxide |
| $M_{23}C_6$ | Chromium rich Carbide/Complex carbide |
| $Ni_{eq}$ | Nickel equivalent |
| $O^{2-}$ | Slag |
| $R_h$ | Reinforcement Height |
| $R_w$ | Reinforcement Width |
| $SiO_2$ | Silicon Dioxide |
| $TiO_2$ | Titanium Dioxide |
| $V_{max}$ | Maximum Surface Velocity |

# ABSTRACT

The productivity of Gas Tungsten Arc Welding/Tungsten Inert Gas (GTAW/TIG) welding is low due to its less penetrating capability due to the less heat input of the process. A well-known process could enhance productivity, i.e., A – TIG (Activated – TIG) welding. This process could be accomplished by applying a thin layer of activated flux before welding. Presently, different grades of stainless steel are used in many industrial applications due to its excellent corrosion resistance and better mechanical properties over mild steel. The edge preparation cost and slow welding speed of the conventional GTAW/TIG welding make the process uneconomical. So, I accomplished different objectives to overcome the limitation of the conventional GTAW/TIG welding and explore the uses of A – TIG welding.

The present dissertation work is an attempt to investigate the A – TIG welding process in the context of metallurgical changes and associated mechanisms. First, A – TIG welding was carried out at a fixed position (so-called stationary A – TIG welding) using different shielding environments to explore the mechanism behind deep penetration and growth of grains, dendrites, dendrite arm spacing and other metallurgical changes. Design of experiment with full factorial design approach has been adopted in the current investigations. The gas-metal and slag-metal reactions study were occurred in A – TIG welding and discussed in detail under Chapter – 4 (4.4.7). The objectives, as mentioned earlier, are accomplished using different stainless-steel grades (AISI 304, AISI 316 and Duplex 2205) and different oxide-based fluxes. A – TIG welding is further explored for a challenging position (i.e., Vertical uphill) and by developing a new hybrid process (Hybrid Arc Welding – HAW). The study of A – TIG welding for the challenging position was also accomplished using different shielding environments and using Taguchi experimental design methodology. Significant welding parameters were identified and discussed for the change in mechanical properties. The new hybrid arc welding process was developed to enhance the traditional submerged arc welding (SAW) and to enrich the A – TIG welding process by combining both the arc welding processes.

Before proceeding to the HAW process, and to find out the optimise parameters, the Taguchi experimental design technique (L 9) was used for both the autogenous A – TIG welding and SAW on 16 mm thick AISI 304 stainless steel plates. After completing the Autogenous A – TIG (AA – TIG) welding and SAW on thick plates, HAW was conducted by combining both AA – TIG and SAW and using significant welding parameters for the qualitative research. Finally, a comparison has been made between the outcomes of the HAW and SAW processes. For further use in the hybrid process, the mechanical and metallurgical properties of the

selected weld samples were analysed for both A – TIG and SAW. The study results show that the HAW process provides better weld quality and significant mechanical properties of the weldment than stand-alone A-TIG or SAW for thick plate welding. Furthermore, the experimental results/outcomes of the study indicated that the HAW could be the best process to achieve the desired mechanical properties of the weldment/weld metal. Finally, it concluded that the HAW process enhances productivity.

# Chapter - 1
# Introduction

## 1.1 Introduction

This chapter introduces the background to enrich stainless steel welding, a brief introduction about the variants of Gas Tungsten Arc Welding (GTAW/TIG welding), 'Flux Activated TIG Welding' (A – TIG) with its mechanism and shielding in GTAW/TIG and A – TIG welding. A brief introduction of the new hybrid process developed is also presented in this chapter. This chapter also covers the aims of this study, research objectives and the methodology used to achieve different objectives. Finally, the present chapter also mentions an outline of the thesis structure.

## 1.2 Enrichment of Stainless-Steel Welding

Stainless steel's excellent corrosion-resistant and good mechanical properties are the main characteristics that distinguish it from ordinary carbon steel and are the most widely used materials for welding in different industries [1]. Stainless steel is comparatively five times costlier than low carbon steel, and the edge preparation for butt welding makes the welding process even more expensive. Moreover, stainless steel is not ideally suited for machining/edge preparation and requires multipass welding to fill the joint. This further reduces the productivity of the welding process, as traditional GTAW process widely welds it with a low heat input rate and less penetrating capability [2]. The right choice of the welding process, consumables, process parameters, and the influence of process associated heat input on the weld microstructure remains a challenge. In recent years, a lot of research work has been carried out to enhance the process capability during welding of different grades of stainless steel. Many fusion welding processes are extensively used for welding different stainless steels by the automobile sector, nuclear plants, chemical industry, food industry, shipbuilding industry, and fabricators, and the selection of the fusion welding process primarily depends on the product design and thickness of the workpiece.

For high-quality welding of stainless steel, Gas Tungsten Arc Welding/Tungsten Inert Gas (GTAW/TIG) welding is widely used by Large Fabrication Industries (Fig. 1). However, one potential problem associated with GTAW/TIG process is the limitation on the thickness of the workpiece that can be welded in a single pass. Higher current values may not always work as it may lead to distortion and increased bead width. In the past few decades, several attempts have been made to improve conventional TIG/GTAW welding by enhancing the power

source's efficiency, or modifying the welding torch or utilizing a mixture of gases to enhance productivity. Most times, argon (Ar) gas is preferred for shielding purposes. To improve productivity to some extent, sometimes helium (He) is blended with Ar, but the availability and cost of He make the process more expensive.

Hence, GTAW/TIG process is an attractive option for researchers and several studies related to new development in the equipment, changes in welding technique or changes in shielding environment have been tried to enhance the productivity of this process. The process offers low productivity, and hence, to overcome the limitation of the TIG/GTAW process, the Paton Institute of Electric Welding developed a new variant in 1960 [3], which is known as A – TIG welding.

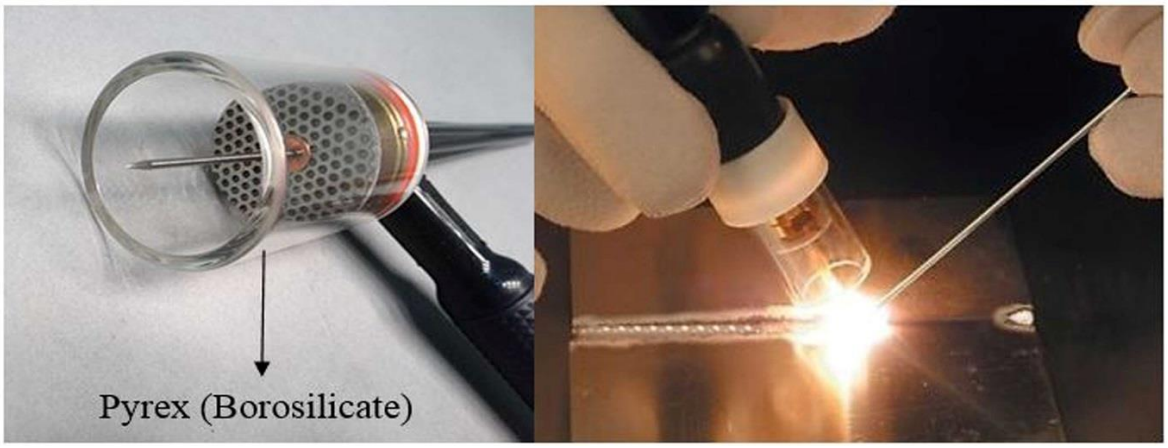


Figure 1. 1: TIG welding torch and TIG welding operation [4]

## 1.3 Variants of GTAW/TIG Welding

Numerous researchers developed various techniques to improve the productivity of GTAW/TIG welding. However, all these techniques are considered to be GTAW/TIG welding variants like Keyhole TIG (K-TIG), Activated TIG (A-TIG), Narrow Gap GTAW (NG-GTAW), Advance Activated (AA-TIG), Ultrasonic TIG (U-TIG), TOPTIG, TIPTIG, and Buried Arc, Dual-Shielded TIG and Multi-Cathode TIG. Among these variants, keyhole TIG (K-TIG) [5] and A-TIG welding techniques are being used to enhance productivity at higher welding speeds. The equipment cost for key-hole TIG (K-TIG) is very high, and it needs a high-power source. K – TIG is preferred for circumferential joints, and it generally supports a fully automated welding system. However, K – TIG also does not require bevel edges and can be done without filler. Compared to K-TIG welding, flux-assisted TIG welding (A-TIG) is simple and easy to handle and need less power consumption. Any skilled GTAW/TIG welder can use this process.

## 1.4 Flux Activated TIG Welding (A-TIG)

A-TIG welding has been developed to overcome the limitation of penetrating capabilities of traditional TIG welding. Flux activated TIG (A-TIG) [3, 6] welding is a conventional GTAW/TIG welding variant. In this process, a flux/oxide coat is applied to the faying surface or on the surface before welding. Flux activated TIG welding, or A – TIG, is the same as ordinary TIG/GTAW welding in operation except that the flux enhances penetration. A highly pure compound is mixed with acetone or ethanol to make a paste, and this is applied by a flat paintbrush 12 mm wide. After a few seconds, the acetone/ethanol completely evaporates, leaving a thin flux layer on the surface (Fig. 1.2). Despite the higher penetration capability, this process is not very popular in the heavy fabrication industry and has not been fully utilized due to a lack of awareness about its capability. The primary objective of A – TIG welding is to increase the depth of penetration with reduced bead width. The deeper penetration in this process is obtained by the combined effect of Lorentz forces and reverse Marangoni convection, [7] which affects the behaviour of ions and electrons during arcing [8–11]. The flux/compounds with enriched oxygen content are expected to promote arc constriction behaviour mechanism [12], which leads to a change in surface tension gradient. Also, instances of reverse Marangoni convection leads to deeper penetration. [8, 12–14] $H_2$ in the shielding environment increases voltage drop and leads to energy concentration [8, 15].

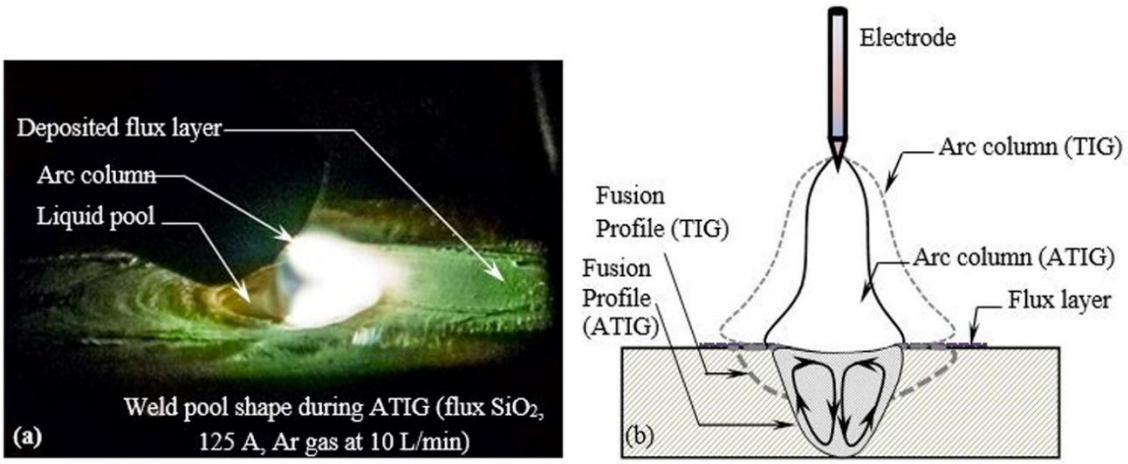


Figure 1.2: (a) Weld pool shape and (b) schematic illustration of flow in ATIG welding [9]

Using A – TIG process, one can reduce overall welding cost by up to 50 %. The factors which can be considered for reducing the overall cost of welding are:

- There is no need for modification in the power source as it uses a GTAW power source.

- Welding can be done in a single pass for thicknesses up to 12 mm, so there is no need for multiple passes, further reducing the cost of shielding gas and power cost for multipass welding.
- Shorter welding time can be achieved with significant penetration at high speed in a single pass.
- Reduced consumption of welding filler wire as there is no need for extensive edge preparation.
- Eliminate the requirement of the joint gap in the case of the square butt joint.
- Causes minimum distortion while using high heat input.
- Produces a higher depth of penetration (DoP) without using extra power.

The A – TIG welding could be used for all positions and can be the best solution to improve GTAW/TIG welding productivity. This technique can be used for different stainless steel, carbon steel, ultra–high strength steel and non–ferrous metals [16].

## 1.5 Mechanism behind A – TIG Welding

The three types of mechanisms that occur during A – TIG welding that play a significant role in achieving higher penetration depth are listed below.

a) **Arc Constriction**
b) **Forces and Associated Material Flow Pattern**
c) **Reverse Marangoni convection**

a) **Arc Constriction**: Under the intense heat of an arc, the flux vapours or the present oxygen elements of oxide-based flux interact with the outer electrons in the periphery of an arc and dissociated atoms to form negative ions for redistribution of charge carrier [10]. Due to this effect, arc constriction behaviour comes into effect. This phenomenon of arc constriction leads to an increase in the temperature at the anode by decreasing the anode root area owing to the higher electric resistance of flux (Fig. 1.3). Hence, a higher depth of penetration (DoP) and reduction in weld bead width can be achieved during A – Tig welding with oxide-based fluxes. This mechanism is more significant for those fluxes with more oxygen elements and could be absent in fluoride or halide-based fluxes.

b) **Forces and Associated Material Flow pattern:** Different types of forces were active during conventional TIG/A – TIG welding. The influence of the associated pattern dominates the weld pool shape and the weld's resulting dendritic structure. The material flow pattern is directly dependent on the magnitude of these forces. During A-TIG welding, the influence of Lorentz Force (LF) and the Surface Tension Force (STF) is found

more than buoyancy and plasma shear force. Both the LF and STF act strongly in case of high heat input. Due to these forces, the molten metal flows downward from the top weld centre and rises along the periphery (Fig. 1.3).

c) **Reverse Marangoni Convection:** When surface tension gradient is positive due to the weld pool's higher temperature, reverse Marangoni convection occurs and results in higher DoP. [17] But the change in chemical composition, surface tension, and positive temperature gradient is possible due to surface-active elements of activated flux. In addition, due to activated flux, which also acts as an insulator, stress increases at the centre of the weld pool. [10] Simultaneously, molten metal flows from the low-stress area to the high-stress area, leading to increased penetration.

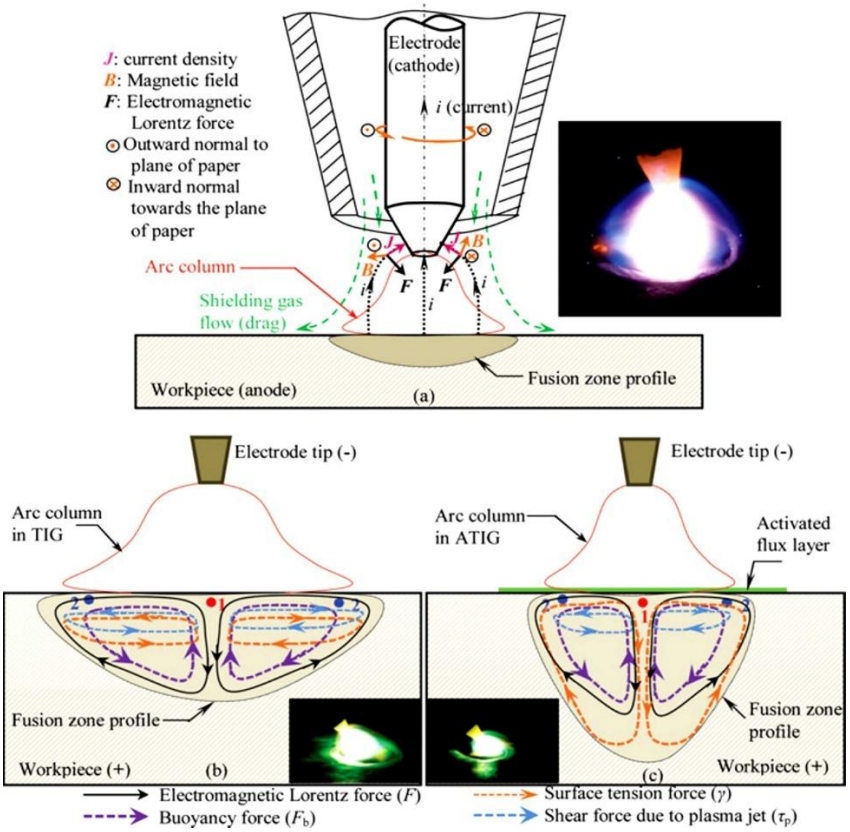


Figure 1. 3: Driving forces and their flow pattern in CTIG and ATIG welding process [13]

## 1.6 Shielding in GTAW/TIG and A-TIG Welding

Different types of inert gases or the mixtures of inert and reducing or reactive shielding environments are used in both TIG and A-TIG welding. The choice of shielding environment/shielding gas depends on the type of base material. A shielding gas primary function is to protect the molten pool and the hot tungsten electrode from oxygen, nitrogen, and water vapours present in the ambient air. In addition, the shielding gases play another

dominant role in changing the arc characteristics and the microstructure of the solidified weld bead. The welding community in this area has done extensive research.[18, 19]

Moreover, different shielding gases and mixtures significantly impact the weld bead profile and the resultant penetration by changing the weld chemistry. Helium alone can be used for shielding purposes, but it may disturb the shielding and need more flow rate, further increasing the cost of welding. The presence of active elements in A-TIG welding changes the shape of an arc. The resultant effect on the weld microstructure is different in different shielding environments, which are explained in the subsequent chapters. Pure argon (Ar) gas could be the first choice in the context of the availability and favourable welding condition for different steel and stainless-steel types.

Table 1.1: Properties of shielding gases used in stainless steel welding

| Type of gas | Boiling point at 1.013 bar (°C) | Molecular weight | Ionization Potential | Density (kg $m^{-3}$) | Chemical Activity |
|---|---|---|---|---|---|
| Argon (Ar) | -185.9 | 39.948 | 15.75 | 1.784 | Inert |
| Helium (He) | -268.9 | 2.016 | 24.58 | 0.178 | Inert |
| Nitrogen ($N_2$) | -195.8 | 28.013 | 14.54 | 1.161 | Reactive |
| Oxygen ($O_2$) | -183.0 | 31.998 | 13.61 | 1.326 | Oxidizing |
| Hydrogen ($H_2$) | -252.9 | 2.016 | 13.59 | 0.083 | Reducing |

Pure argon (99.9%) and a mixture of Ar + 2.5 % $H_2$ has been used in the present work, so the same are discussed below:

**i. Argon (Ar):** Argon is an odourless, colourless, and inert/ noble gas present in the earth's atmosphere. It is attained by the method of separation of liquefied air with other products like oxygen and nitrogen. As argon is denser than air and reactionless, it is very useful for shielding purposes. It produces a quiet and smooth arc in the case of GTAW/TIG welding. With the help of **'Ar'** gas, arc initiation is very easy due to low ionisation potential compared to 'He' gas and requires a lower gas flow rate and a low voltage. The influence of Ar shielding on the growth rate of dendrite was found more significant in the case of A-TIG welding compared to conventional GTAW/TIG welding with **'Ar'** shielding [20]**.**

**ii. Helium (He)**: Helium is also an inert gas with a low density and could be used in conventional TIG and A – TIG welding. The main problem associated with He alone is that it causes turbulence and the weld surface needs cleaning after welding. Helium is a light gas compared to Ar, so it needs more gas flow rate, adding to more cost. The mixture of both Ar and He could be a better choice in place of a single gas shielding environment. The mix of these gases influences the welding speed, and the resultant weld bead is satisfactory [21].

**iii. Hydrogen ($H_2$):** Hydrogen is the smallest element, and as a gas, it is the lightest gas that is highly combustible. Hydrogen is generally reactive, but when mixed with argon (Ar) gas, it behaves as reducing gas and increases the thermal conductivity. That results in a significant increase in welding speed, which further helps to enhance productivity. At high temperatures, hydrogen reacts with metals, and it helps to reduce delta ferrite in the resultant microstructure of austenitic stainless steel. It possesses a high diffusion potential due to its small atomic diameter. Higher content of alloying elements like chromium, nickel and manganese reduces the diffusion rate of hydrogen in iron [22]. Research shows that the small addition of $H_2$ gas (1-10%) increases the arc energy significantly at the constant parameters than the pure 'Ar' shielding environment [8, 9]. The austenite phase in stainless steel can dissolve hydrogen more than the ferrite phase. During solidification of fusion zone or phase transformation process, i.e., austenite-to-ferrite, the solubility of hydrogen is quickly reduced. Enthalpy of hydrogen ($H_2$) gas is higher than argon (Ar), which produces more heat owing to its higher thermal conductivity and leads to change the Gibbs free energy ($\Delta G^*$). When it has a negative value then a transformation occurs spontaneously. The enthalpy of hydrogen increases significantly under the presence of activated flux. The combined reaction of oxide-based fluxes and hydrogen under the intense heat of an arc of GTAW generate more heat which finally influences the depth-of-penetration (DoP) with dendrite growth.

## 1.7 Hybrid Process (SAW + A-TIG)

In the last decade, the welding of stainless-steel plates with large thicknesses has been challenging for the fabrication industries. However, it is nowadays performed with Submerged Arc Welding (SAW), which has a high deposition rate. The primary constraint for the large thickness is the edge preparation of stainless steel for butt welding the plates or pipes, which is very difficult to machine, uneconomical, and time-consuming. The hybrid welding process includes using a minimum of two welding processes simultaneously to achieve the best result in terms of mechanical properties by using the combined effect process advantages.

To date, all efforts have been focused on high energy source welding like a laser beam [23]. In recent years, researchers tried to use a laser beam with conventional arc welding processes like Gas Metal Arc Welding, Plasma Arc Welding, Submerged Arc Welding and Gas Tungsten Arc Welding (GMAW, PAW, SAW, and GTAW) [23, 24]. Hence, it could be used as a hybrid process for heavy industrial applications [23–28]. However, it may lead to the formation of brittle phases and porosity due to the fast cooling rate of the weld metal [29, 30]. High power laser welding is also costly, and a precise joint setup is required for better results. The energy

conversion efficiency is very low in the case of laser beam welding (LBW), and industrial robots perform welding. The LBW reflectivity of a laser beam is another problem for specific materials. Moreover, LBW is mainly used for precise work. SAW is considered a highly productive welding technique to achieve a higher deposition rate in thick steel plates [31]. It can also be used for the welding of austenitic stainless steel. On the other hand, high power laser beam welding has unique features of high energy density, making it useful for single-pass welding of thick steel sections up to 15 mm in a single pass.

Two arc welding processes (SAW + A-TIG) have been used to develop a new hybrid process in the present research. A-TIG has been used as a leading process for the newly developed Hybrid Arc Welding (HAW), maintaining a minimum gap between the SAW and GTAW torch. The significant difference between the SAW and A-TIG welding is the source of shielding. In SAW, flux is used for shielding, whereas Ar or a mixture of Ar + $H_2$ is used for A-TIG welding. In the present work, pure Ar was used for shielding purposes in the case of A-TIG welding. The detailed experimental procedure, material, power source used with fixed and variable parameters are discussed in the subsequent chapters. The schematic diagram of this process is shown in Fig. 1.4.

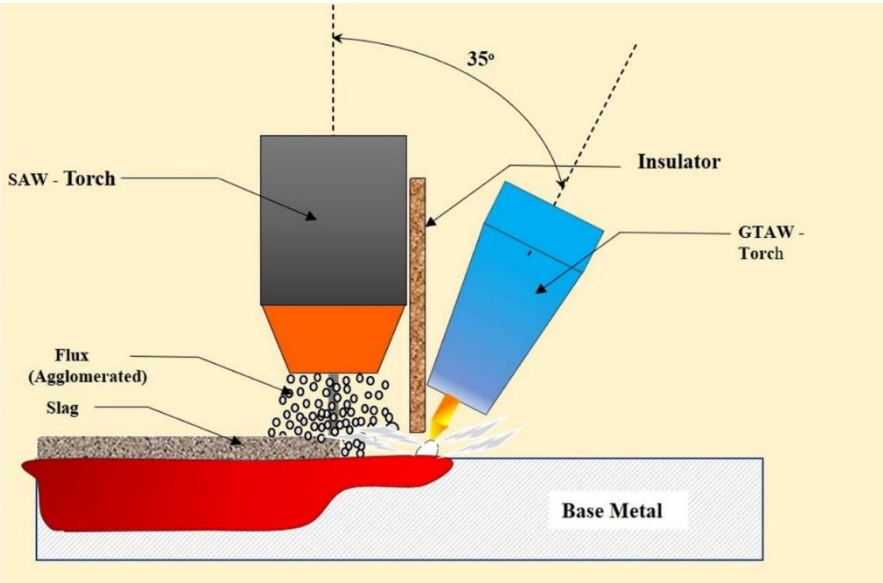


Figure 1.4: Schematic diagram of the hybrid process (A-TIG + SAW)

## 1.8 Aims and Objectives

To overcome the limitations of TIG welding and to explore the A – TIG welding, a systematic study was planned and undertaken to modify the known A-TIG welding process to increase the depth of penetration without any edge preparation while retaining the existing properties of the

raw material. Modification of the A-TIG welding process included developing a Hybrid Arc Welding (HAW) process that has not been reported before in the literature.

## 1.9 Proposed Research Work and Research objectives

Many studies have been found to enrich A-TIG welding in evaluating the individual process performance and clubbing this method with submerged arc welding (SAW) to develop a new hybrid process. Hence, based on the previous literature review, its summary and scope, the following objectives were identified.

The following are the key objectives of the study:

- Study the weld profile development during Activated TIG (A-TIG) welding for different grades of stainless steel at different exposure times.
- Evaluate the performance of A-TIG welded joints for difficult positions with different shielding environments.
- Study the profile of the weld bead during SAW for AISI 304.
- Develop a hybrid welding process (A-TIG + SAW) and study of weld bead profile obtained on AISI 304.

## 1.10 Methodology

### 1.10.1 Study of Weld Profile

In this study phase, A-TIG welding was performed on Austenitic Stainless Steel (AISI 304 and AISI 316) and duplex stainless steel (Duplex 2205). The profile development was executed with different types of fluxes/compounds. The profile was achieved by varying arc exposure time (seconds) at a fixed location and then measuring the cross-sectional shape of the fusion zone. A parametric study on weld profile development/ bead quality improvements was evaluated by varying factors like shielding gas (Ar, Ar + 2.5% H2), at 10 L/min flow rate types of fluxes, using 150 A current and 60° vertex angle of the electrode. Finally, it was compared with conventional GTAW/TIG welding as per the detailed flow chart Fig. 1.5.

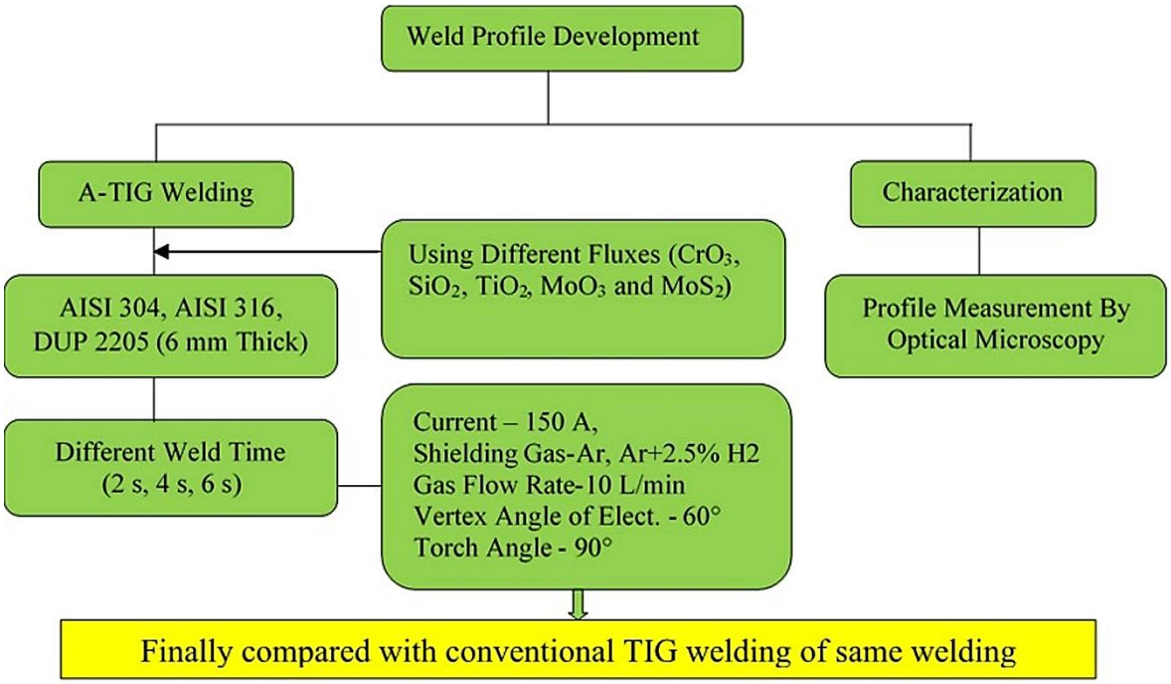


Figure 1.5: Flow diagram of the methodology used for weld profile development in stationary A – TIG welding

### 1.10.2 A-TIG Welding for Difficult Weld Position (Vertical/Uphill)

For enhancing the capability of the A-TIG welding process and the feasibility of its use during difficult positions (Vertical/Uphill), A-TIG welding with coated filler (with activated flux) was carried out on 5.74 mm thick austenitic stainless-steel plates (AISI 304) with the help of Taguchi's L18 orthogonal array. For A – TIG welding, a precoated filler was also used to compensate for the loss of flux coating due to the gravitational effect. The joint properties were evaluated by measuring their mechanical properties and then compared with conventional GTAW/TIG welded joints. The methodology used for difficult position welding is shown in Fig. 1.6.

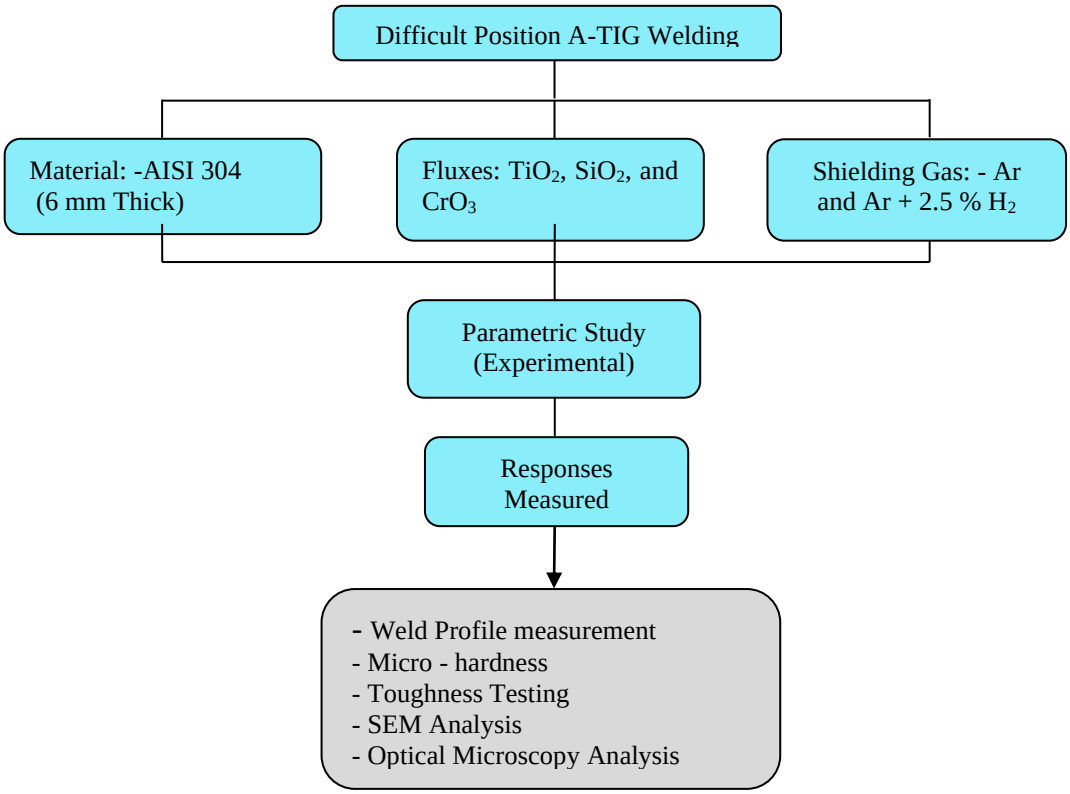


Figure 1.6: Flow chart of the methodology to be used for difficult (Uphill/Vertical) position welding

### 1.10.3 Submerged Arc Welding (SAW)

To quantify the impact of the new HAW process, the results from the conventional SAW process were studied for comparison purposes. Effect of welding parameters like voltage, speed and electrode stick-out was evaluated using conventional submerged arc welding (SAW) for microstructural analysis. A weld bead was formed on 16 mm AISI 304 steel plates without edge preparation. Taguchi's L – 9 orthogonal array was used to design the study. Though a higher value of penetration is possible during SAW welding, the current was kept at a nominal value (380 A) after a preliminary investigation of several runs. The primary purpose of this study was the optimization of welding parameters, which could be used in the hybrid process.

### 1.10.4 Autogenous A-TIG welding

As mentioned in section **1.10.3**, a similar study was also undertaken to evaluate the effect of variable welding factors and their contribution during A-TIG welding with oxygen-rich oxides on the 16 mm thick AISI 304 stainless steel plates. After preliminary investigation using different current levels, an A-TIG weld bead was formed at 310 A at two levels of welding speeds (4 mm/s and 5 mm/s) using $CrO_3$, $SiO_2$ and $TiO_2$ fluxes.

### 1.10.5 Hybrid Arc Welding (HAW) Process

In this phase, the development and performance evaluation of a novel hybrid process (A-TIG + SAW) was evaluated on AISI 304 stainless steel without edge preparation. Finally, the mechanical properties of weldment with this hybrid process were compared with the conventional submerged arc welding. The flow chart of the methodology to be used for the hybrid process is shown in Fig. 1.7. Agglomerated flux with high basicity index was used in the hybrid process.

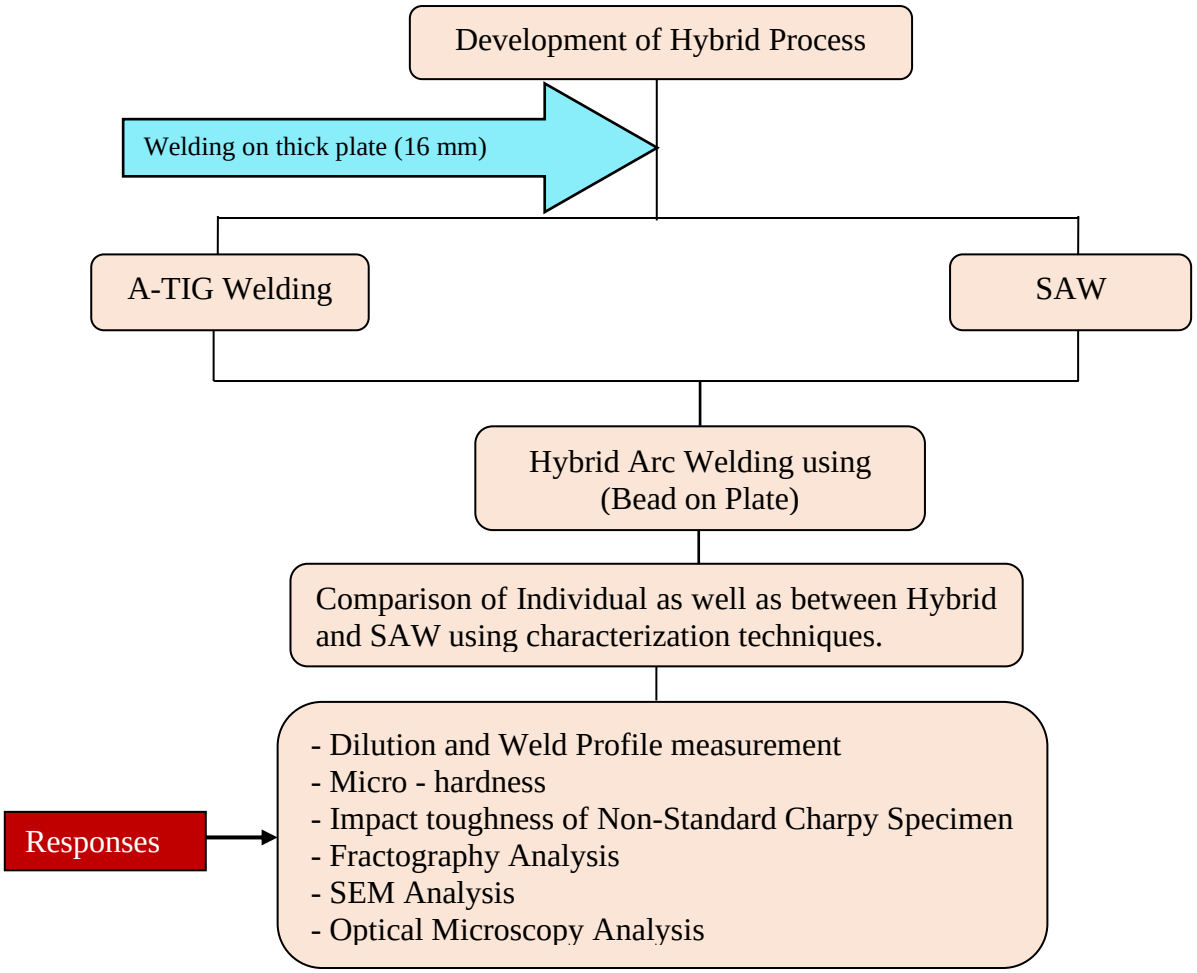


Figure 1.7: The flow diagram of the methodology used for the development of the hybrid process (A-TIG + SAW).

## 1.11 Thesis Structure

### Structure of the Thesis Work is as Follows

**Chapter 1** includes the background of stainless-steel welding, a brief introduction about the variants of Gas Tungsten Arc Welding (GTAW/TIG welding), 'Flux Activated TIG Welding' (A – TIG) with its mechanism and shielding in GTAW/TIG and A – TIG welding. A brief introduction of the new hybrid process developed is also presented in this chapter. This chapter also covers the aims of this study, research objectives and the methodology used to achieve different objectives. Finally, the present chapter also mentions an outline of the thesis structure. and the appropriate selection of process parameters to enrich the process and overcome some of its limitations.

**Chapter 2** covers two sections, which include the study of weldability and welding metallurgy of different stainless steels and their associated problems. It also includes a summary of the reported work and gaps in the literature which have been used to formulate this study.

**Chapter 3** reports detailed experimentation to study the effect of stationary A-TIG welding (to study the weld profile) on three types of stainless steels (AISI 304, AISI 316 and Duplex 2205) by using Argon as a shielding environment. The outcomes measured include weld profile, aspect ratio, weld morphology and its related properties, microstructural analysis, weld chemistry, thermal energy of arc (heat produced by arc), microhardness, Gas metal and slag metal reaction and Peclet number.

**Chapter 4** reports a trial on the study reported in Chapter 4 with Ar + 2.5 % $H_2$ shielding environment. The results obtained with the two kinds of shielding environments (Ar & Ar+2.5%$H_2$) have been compared for Duplex 2205 steel.

**Chapter 5** covers issues related to A-TIG welding for vertical or uphill positions to explore the suitability of this process for difficult positions. It also includes analysis of microstructure, weld profile and their validation for its mechanical properties.

**Chapter 6** reports the results of a comprehensive parametric study of the SAW process on thick austenitic stainless-steel plates as it is the most widely used with the hybrid process.

**Chapter 7** includes a systematic study of "Autogenous SAW" on 16 mm thick plates on austenitic stainless steel as a preliminary investigation and the associated results.

**Chapter 8** covers the development of the "Hybrid Arc Welding" – HAW process (combination of A-TIG + SAW). The outcomes of this study have been compared with conventional SAW for both metallurgical and mechanical properties.

**Chapter 9** reports the conclusions and suggestions for future work on A-TIG and Hybrid process.

# Chapter - 2
# Literature Review

## 2.1 Introduction

This chapter contains two sections, and section one covers a brief review of the literature on the types of steel, weldability of different kinds of stainless steel and the problems associated with the welding. The second section covers the literature on the studies related to GTAW/TIG, A-TIG welding, activated fluxes, the metallurgy of A – TIG welding and hybrid processes of a different kind on a variety of stainless-steels using different welding parameters.

## 2.2 Types of Stainless Steels and Their Weldability

Stainless steel is iron-base alloys having at least 12 % or more chromium. Stainless steels are alloyed with some essential elements to improve the corrosion resistance by forming a passive film on the surface. By varying the quantity of different alloying elements, it is possible to meet the specific manufacturing requirements or achieve desired properties for various applications in different environments. Stainless steel may be broadly classified into different categories depending on its microstructure and the percentage of alloying elements. Different types of stainless steel are used in various working environments and applications.

Classification of stainless steels as per their structure matrix is as follows:

i. Austenitic Stainless steel
ii. Ferritic Stainless steel
iii. Martensitic stainless steel
iv. Duplex Stainless steel (ferrite and austenite-50%)
v. Precipitation Hardening Stainless Steel (PH stainless steel)

The present work focuses on A-TIG welding of AISI 304, AISI 316 and Duplex 2205 stainless steel, which includes stationary A-TIG welding performed at different arc exposure times, Vertical A-TIG welding on AISI 304 and a hybrid process (A-TIG + SAW). A – TIG welding has been accomplished with and without filler.

### 2.2.1 Austenitic Stainless Steel (ASS):

Austenitic stainless steels are the most widely used steels for industrial fabrication and welding. Austenitic stainless steel contains a minimum of 16% and a maximum of 26% chromium and 6 – 22% nickel [32]. The other elements such as Mo, Ti, Nb (Cb) and Ta are also added in small quantities in different austenitic stainless steel grades [32]. It includes the 200 and 300 series, out of which type 304 is the most common, used in general fabrication like storage tanks

and containers. The primary alloying additions of this type are chromium and nickel. In stainless steel, the Cr, Mo, Ti, and Nb are the ferrite promoters, and Ni, C, and Ni are the austenite promoters, whereas Mn, Si, and Se provide the neutral effect. [33, 34] Austenitic stainless steel is generally non-magnetic and is not hardened by heat treatment. Manganese promotes the stability of austenite at room temperature. Alloys such as Cr, Ni and Mn are characterized by good strength, high toughness value and provide oxidation resistance over a temperature of 538°C [33]. The 300 series includes 302, 304, 310, 316, 321 and 347 with varied alloying elements. [33] In the series of 300, both AISI 304 and AISI 316 stainless steel have a small carbon percentage, and 2 – 3 % molybdenum in type 316 helps to improve corrosion resistance. AISI 321 and AISI 327 stainless steel are stabilized against the problem of carbide precipitation. The machinability of ASS can be improved by adding elements like Molybdenum, Titanium and Copper. All the austenitic stainless-steel grades can be easily welded except for free machining grades.

#### 2.2.1.1 Weldability and Welding metallurgy of ASS

During welding of austenite stainless steel, the primary consideration is given on heat input, contamination, porosity, carbide precipitation, and cracking of weld. The excess heat input resulted in a large thermal gradient across the joint, affecting corrosion resistance and its strength. The value of the coefficient of thermal expansion for the austenitic stainless steel is approximately 30% higher than that of carbon steel, and this must be considered during welding. However, due to austenitic stainless steel's low thermal and electrical conductivity, it can be readily welded as heat dissipates at a lower rate, so less heat input is required to make a sound weld.

- Two significant problems are encountered during welding of the austenitic stainless steels:

***a)* Sensitization**

The presence of chromium carbide at the grain boundary is called sensitization or weld decay. The sensitization leads to inter-granular corrosion, which occurs at some distance (in the heat-affected zone – HAZ) from the fusion boundary. The inter-granular corrosion caused by the precipitation and chromium carbide formation at the grain boundary is shown in Fig. 1.3. This type of attack/sensitization occurs at 600 to 850 °C by removing chromium from the solution near the grain boundary.

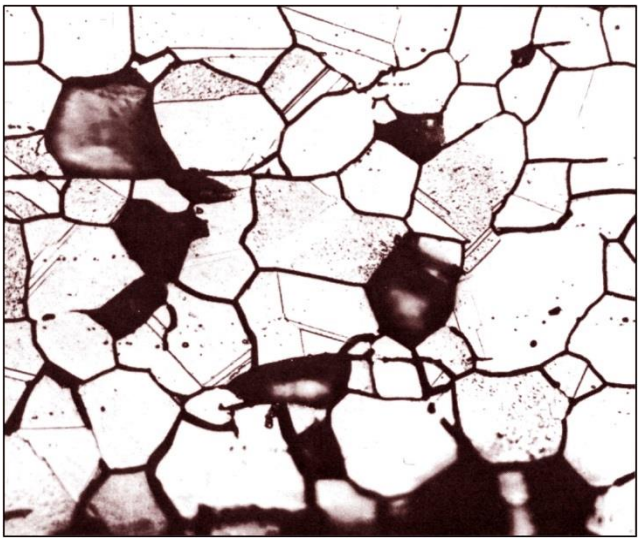

Figure 2.1: Inter-granular corrosion in HAZ of Austenitic Stainless Steel [33]

Mostly chromium-rich carbides ($M_{23}C_6$) form along the grain boundaries in HAZ of austenite stainless steel. This area in the HAZ resulted in a chromium-depleted zone called "sensitive" to corrosion attack, and the term sensitization represents the microstructure corresponding to inter-granular corrosion. Above 800 °C temperature, carbon moves back to solution and makes that zone carbide free and at the assumed fast cooling condition, it could suppress the carbide precipitation. So, the following remedies could be helpful to minimize the problem of sensitization.

- Sensitization can be controlled by adding Nb and Ti elements because these elements have a great affinity for carbon than chromium. [32]
- Rapid quenching may restrict carbide precipitation. [32]
- By limiting the carbon content up to 0.03% in the stainless steel.
- Post weld heat treatment may distribute the carbide into the solution, followed by quenching. [32]
- By choosing a suitable welding process to minimize the HAZ.
- Adding molybdenum to base metal like in AISI 316 provides more localized corrosion resistance to many chemicals.

***b) Hot cracking of weld metal***

Austenitic stainless-steel weld metal is sometimes noticed with interdendritic cracking, which is known as hot cracking or micro fissuring (generally not visible with naked eyes). The name hot crack is so-called because the cracks occur at high temperatures. This type of problem is found when the stress imposed on the weld metal is high. The whole austenitic structures are highly prone to this type of defect. Hot cracking is mainly caused by low melting liquid, which

includes compounds of sulphur and phosphorous, which tend to penetrate grain boundaries, cracks appear after solidification, and shrinkage stresses develop. Hot cracking can be controlled by altering the composition of the base material and filler material. So, it obtains a microstructure having ferrite in the austenite matrix when deposited. [33]

The weld microstructure depends on both solidification behaviour and phase transformation. After solidification, stainless steel solidified with austenite or ferrite as a primary phase. In the case of austenitic steel, the primary phase may be austenite. So, the ferrite number (FN) should be in specific range and it can be understood from the constitution diagram.

The importance and use of constitution diagrams like Schaeffler diagram (SD), DeLong diagram and WRC-1992 diagram are vital to predict different phases in the resultant weld structure or weld bead of stainless steel. However, the ferrite percentage of the ferrite content can be expressed in terms of ferrite number (FN). The Schaeffler diagram (SD) is used in the present work as no nitrogen was found in the parent metal and the resultant weld metal. The solidification mode also depends on the ferrite number in the weld matrix and ultimately affects the weld joint's toughness. If the ferrite number increases, it will lead to pitting corrosion because delta ferrite is rich in chromium content, and there may be a loss of chromium in the nearby region of the weld structure.

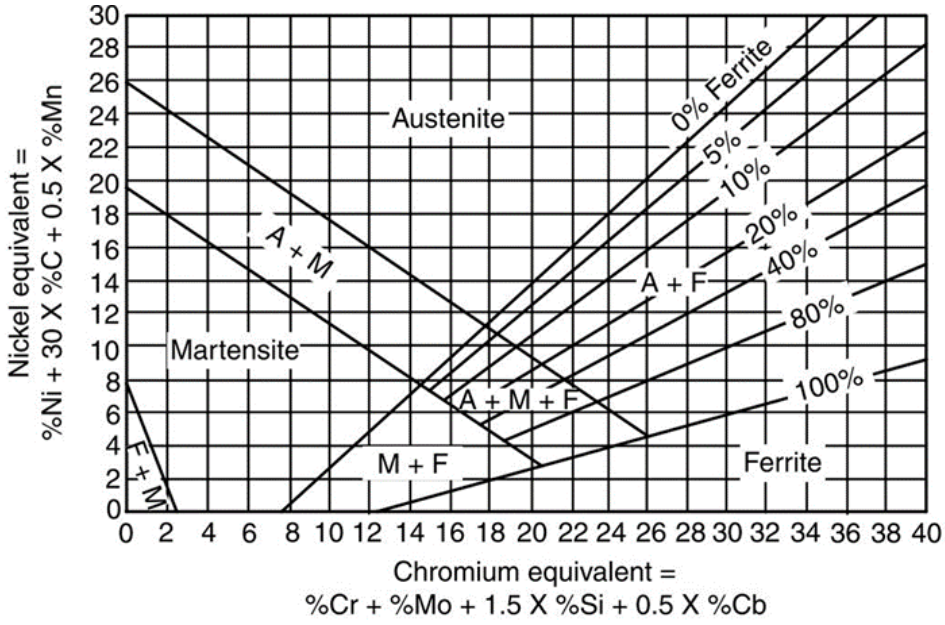


Figure 2.2: Schaeffler Diagram [32]

## 2.2.2 Ferritic Stainless Steel (FSS):

Ferritic stainless steels (FSS) contain approximately 11.5 to 27 % chromium with no or significantly little addition of nickel. [32] The predominant phase of the microstructure of this steel is ferrite, so the name called ferritic stainless steel. [34] High-temperature ferritic steel

does not transform to austenite and has intermediate corrosion resistance in general, high resistance to stress corrosion cracking and pitting corrosion. The standard grades of 400 series ferritic stainless steel are AISI 405, AISI 409, AISI 430 and AISI 430Ti. They exhibit body-centred cubic (BCC) structure at room temperature, called *ferrite*. Ferritic stainless steels have lower ductility and significantly decreased toughness at low-temperature working conditions. This steel is ferromagnetic and characterized by weld and HAZ grain growth, resulting in low toughness of welds. Ferrite steel is generally used in sulphurous atmospheric conditions because nickel percentage is very minimal or nil, which may react with sulphur like austenite steel. Ferritic stainless steel like AISI 409 is used in the exhaust system of vehicles and applications requiring corrosion protection beyond the capability of carbon steel.

#### 2.2.2.1 Weldability and Welding Metallurgy of FSS

Since the ferritic stainless steels attain the ferritic microstructure on cooling and do not transform to austenite, the weldability of ferritic stainless steel is closely associated with high-temperature embrittlement, hydrogen-induced cracking and weld solidification cracking. [34] The ferritic grades do not give good welding properties because of their inherent carbon content, which made them brittle and relatively with poor corrosion resistance. The diffusion rate of C and Cr is generally high in ferrite, which has a body centre cubic (BCC) structure and a fast-cooling rate during welding resulting in precipitation of Cr at the grains boundary, which further leads to inter-granular corrosion. As the weld decay or sensitization lies above 925$^{o}$C in FSS. So, post-weld heat treatment could be a better choice to resist intergranular corrosion because it helps redistribute the Cr in the region near the chromium carbide precipitates. During solidification, grain growth in the HAZ can be controlled using less heat input. Ductility loss can be prevented by choosing the appropriate filler (by choosing austenitic filler). FSS can be alloyed with titanium (Ti) and niobium (Nb) to improve weldability. These elements addition produces austenite, which is susceptible to martensite formation at rapid cooling rates. Due to the impurity and segregation of alloy, the solidification cracking may occur during the cooling of molten metal. Another associated problem is the coarsening of grains and the presence of martensite in the Heat Affected Zone (HAZ), which leads to embrittlement in the HAZ.

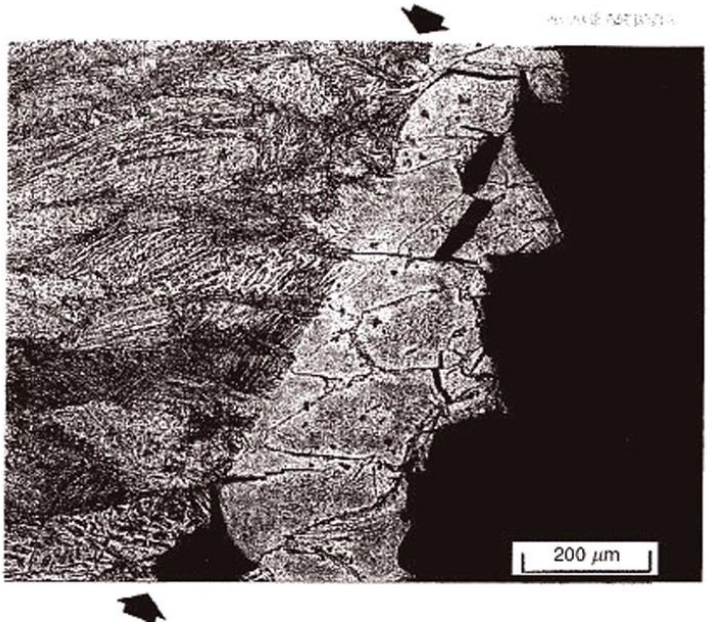


Figure 2. 3: Inter-granular corrosion in HAZ of Austenitic Stainless Steel [34]

Ferrite is the primary phase that appears in the microstructure during the solidification of the weld pool. Sometimes, it is also associated with martensite (needle structure) by transforming austenite into martensite. The martensite structure appears at the ferrite grain boundary.

### 2.2.3 Martensitic Stainless Steel (MSS):

Martensitic stainless steels (11-18% Cr with more than 1%C) are among the first stainless steels developed due to their incapability to produce low carbon steel. These steels are generally magnetic, and the metallurgical structure of these steels is martensitic. AISI 403, 410, 414, 416 and 420 etc., are the ordinary standard martensitic steels. Modification of these steels involves the addition of V, Mo, Ni and tungsten, which leads to the increase in carbon content, so the problem of cracking cannot be avoided. Cracking is a common problem in the welding zone, and it can be tackled/rectified with pre-heating and post-weld heat treatment.

#### 2.2.3.1 Weldability and Welding Metallurgy of MSS

This steel is least weldable due to the formation of a crack in the HAZ. These steels can be welded, but caution needs to be taken during welding as they can produce a tough and brittle phase. These steels are generally welded with austenitic filler rods to increase the ductility of the weld joint. When these steels are heated to a significant temperature, the present martensite transforms into austenite, and on cooling, it regains the martensitic structure. Preheating could be a good option for welding, and it is required to be preheated at a temperature ranging from 200$^{o}$C-300$^{o}$C, and post-weld heat treatment could be done at 700$^{o}$C to tackle brittleness related issues.

## 2.2.4 Duplex Stainless Steel:

Duplex stainless steels (DSS) derive their name from the dual microstructure that exhibits. It is having an approximately equal quantity of ferrite and austenite at room temperature. Several commercial grades of DSS are available, from lean duplex grades (2101, 2304) to highly alloyed super duplex grades (2507, 4501). DSS are ferromagnetic and exhibits good weldability when compared with the other types of stainless steel. The DSS has a narrow nickel range of about 4-7%. It contains both austenite and ferrite phases and having high mechanical strength. In recent years, some new development is done by increasing the alloy compositions (2707 grade) with excellent mechanical properties and adding a small quantity of nitrogen during manufacturing of this steel, an austenite stabilizer. Nitrogen provides strength and helps to increase the pitting corrosion resistance in the chloride atmosphere.

### 2.2.4.1 *Weldability & Welding Metallurgy of DSS*

Generally, GTAW and SMAW processes are used to weld duplex stainless steel. For the duplex grade of 2205, 2209 is used as a standard filler material with an extra nickel. The nickel content in duplex steel helps to maintain the ferrite/austenite structure (50/50) in the weld bead, thus maintaining strength, ductility and corrosion resistance. After cooling of DSS weld, both ferrite and austenite dendrites are present in the microstructure. The ferrite to austenite transformation depends on the cooling rate and the weld metal composition. For a faster cooling rate, less amount of austenite transformation takes place.

In contrast, a more austenite phase appears at a slow cooling rate, leading to a Widmanstatten austenite structure. Sometimes, this Widmanstatten type structure has occurred during ferrite transformation and has inferior mechanical properties. The microstructure of the welding/fusion zone can be controlled by proper selection of filler metal, dilution, by the cooling of weld and base metal. The cooling rate is the primary factor in HAZ, which decides the percentage of ferrite and austenite in this zone. Processes like electron beam, laser beam welding, and resistance welding have a fast-cooling rate compared to other processes, so the transformation of austenite from ferrite is retarded. Resistance to pitting corrosion is affected by the ferrite content in the weld metal, and resistance increases with an increase of ferrite content up to 50% of the ferrite content. GTAW/TIG welding is commonly used to weld duplex stainless steel, but it has a low deposition rate. Duplex stainless steels have lower thermal expansion as compared to austenitic steel.

Formation of secondary austenite is also observed in multipass welding of duplex stainless steel in both weld-metal and HAZ.

### 2.2.5 Precipitation Hardening Stainless Steel (PH stainless steel)

The latest developments in special stainless steel are precipitation hardening steel (PH steel), which combine good strength with high corrosion resistance. The critical elements of this type of steel are Cu, Cb, Ti and Al. During ageing, they precipitate, which render a more complex and more robust matrix. These steels are divided into three different categories depending upon their structural matrix. These are martensitic, semi austenitic and austenitic precipitation hardening steel.

In martensitic PH steel, if the variation of alloying elements varies, it can lead to excess delta ferrite. If a large amount of stable austenite is present, it can be retained at room temperature after annealing. If carbon and nitrogen increase, it may contaminate the weld structure, which also can deteriorate its mechanical properties.

The exact composition of filler metal is used for groove and fillet joints. The austenitic PH steel is generally non-magnetic, and it has an austenitic structure. The semi austenite PH steel is not subjected to cracking because they are typically welded under annealed conditions, and they are precipitated hardened in the 450-600ºC temperature range. The hardness of this steel is also lower than the other two types of PH steel.

#### 2.2.5.1 Weldability & Welding Metallurgy of PH Stainless Steel

For suitable quality welding, the preheating of the base metal and post-heating of the welded structure should be chosen to obtain the required weld metal properties. The austenitic PH stainless steel is more difficult to weld because of hot cracking and liquation problems. As PH stainless steel exhibits a low percentage of carbon content in the base metal, hydrogen-induced cracking is absent during the welding of PH stainless steel. Standard martensitic stainless steel reveals a primary '*FA'* or '*F'* phase during solidification. The change in phase from liquid to solid or the sequence of phase changes for the martensitic and semi-austenitic PH stainless steel follow the following series.

$$L \rightarrow L + F_p \rightarrow F_p \rightarrow F_p + A \rightarrow F_p + A + M \rightarrow F_p + M \qquad [34]$$

## 2.3 Effect of Alloying Elements in Stainless Steel

Stainless steel includes several alloying elements, which are intentionally added to achieve the desired mechanical, metallurgical, and corrosion resistance properties by optimizing the percentage of the essential alloying elements. The following sections define the alloying additions with the specific reasons for their presence.

***Interstitial Element - Carbon (C):*** Iron is alloyed with carbon to make steel, giving hardness and strength. A small percentage of carbon is added in the case of austenitic and ferrite steel to

achieve a carbide precipitation free weld. Without carbon, it is impossible to give strength in the case of pure iron by heat treatment. It eliminates the chances of intergranular corrosion as it existed in earlier stainless steel due to carbide.[33]

***Interstitial Element - Nitrogen (N):*** Nitrogen is intentionally added in small quantities in duplex stainless steel grades. some of the austenite stainless steel grades improve the strength of the steel by enhancing austenite in the microstructure. [34] But the solubility of nitrogen is significantly less in the case of stainless steel. For DSS welding, nitrogen is sometimes added to the shielding gas to compensate for nitrogen loss through welding. On the other side, it harms the toughness of ferritic and martensitic stainless steel. [35]

***Chromium (Cr)*:** Chromium is the most significant alloying element added to steel to increase the oxidation resistance. The corrosion resistance increases as more chromium are added. In duplex stainless steel (DSS), its range is 20-29% to the ferrite phase in the microstructure. Chromium is a significant ferrite promoter element, and on the other side, it also promotes carbide, and it is the crucial ingredient of intermetallic compounds in duplex stainless steel. The well-known complex form of carbide like $M_{23}C_6$ is also found in duplex stainless steel weld metal during welding at high temperatures. The most predominant element in this carbide precipitation is Cr and C, with Mo and Fe elements. Sometimes other carbides like $M_7C_3$ and $M_6C$ were also precipitated in the microstructure.

***Nickel (Ni):*** Nickel is a strong austenite stabilizer. It is an essential element in both austenitic and duplex stainless steel. It provides ductility, toughness, strength by promoting austenite even at low temperatures. It is also favourable in an acidic environment to resist pitting corrosion. The optimum quantity of Ni with other essential elements like ***Cr*** and ***Mo*** results in a balanced microstructure, especially in duplex stainless steel. A significant increase in impact toughness is also noticed at low temperatures.

***Molybdenum (Mo):*** The melting point of molybdenum is 2623°C, making it essential to use in stainless steel with other alloying elements to give strength at high temperatures. Molybdenum is also an austenite promoter, and the addition of this element improves the resistance to uniform and pitting corrosion in the acidic environment. [36] Molybdenum is also responsible for forming secondary phases in different types of stainless steel, such as ferritic, austenitic and duplex stainless steel. [35] As a ferrite promoter, it also increases carbide precipitation formation and results in the high hardness in some martensitic stainless steel.

***Manganese (Mn):*** Indeed, manganese is added to every type of steel. In most of the austenitic grades, it is added up to 2 % and martensitic stainless steel. Its percentage is less than 1.25% in a variety of stainless steel. [33] Manganese is considered an austenite promoter, but the

amount of austenite growth depends on the amount of nickel present in the steel. The temperature decides the stabilization of different phase, i.e. at low temperature, it promotes/stabilize the austenite and at a higher temperature. It enables/stabilize ferrite in the microstructure. Its presence increases the chances of solubility of nitrogen. Manganese also helps in austenite distribution in the microstructure.[35]

***Silicon (Si):*** Virtually, it is present in all types of stainless steel, and it acts as a wetting agent. It is also considered a deoxidant element that plays a vital role at both higher and low temperatures. In addition, a higher percentage of silicon helps to promote ferrite. In most of the grades, its weight percentage lies near 1%.

***Other Significant Elements:*** In addition to the above elements, some other elements are also added to different stainless steel, which performs various functions. The aspects like titanium (Ti), Niobium (Nb), tungsten (W), tantalum (Ta), and vanadium (V) are added to promote carbide formation. Niobium (Nb) and titanium (Ti) are used to stabilize the carbon to avoid intergranular corrosion in austenitic stainless steel. Whereas tantalum (Ta), tungsten (W), and vanadium (V) help to increase the strength at elevated temperature by carbide dispersion in the form of fine particles. [34] However, copper's small addition improves machinability and formability and enhances corrosion resistance.

## 2.4 Literature Review

In this chapter, a brief review of the literature on the studies related to GTAW/TIG, A-TIG welding and hybrid processes of a different kind on a variety of stainless-steels using different welding parameters are discussed. The welding community has carried out numerous research studies for predicting and enhancing mechanical properties of the GTAW/TIG welded joint. GTAW/TIG welding can weld different kinds of steel and other metals. Researchers try its variants to determine the influence of various process parameters on mechanical properties and their microstructures. Weld penetration depth (weld morphology) and the factors responsible for this change have been reported by many researchers. Some researchers have carried out their study on the effect of different shielding gases and their mixtures on different types of steel. The available literature is categorized into the following broad categories:

- Influence of Activated Flux on Microstructure and the Mechanical Properties.
- Impact of Current and Shielding Gas on the Bead Characteristics.
- Effect of Activated Flux on Marangoni convection and Arc Constriction.

- Effect of Process Parameters on Temperature Distribution and Associated Properties
- Effect of Hybrid Process.

### 2.4.1 Influence of Activated Flux on Microstructure and Mechanical Properties

**Arunkumar et al.** [37] studied the effect of activated flux on the microstructure and mechanical properties of 9Cr-1Mo steel. A-TIG welding was performed with a single pass, while the multipass welding run was made with conventional TIG welding. The authors concluded that the constriction behaviour of A-TIG welding helps to achieve a higher depth of penetration. The higher strength of the joint was achieved by A-TIG welding compared to multipass conventional TIG welding, but the multipass TIG welding possessed higher toughness than the A-TIG weld joint after post-weld heat treatment (PWHT). No degradation was observed in the microstructure, and mechanical properties of the A-TIG welded joint as compared to the joints produced by the conventional TIG welding process.

**Arivazhagan &Vasudevan** [38] studied A-TIG welding of 12 mm thick 2.25 Cr-1Mo (P22) steel with in-house developed activated fluxes. The researchers examined the effect of post-weld heat treatment (PWHT) on the impact toughness. Double layers were used to complete the joint at 250 A current. No crack was detected in the weld. There was no pro-eutectoid ferrite in the weld metal, and the toughness was found to be 133 J. After PWHT at 730°C for one hour, its toughness value increased to 177 J.

**Chern et al.** [39] studied the influence of the single compound fluxes in the TIG welding on surface appearance, weld morphology, distortion, mechanical properties, oxygen in activated fluxes, and arc constriction microstructures on duplex stainless steel. A significant increase in weld penetration was found with oxide-based fluxes like $SiO_2$, $MoO_3$, and $Cr_2O_3$ fluxes. Hence, the A-TIG welding process increases weld bead penetration, and the weld depth-to-width ratio reduces the angular distortion and improves tensile strength.

**Hosseini et al.** [40] conducted an experimental study on nitrogen loss and its effects on the microstructure of multipass TIG welding of a super duplex stainless steel. They experimented on two different welding speeds on a 6 mm thick plate by using pure Ar shielding. They found ferrite contents increased from 55% in the base metal to 75% and 79% after four passes in the weld metal at LH & HH input. Nitrides formed with an increasing number of passes, especially for low heat input welds. Nitrogen content decreased from 0.28 wt. % to 0.17 wt. % and 0.10 wt. % after four passes & the grain widths increased by around 29 μm and 48 μm after three additional passes with low and high heat input.

**Sakthivel et al.** [41] investigated the creep rupture strength of austenitic stainless steel (AISI 316) joints using single-pass A-TIG and multi-pass TIG (MP-TIG) welding processes. Coating of a mixed component flux was applied on the weld line surface. The authors found that the weld zone in both types of welding joints possessed columnar and equiaxed dendrites with δ-ferrite at the border of fusion and HAZ. Their result revealed that both the weld joints consisted of lower creep rupture strength than the base metal, but the A – TIG welding joint exhibited higher creep-rupture strength than the MP-TIG joint. Both the MP – TIG and A – TIG were fractured from the weld centre during the creep rupture test. Reduced creep cavitation's in the weld zone of the A – TIG joint was also observed.

**Ruan et al.** [42] did a study by employing double wire metal inert gas welding (MIG) on a 6082-T6 Al-alloy plate. $SiO_2$ activated flux was applied partially on the plate surface. Optical, scanning electron microscopy and energy dispersive spectroscopy were employed for microstructural analysis. The authors observed no significant difference in micro-hardness and tensile strength of the joints prepared with the coated and uncoated surface. The wider heat-affected zone (HAZ) with $SiO_2$ flux was observed as compared to without flux. The penetration with $SiO_2$ flux was found 26% higher than without flux penetration but did not significantly impact the tensile strength.

**Vasudevan and Vasantharaja** [43] studied the influence of A-TIG welding of low activated ferritic/martensitic (LAFM) steel on the square butt joint configuration on both sides of the joint. The authors found different types of martensite in the fusion zone (FZ) and heat-affected zone (HAZ). Coarse and harder martensite (420–430 VHN) was found in the weld and HAZ, while PWHT condition possessed tempered martensite (256 VHN). As the fracture always occurred from the base metal, A – TIG welding joint exhibited good tensile strength. It also reported that the mechanical properties like strength and ductility of A – TIG welded joint were slightly less than the electron beam welded joint and the base metal but can be improved by the PWHT process. (expand PWHT)

**Fu and Yang** [44] did a study on "Crystallography and morphology of a lathy ferrite in Fe–Cr–Ni alloys during directional solidification". They maintained a temperature gradient in the liquid of about 20 K/mm, and the pulling rate of the sample was 50 μm/s. The voltage and time for the etching were 22 V and 60 s, respectively. They found that the lathy ferrite is arranged in an entangled cluster and is enveloped by austenite. That is a typical characteristic of peritectic transformation.

**Xie et al.** [45] investigated the influence of nano-particles strengthening activating flux on the microstructural changes and mechanical properties of TIG-welded joints of AZ31 magnesium

alloy. The authors used mixed $TiO_2$, and nano-SiC particles (60:40) coated on the samples before welding tests. An increase in penetration observed due to the application of $TiO_2$. The author reported that part of SiC particles decreased the precipitation of the β-$Mg_{17}Al_{12}$ and reacted with AZ31 magnesium alloy to produce $Al_4C_3$ and $Mg_2Si$ phases. Microhardness in HAZ decreased due to the coarsened α-Mg grains. The author also reported that the UTS of welding joints increased initially because of the refinement of α-Mg grains and strengthening effects of distributed particles including β-$Mg_{17}Al_{12}$, $Mg_2Si$ and SiC, but then decreased speedily due to accumulations of the nano SiC particles.

**Sharma et al.** [46] studied dissimilar metal joining, i.e., P-92 and 304-H steel, using activated TIG welding with oxygen-rich fluxes ($SiO_2$, $TiO_2$, $MoO_3$, and $Cr_2O_3$) on the 8 mm thick plates. Their finding reveals the presence of untempered martensite with a gradual increase of microhardness in the weld zone and HAZ. They also concluded that the tensile strength of the joint provided a significant value, i.e., 688.6.2 MPa with a lower strain value and a lower toughness value, i.e., 30 J.

**Sharma et al.** [47] carried out another study comparing multipass TIG and A-TIG welding on dissimilar metals ( P-92 and 304-H) of 8 mm thickness. Their study proved that the A- TIG welding is economically better than multipass TIG welding, as A-TIG requires no edge preparation and can be completed in a single run. The tensile strength results were also found better than conventional TIG welding.

**Vasantharaja et al.** [48] studied the residual stress and distortion in SS 316LN made by TIG and A-TIG welding processes that involved different joint configurations. The authors concluded that different joint designs exhibited different microstructures, peak tensile residual stress and angular distortion values. The double side joint of A-TIG welding creates coarser grain with lower ferrite content and low tensile residual stress. In contrast, the double-side joint of the TIG weld produces small grain with higher ferrite content and helps to form higher tensile residual stress values. They found a significant difference between values of residual stress and distortion. The main difference in values was due to the lower (straight edge) and higher (v-groove) weld metal volume. The author recommended A – TIG welding process to minimize residual stress and distortion in the weld joint.

### 2.4.2 Impact of Current and Shielding Gas on Bead Characteristics

**Tathgir et al.** [8] studied the influence of shielding gas environment and current in $TiO_2$ assisted A – TIG welding on different grades of stainless – steels, namely AISI 1020, AISI 304, AISI 316, and Duplex 2205, using 140 A and 170 A with pure Ar and Ar + 5 % $H_2$ shielding

environment. A significant increase in DOP and reduction in width to penetration was reported when A-TIG was performed with Ar + 5 % $H_2$ shielding the gas environment. The use of flux was found more significant to achieve higher DoP in the case of Duplex 2205 (124%) followed by AISI 316 (47%), AISI 304 (44.3%) and AISI 1020 (37.8%), respectively. Microstructure observations revealed more austenite in AISI 304 and AISI 316 stainless – steel. Sufficient austenite transformation from ferrite took place in the case of Duplex stainless steel.

**Tusek and Suban** [15] investigated the impact of hydrogen blended argon shielding gas in TIG and MIG welding of high-alloy stainless steel. This study was carried out with different volume per cent additions of hydrogen to the argon, i.e., 0.5, 1.0, 5.0, 10 and 20%. Five welds were produced using three levels of currents, i.e., 150 A, 200 A and 250 A in different Ar and $H_2$ mixture shielding environments. TIG welding was performed on 8 mm thick, and MIG welding was performed on a 10 mm thick workpiece. The addition of hydrogen to argon increased the melting rate of the job by 10-30%. It was also reported that the mixture of Ar + $H_2$ found a stable process and produced quality weld in the case of TIG welding of high alloy austenitic stainless steel. Finally, the authors recommended the 20% addition of hydrogen in argon, but the same was not valid for MIG welding.

**Durgutlu** [49] investigated the effect of hydrogen mixed argon as a shielding gas on the TIG welding joint of AISI-316 stainless steel. The author used three different volume percentages of shielding gas for his experimental study, i.e., pure argon, Ar + 1.5% $H_2$ and Ar + 5% $H_2$. The highest tensile strength of the AISI 316 TIG was achieved with shielding gas of Ar + 1.5% $H_2$. After the bend test, no surface cracks were found on the samples that were welded with three variants of gas mixtures. The result revealed low hardness of weld metal as compared to HAZ and base metal hardness. The author also reported that the more hydrogen content present in the shielding gas affects the mean size and orientation of the weld metal, resulting in deviations of the grains.

**Gulenc et al.** [50] studied the effect of hydrogen mixed argon as shielding gas in metal inert gas welding of 10 mm thick AISI 304L stainless steel using 1.2 mm diameter of filler wire. MIG welding was carried out with different mixtures of shielding gas, which include pure argon, Ar + 1.5% $H_2$ and Ar + 5% $H_2$ at three levels of current, 140, 180 and 240 A. Maximum tensile strength was achieved with Ar + 1.5% $H_2$ shielding environment and with maximum current, i.e., 240 A. They observed that the specimens welded with pure Ar contributed less tensile strength as compared to the mixture of hydrogen and argon. Results revealed that the impact strength of the welding increases with Ar + 5% shielding mixture (high $H_2$ content) and

higher heat input. In addition, base metal hardness was found more than the hardness of HAZ and weld metal.

**Michler** [51] studied the toughness and hydrogen compatibility of austenitic stainless-steel weld at cryogenic temperature. The author used different types of austenitic steel with a suitable combination of filler wires for the multipass TIG welding of 12 mm thick steel sheets. The toughness test (Charpy) was performed for each specimen compared with -196°C, and no significant difference was found. All the toughness value was greater than the standard values of toughness at -10°C. For martensite presence, samples were cut from all weld specimens and kept at -269°C. Cooling at such a low temperature and the presence of δ-ferrite could not produce more martensite. No correlation was found between δ-ferrite and toughness.

**Lu et al.** [52] investigated the effect of the reverse of Marangoni convection on the weld bead profile. The stationary TIG welding experiments were done on AISI 304 stainless steel with a lower oxygen content of 0.0038 w% and sulphur content 0.0005 w% by using direct current. Two variants of shielding gas mixtures, i.e., Ar + 0.1% $O_2$ and Ar + 0.3% $O_2$, were used for TIG welding. Authors found that the high percentage of oxygen content in the shielding environment (Ar + 0.3% $O_2$) changes the surface tension gradient from negative to positive, consequently changing the flow of molten metal from outward to inward.

**Naumann and Michler** [53] studied hydrogen embrittlement of orbital TIG-welded austenitic stainless steels at -50° C. The 5% δ-ferrite (approximate) content was found in all TIG welded joints. Joints were welded under hydrogen atmosphere and helium atmosphere. During the tensile test, the specimens of hydrogen atmosphere were fractured from the base metal, and specimens of helium study were fractured from fusion/HAZ. They concluded that the δ-ferrite content did not influence the hydrogen embrittlement environment (HEE) compared to the base metal. The authors also concluded that variations in local Ni contents are more critical for HEE than welding.

**Lu et al.** [54] investigated the weld morphology and the effect of oxygen on tungsten electrode under two shielding gas environments. Ar and Ar + $CO_2$ double-shielded TIG welding of SUS 304 stainless steel was performed with a special torch to impinge two shielding gases on the weld pool. They concluded that the flow rate of inner shielding gas had undergone a significant impact on the weld shape and consequently produced oxidised and wide weld beads with less penetration. On the other hand, the outer layer shielding environment with an active gas ($CO_2$) dissolved well in the molten metal and tended the outward flow of molten metal to the inward direction. Hence the authors also prove that Marangoni convection occurred when weld metal oxygen content reached above $70\times10^{-6}$.

**Li et al.** [55] carried out a comparative study for conventional TIG welding using pure He with a double shielding environment (He + 20 % $O_2$) by varying process parameters (such as welding speed, arc length and current) on martensitic stainless steel having less than 5% Ni content. They found that the oxygen mixed helium gas produced narrow and deeper weld beads compared to single shielded gas. Deep penetration was achieved with a minimum gap of 1.5 mm and vice versa. The authors also reported that arc length was significant in the case of the double shielding method compared to the pure helium or single shielding method. The high oxygen content enhances inward flow, but the thick oxide layer on the weld pool crate reverse effect and deteriorate mechanical properties.

**Niagaj** [56] carried out an experimental investigation to study the effect of A-TIG welding on the deformation of austenitic steel components. It was investigated that with the use of TIG and A-TIG welding, there is a reduction in angular distortion in austenitic stainless steel with activated flux BC-31. It was found that welding pipe connectors with austenitic steel plates produced four times less distortion as compared to the traditional TIG welding process.

**Zou et al.** [57] investigated the effect of oxygen content in the outer layer of shielding with Ar as inner shielding gas on the weld shape with the AA-TIG (advance activated TIG) welding of duplex stainless steel. It was found that the increased oxygen content helps to improve both the depth to width ratio and the density of oxide film. In addition, the authors observed a KS relationship between the Widmanstatten austenite phase and the crystallographic orientation of the ferrite phase. Thus, the oxide layer present on the weld pool plays an essential role in affecting the crystallographic orientation relationship between the intragranular and ferrite phases.

**Lothongkum et al.** [58] experimented with TIG pulse welding of 304L austenitic stainless steel of 3mm thick plate in flat, vertical and overhead positions. The authors concluded that the nitrogen content of 3-5% (v/v.) in the argon gas was enough to control the delta (δ) ferrite contents in the generally accepted range of 3-12% (v/v.). They found that the welding speeds in three different positions were limited to 3.4 mm/s at 55% on time with appropriately adjusted pulse and base currents.

**Hosseini et al.** [59] studied multipass TIG welding using different heat inputs, i.e., low and high, on super duplex stainless steel to find out the microstructural change and the corrosion resistance. Their study found that the reheating of weld metal in multipass TIG welding produced nitrides at the fusion zone boundary, and the weld zone is enriched with larger ferrite grains with intergranular nitrides. Furthermore, the precipitation of the sigma phase was

observed near the fusion zone and a loss of nitrogen in the weld zone. Therefore, they suggested the use of nitrogen in shielding and higher heat input for this type of steel.

**Sridhar et al.** [60] performed a study to find the effect of welding current on the bead profile of both sides welded joints of austenitic stainless steel by SAW. For this study, they use 12 mm thick plates and experimented with three current levels, i.e., 400, 430 and 460 A. This study found that the varied value of current significantly increases the penetration area, bead height and reinforcement area, and penetration area with a bit of change in bead width. They also found that a high value of current also produces maximum tensile strength. The resultant microstructure of the weld zone contained a mixed morphology of delta ferrite dendrite (lathy and skeletal), and no equiaxed grains were found in the fusion zone.

**Migiakis et al.** [61] studied plasma keyhole welding using argon or argon with 2 vol % addition of nitrogen in the plasma and shielding gas on super duplex stainless steel to improve the resultant austenite and ferrite balance of the fusion zone. The ratio of austenite to ferrite increases with the addition of 2 % $N_2$ in the plasma. However, a globular austenite morphology was observed with the addition of $N_2$ in Ar gas. In addition, a Widmanstatten austenite morphology was observed in the fusion zone with Ar shielding. A significant increase in hardness of the fusion zone was reported with Ar + 2 % $N_2$, and all the toughness specimens showed good toughness value but less than the parent metal.

### 2.4.3 Effect of Activated Flux on Marangoni Convection and Arc Constriction

**Modenesi et al.** [3] studied A-TIG welding on austenitic stainless steel (AISI 304) plates of 5 to 8 mm thickness with a single element/flux. In this study, weld geometry change was compared to variations in the electrical signals from the arc and the arc shape. The use of fluxes, like $SiO_2$, $TiO_2$, $Cr_2O_3$ and $AlF_3$, and arc constriction behaviour significantly enhance penetration as compared with conventional TIG welding. Result reveals that single component flux significantly increased the penetration of the weld bead (up to 300%) with < 3% change in voltage. Furthermore, the only 0.4 % difference of mean delta ferrite in the weld zone of TIG and A – TIG was observed (i.e., 5.7 % in the case of TIG and 6.1 % in case of A – TIG).

**Tathgir et al.** [9] studied the effect of fourteen different activated fluxes on penetration was evaluated on four different plates of steel namely AISI 1020, AISI 304, AISI 316, Duplex 2205 at 125 A current under Ar shielding gas at a travel speed of 2.2mm/sec. Based on the highest DoP, five oxide-based fluxes (i.e., $SiO_2$, $TiO_2$, $MoS_2$, $MoO_3$, and $CrO_3$) were selected to study the influence of mixed shielding environment of 95% Ar + 5% $H_2$ and 70% Ar + 30% He. The addition of $H_2$ in shielding gas helps increase the thermal efficiency/heat conduction, increasing

the DOP. In addition, the authors found that arc constriction behaviour of arc column and positive surface tension-gradient changed material flow pattern from periphery to centripetal direction.

**Bhattacharya** [13] investigated the metal flow behaviour in flux activated tungsten inert gas welding (A-TIG) of revisited arc. The author experimented on AISI 304 steel of a 6 mm thick plate and compared the result with conventional TIG welding. He proved that the surface tension induced by Marangoni flow reverses the direction using activated fluxes. In the case of traditional TIG welding, the electromagnetic Lorentz force acts in a downward trend but in surface tension driven Marangoni flow works along the centrifugal direction. It was also found that the presence of oxygen in activated fluxes, arc constriction was observed.

**Dhandha & Badheka** [62] explore the effect of activating fluxes on weld bead morphology of P91 steel (modified 9Cr–1Mo or P91 steel) using CaO, $Fe_2O_3$, $TiO_2$, ZnO, $MnO_2$ and $CrO_3$ fluxes. The author concluded that the activating flux considerably affects the penetration depth and the decreased bead width with $Fe_2O_3$, ZnO, $MnO_2$, and $CrO_3$. In addition, they reported that the Marangoni effect, arc constriction, electromagnetic force, and buoyancy force played a major role in increasing penetration depth.

**Ruckert et al.** [63] proposed optimization of silica coating design to increase TIG welding productivity on 304L stainless steel. Two coating designs were investigated. One was a 20 mm wide coating, and the second design was investigated by two parallel coatings 1–7 mm apart around the weld line. The welding was carried out on 6 mm thick sheet with a 2.4 mm diameter of the electrode at three levels of current (100 A, 125 A and 150 A) with an Ar shielding environment. The weld penetration firstly increased with coating up to 50–70 µm and subsequently decreased. The authors found that the optimized coating thickness in A-TIG should be 40 and 70 µm depending on the heat input, and for FB-TIG welding, it was justified for an extensive range of thickness coats.

**Lin and Wu** [64] carried out an experimental study to explore the influence of activated fluxes and process parameters on the weld penetration and depth-to-width ratio (DWR) of the Inconel alloy joint. The authors used both A-TIG and face bound TIG (FB-TIG) for their study. In the initial research, they used single-component fluxes, and after the initial research, four different fluxes were selected to make six new mixtures of 50% ratio of each. The DWR of Inconel 718 alloy welds improved from 60° to 75° of electrode angle was 28%. They concluded that the weld bead geometry via FB-TIG with a 1.2 mm gap is slightly less than applying A-TIG. Results revealed that the FB-TIG process produced full penetration in a single pass weld for a 6.35 mm thick job.

**Sambherao** [65] investigated the use of activated flux for increasing penetration depth with the GTAW process in austenitic stainless steel. The effect of multi-component fluxes of specific oxides on the surface appearance, weld morphology, and retained delta-ferrite content with TIG process on 6mm thick AISI 316 steel was investigated. It was found that $TiO_2$ flux has a significant effect on the depth of penetration for this steel. The author reported that Marangoni convection and constriction of arc are the main factors behind this. The addition of Fe2O3 with TiO2 flux found the Marangoni convection effect, leading to more weld depth than that of $TiO_2$ flux only.

### 2.4.4 Effect of Process Parameters on Temperature Distribution and Associated Properties

**Okano and Mochizuki** [66] studied the transient distortion behaviour during TIG welding of thin steel plates (2.3 mm). They found longitudinal bending and angular distortions monotonically increased with welding heat input. The authors also concluded that the evolution of the plastic strain developed during TIG welding was influenced by the temperature distribution and the transient distortion behaviour during welding.

**Zhang et al.** [67] carried out a study to find the effect of welding parameters on temperature distribution in the case of twin-electrode (separated and insulated) coupled TIG welding arc. The author used a 3.2 mm diameter tungsten electrode with argon shielding. The arc temperatures were measured, and the maximum temperature was found in the middle of both electrodes. The authors concluded that the arc length affects the peak temperature and found it increased when the arc length decreased and vice versa due to reduced current and thermal density by the large area of contact with an arc.

### 2.4.5 Effect of Hybrid Process

**Ding et al.** [68] studied TIG–MIG hybrid welding of ferritic stainless steels and magnesium alloys with Cu interlayer of different thicknesses. They tried different thicknesses of Cu foil as an interlayer between two dissimilar metals. They found that melted Mg weld metal wets the ferritic stainless steels surface to form a brazed Mg–Cu to steel when the interlayer thickness of 0.02 mm was used. The results revealed that the tensile-shear strength with 0.1 mm thickness Cu interlayer improved by 47% compared to 0.02 mm thickness Cu interlayer joints.

**Shanghai et al.** [69] carried out an experimental study to find the technology and welding joint properties of hybrid Laser-TIG welding on a 16 mm thick plate. Hybrid welding was found significant for lowering the aspect ratio of the weld. Hence the gas in the molten pool can rise and escape quickly. They concluded that the hybrid process enhances welding speed and

optimizes the energy input. The transition and grain size of the microstructure of the hybrid welding joint was found better with a higher hardness value than the base material. The tensile strength and impact toughness were observed as good as the base metal.

**Reisgen et al.** [24] investigated a hybrid process of laser beam GMAW and laser beam submerged arc welding on 38 mm (with GMAW setup) and 35 mm (with SAW setup) thick plates which had double 'Y' joint configuration. They found that the hybrid welding via GMAW setup could not fill the groove in a single pass, and hybrid welding with SAW set-up with 3 mm wire filled the groove in a single pass. In the case of the GMAW set-up, pores were produced in the fusion zone, and no pores were observed in the SAW-dominated region. Refined grains were observed in LB-dominated areas, whereas coarse grains were found in SAW-dominated areas. Tensile test results revealed that the fracture took place out of fusion and HAZ. The specimens of LB dominated space for toughness produced better values with slightly higher hardness values.

## 2.5 Summary of Literature

The present research focuses on the A – TIG welding and hybrid process to explore the use of the A – TIG process to increase the productivity of both the GTAW/TIG welding and the SAW process. So, literature was studied extensively and divided into different segments, summarized below.

### ➢ *Influence of Activated Flux on Microstructure and Mechanical Properties*

- A study of multipass TIG and A-TIG welding on dissimilar metals (P-92 and 304-H) of 8 mm thickness reveals that A- TIG welding is economically better than multipass TIG welding and produces good tensile strength. [46, 47]
- The mean delta ferrite contents in the weld zone were reported as 5.7 % and 6.1 % for the TIG and A-TIG processes. [70]
- A-TIG and multi-pass TIG (MP-TIG) welding of AISI 316 stainless steel showed that the weld joints had lower creep rupture strength than the base metal, but A-TIG welding exhibited higher creep-rupture strength than the MP-TIG joint. [41]
- Toughness value increases with $H_2$ content in Ar, but the tensile strength increases up to a maximum with 1.5% $H_2$ in Ar. [54, 60]

### ➢ *Influence of Activated flux and Shielding Gas Environment on Bead Geometry*

- The optimized coating thickness to increase penetration in A-TIG was reported in the range of 40 and 70 µm depending on the heat input. [63]

- Single component fluxes & mixed fluxes increased penetration and DWR. Bead geometry using FB-TIG with a 1.2 mm gap was observed smaller than the A – TIG process. [64]
- Ar + $CO_2$ mixed shielding TIG welding of AISI 304 stainless steel study reveals that the presence of oxygen changes outward flow of molten metal to inward direction. [54]
- $H_2$ mix shielding enhances DOP, and more than 200–300% increase was observed as compared to pure Ar with $TiO_2$, $SiO_2$, or $MoO_3$ fluxes. [49]
- AISI 304 welded with Ar + 0.3% $O_2$ changes the surface tension gradient from negative to positive, promoting reverse Marangoni convection. [52]

### ➢ *Influence of Activated Flux on Marangoni convection and Arc Constriction*

- Activated flux promotes reverse Marangoni effect along with Lorentz force, and arc constriction mechanism causes deeper penetration by reducing the anode root area. [37, 41, 49, 60, 62, 64, 71]
- Marangoni convection occurred when weld metal oxygen content reached above $70\times10^{-6}$. [72]

### ➢ *Influence of Hybrid Process*

- TIG–MIG hybrid welding of ferritic stainless steels and magnesium alloys with Cu interlayer of different thicknesses reveals that the tensile-shear strength with 0.1 mm thickness Cu interlayer improved by 47%. [68]
- Hybrid Laser-TIG welding on 16 mm thick HSLA steel shows that the process is significant for lowering the aspect ratio of weld and easy escape of gas. [69]
- Research of the hybrid process of laser beam GMAW and laser beam SAW on 38 mm and 35 mm plates concluded that GMAW set-up produced pores in the fusion zone, and no pores were observed in the SAW-dominated region. Laser beam dominated area produced good mechanical properties with a slight increase in hardness. Whereas coarse grains were found in the SAW-dominated area. [73]

## 2.6 Gaps in The Existing Literature and Analysis:

In recent years the main focus of the researchers was to achieve more depth of penetration at higher welding speed to improve productivity. So, productivity improvement could be possible only by eliminating the need for edge preparation without affecting the mechanical properties. Hence, some authors have also tried a hybrid process by using a high energy source like LBW with other arc welding processes. However, areas of improvements, techniques, suggestions and limitations based on the literature review are discussed below:

- Weld profile development during stationary A-TIG welding and associated mechanism to achieve deep penetration, change in the weld microstructure, including dendrite and grain growth at different arc exposure of time using different shielding environments, has not been reported.
- Surface active elements in A-TIG welding undergo slag and gas metal reactions and are not found in the literature.
- The thermal energy of arc responsible for a higher depth of penetration has not been quantified.
- The possibility of A-TIG welding in a difficult welding position with coated filler has not been investigated.
- The pattern of retained delta ferrite in the microstructure of the hybrid process (A-TIG + SAW) is another area of study, and no literature is available.
- The presence of oxygen elements in activated flux and their significant participation to change the chemistry of molten metal has not been appropriately addressed.
- A-TIG welding is still not adventure by a hybrid process to weld more than 12 mm thick plates at fast speed and to achieve a higher deposition rate in a single pass.
- During submerged arc welding (SAW) of austenitic stainless steel (AISI 304), the influence of high Basicity Index Flux (B.I – 3.1) and voltage on weld quality and its associated mechanical properties have not been effectively addressed.

# Chapter - 3
## Stationary A-TIG Welding (with "Ar" shielding)

## 3.1 Introduction

The excellent weld quality, stable heat source, and optimum equipment cost in the Gas Tungsten Arc Welding (GTAW) process are essential factors, making this process most widely acceptable for stainless steel [74]. The shallow penetration, lesser dilution, and low deposition rate in a single pass are the main constraints for using GTAW/TIG welding process for thick plates [54, 74, 75]. However, process parameters (such as current and voltage) need to increase to attain deeper penetration, affecting the material properties and further leading to distortion [76] owing to increased thermal energy of arc. Depth of penetration (DoP) or penetration is a vital response parameter in TIG welding, which significantly controls the production rate in autogenous welding. The present study investigates the effect of activated fluxes ($CrO_3$, $SiO_2$, $TiO_2$, $MoS_2$, $MoO_3$) on penetration, dilution, weld chemistry, weld microstructure, and gas and slag metal reactions which is resulted from the extra thermal energy of arc produced. Differently, oxide-based fluxes were investigated in the context of thermal energy of arc, associated penetration, dilution, and weld pool properties.

Oxide-based fluxes decompose at higher temperatures during welding. The surface-active elements in flux decomposed oxygen together result in an increase of the thermal energy of arc in the weld. Furthermore, the thermal energy of arc increases with an arc exposure time, further enhancing penetration and changing the weld pool shape with increased temperature [13]. For this study, an effect of different arc exposure times (2, 4, and 6s) with varying environments of shielding (Ar and Ar + 2.5% $H_2$), with five different oxide-based fluxes, has been studied. Finally, the result has been compared with conventional TIG welding to study their impact on the process.

## 3.2 Materials and Methods

As received, stainless steel plates of 100 mm x 50 mm x 5 – 6 mm (Table 3.1) were used to prepare weld coupons using stationary beads (spots). The chemical composition of the workpiece materials was measured using Foundry Master (optical emission spectroscopy, make: WAS Germany) and is presented in Table 3.1. A-TIG welding was performed on three different stainless plates of steel (i) AISI 304, (ii) AISI 316, and (iii) DUP 2205. All the

experiments were conducted with two different shielding environments, i.e., (i) Ar and (ii) Ar + 2.5% $H_2$ fed at a stream rate of 10L/min.

Table 3.1: Chemical compositions of different workpieces used in the study

| Material | % Composition | | | | | | | | | | | | Thickness (mm) |
|---|---|---|---|---|---|---|---|---|---|---|---|---|---|
| | C | Mn | Si | Cr | Ni | S | P | Mo | Cu | W | Nb | Fe | |
| **AISI 304** | 0.07 | 1.23 | 0.45 | 18.7 | 9.27 | 0.02 | 0.05 | 0.17 | 0.30 | 0.04 | 0.012 | Balance | 5.74 |
| **AISI 316 (for Ar Study)** | 0.005 | 1.28 | 0.21 | 17.6 | 9.49 | 0.02 | 0.06 | 2.1 | 0.45 | 0.14 | 0.026 | Balance | 6.1 |
| **AISI 316 (for Ar + 2.5% $H_2$ Study)** | 0.07 | 1.44 | 0.40 | 18.1 | 9.69 | 0.02 | 0.04 | 1.9 | 0.43 | 0.09 | 0.023 | Balance | 6.1 |
| **Duplex 2205** | 0.036 | 1.83 | 0.397 | 25.1 | 4.68 | 0.005 | 0.027 | 3.08 | 0.183 | 0.02 | 0.002 | Balance | 5.13 |

At first, the weld coupons were ground with the precision grinder and then cleaned with acetone to ensure a contamination-free workpiece surface. Next, fine-grained high purity flux was mixed with acetone to make a paste and then applied on the work surface as a flux coating. The flux paste was then allowed to get dry completely. During this study, conventional GTAW/TIG and A-TIG welding were carried out on Austenitic Stainless Steel (AISI 304 and AISI 316) and Duplex stainless steel (Duplex 2205) using conventional GTAW. Welding was performed under the presence of Ar and Ar + 2.5 % $H_2$ as shielding environment at a flow rate of 10 L/min flow rate, 150 A current, and five different types of fluxes/compounds (Table 3.2). The TIG welding transformer make: 'Techno-Weld 350' was used to conduct the experiments with a 3.2 mm diameter tungsten (2% Th) electrode. The arc length for this study was kept fixed at 3 mm.

Table 3.2: Factors and their levels varied during the study

| Factor | Level | | | | | |
|---|---|---|---|---|---|---|
| | 1 | 2 | 3 | 4 | 5 | 6 |
| Exposure Time (s) | 2 | 4 | 6 | - | - | - |
| Shielding environment | Ar | Ar+ 2.5% $H_2$ | - | - | - | - |
| Flux | No Flux | $CrO_3$ | $SiO_2$ | $TiO_2$ | $MoS_2$ | $MoO_3$ |
| Workpiece material | AISI-304 | AISI-316 | DUP-2205 | | | |

The schematic presentation of stationary spot/beads is presented in Fig. 3.1, which shows the arc hold time (arc exposure time) as 2, 4, and 6 sec for each run.

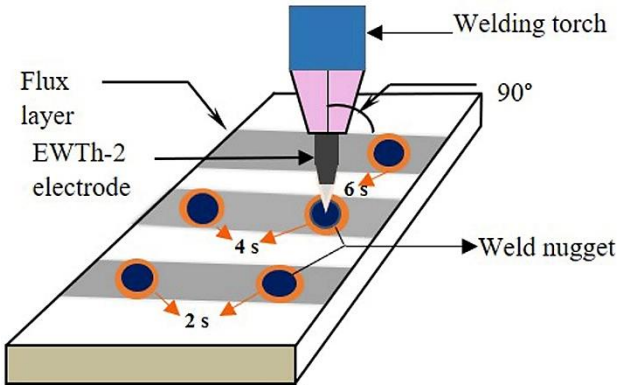


Figure 3.1: Schematic illustration of stationary A-TIG welding

The test specimens were extracted from the weld coupons from the centre of the weld spot for further investigation. The samples were used for optical emission spectroscopy (OES) of Foundry Master-World Wide Analytic System make, Optical Microscopy (OM) with DMILM - Leica make, SEM (JEOL_JSM_6510LV), Energy Dispersive Spectroscopy (EDS), and micro-hardness (Metatech_MVH-1) tests and measurements.

## 3.3 Results and Discussion (Ar Shielding)

### 3.3.1 Effect of Activated Flux on Bead Appearance and Penetration on AISI 304:

The as-welded weld coupons with and without activated fluxes are shown in Fig. 3.2 (AISI 304), which shows the weld surface appearance and effect of different arc exposure times. Due to the effect of reverse Marangoni convection and Lorentz force, the cone formation was observed in the case of A – TIG welding, which also shows the material flow pattern. It was observed that the cone depth increases with the increase of arc exposure time, which consequently increased the penetration of the weld spot (Fig 4.2). In comparison, no cone formation or significant increase in penetration was observed in the case of conventional TIG welding. The presence of activated flux helps in arc constriction/Plasma constriction due to electron capturing phenomena from the periphery/outer zone of the arc and redistribution of the arc column. So, the maximum penetration was observed in the case of $CrO_3$ flux, where more oxygen elements were available in flux vapours for the interaction with the free electrons of the GTAW arc. On the top side of the weld, some amount of flux residue is visible, which should be removed after welding.

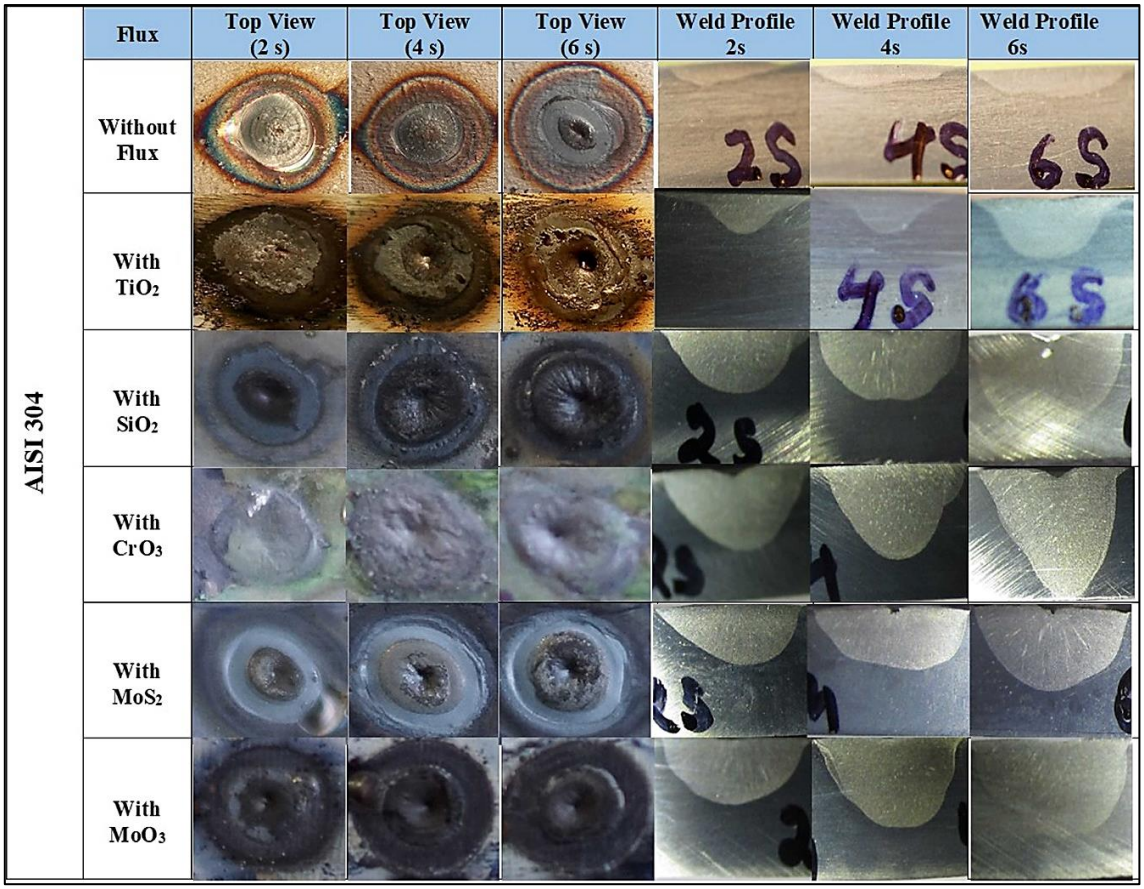


Figure 3.2: Showing the top surface and penetration of TIG and A-TIG welding of AISI 304 at different arc exposure times (i.e., 2s, 4s and 6s) using Ar shielding

### 3.3.2 Effect of Activated Flux on Microstructure of AISI 304:

After conventional TIG and A – TIG welding, all the welding samples were cut from the centre with a margin for surface grinding and polishing. After polishing, all the representative samples of different arc exposure times were etched by "Carpenter Etchant" and observed under the metallurgical microscope. The microstructure of the interface region fusion zone and the parent metal of different magnification such as 10 X, 20 X, and 50 X are presented in Fig. 3.3 to Fig. 3.8. No significant difference in present phases was observed. Still, an increase in the concentration of resultant delta ferrite was observed while comparing the microstructures of 2-sec arc exposure with 6-sec arc exposure time (Fig. 3.3 to Fig. 3.8). In the case of no flux condition, more concentration of the resultant delta ferrite was observed than with flux condition for all arc exposure times. However, in the case of flux condition, at 2-sec arc exposure time, the resultant delta ferrite was not fully developed due to fast cooling. Whereas, in 6 sec, the resulting ferrite matrix was observed as fully developed due to a slow cooling rate. In some cases, the only change in the morphology/type of the resultant delta ferrite content was

observed. In the case of A – TIG with $TiO_2$ flux produces the equiaxed delta ferrite content in the fusion zone at 4 sec arc exposure time (Fig. 3.6_ 50 X).

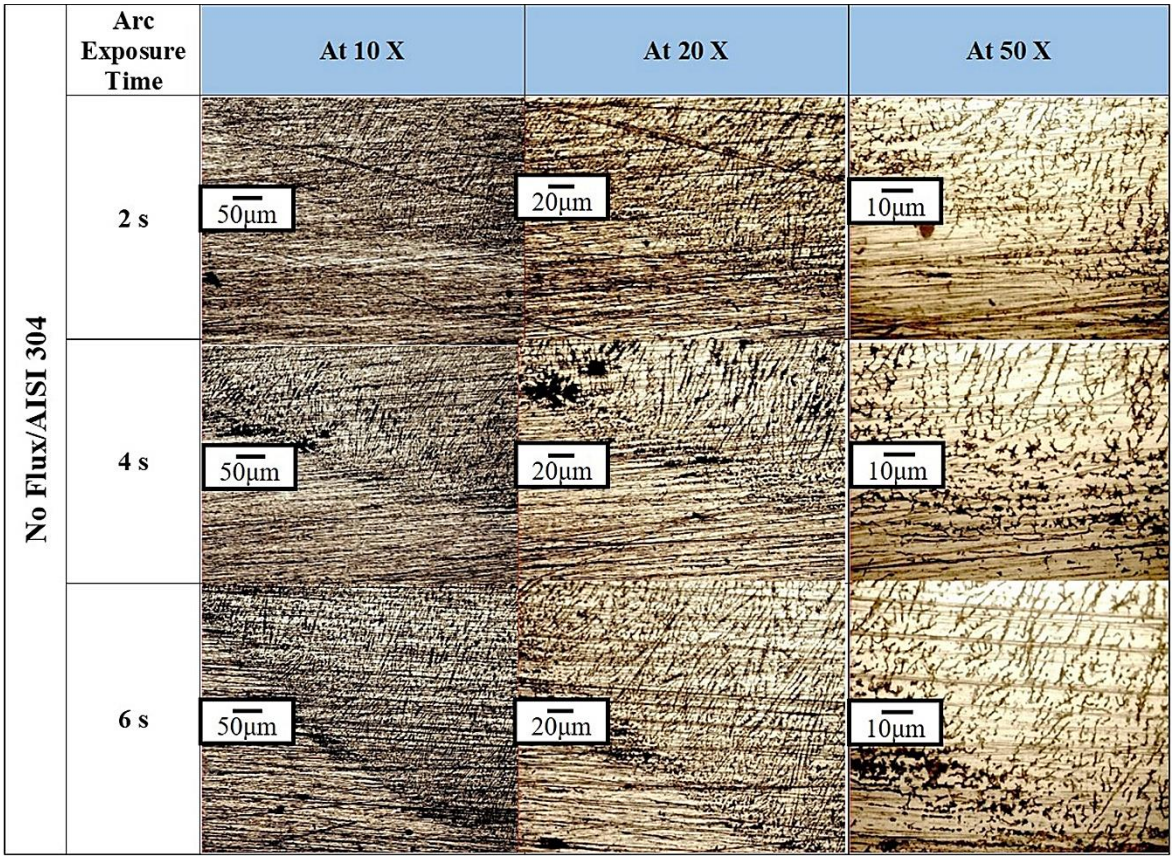


Figure 3.3: Microstructure of different arc exposure time (2s, 4s and 6s) of conventional GTAW/TIG weld on AISI 304 using150 A, Ar shielded with 10 L/min gas flow rate

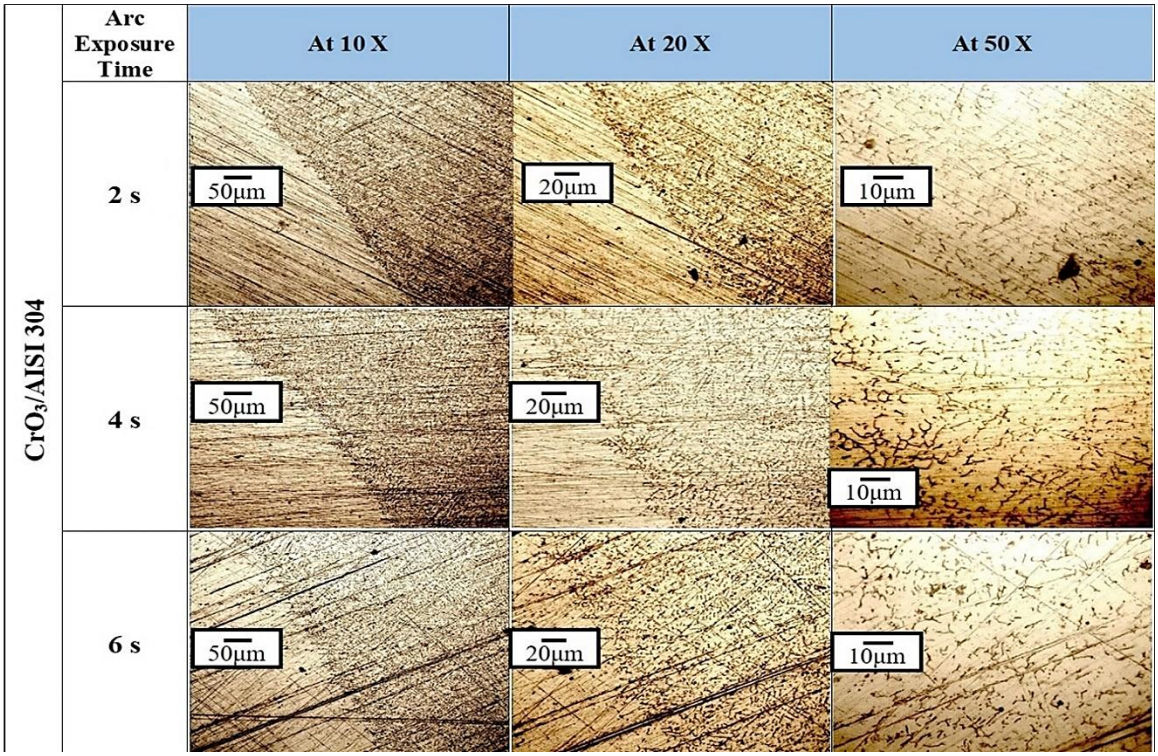


Figure 3.4: Microstructure of different arc exposure time (2s, 4s and 6s) of A-TIG weld with $CrO_3$ on AISI 304 using150 A, Ar shielded with 10 L/min gas flow rate

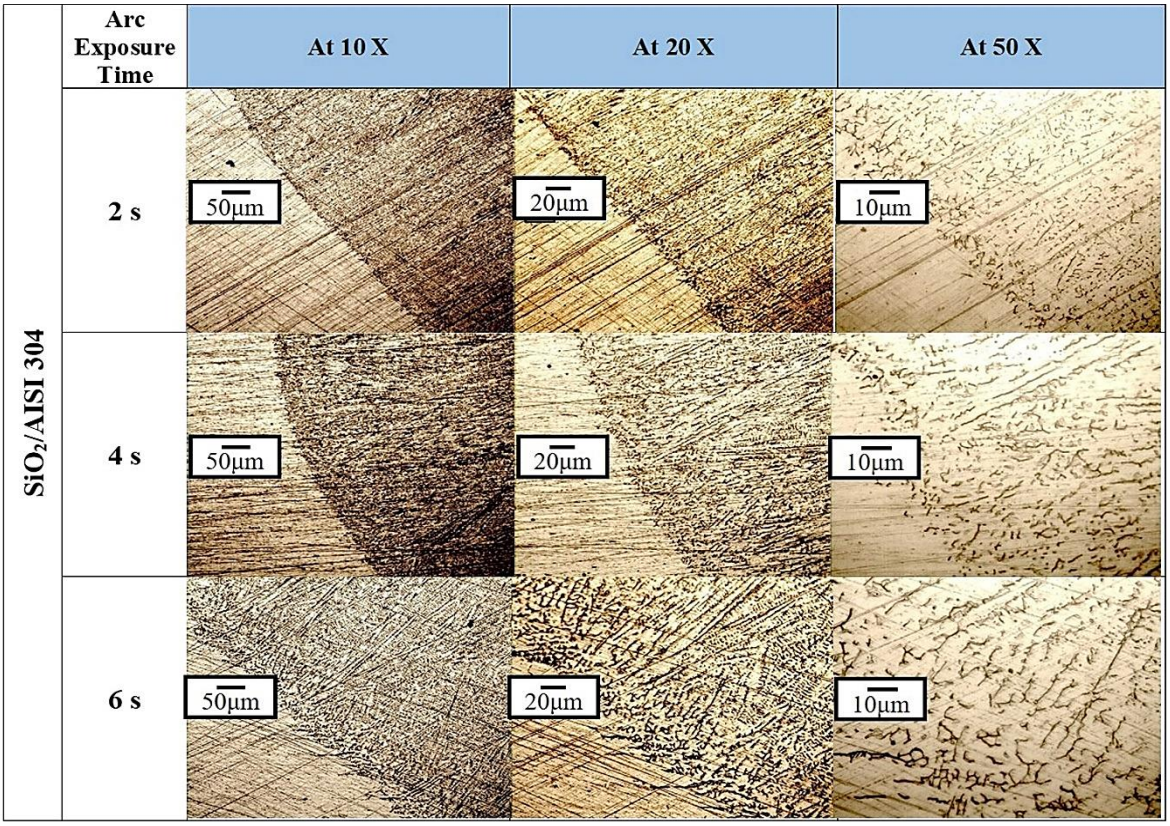


Figure 3.5: Microstructure of different arc exposure time (2s, 4s and 6s) of A-TIG weld with $SiO_2$ on AISI 304 using150 A, Ar shielding with 10 L/min gas flow rate

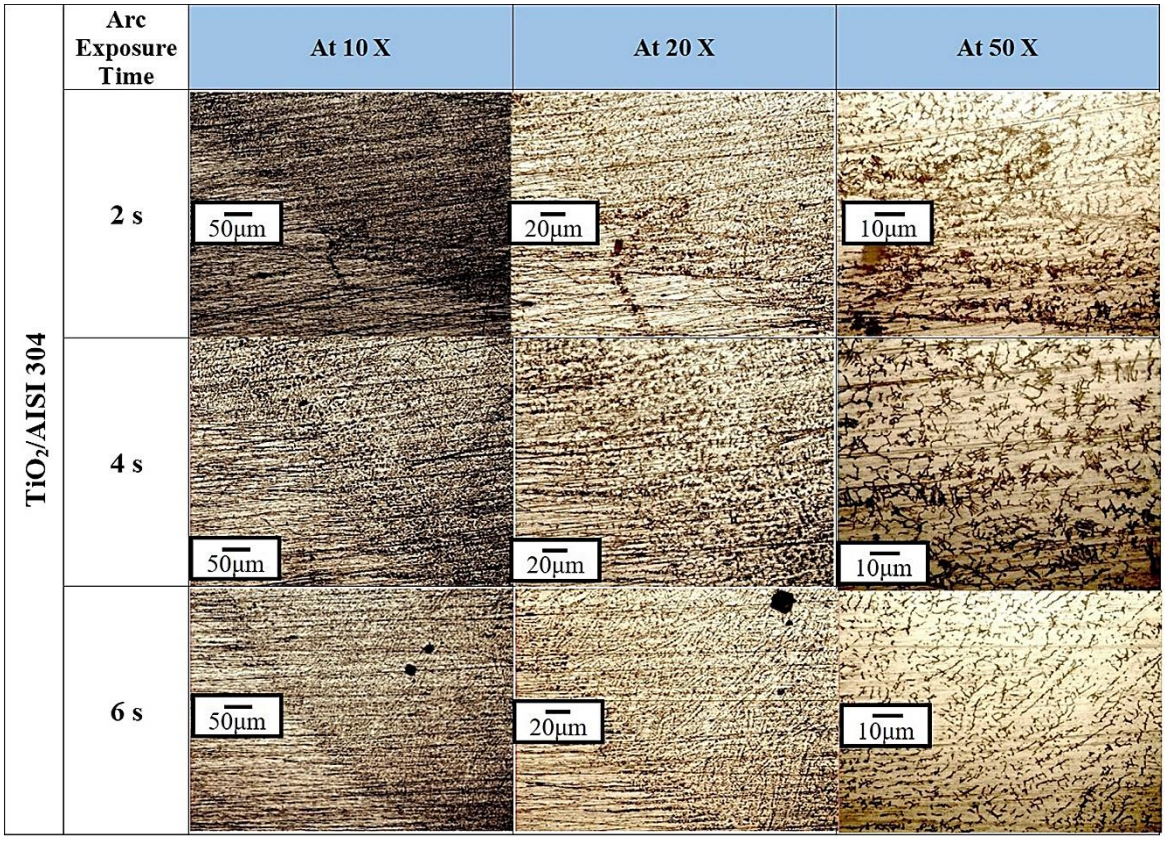


Figure 3.6: Microstructure of different arc exposure time (2s, 4s and 6s) of A-TIG weld with $TiO_2$ on AISI 304 using150 A, Ar shielding with 10 L/min gas flow rate

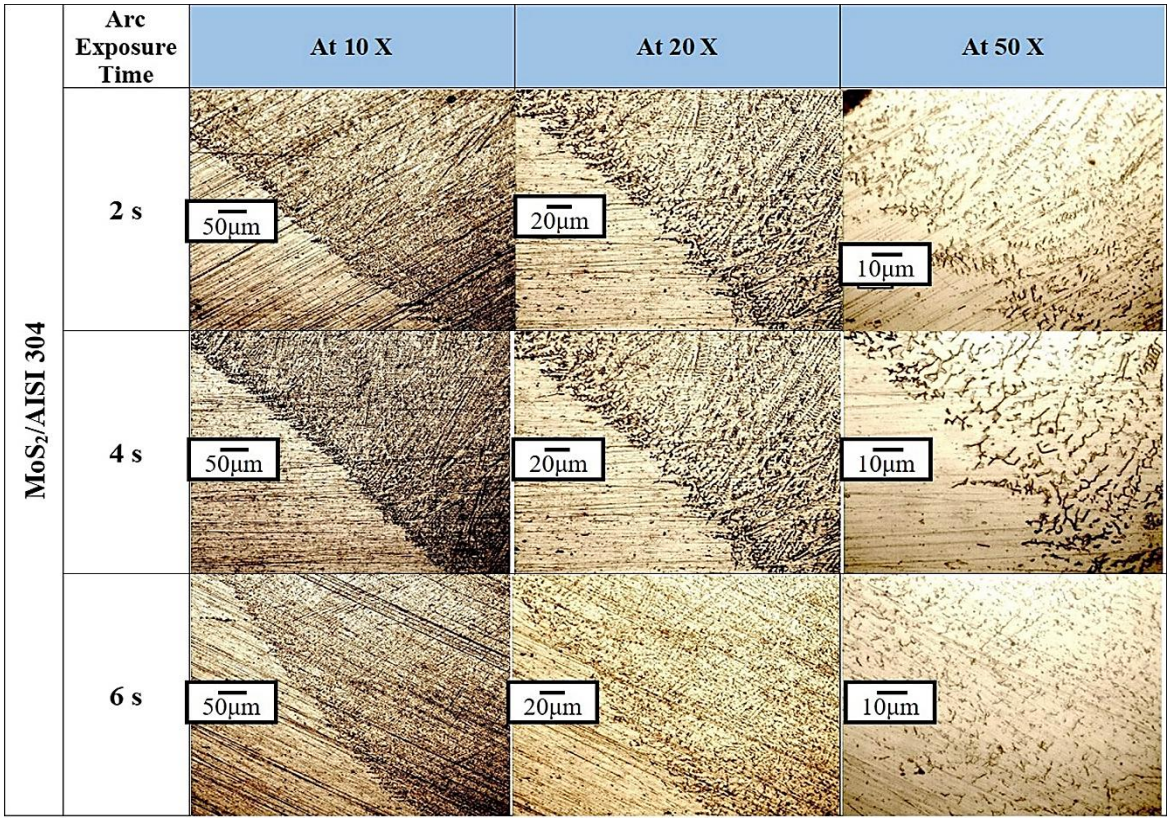


Figure 3.7: Microstructure of different arc exposure time (2s, 4s and 6s) of A-TIG welding with $MoS_2$ on AISI 304 using150 A, Ar shielding with 10 L/min gas flow rate

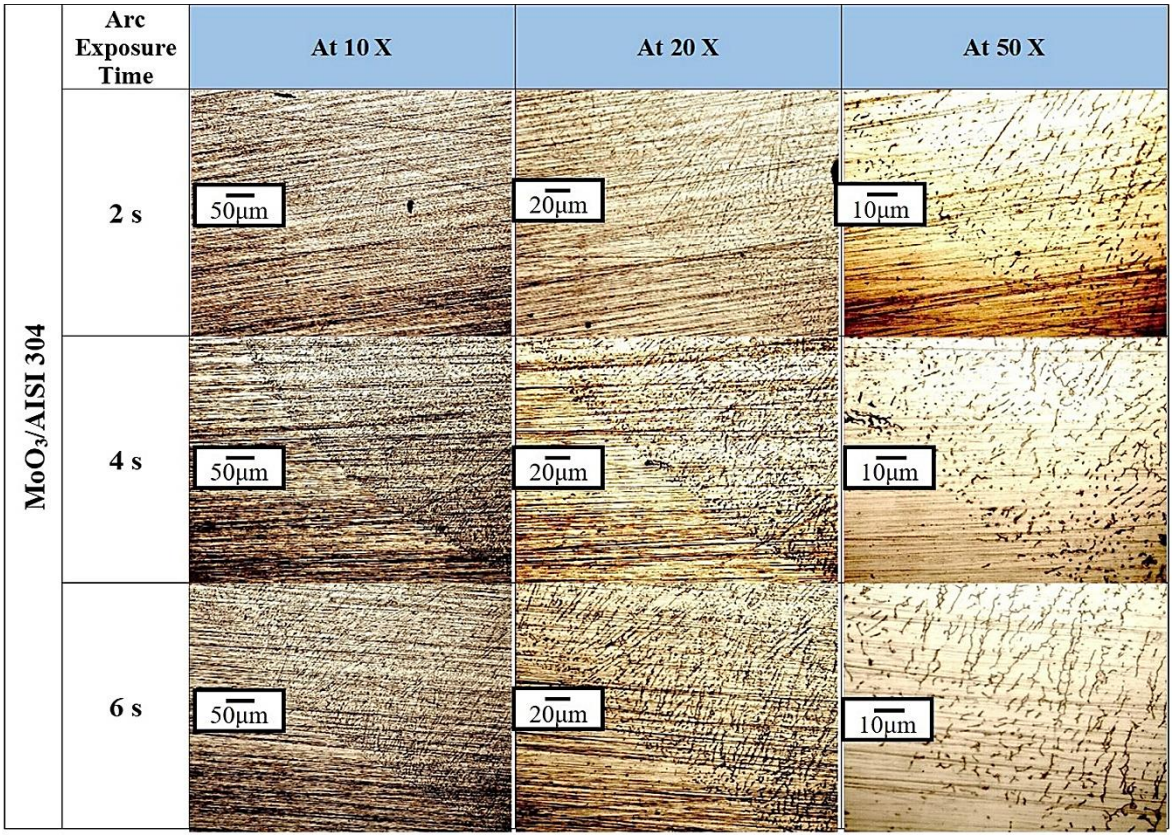


Figure 3.8: Microstructure of different arc exposure time (2s, 4s and 6s) of A-TIG welding with $MoO_3$ on AISI 304 using150 A, Ar shielding with 10 L/min gas flow rate

### 3.3.3 Effect of Activated Flux on Bead Appearance and Penetration on AISI 316:

Similarly, the same effect of flux and arc exposure time was observed in the case of AISI 316, which is shown in Fig. 3.9. The impact of arc exposure time shows the difference of penetration and cavity formation effect on the surface, wherein in the case of 6 sec, the cavity is more precise and profound. It also shows the metal flow pattern of molten metal in all the stationary A-TIG welds, whereas in the case of no flux condition, it was absent. The maximum penetration was observed again in $CrO_3$ flux because of more oxygen elements present. The $MoO_3$ flux also showed a good response in terms of penetration due to more oxygen present in the base metal, which may participate during the decomposition of flux and generate more heat.

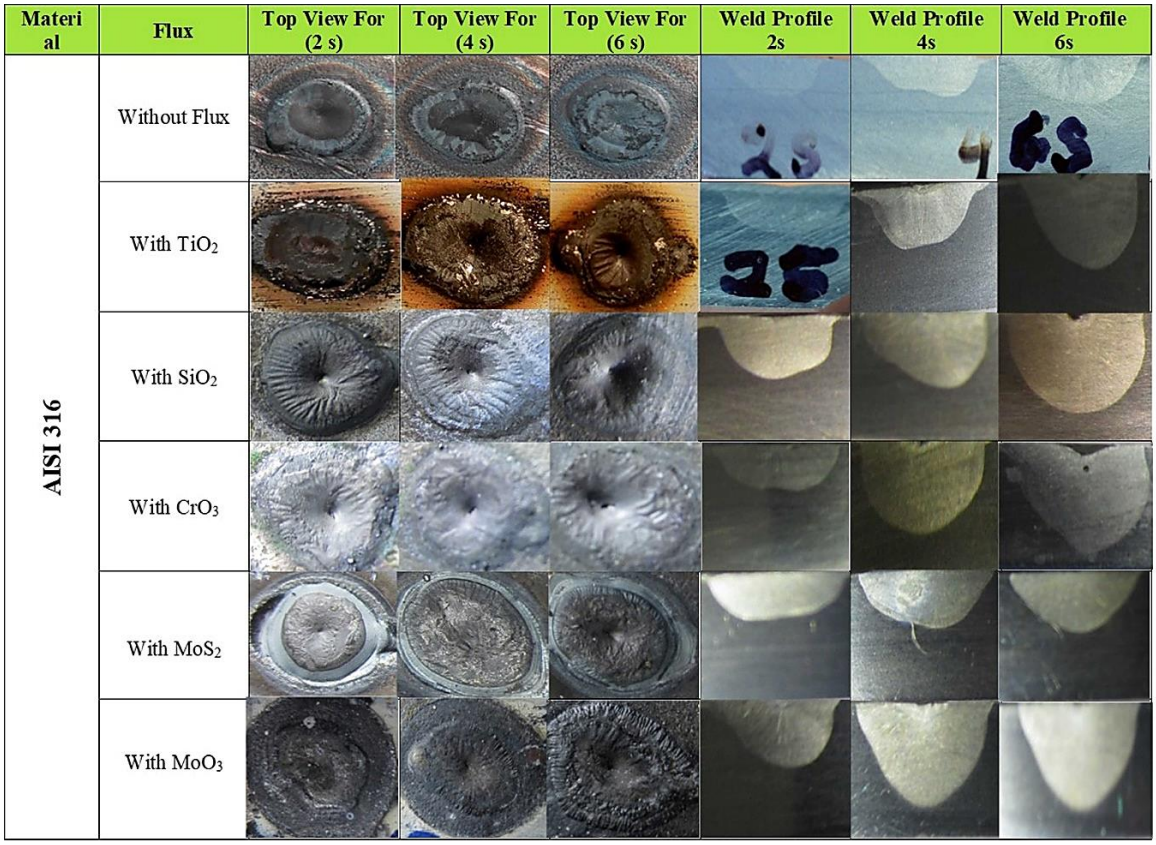


Figure 3.9: Showing the top surface and penetration of TIG and A-TIG welding of AISI 316 at different arc exposure times using Ar shielding

### 3.3.4 Effect of Activated Flux on Microstructure of AISI 316

The microstructure of the interface region of no – flux and with flux welds for AISI 316 steel is presented in Fig. 3.10 to Fig. 3.15. The same magnification level was maintained, which was used for AISI 304 steel. Similar changes in the morphology of the resultant ferrite content were observed in some cases, as found in AISI 304 stainless steel. A mix morphology of lathy and lacy ferrite is visible in all the A-TIG welded coupons microstructures.

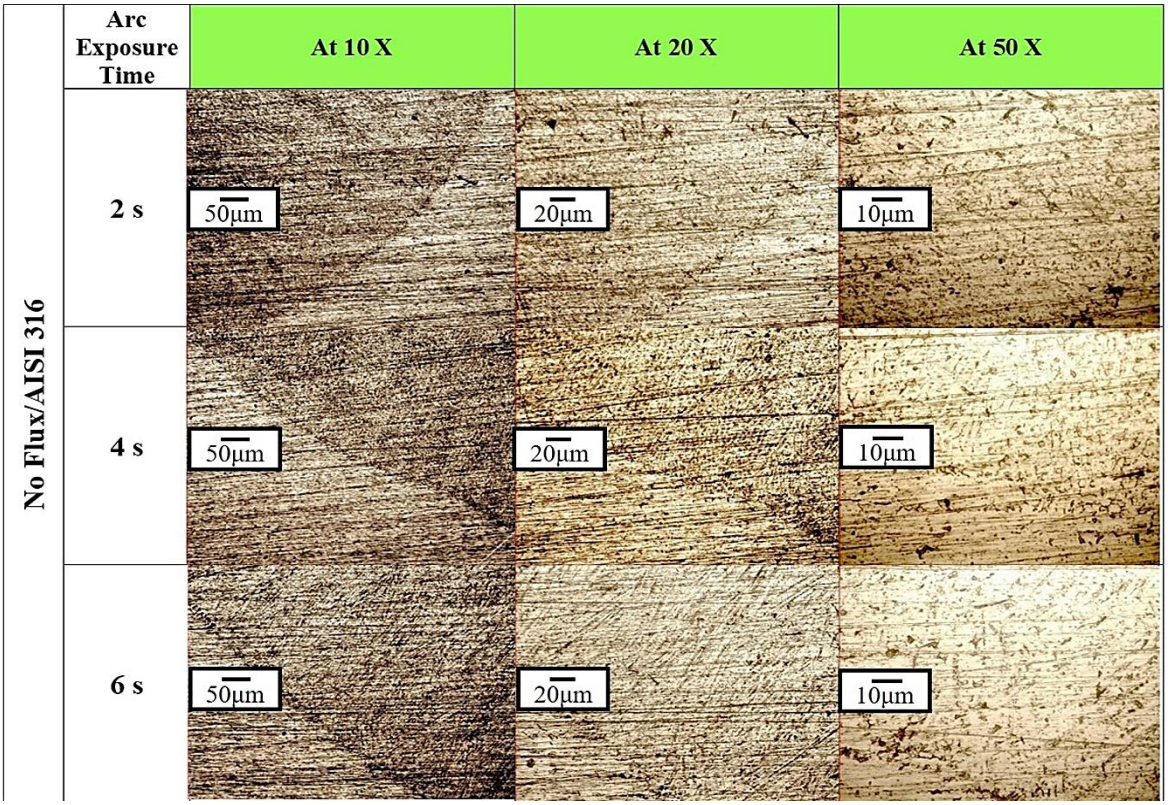


Figure 3.10: Microstructure of different arc exposure time (2s, 4s, and 6s) of conventional GTAW/TIG welding on AISI 316 using150 A, Ar shielding with10 L/min gas flow rate

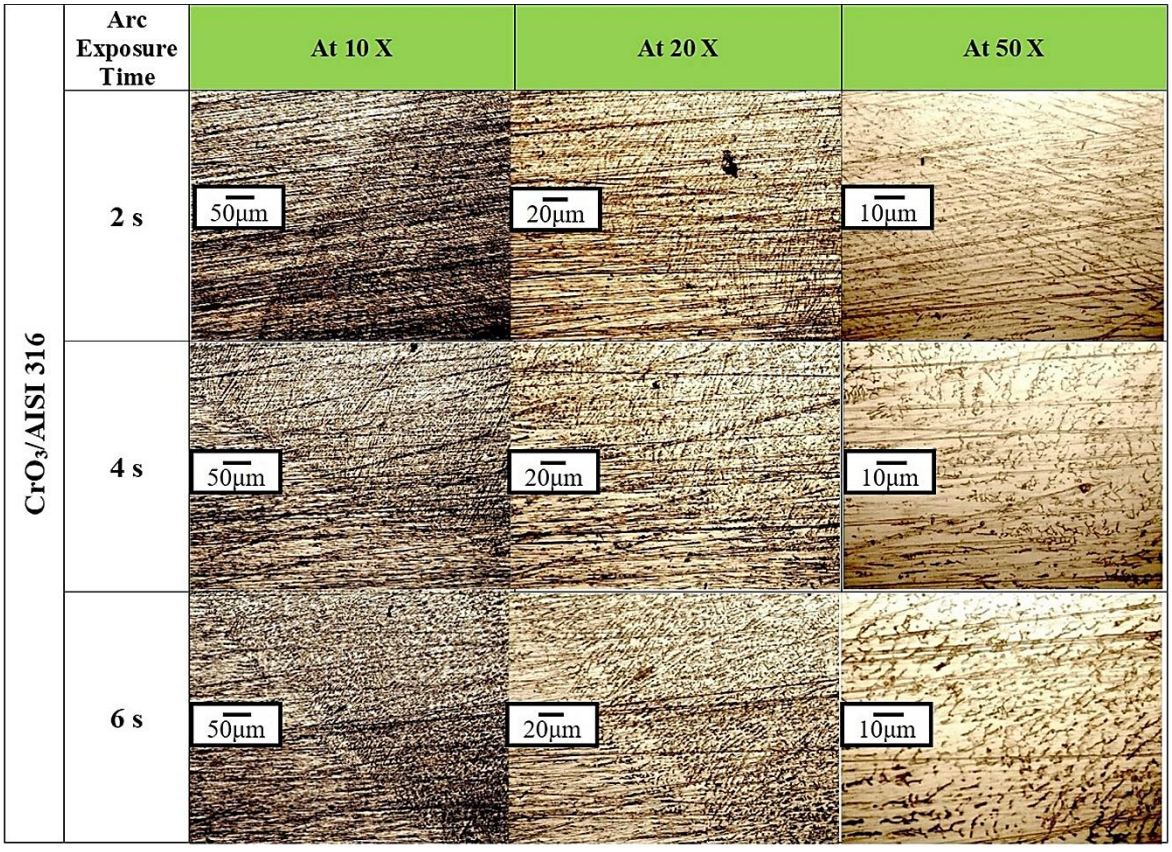


Figure 3.11: Microstructure of different arc exposure time (2s, 4s, and 6s) of A-TIG weld with $CrO_3$ on AISI 316 using150 A, Ar shielding with 10 L/min gas flow rate

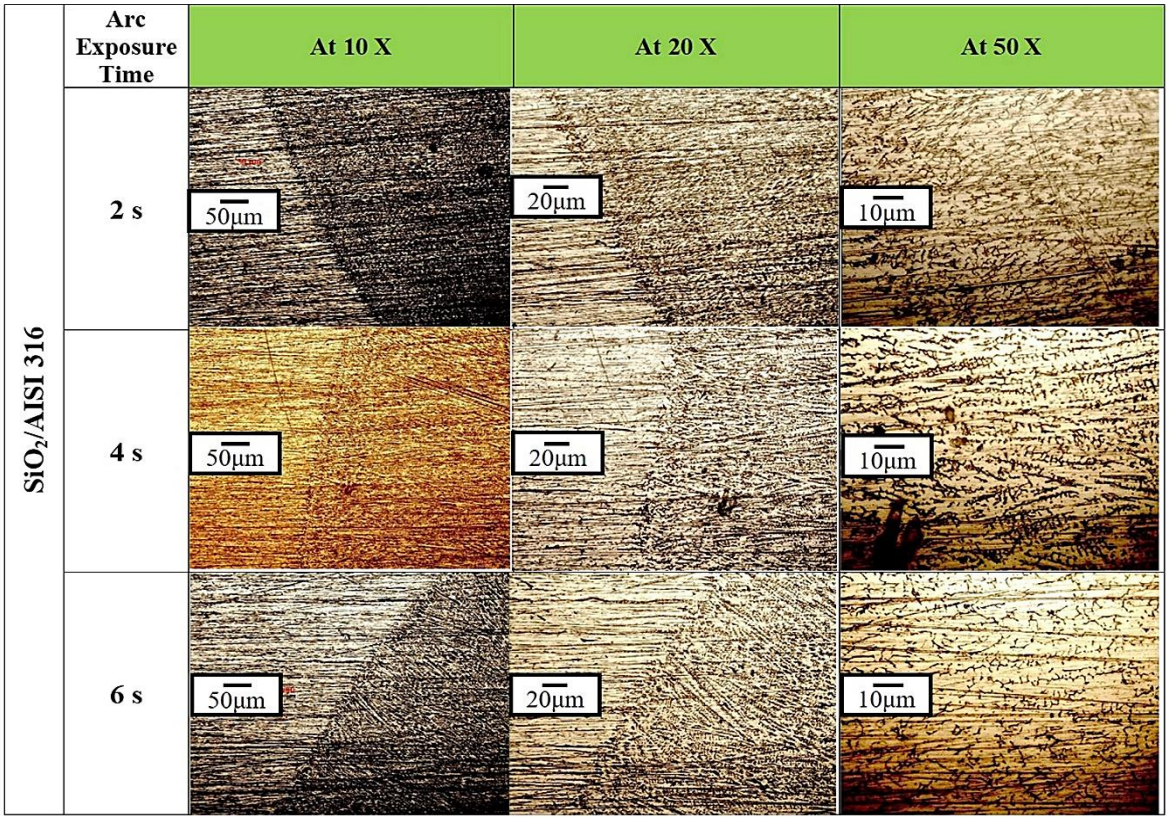


Figure 3.12: Microstructure of different arc exposure time (2s, 4s, and 6s) of A-TIG weld with $SiO_2$ on AISI 316 using150 A, Ar shielding with10 L/min gas flow rate

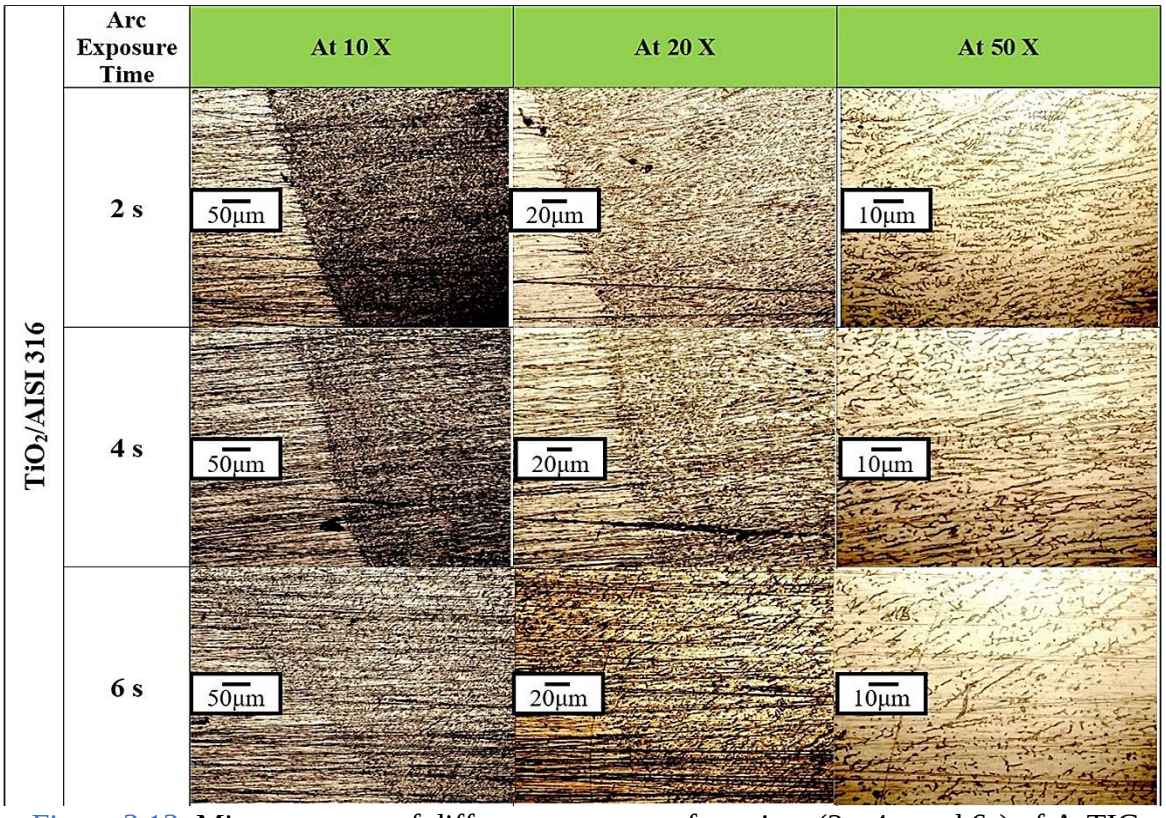


Figure 3.13: Microstructure of different exposure of arc time (2s, 4s, and 6s) of A-TIG weld with $TiO_2$ on AISI 316 using150 A, Ar shielding with 10 L/min gas flow rate

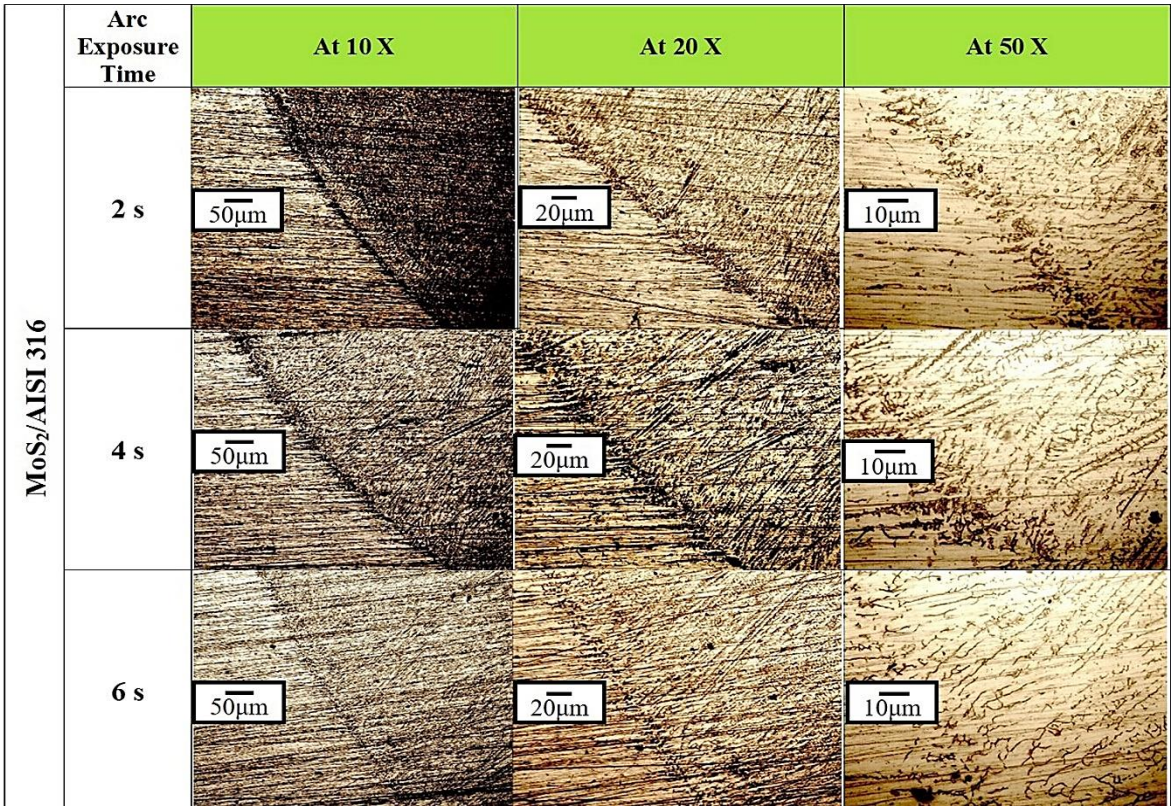


Figure 3. 14: Microstructure of different exposure of arc time (2s, 4s, and 6s) of A-TIG weld with $MoS_2$ on AISI 316 using150 A, Ar shielding with gas 10 L/min gas flow rate

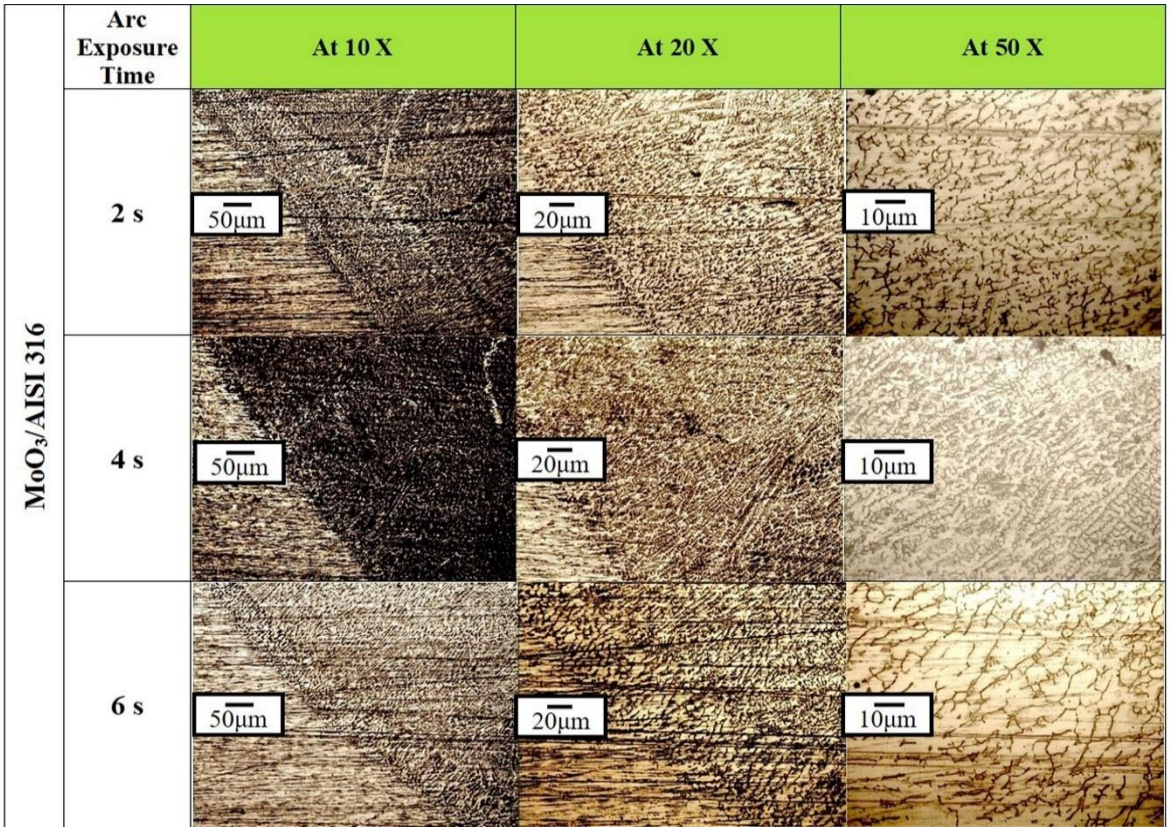


Figure 3. 15: Microstructure of different arc exposure time (2s, 4s, and 6s) of A-TIG weld with $MoO_3$ on AISI 316 using150 A, Ar shielding with 10 L/min gas flow rate

### 3.3.5 Effect of Activated Flux on Bead Appearance and Penetration on DUP 2205

Similarly, in the case of DUP 2205, the top surface of weld and associated penetration is presented in Fig. 3.16, which also shows the effect of reverse Marangoni convection and Lorentz force. DUP 2205 has two phases structure, i.e., ferrite and austenite, in approximately equal proportion. So, after etching of weld cross-section, two types of the dendritic structure was appeared in fusion zone (FZ), all of the A – TIG welding and in conventional GTAW/TIG welding. The flux residue is also visible in the case of all the A – TIG welds. The extra heat produced by the activated flux and associated cooling rate affects the directional growth of the dendrites.

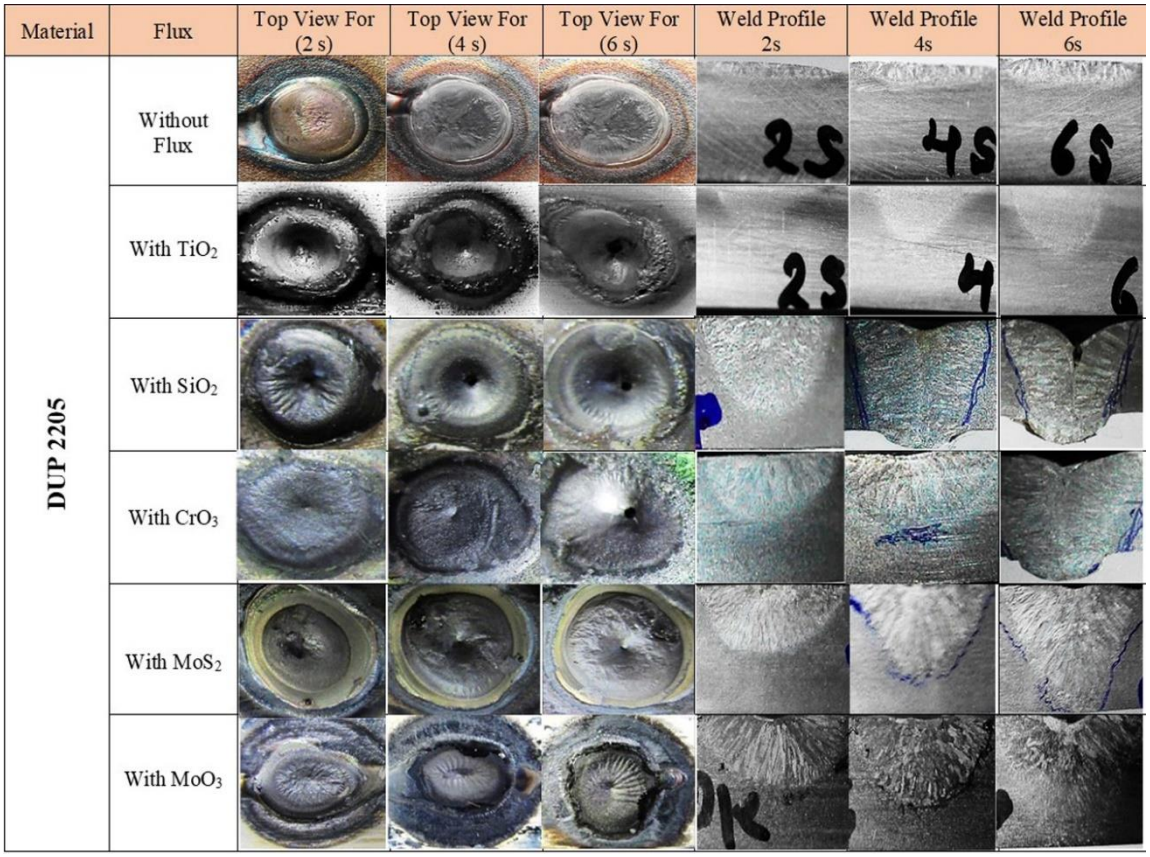


Figure 3. 16: Showing the top surface and penetration of TIG and A-TIG welding of Duplex 2205 at different arc exposure times using Ar shielding

### 3.3.6 Effect of Activated Flux on Microstructure of DUP 2205:

Fig. 3.17 to Fig. 3.22 shows the microstructure of the interface region (fusion zone and base metal) of Duplex 2205 steel, captured by metallurgical microscope at the same magnification which was taken in case of AISI 304 and AISI 316 magnification. These microstructures show that the extra heat of A – TIG welding influences both the ferrite and austenite dendrites. It was observed maximum in case of 6 sec arc exposure time.

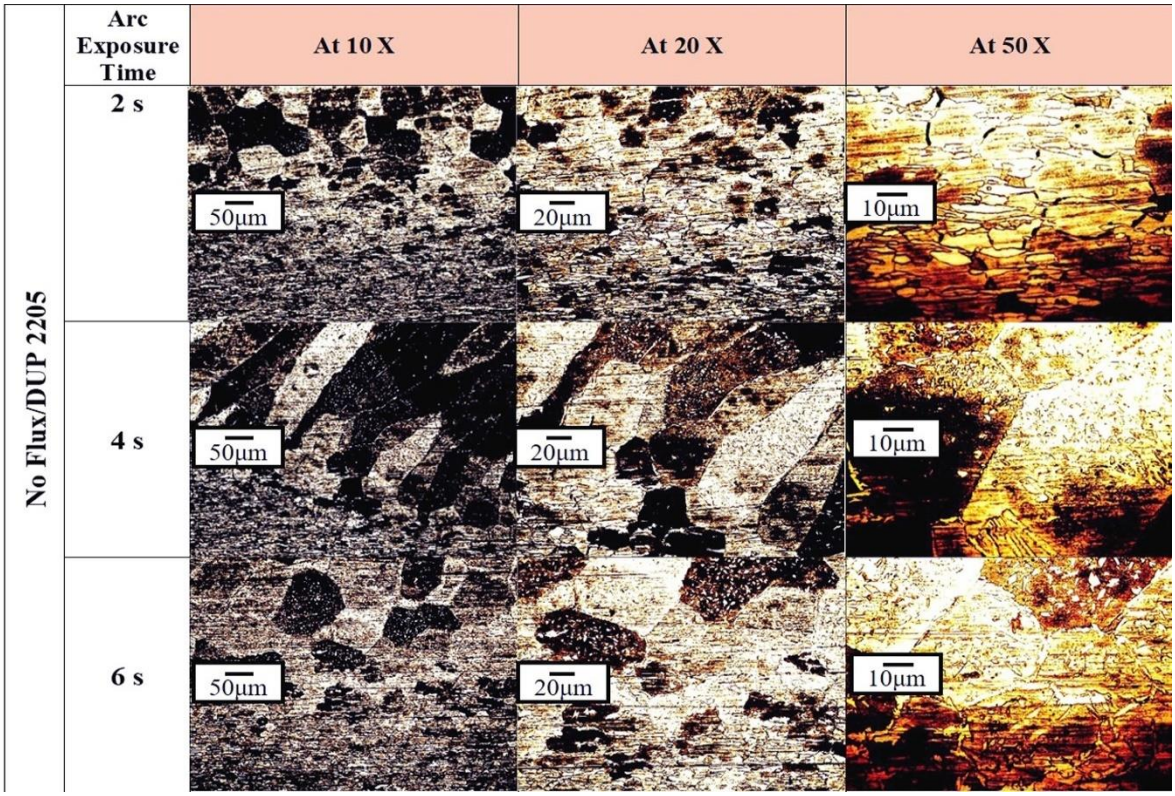


Figure 3.17: Microstructure of different arc exposure time (2s, 4s, and 6s) of conventional GTAW/TIG welding on DUP 2205 using 150 A, Ar shielding, 10 L/min gas flow rate

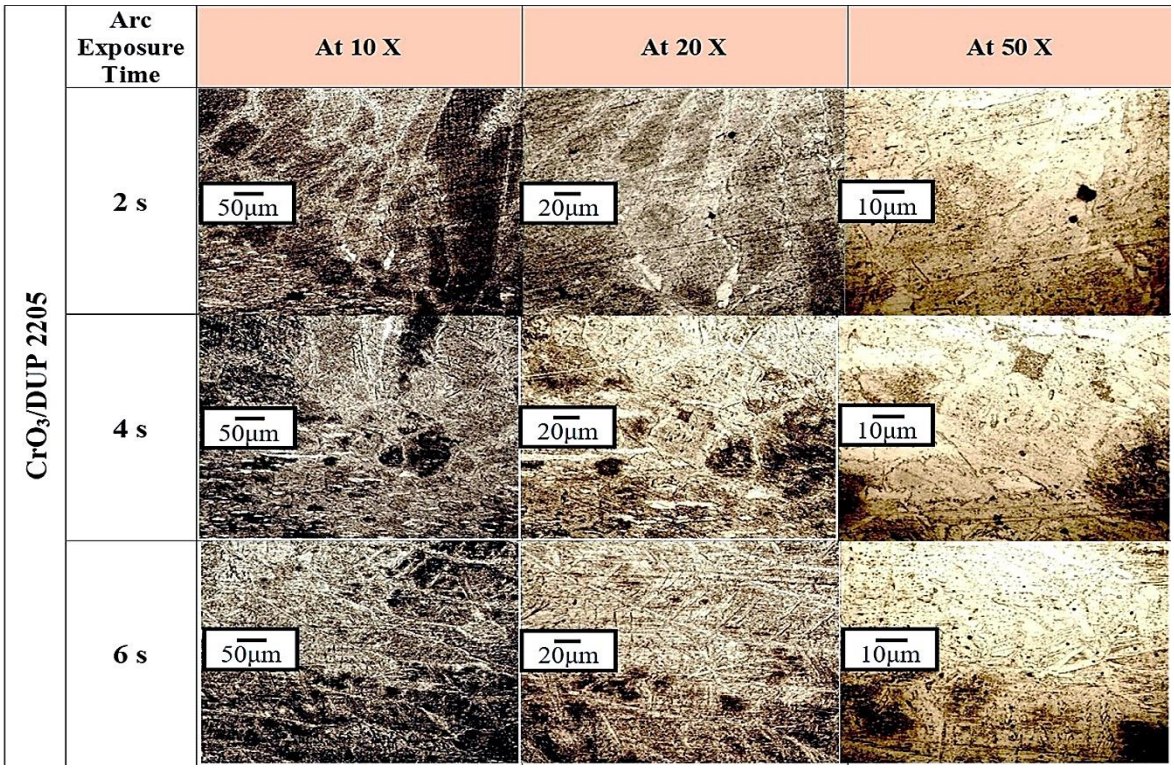


Figure 3.18: Microstructure of different arc exposure time (2s, 4s, and 6s) of A-TIG welding with $CrO_3$ on DUP 2205 using 150 A, Ar shielding, 10 L/min gas flow rate

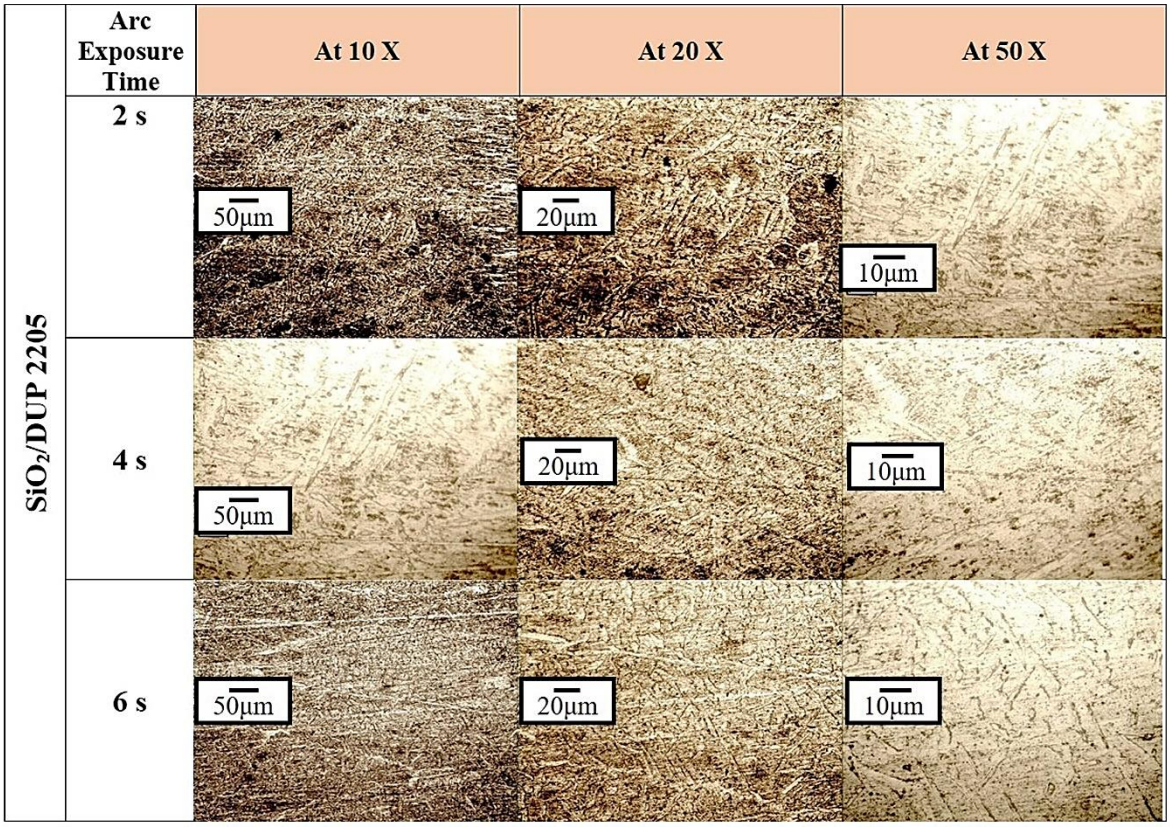


Figure 3.19: Microstructure of different arc exposure time (2s, 4s, and 6s) of A-TIG welding with $SiO_2$ on DUP 2205 using 150 A, Ar shielding, 10 L/min gas flow rate

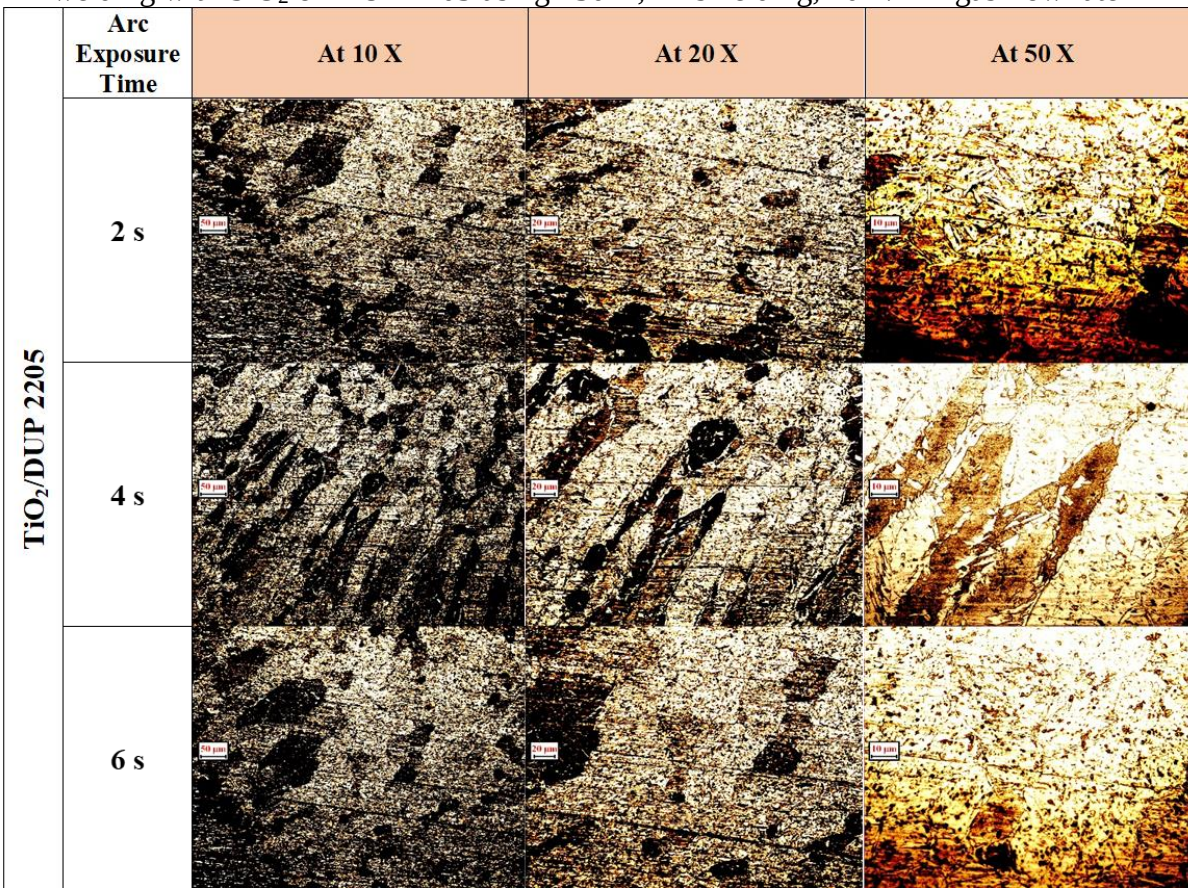


Figure 3.20: Microstructure of different arc exposure time (2s, 4s, and 6s) of A-TIG welding with $TiO_2$ on DUP 2205 using 150 A, Ar shielding, 10 L/min gas flow rate

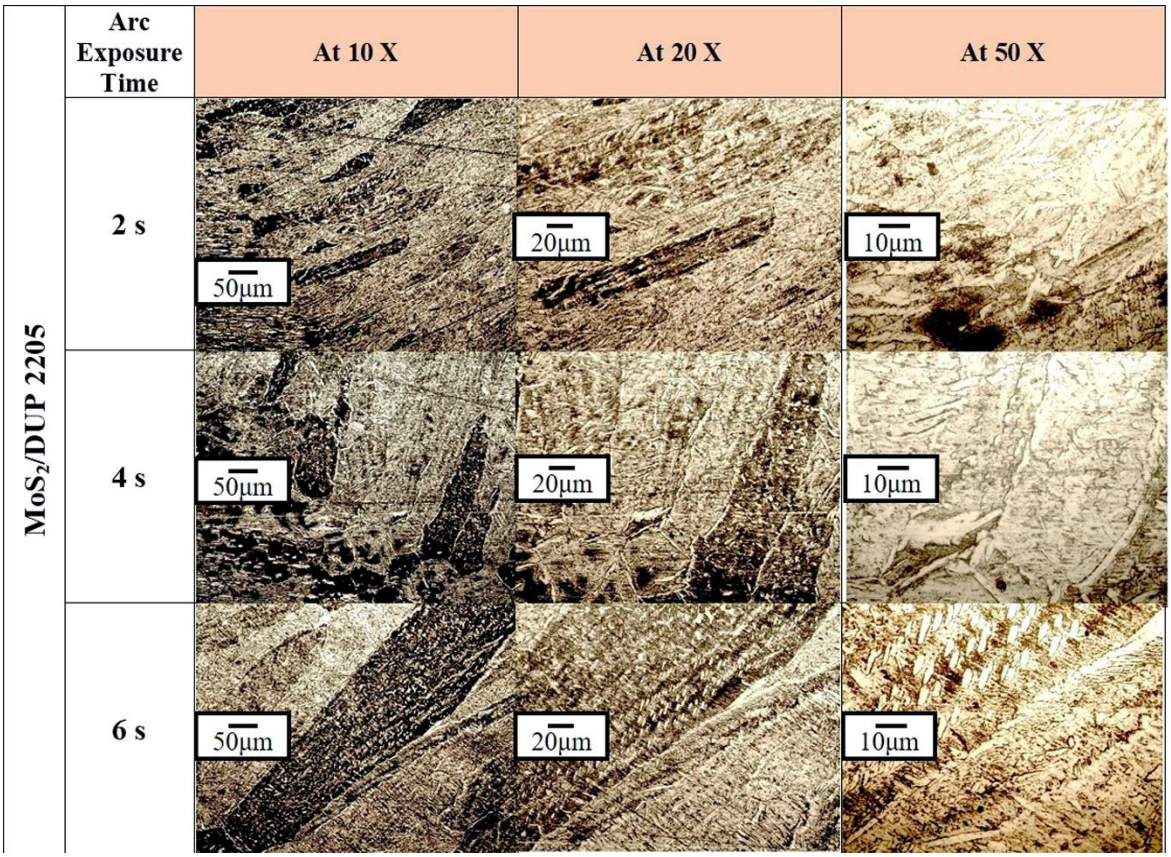


Figure 3. 21: Microstructure of different arc exposure time (2s, 4s, and 6s) of A-TIG welding with $MoS_2$ on DUP 2205 using 150 A, Ar shielding, 10 L/min gas flow rate

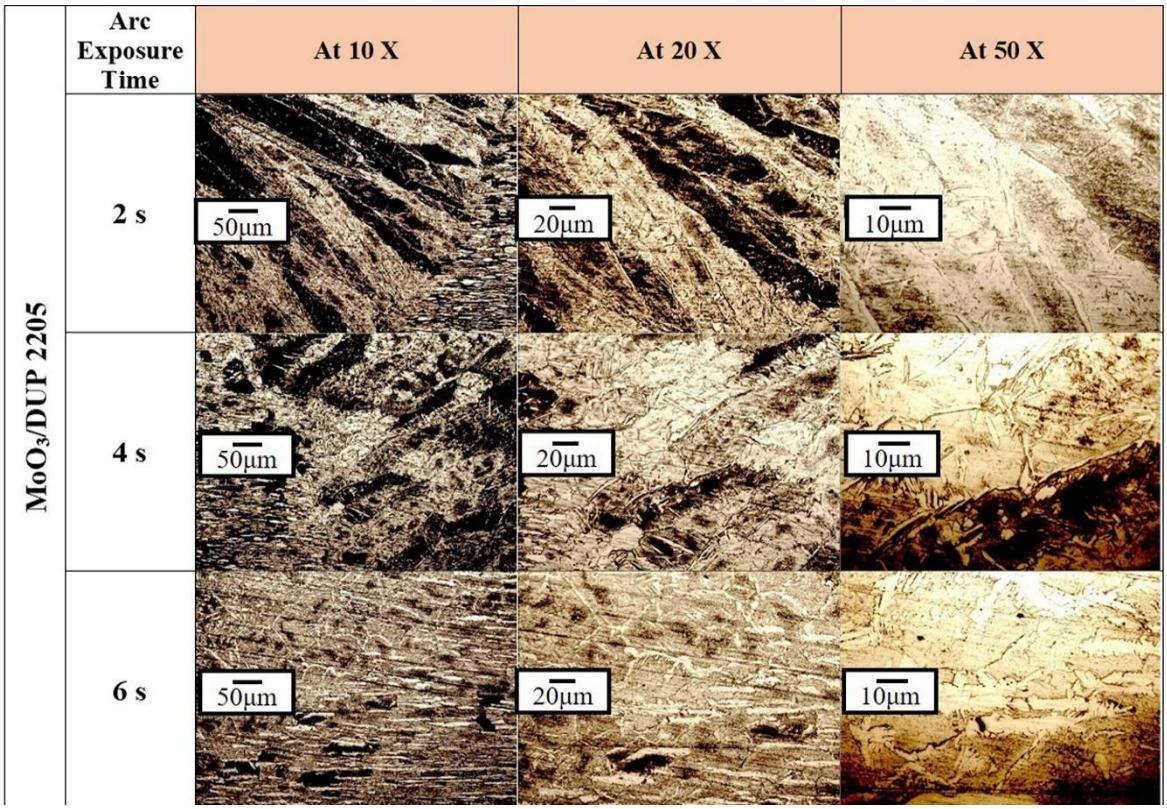


Figure 3.22: Microstructure of different arc exposure time (2s, 4s, and 6s) of A-TIG welding with $MoO_3$ on DUP 2205 using 150 A, Ar shielding, 10 L/min gas flow rate

### 3.3.7 Effect of Activated Flux on Weld Profile and Aspect Ratio

The significant change in weld profile in terms of depth of penetration (DoP) and weld width for Ar shielding environment is presented in Fig. 3.23 to 3.25. In the case of A – TIG welding, the effect of different arc exposure times on three different types of stainless steel clearly show more change in DoP than weld width. Whereas, in the case of conventional GTAW/ TIG welding, the effect was insignificant. A maximum DoP of 2.56 mm was observed in traditional GTAW/TIG weld in the case of AISI-316 steel. The surface tension gradient was found to be negative in conventional TIG welding, and the same has been validated by weld profile development, shown in Fig. 3.23 to 3.25. whereas in case of A-TIG welding with different fluxes shows the presence of a positive surface tension gradient.

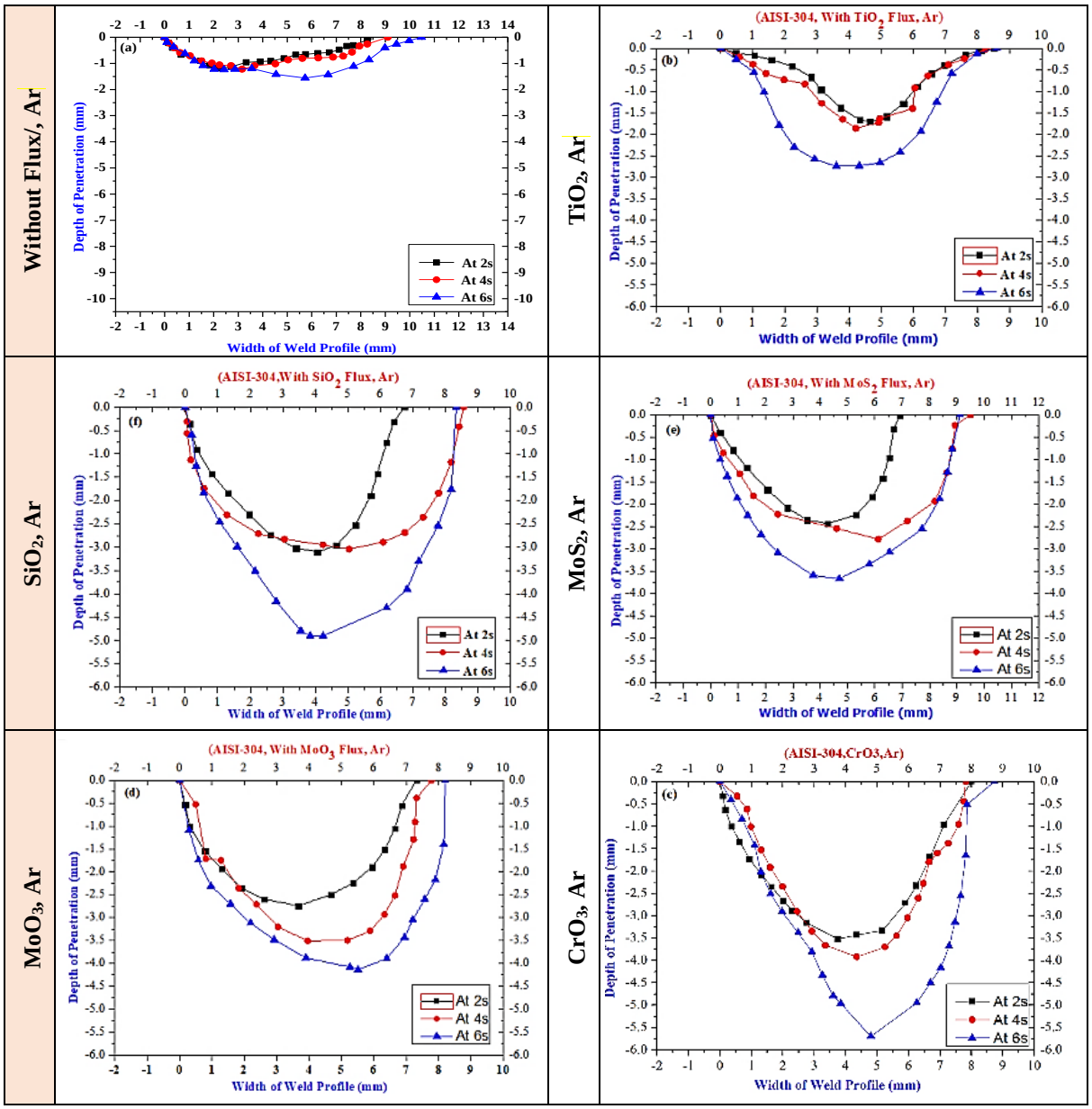


Figure 3.23: Weld profile of without flux and with flux with different arc exposure time and Ar shielding on AISI-304

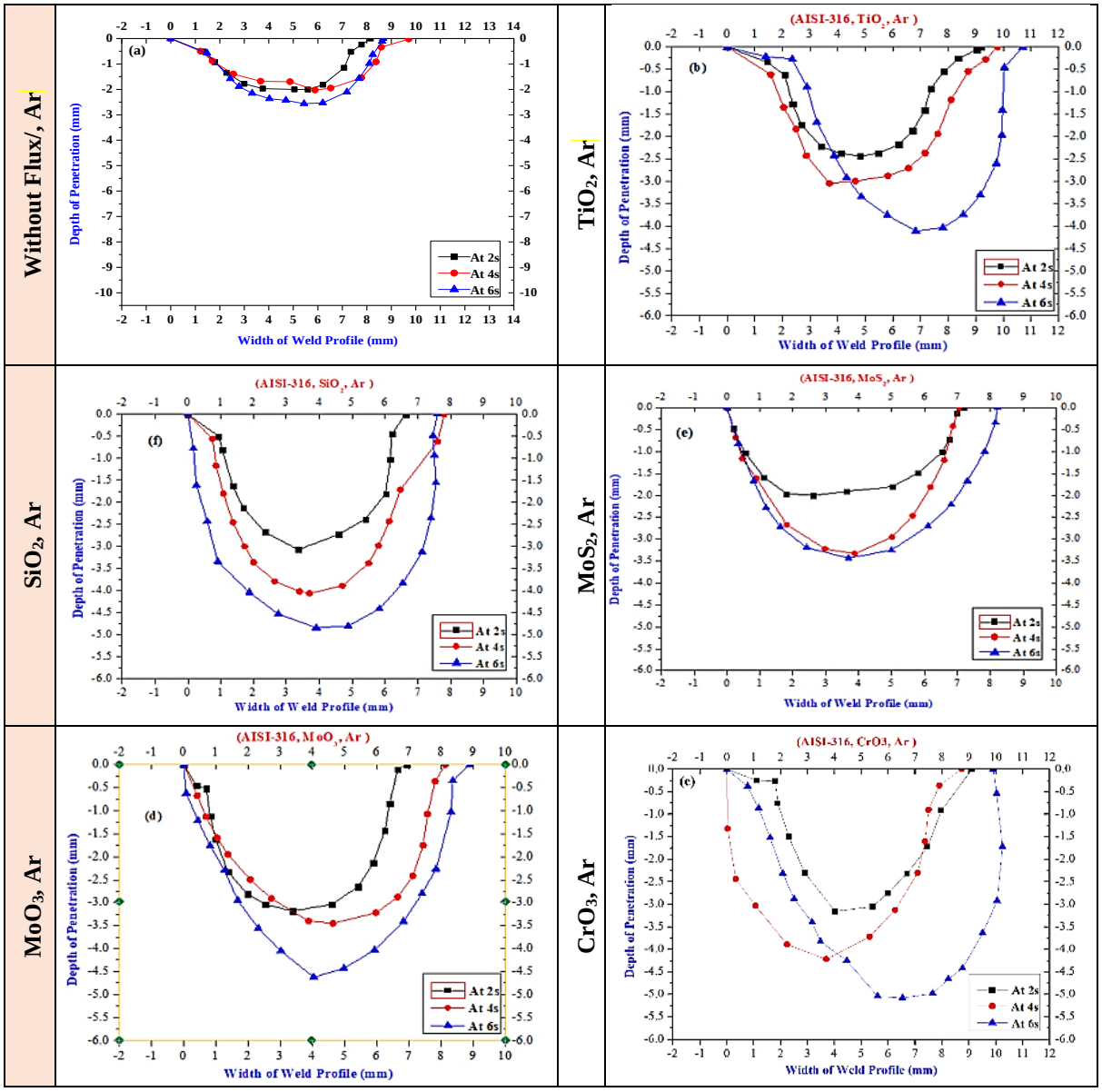


Figure 3. 24: Weld profile of without and with flux with different arc exposure time and Ar shielding on AISI-316

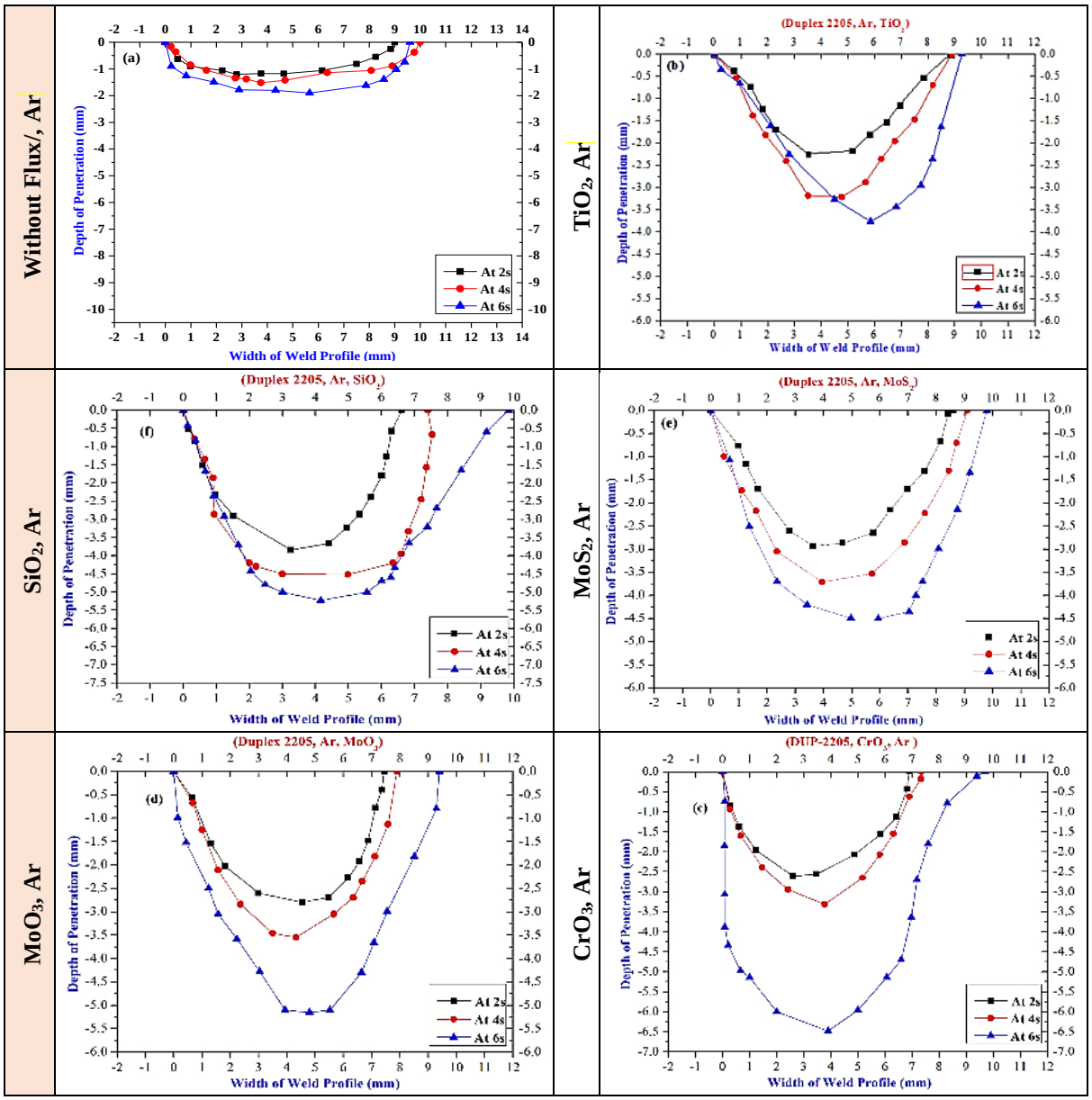


Figure 3.25: Weld profile of without and with flux with different arc exposure time and Ar shielding on DUP 2205

Figure 3.26 compares the aspect ratio (i.e., width to penetration ratio) with argon shielding environment for all the three types of steel with a trend line (with $CrO_3$). The trend line for $CrO_3$ flux shows that the aspect ratio decreases with the increase of arc exposure time, which is more significant in duplex stainless steel (DUP 2205) stainless steel. Both the austenitic stainless steel and duplex stainless steel have some fluctuations for different types of fluxes. Therefore, these results generate further curiosity for further investigation which is presented in subsequent sections.

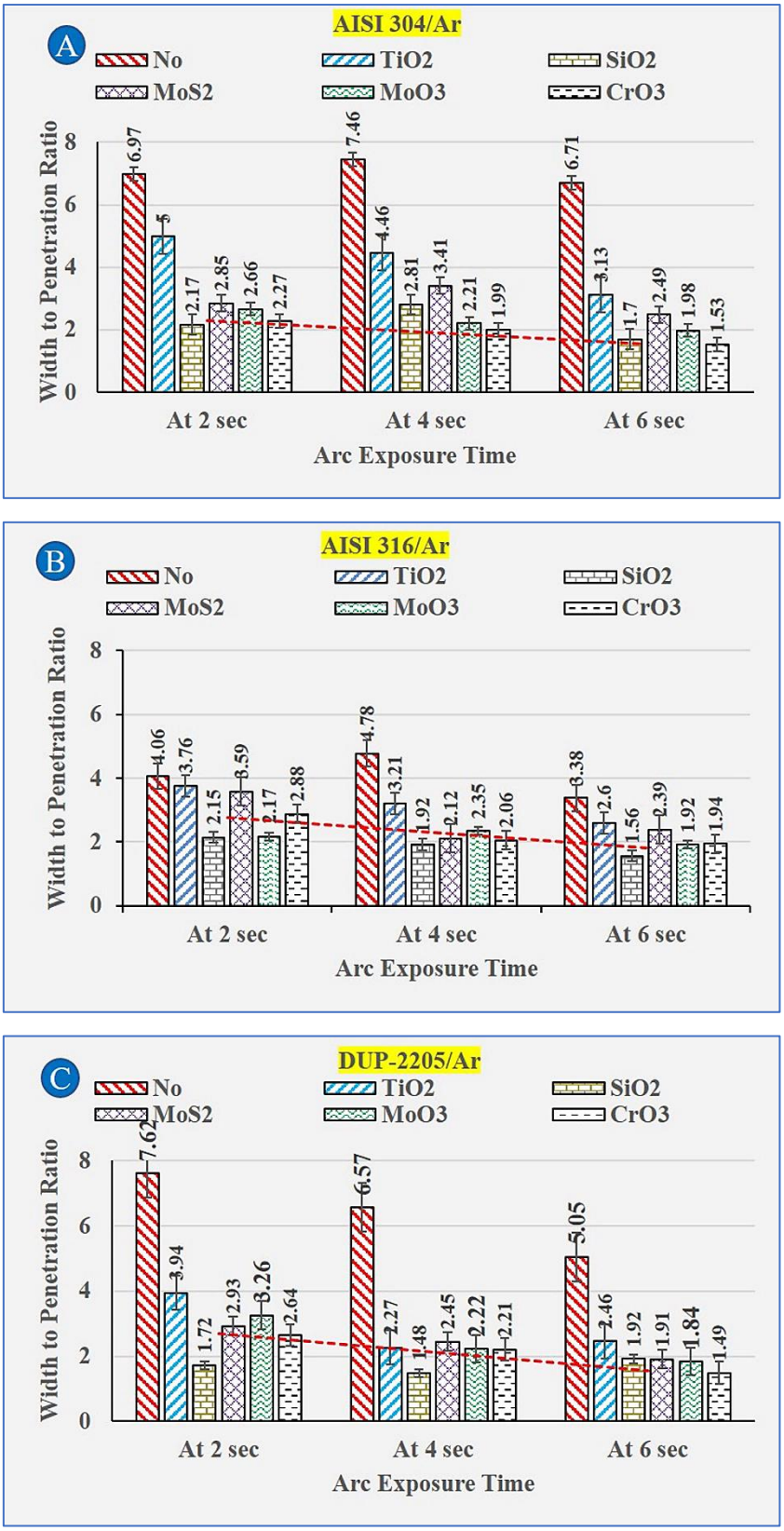


Figure 3.26: Comparison of the aspect ratio of width to penetration with Ar shielding for no flux and with different fluxes on (A) AISI 304 (B) AISI316 (C) Duplex 2205 stainless steel

## 3.4 A-TIG Welding of Duplex Stainless Steel (2205) with Ar shielding [20]

Duplex Stainless Steel' (DSS) AISI 2205 type is an extensively used material in oil and gas extraction industries due to its better mechanical and corrosion properties. The two-phase structure of austenite and ferrite in equal proportion helps retain the desirable properties at room temperature [34, 77]. However, these properties degraded at elevated temperatures [78]. Welding of Duplex stainless steel (DUP 2205) by Tungsten Inert Gas (TIG) welding [79] could lead to the formation of sigma (σ) and chi (χ) phases in weld metal as well as grain size variations in heat-affected (HAZ) owing to cooling rate and temperature [80]. The burning of activated flux has produced fumes and a certain amount of residue particles like slag around the weld bead/weld spot (Fig. 3.27) during welding. Delta (δ) ferrite present in weld prevents micro-cracks and refines the grain size of the as-solidified weld metal [34]. The dual-phase structure of austenite and ferrite in DSS is also sensible to the separation of phases owing to stresses formed [81]. Therefore, it could be possible during the decomposition of oxide-based fluxes. In the present study, the influence of surface-active elements with arc holding time of 6 seconds (6 s) using pure argon gas (Ar) shielding has been investigated. Oxide based fluxes like $SiO_2$ and $CrO_3$ and surface-active elements like sulphur (S) in $MoS_2$ flux were used for investigation. The investigation has been carried out for determining the thermal energy of arc developed due to different fluxes and discussed with the role of oxygen. Due to extra heat generated by the activated flux could results into the dendritic growth and it also participate in the gas metal and slag metal reaction. The mechanism behind the extra penetration and the relation with the thermal energy of arc are elaborated in further sections.

The investigation has been carried out using different characterization techniques. It includes microstructure analysis, micro-hardness, energy dispersive spectroscopy (EDS), and scanning electron microscopy (SEM). This study also provides the role of extra thermal energy of arc produced during A-TIG welding. The heat produced by the conventional TIG welding process (V*I*time) at the spot has been quantified based on dilution area. Similarly, the oxygen content in each case has been measured and compared qualitatively. The obtained results have been discussed for the penetration mechanism based on thermal energy of arc and the gas-metal and slag-metal reactions. Hence, the role of activated flux and surface-active elements in thermal energy of arc, penetration, and microstructural variations in weld along with associated mechanisms are elaborated in the study.

### 3.4.1 Weld Pool Morphology and Properties

An activated flux or surface-active elements could significantly influence the weld bead surface appearance, as accessed from Fig. 3.27. It is visible from the top surface of flux-assisted TIG welds that show the metal flow from the periphery of the weld nugget to the centripetal downward direction and found in complete agreement with the reverse Marangoni convection. So, to identify the reverse Marangoni convection and Peclet number, the heat source diameter is considered the vital aspect of the spot weld. In the stringer bead (straight bead), the radius can be calculated from bead width ('X' direction). However, the 'Y' direction of the weld bead will be completely dependent on welding speed. Hence, to nullify the effect of welding speed and maintain the identical nature of heat source (heat flow) diameter, the 'X' and 'Y' direction could be the accurate and identical representation in the stationary weld. Thus, the stationary bead can identify the reverse Marangoni convection and Peclet number more reliable.

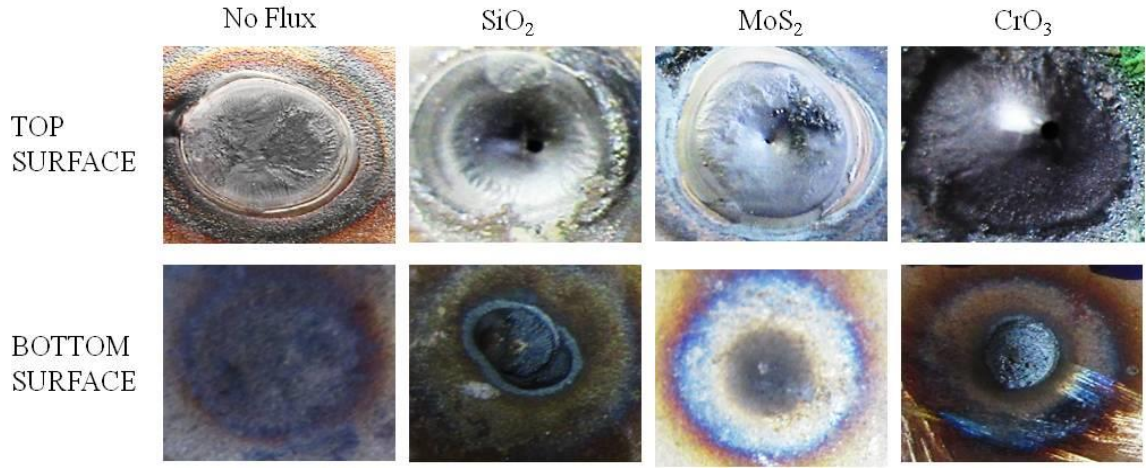


Figure 3. 27: As-welded weld coupons showing the top and bottom surfaces of the welds

The weld shape in without flux condition depicts the predominant pattern of outward liquid metal flow. However, while using activated fluxes (enriched oxygen content), the surface tension gradient ($d\gamma/dT$) [13, 54] could change its trend from negative to positive, and that further drifts the liquid metal down to the axis of the weld pool. Such a phenomenon represents the reverse Marangoni convection [69]. The same can be seen in weld surface appearance shown in Fig. 3.27 and Fig. 3.28 for weld coupons with activated flux with increased penetration depth and dilution area. The weld surface appearance and macrograph (Fig. 3.27) show that the presence of flux helps in constriction of arc, which further assists in achieving higher penetration and the associated gas/slag metal reactions to form gas that further raises to the formation of the cavity as shown in Fig. 3.28. The forces responsible for the weld nugget appearance and weld morphology are electromagnetic Lorentz force, buoyancy force, surface

tension force, shear force, and drag force of shielding gas [13]. The weld arcing was done at the spot, so the weld pool boundary at the weld centreline and fusion line could not be distinguishable. Hence, the temperature gradient (G) and growth rate (R) would remain identical [32], and in the present study, it has not been considered as a dependable parameter on the welding speed.

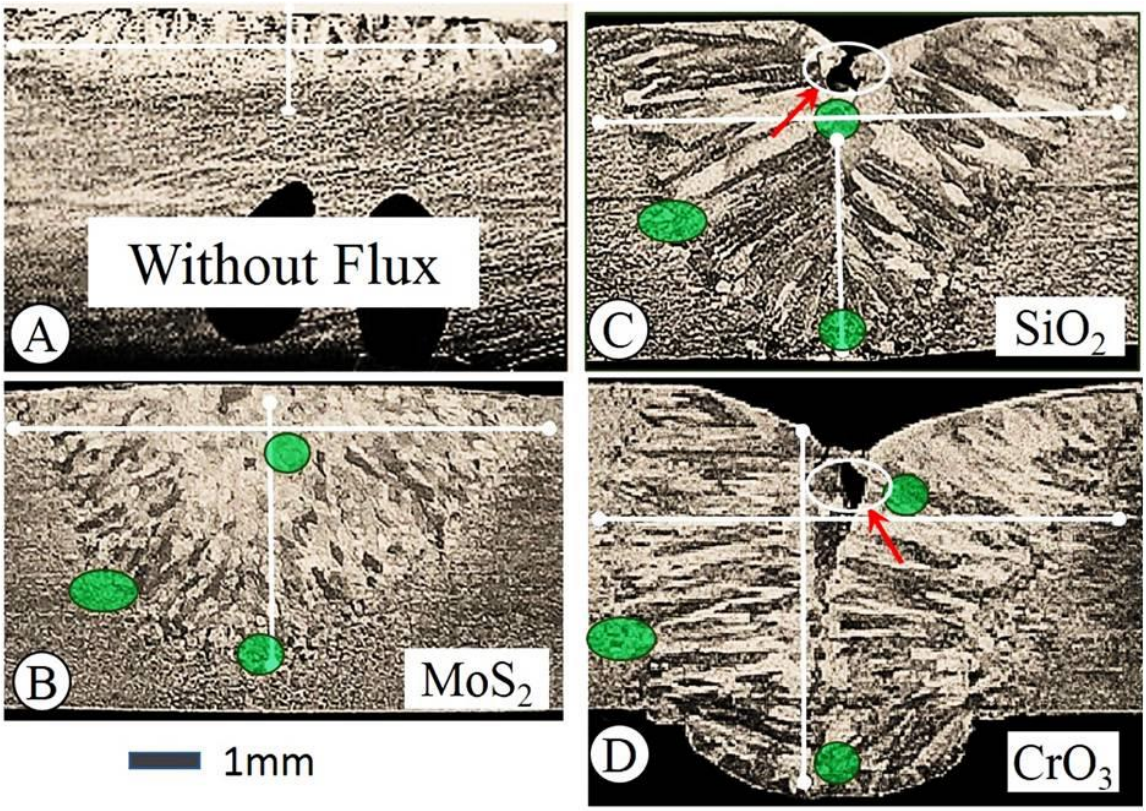


Figure 3. 28: Macrograph showing the extent of the general grain structure of the welds and lines showing micro-hardness, SEM, EDS, and optical microscopy regions

Considering the macrostructure of Fig. 3.28, the dendrite growth has been found almost vertical (i.e., ~5$^o$ – the angle measured from the vertical weld centreline). However, the angle of dendrite growth with $SiO_2$ and $MoS_2$ has been noticed with ~45$^o$ with weld centerline. On the other hand, the dendrite growth in $CrO_3$ flux was almost horizontal (~85$^o$), and the dendrite growth is a function of cooling direction and rate, which would govern the planes of grain structure. The cooling rate (G x R) is higher at the weld centreline and lower at the fusion line. It could suggest that the dendrite arm spacing decreases from the fusion line to the centreline because the dendrite arm spacing decreases with the increased cooling rate (G x R) [32]. It can be evidenced by Fig. 3.28 A and Fig. 3.28 B, suggesting the higher heat input/heat produced in the case of $SiO_2$ and $CrO_3$ fluxes (Fig. 3.28 C and Fig. 3.28 D). Hence, the heat produced during welding can be correlated with the angle of dendrite growth, and the same has been shown in

Fig 3.28 A-D. The dendrite arm spacing/width with $SiO_2$ and $CrO_3$ flux has been observed to be significantly more than $MoS_2$ and without flux conditions. The heat input with $SiO_2$ and $CrO_3$ flux has been observed to be more than $MoS_2$ and without flux conditions. This indicates that with spot arcing (zero welding speed), higher heat input lowers the temperature gradient (G) and hence lowers the ratio G/R. Therefore, with lower G/R, the columnar dendrite formation is prevalent (Fig. 3.28 C and D); however, the cellular dendrite prevails in higher G/R as in the case of Fig. 3.28 A and B. The further analysis of this morphology has been discussed in the subsequent section of microstructure evaluation.

Higher oxygen content in different fluxes ($CrO_3$ and $SiO_2$) interacted considerably with the electrons and ions involved in arcing and redistributed the charge carrier that causes the constriction behaviour of the plasma column. Although further to the above action, comparatively more oxygen exists in $CrO_3$ than $SiO_2$, the slag metal reaction and gas metal reaction promotes the formation of CO and $CO_2$. This would lead to forming blows or cavities in the molten weld metal and can be seen in the micrograph of Fig. 3.28; however, such cavities have not been observed in $MoS_2$ flux and without flux conditions.

The detailed reaction and mechanism have been explained in subsequent sections. The oxygen present in the flux could affect the width of dendrite arm spacing. In addition, the temperature gradient (G) and growth rate (R), and associated ratio (G/R) and G x R could influence the dendrite size and dendrite arm spacing [32, 82]. However, the above parameters are dependent on the heat input/heat produced in the weld, and oxygen content in the flux has played a significant role in heat produced. This is confirmed by the dilution and penetration level with $SiO_2$ and $CrO_3$ fluxes compared with the $MoS_2$ and without flux conditions. Hence, from the study, it can be suggested that the oxygen-based fluxes could also govern the dendrite spacing as well as length. The further quantification and analysis of this morphology have been discussed in the subsequent section of microstructure evaluation.

### 3.4.2 Thermal/Heat Energy Correlation and Validation

The penetration achieved in GTAW (No flux condition) was estimated and correlated with arc energy/heat energy (heat produced by the arc). So, the total heat energy generated and used for welding was calculated as V×I ×t, where 'V' is the voltage (in volts), 'I' is the current (in amperes), and 't' is the time in seconds (s). Therefore, the thermal /heat energy of arc produced in the case of no-flux welding conditions was estimated to be 9000 J for 6 sec. However, the activated flux causes a certain amount of more thermal energy produced during welding. The arc exposure time for each weld was the same as 6 sec. Therefore, the thermal energy can be

measured in watts (W). Without flux, the thermal energy (V*I) would be 1500 W. This thermal energy based on process parameters will remain the same in each condition. However, additional heat owing to activated fluxes would cause increased dilution. This energy has been correlated and validated using the geometrical relationship based on dilution (area) / penetration.

The dilution area has been considered a measure of penetration and the width of the weld bead. However, the depth to penetration (d/p) ratio was an important parameter in several kinds of research [57, 74, 83]. Considering the macrostructure in Fig. 3.28 and measured area plots are shown in Fig. 3.29, the total dilution area in each case has been measured with Image J software and cross-validated using a travelling microscope. The dilution area A1 (without flux) is 7.45 $mm^2$, A2 ($MoS_2$) is 20.15 $mm^2$, A3 ($SiO_2$) is 25.12 $mm^2$ and A4 ($CrO_3$) is 32.94 $mm^2$. The heat produced due to process parameters (1500 W) in without flux condition by conventional TIG would be correlated with dilution area A1 (without flux) 7.45 $mm^2$. This further suggests that 1 $mm^2$ dilution needs the thermal energy of 201.32 W. Using this relationship and measured dilution areas, the thermal energy produced in each case of activated flux has been estimated. Thermal energy/arc energy in the $MoS_2$ flux condition was estimated as 4057 W; in $SiO_2$, it is 5058 W, and in the $CrO_3$ flux condition, it was observed to be 6632 W. The thermal energy/arc energy in activated flux has been increased, and it is associated with active elements and oxygen content. These active elements and oxygen increase the voltage and cause thermal energy changes. The welding arc contains many free electrons, and decomposed flux additives attract electrons, causing the welding arc to constrict and increase arc voltage [75, 83]. Such phenomena would lead to increased thermal energy. In the present study, we have estimated the net heat produced. However, the voltage effect has not been quantified. Arc exposure of 6 seconds results in high energy density, higher arc temperature, and more time is available for electromagnetic Lorentz force, which further endorsed sinking of the molten metal [8, 84]. Surface active elements present in the flux (oxides) change the temperature gradient of surface tension of weld pool from negative to positive [74] that could govern the heat produced in the weld. By considering dilution area, penetration and heat produced, it is evident that the thermal energy increased with increased oxygen content. It has been observed to be highest in the $CrO_3$ flux condition, almost 4.42 times more than the without flux (based on process parameters only) condition.

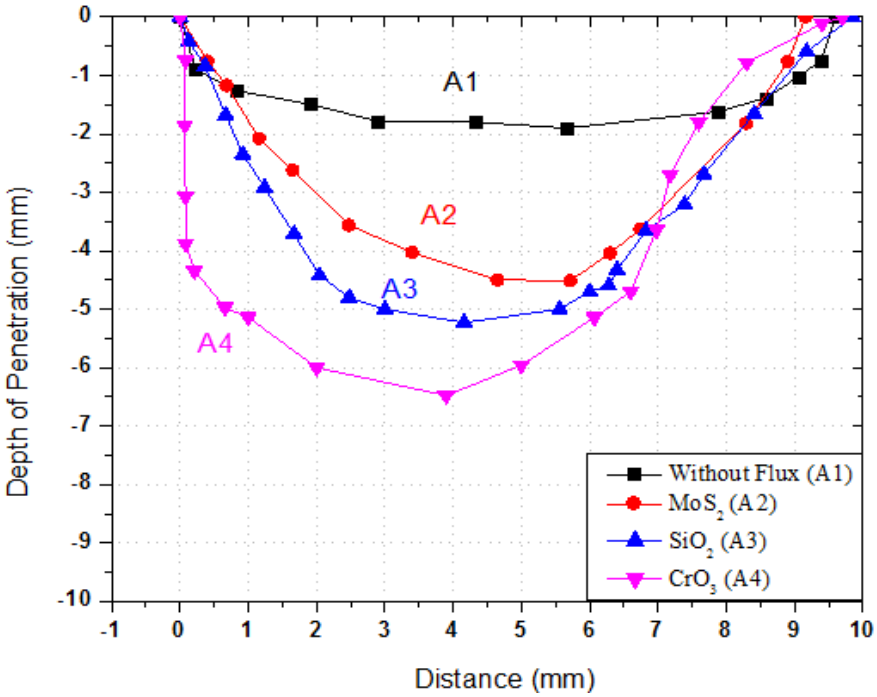


Figure 3. 29: Depth of penetration, weld width, and overall area of penetration in each case of activated flux and without activated flux

### 3.4.3 Weld Chemistry and Oxygen absorption

The oxygen content in weld would be the function of decomposition of flux and absorption of oxygen in the molten weld metal. However, the decomposed flux elements like Cr, Mo, S, and Si would also contribute to weld chemistry. Such variations in major alloying elements of weld metal have been measured with optical emission spectroscopy (OES), and further, the results were validated using energy-dispersive spectroscopy (EDS). The EDS results are observed to agree with OES results for major alloying elements. Hence, using a small concentration of elements and oxygen (O) obtained with EDS were used for qualitative comparison among the specimens used in the study.

### 3.4.4 Oxygen absorption and Marangoni convection

The EDS spectrum for weld metal location without flux condition and $MoS_2$ flux is shown in Fig. 3.30 A and 3.30 B, respectively. Similarly, the EDS spectrum for $SiO_2$ and $CrO_3$ fluxes are shown in Fig. 3.31 A and 3.31 B, respectively.

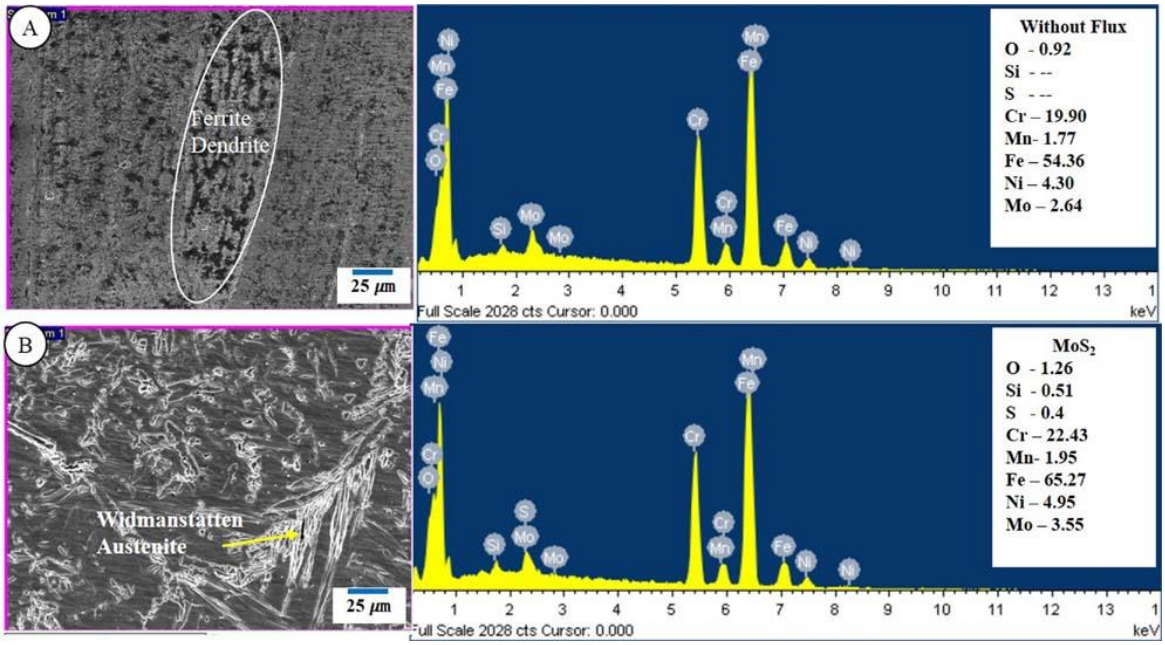


Figure 3.30: EDS spectrum showing peaks of elemental composition in weld nugget for (A) Without flux and (B) $MoS_2$ activated flux

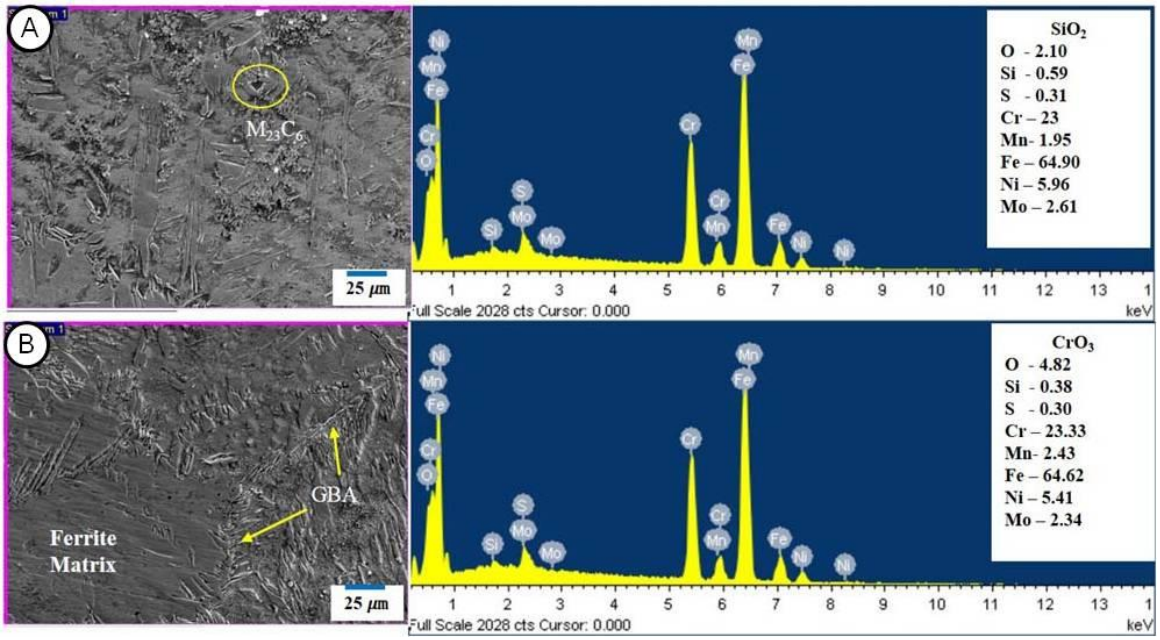


Figure 3.31: EDS spectrum showing peaks of elemental composition in weld nugget for (A) $SiO_2$ activated flux and (B) $CrO_3$ activated flux

Considering the accuracy in measurement from EDS, the qualitative comparison for oxygen has been conducted validates the increase of oxygen in $SiO_2$ weld and further increases in $CrO_3$ weld due to its composition (extra oxygen molecules). The dilution could also be considered the measure of penetration to width ratio (P/W); hence, the dilution would increase when oxygen content increases more than $70x10^{-6}$ [83]. Thinking the data qualitatively, the higher dilution noticed in $CrO_3$ weld, however, lowest in without flux condition and the role of oxygen

in increasing the dilution and penetration can be confirmed from the oxygen contents in weld (Fig. 3.30 and Fig. 3.31). The temperature coefficient of surface tension (dσ/dT) is always negative for the Fe-O system with low oxygen content [74, 83]. However, it changes from negative to positive when oxygen content exceeds the critical value [74, 83], as observed in the present study. In stainless steel, S and O are the active elements [74, 83], and in $MoS_2$ and oxide-based ($SiO_2$ and $CrO_3$) fluxes, the content of these elements increased in the weld metal. When the active elements exceed the specific values (critical), the temperature coefficient of surface tension (dσ/dT) changes from negative to positive, that is dσ/dT > 0, and the direction of Marangoni convection in weld pool changes to the inward flow. This would transfer the heat flux from centre to bottom and deeper penetration and narrow weld shape forms [74, 83]. The active elements vary according to the described phenomena that have been observed in the EDS spectrum of Fig. 3.30 and Fig. 3.31. However, the increase in Mo and S was also noticed in $MoS_2$ flux while an increase in the content of Si and Cr in $SiO_2$ and $CrO_3$ is also validated with OES for the present study.

### 3.4.6 Peclet number and Marangoni convection

It has been observed that the weld pool shape is controlled by heat transfer due to a combination of convection and conduction in the molten pool. The ratio of heat transfer by convection and conduction is different for different materials, and the Peclet number (Pe) can determine it. The Peclet number can be defined as $Pe=L*V_{max} / 2\alpha_l$ [83, 85, 86]. The maximum surface velocity Vmax can be taken as 0.12 m/sec [85, 86] for stainless steel. $\alpha_l$ is the thermal diffusivity of liquid, and $L$ is the characteristic length of the weld pool. This length has been taken as the radius of the weld pool in without flux condition, and depth of penetration has been taken in activated flux condition [83, 86]. The thermal properties of DSS are taken from the manufacturer catalogue [87]. The Peclet number for all weld profiles shown in Fig. 3.28 are calculated for comparison and analysis purposes.

The Peclet number without flux condition is determined as 19.61 (Fig. 4.28 A) and for MoS2, SiO2 and CrO3 the Peclet numbers were found to be 48.52, 52.86 67.10 for the macrographs, shown in Fig 3.28 B-D, respectively. Heat transfer in the weld pool is dominated by conduction for $Pe << 1$, while $Pe >> 1$, the heat transfer in the weld pool is dominated by convection [83]. The high Peclet number suggests the heat transfer in the molten pool in this study is dominated by convection mode. Therefore, the A – TIG weld pool behaviour and shape largely depend on the fluid flow mode in the weld pool, which is governed by the combined effect of

electromagnetic arc plasma [74, 83]. Hence, these factors further govern the fluid flow behaviour and the inverse Marangoni convection.

### 3.4.7 Gas-metal and Slag-metal reactions

The gas-metal reactions occur due to the presence of oxygen in the $SiO_2$ and $CrO_3$ fluxes. The oxygen and other elements in flux are decomposed under the intense heat of arc plasma. In $SiO_2$ flux, the oxygen atom reacts with carbon atoms of the base material, and that leads to the formation of $CO/CO_2$. The carbon content in base metal is oxidized due to decomposed oxygen in the molten weld metal. The formation of $CO/CO_2$ would increase the volume (as gas) in solidus/liquidus weld metal. This volumetric expansion would lead to the formation of crack at the end of the cavity or void that would form due to gaseous expansion. These cavities or voids are encircled in Fig. 3.28 C and D of the oxide-based fluxes. Such cavity/voids are not noticed with $MoS_2$ flux. Hence, the role of oxygen in void formation can be ascertained. While using $CrO_3$, the oxygen atoms are comparatively more than $SiO_2$ and could form the $CO_2$ due to excess oxygen. Hence, the cavity in the centre (cone) has been noticed and encircled in Fig. 3.28 D. If a further increase in CO or $CO_2$ formation, the size of the cavity could increase, and that may lead to hot crack propagation. The same thing has been discussed in the subsequent microstructure section. The slag metal reaction needs to consider while using the activated flux, and this would also support the reverse Marangoni convection. An electrochemical reaction takes place between the electrode and the weld coupon under the intense heat of an arc. In A-Tig welding, the plasma of the arc results in melting of the base metal surface, and the oxides in the form of a thin layer (flux) become reactive and mixed in the molten pool. The reactive flux changes the temperature coefficient of surface tension from negative to positive, which further moves in the centripetal direction with the molten pool. The stationary arcing for 6 sec is sufficient for producing heat, which would decompose the flux into metal and oxides. The entrapment of such oxide inclusion cannot be denied, and some oxide residue could remain present near the weld pool. This can be visualized in Fig. 3.27 for oxide residue which is significant for the $CrO_3$ flux condition. The slag-metal reaction which occurs in the present work are as follows:

$$(SiO_2) = SiO(g) + ½\ O_2\ (g) \qquad (1)$$

Due to further decomposition of SiO into ‘Si’ and ‘O’ atoms and capturing the electron from the outer region of the arc results in the formation of slag and metal. The chemical reaction is as follows:

$$SiO\ (g) = Si + O \qquad (2)$$

$$Si^{4+} + 4e^{-} = Si\ (Metal) \quad (3)$$

$$O\ (Metal) + 2e^{-} = O_2^{-}(Slag) \quad [32] \quad (4)$$

$$\text{Similarly, } 4\ CrO_3 = 2\ Cr_2O_3 + 3\ O_2 \quad (5)$$

$$3\ CrO_2 = 3\ CrO + O_3 \quad (6)$$

$$CrO = Cr + O \quad (7)$$

$$O\ (Metal) + 2e^{-} = O^{2-}\ (Slag) \quad (8)$$

Considering the above reaction, the extra Cr participates in forming a complex Cr enriched phase. Such weld chemistry could influence the resulted phase structure and associated metallurgical properties. The presence of Cr could also participate in a deep hot crack propagation owing to the non-mixing of different phases. The extra oxygen may further participate in increasing the net thermal energy of the constricted arc, which results in deeper penetration.

### 3.4.8 Weld Microstructure and Micro-hardness

The microstructure obtained after welding is strongly influenced by the local variation in cooling rates, the heat flow direction, and the chemical composition of base metal as well as fillers. Figure 3.28 shows the macrograph of different weld coupons without flux conditions and the other three activated fluxes. The different ferrite and austenite structures for equiaxed grains and dendrite are visible in Fig. 3.28 A-D. The macrostructure was observed with a dark phase of ferrite and a bright phase of austenite. The white horizontal and vertical lines in the macrograph are representing the region of micro-hardness data points. The white encircled region shows the portion where a cavity/void was formed after A-TIG welding. It is evidenced from macrograph that, in without flux condition, the depth of penetration (DoP) is very less as compared to the width of weld, whereas in the case of $MoS_2$ flux, the DoP is higher and due to more oxygen element in $SiO_2$ and $CrO_3$ fluxes, DoP increases with increase in oxygen content. Due to coarser columnar grains, a solidified crack (trans-granular) appeared in the case of $CrO_3$ flux, and the phenomena have been elaborated in this section. A mixed matrix of both ferrite and austenite phases is noticed in Fig. 3.28 A, B; however, marginally more ferrite is visible in the case of both $SiO_2$ and $CrO_3$ flux conditions compared to the austenite.

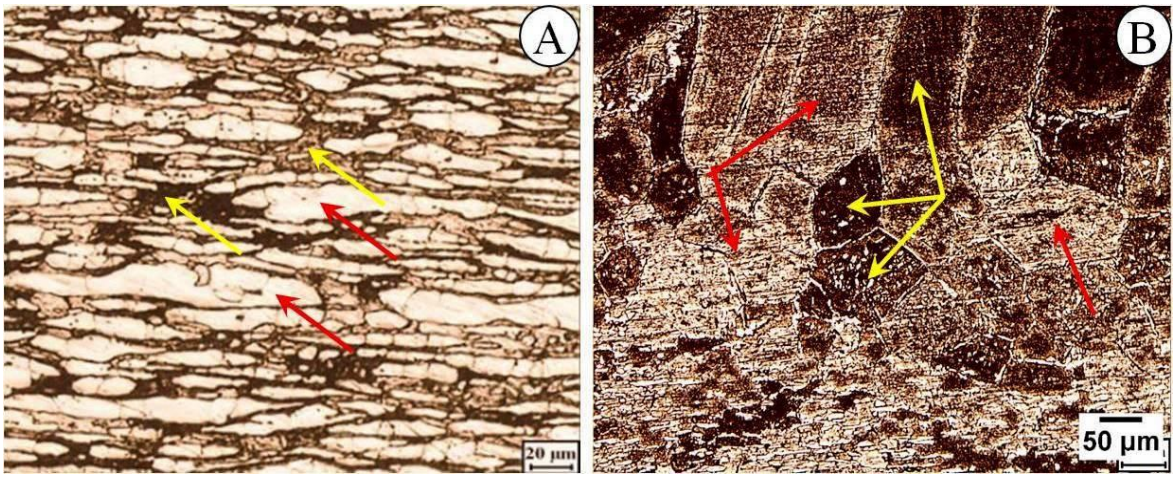


Figure 3.32: Optical micrograph of (A) Base Metal and (B) weld metal without flux weld

The hot crack occurred in A-TIG welding using $CrO_3$ flux, which is visible in the micrograph. Duplex steels are usually solidified in ferrite mode, and a higher $Cr_{eq}/Ni_{eq}$ ratio is one of the main reasons for cracking susceptibility. The dendrites are generally surrounded by low melting point elements in the fusion zone. Due to solidification and shrinking strain at this stage of solidification, hot cracks may initiate and propagate [78, 82]. Moreover, the formation gas ($CO/CO_2$) due to carbon oxidation, the volumetric expansion also accelerates the crack propagation during the solidus/liquidus nature of weld metal. The weld pool shape or weld profile is also responsible for solidification cracking susceptibility. The direction of columnar grain growth is perpendicular to the solid/liquid interface. The occurrence of reverse Marangoni convection may also promote hot cracking susceptibility in case of low melting point impurities if available in the centre region of the weld pool. The equal phase matrix of austenite and ferrite can be seen in the micrograph of base metal in Fig. 3.32 A by yellow (Ferrite) and red (Austenite) arrows. The HAZ and weld metal interface shows the epitaxial growth in the case of without flux in Fig 3.32 B. The HAZ grains and dendrite arm spacing for austenite and ferrite are shown in Fig. 3.32 B using red and yellow arrows, respectively. It is noted that the delta ferrite matrix is uniformly distributed, and both ferrite and austenite were present at the grain's boundary. The weld pool solidifies from the liquid to a complete ferritic phase due to a significant amount of chromium and molybdenum present in the base metal (ferrite stabilizers). The austenite grain size (AGS) for parent metal was observed to be ~35 microns (ASTM E112-96 number – G 6.5 – 7); however, ferrite grain size (FGS) was noticed to be ~20 microns (ASTM E112-96 number – G 8 – 8.5), and this can be observed in Fig. 3.32 A. The parent metal's grain size has been used to compare grain growth that occurred in the respective heat-affected zone (HAZ). The HAZ grain size is dependent on the heat input and

peak temperature during welding; hence, the comparison for heat produced has been made by quantifying the HAZ grain size.

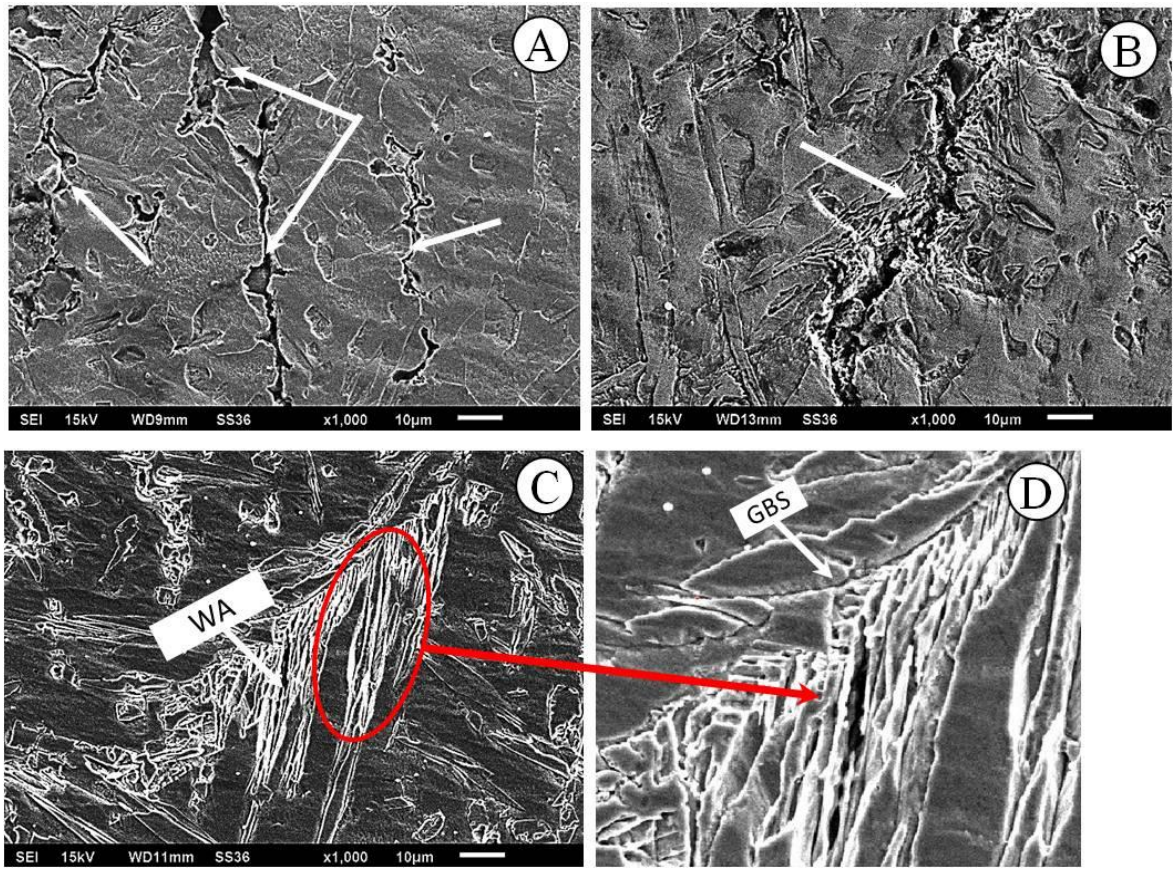


Figure 3.33: SEM image of A-TIG welded samples with (A) $SiO_2$ (B) $CrO_3$ (C) $MoS_2$ fluxes showing micro-cracks and grain boundary separation

Figure 3.33 shows the weld metal microstructure of A-TIG specimens captured with SEM. As the material cools down to room temperature, a substantial amount of austenite could be distributed, and similar behaviour can be observed with all microstructures shown in Fig. 3.33. The duplex series steel is solidified in ferrite mode first and later on in austenitic mode. Solidification cracking would be predominant in another type of steel (austenitic) when they are solidified in FA mode. However, a similar phenomenon for cracking has been investigated in the present study. The presence of ferrite –ferrite boundary at the end of solidification could be considered the reason behind this. The analysis of the top centre zone of A-TIG welded samples is discussed in this section using Fig. 3.33 A-C. In Fig. 3.33 A, B, the approximately larger area is covered by a ferrite matrix with a small fraction of austenite at the grain boundary. The crack was observed in A-TIG welded samples of $SiO_2$ and $CrO_3$ fluxes, and the same is shown in Fig. 3.33 A, B. The cracks were noticed after complete solidification, which was formed due to the volumetric expansion of solidus weld metal owing to the formation of

$CO/CO_2$ as discussed in earlier sections. In $SiO_2$ flux, the micro-crack appeared in ferrite grain; however, with $CrO_3$ flux, the crack formation was visualized after the volumetric expansion of $CO/CO_2$ void in the solidus weld metal and can be seen with Fig. 3.33 A, B. It can be observed from Fig. 3.33 that ferrite was the first phase developed after solidification. The segregation of grains due to the presence of impurity elements, which have low melting points, leads to grain boundary separation (GBS). This phenomenon was also noticed in the SEM micrograph of the sample, which was welded with $MoS_2$ flux. Due to the low melting point of impurities, which may further lead to liquation, the film is the main cause of GBS. Moreover, the micro-crack is also obtained owing to impurities within the austenite dendrite, and the enlarged portion of the micro-crack is shown in Fig. 3.33 D. Widmanstatten austenite (WA) [77] was observed in sample welded with $MoS_2$ flux and shown in Fig. 3.33 C.

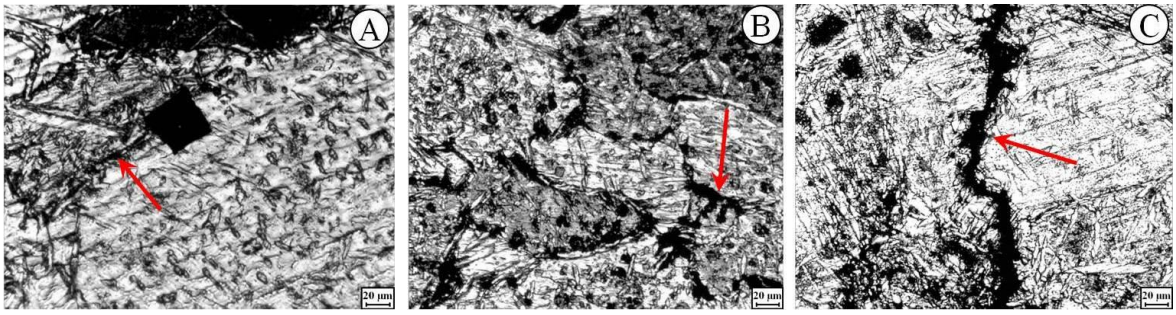


Figure 3. 34: Optical micrograph of weld metal using (A) $SiO_2$ (B) $MoS_2$ (C) $CrO_3$ fluxes showing cracking susceptible area

The micrographs shown in Fig. 3.34 are susceptible to the hot cracking phenomenon, and the region of cracks, which were not clear in Fig. 3.28 due to lower magnifications, are presented. The cracks formed at the top region (near to void) are presented in Fig. 3.33 using SEM; however, in the interior of the weld, some cracks have been seen and shown in Fig. 3.34 A-C for $SiO_2$, $MoS_2$, and $CrO_3$ flux respectively. In Fig. 3.34 A-C, the cracks (black shade) are comparatively larger than Fig. 3.34 B (smaller cracks at grain boundaries indicated by arrow) along with impurities and second phase particles with almost equiaxed grains.

The austenite has been formed at grain boundaries, which originated from the ferrite matrix [72] can be visible from Fig. 3.35. A small number of austenite pallets are visible within ferritic grains. The weld metal microstructure in Fig. 3.35 A – C represents the optical micrographs for quantification of austenitic dendrite arm spacing (ADAS) and ferritic dendrite arm spacing (FDAS).

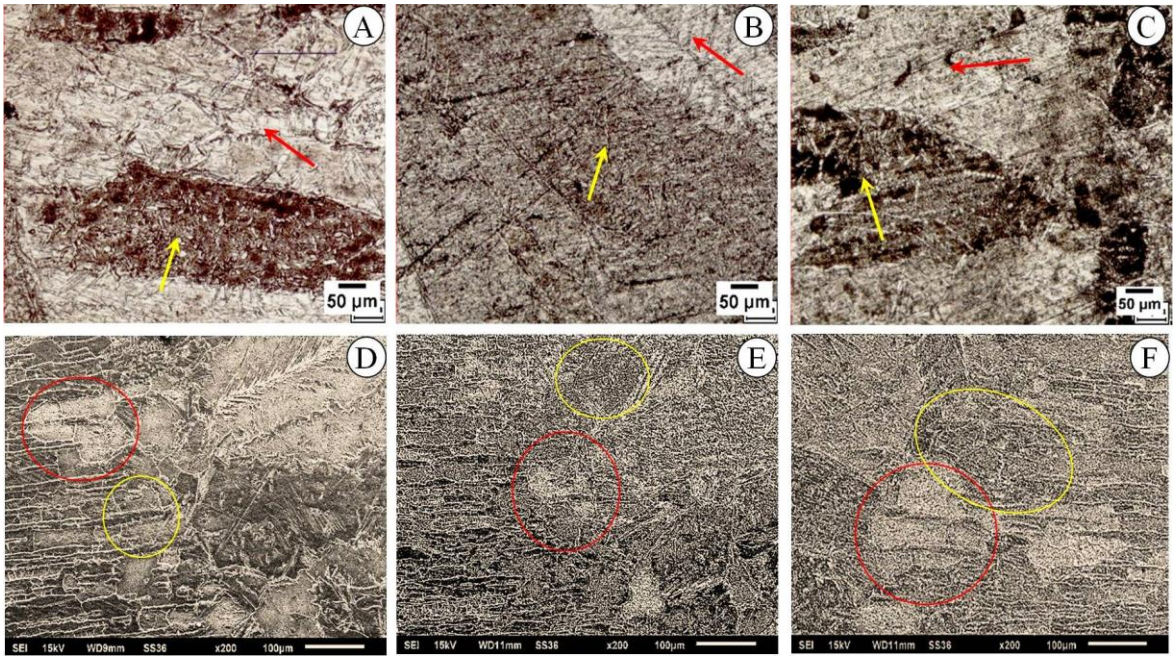


Figure 3.35: Optical micrograph of weld centre of (A) $SiO_2$, (B) $MoS_2$, (C) $CrO_3$, and HAZ region of (D) $SiO_2$, (E) $MoS_2$ (F) $CrO_3$ fluxes

The austenite grains are shown with a red arrow. However, the yellow arrow indicates the ferrite dendrites. The FDAS in $SiO_2$ flux was measured as ~234 microns (average) with ~1644-micron length and ADAS as ~258 microns with ~2173-micron length. Similarly, FDAS was noticed to be ~125 microns with ~498-micron length and ADAS as ~131 microns with ~590-micron length in $MoS_2$ flux. While, in $CrO_3$ flux, the FDAS was observed as ~199 microns and ADAS as ~ 218 microns with ~1841 and ~1853-micron length, respectively. The quantified data can be confirmed with Fig. 3.28 as it has been represented in Fig. 3.35. The quantified data for different flux conditions have been compared with those without flux conditions. The FDAS in without flux condition has been noticed as ~99 microns and ADAS as ~83 microns with ~465 and ~769-micron dendrite length in the respective case. It is evidenced that the austenitic dendrite length is significantly more than ferritic dendrite length in all conditions of with and without fluxes. This could signify the complete primary solidification of ferrite followed by austenite with the growth of dendrite arms. With $SiO_2$ and $CrO_3$ (oxide) fluxes, the ADAS is marginally more than the FDAS; however, this effect was not observed to be significant with $MoS_2$ flux and found to be reversed in the case of without flux condition. Hence, dissociated oxygen content in weld could influence the dendrite arm spacing, which would be predominant for the growth of austenite than the ferrite in the weld metal.

As discussed earlier, the grain growth in HAZ would be the function of heat produced, cooling rate, and peak temperature. Therefore, the grain size of austenite and ferrite in HAZ in each

case of flux condition would give vital information on the heat produced and be compared with parent metal grain size. The ferrite grain size (FGS) in HAZ without flux was noted as ~60 microns (ASTM E112-96 number – G5 – 5.5), and austenite grain was observed to be ~66 microns (ASTM E112-96 number – G4.5 – 5). The heat produced is expected to increase the grain size in HAZ of different flux conditions. It has been confirmed from the grain size that the $CrO_3$ flux has produced higher heat, followed by $SiO_2$ and $MoS_2$. The AGS in weld metal of $CrO_3$, $SiO_2$, and $MoS_2$ fluxes are ~139 microns (G2.5 – 3), ~107 microns (G3 – 3.5), and ~104 microns (G3 – 3.5), respectively. However, the FGSs are ~136 microns (G2.5 – 3), ~104 microns (G3 – 3.5), and ~80 microns (G4.5 – 4), respectively, for $CrO_3$, $SiO_2$, and $MoS_2$ fluxes.

Secondary austenite was observed in the micrograph of weldment in little percentage after the complete solidification and dilution process. Therefore, it may help reduce pitting corrosion [32]. The austenite stabilizers and formers like Ni and Mn cannot be increased in weld (as no filler metal), and the nitrogen is not present in the parent metal. However, the decomposition of flux Cr, Mo, and Si could increase the weld metal, which is ferrite formers. Hence, ferrite growth is predominant, and this leads to growth at low ferritic solvus temperature. According to the WRC-1992 diagram [88] and chemical composition of Duplex 2205 steel (Table - 3.1), the values and equations used to determine the $Cr_{eq}$ and $Ni_{eq}$ [82], their ratio and the solidification field are:

$$Cr_{eq} = Cr + Mo + 0.7\ Nb = 28.1814\ [82]$$

$$Ni_{eq} = Ni + 35\ C + 20\ N + 0.25\ Cu = 6.4$$

$$\text{Hence, } Cr_{eq}/\ Ni_{eq} = 4.40$$

The observed $Cr_{eq}/\ Ni_{eq}$ ratio in the present study is sufficient for solidification cracking [34] along with the previously explained mechanisms for observed cracks.

The Vickers micro-hardness for all weld coupons in the region shown in Fig. 3.28 are given in this section. A dwell time of 20 sec with a load of 500 gf has been used in this study. The schematic locations hardness indentations are given in Fig. 3.36 A, B.

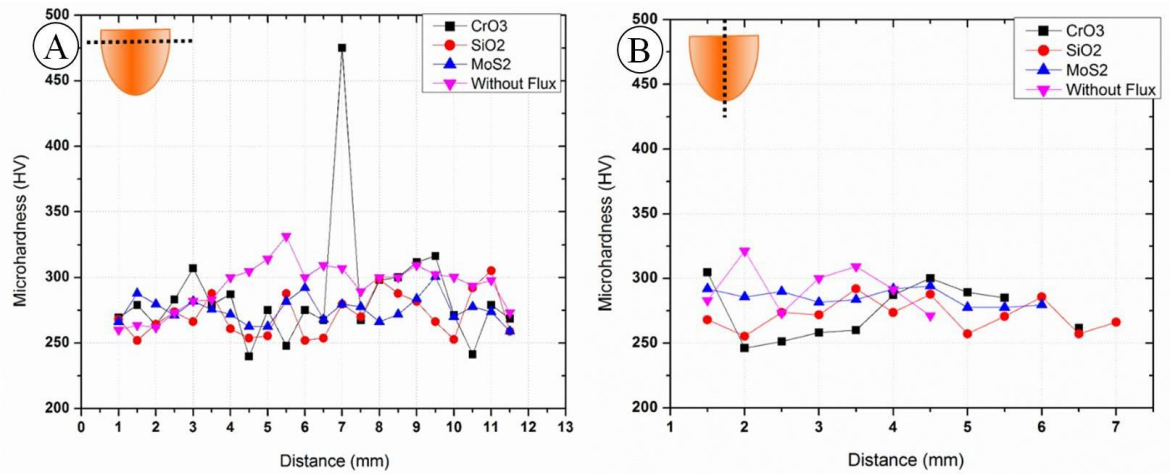


Figure 3.36: Micro-hardness comparison graph between no flux condition and other samples welded with different fluxes

The average micro-hardness of the conventional TIG weld is marginally higher than the rest weld coupons of activated flux conditions. It was observed to be a thermodynamic effect (faster cooling rate) than the weld composition chemistry. It can be justified that the cooling rate is faster in an earlier case due to less heat produced than the activated flux condition. However, the hardness variations within the different flux conditions are not significant and not observed with a valid reason to fluctuate significantly. In the $CrO_3$ flux condition, one instant of high micro-hardness value has been observed, and the location suggests that the region of hardness is near to the void, an associated crack due to the complex structure. It could be due to the formation of Cr enriched sigma phases, as discussed in the previous section. It is observed from hardness analysis that the hardness of A-TIG welding is marginally less than TIG welding. There is no significant variation in weld metal hardness among the different flux conditions except the thermodynamic effect cooling rate.

## 3.5 Summary

Activated fluxes generate extra thermal energy  with the same process parameters and cause deeper penetration and increased dilution. The weld shape formed without flux depicts a predominant outward liquid metal flow pattern. However, with activated fluxes (enriched oxygen content), the surface tension gradient ($d\gamma/dT$) [13, 54] changed its trend from negative to positive, and that further drifts the liquid metal down to the axis of the weld pool. Heat transfer in the molten pool is dominated by convection mode due to activated fluxes, which is reflected from the higher Peclet number (Pe). The presence of oxygen / oxide-based fluxes leads to the formation of CO / $CO_2$ in the weld. That could be the main reason for void/cavity formation and associated cracking due to the volumetric expansion of gas. The oxygen content in activated flux has played a significant role in hot cracking and void formations in the weld. Similarly, it has also changed the surface tension gradient of the weld pool significantly. Dendrite growth is predominant in oxide-based fluxes, and this growth in austenite and ferrite dendrite has been evidenced as a function of oxygen content.

# Chapter - 4
## Stationary A-TIG Welding (with "Ar+2.5% $H_2$"-shielding)

## 4.1 Introduction

This chapter includes a study similar to chapter **3** with the only difference of shielding environment. All the experiments were performed using Ar + 2.5 % $H_2$ shielding environment on the same stainless steels, i.e., AISI 304, AISI 316, and DUP 2205, which were used for the Ar shielding environment. This study aims to find out the role of the $H_2$ mixed shielding environment on the weld microstructure. The net heat generated during the process correlates with the dendrite and grain growth, other microstructural changes, and other related properties. The use of activated flux in the GTAW process enhances the metal penetrating capability and improves process capability [8, 9, 13, 20, 89]. The presence of hydrogen ($H_2$) gas in the plasma would generate more heat by dissociating molecules into hydrogen atoms. In the presence of oxygen elements, this would result in higher arc temperature and more heat generation owing to high thermal conductivity [90]. Thus, a small amount of hydrogen gas in shielding gas (Ar) could enhance penetration [6, 13, 45] by increasing melting efficiency and improving the weld characteristics. On the other hand, the presence of $H_2$ in the shielding environment causes an increase in the voltage drop and leads to energy concentration [8, 15, 49, 91].

Similarly, the presence of oxygen during welding also affects the weld pool behaviour [83]. Using a mixed shielding gas environment (inert gas + reducing + reactive gas) could lead to an increased depth of penetration. Hence, the instances of hydrogen and oxygen in the shielding environment will affect the weld pool behaviour by the dissolution of oxygen and oxide formation (Hydrogen as chemically reducing agent) in context to weld pool behaviour, deeper penetration, and reverse Marangoni convection [15, 83].

A small amount of hydrogen ($H_2$) gas in the plasma would generate additional heat by dissociating molecules into hydrogen atoms. In the presence of oxygen elements, the amount of generated heat can increase significantly [90]. Thus, a small amount of reactive hydrogen gas in shielding gas (Ar) could enhance penetration [6, 13] by increasing melting efficiency and improving the weld characteristics. The presence of $H_2$ in the shielding environment causes an increase in the voltage drop and leads to energy concentration [8, 15]. Similarly, the presence of oxygen during welding also affects the weld pool behaviour [83]. Mixing of shielding gases and shielding with a dual gas environment [92] could increase penetration depth. Hence, the

instances of hydrogen and oxygen in the shielding environment will affect the weld pool behaviour by the dissolution of oxygen and oxide formation (Hydrogen as chemically reducing agent) in context to weld pool behaviour, deeper penetration, and reverse Marangoni convection [15, 83, 92].

Oxygen content from the oxide-based fluxes, other active elements, and $H_2$ in shielding can govern the weld pool morphology, behaviour, depth of penetration, and reverse Marangoni convection. Adhering, it could control ferrite formation in the austenite matrix, which considerably affects corrosion resistance and hot cracking phenomena. Under Ar shielding environment, the oxygen-rich activated fluxes/Compounds ($SiO_2$, $MoS_2$, and $CrO_3$) have different elements like Si, Mo, and Cr that act differently by changing metal chemistry. Hence, the same oxide-based fluxes, including $TiO_2$ under $H_2$ mix (Ar + 2.5% $H_2$) shielding environment, need to be evaluated on the same welding parameters based on variation in the microstructure, dilution, and Peclet number. The activated flux acts as an insulator and forms a barrier [2, 14] in the path of the current flow direction. The present study investigated the effects of surface-active elements in decomposed oxygen and hydrogen in a shielding environment. Hydrogen (2.5 wt. %) was mixed in argon gas to conduct experiments, and four different oxide and sulfur base fluxes were used in the present study.

The investigation addresses the effect on weld pool behaviour, depth of penetration, weld pool chemistry, reverse Marangoni convection, Peclet number variation, and weld-pool microstructure evolution. In addition, heat input produced due to variables like the flux and the shielding environment has been discussed and compared with the un-fluxed condition. Finally, the distinctive observations are elaborated in the study with an associated mechanism, which explores the understanding of the process.

## 4.2 Materials and Method

This study is a part of stationary A – TIG welding, so the materials and method are the same as described in Chapter 3 with the difference in shielding environment, i.e., Ar + 2.5 % $H_2$ was used instead of pure Ar. The schematic of the process with the arc constriction mechanism is shown in Fig. 4.1.

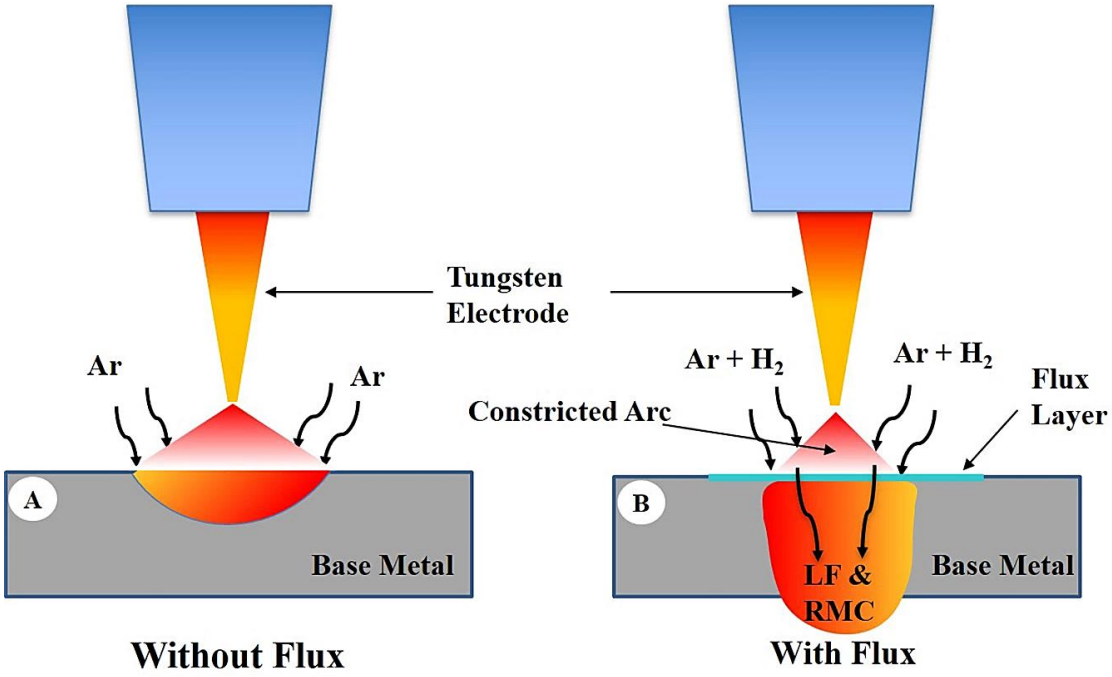


Figure 4.1: (A) Schematic representation of the process of stationary TIG welding (B) Stationary A – TIG welding with arc constriction behaviour

## 4.3 Results and Discussion (Ar + 2.5 % $H_2$ Shielding)

### 4.3.1 Effect of Activated Flux on Bead Appearance and Penetration on AISI 304

The as-welded Ar + 2.5 % $H_2$ shielded weld coupons of conventional TIG and A-TIG welding on AISI 304 are shown in Fig. 4.2, which shows the top surface appearance and effect of different arc exposure times (i.e., 2 s, 4 s, and 6 s). The effect of reverse Marangoni convection and Lorentz force and associated material flow pattern is validated by the cone formation in the case of all the A – TIG welding. A small cavity was also observed in the case of conventional TIG welding (Fig. 4.2) due to the $H_2$ shielding environment. This effect was not observed in the case of pure argon shielding (Chapter 4). As in Ar shielded A-TIG welding, in this study, the depth of cone type cavity is also increasing with the increasing of arc exposure time, consequently increasing the penetration of weld (Fig 4.2). In the case of $TiO_2$ and $CrO_3$, the effect of activated flux and $H_2$ mixed shielding is more significant, where the penetration goes beyond the thickness of the metal as the $H_2$ gas has a high enthalpy rate, so it increases the temperature at the anode. At higher temperatures, the surface-active elements present in the oxide-based fluxes help change the surface tension gradient from negative to positive, which would be the primary cause of the reverse Marangoni effect. In the case of $MoO_3$ flux, a minute crack was observed after the etching. Some flux residue was also observed in all A – TIG welding which should be removed after welding.

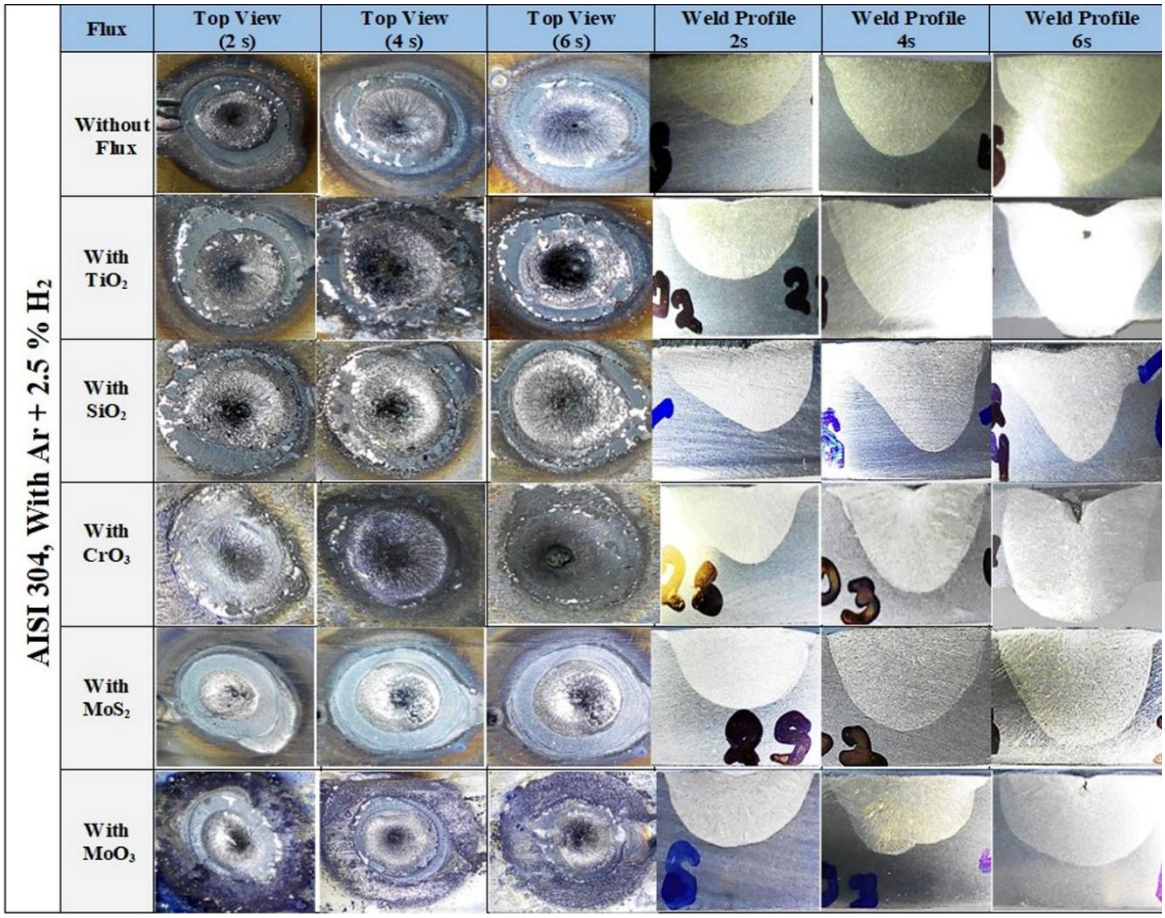


Figure 4.2: Showing the top surface and penetration of TIG and A-TIG welding of AISI 304 at different arc exposure times using Ar + 2.5 % $H_2$ shielding

### 4.3.2 Effect of Activated Flux on Microstructure of AISI 304:

After the experiment, all the welding samples were cut from the centre with a surface grinding and polishing margin. A standard metallurgical procedure was adopted for this study. And all the specimens were etched by "Carpenter Etchant" and observed under a metallurgical microscope. Fig. 4.3 to Fig. 4.8 shows the microstructure of the interface region of three magnification levels, i.e., 10 X, 20 X, and 50 X. No significant difference in terms of phase was observed in the microstructures of AISI 304 steel, but an increase in the concentration of resultant delta ferrite was observed. More concentration of resultant delta ferrite was observed in the case of without flux condition as compared to with flux condition. In the case of 2-sec arc exposure time, the consequent delta ferrite was not fully developed due to fast cooling. Whereas, in the case of 6 sec fully developed resultant ferrite matrix was observed to slow cooling rate. In some cases, the only change in the morphology/type of the resultant delta ferrite content was observed.

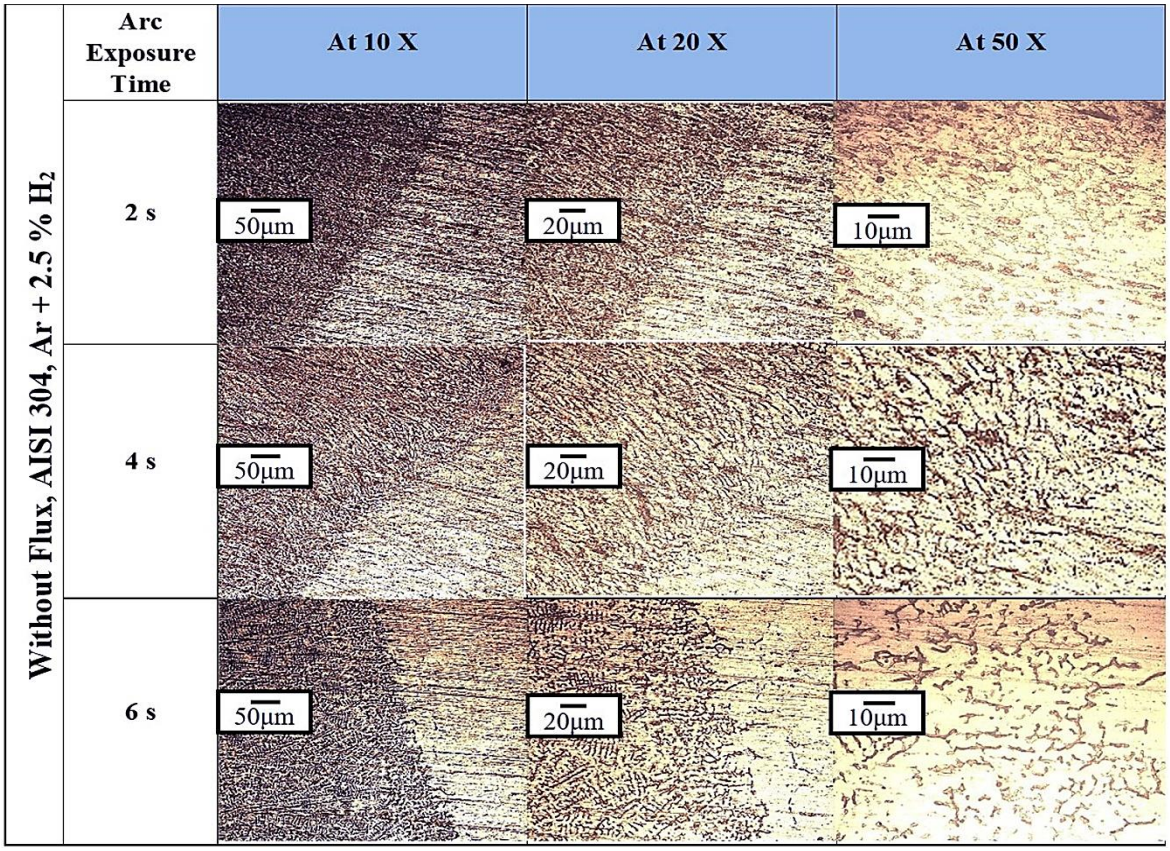


Figure 4.3: Microstructure of different arc exposure time (2s, 4s, and 6s) of conventional TIG welding on AISI 304 using150 A, Ar + 2.5 % $H_2$ shielding with 10 L/min gas flow rate

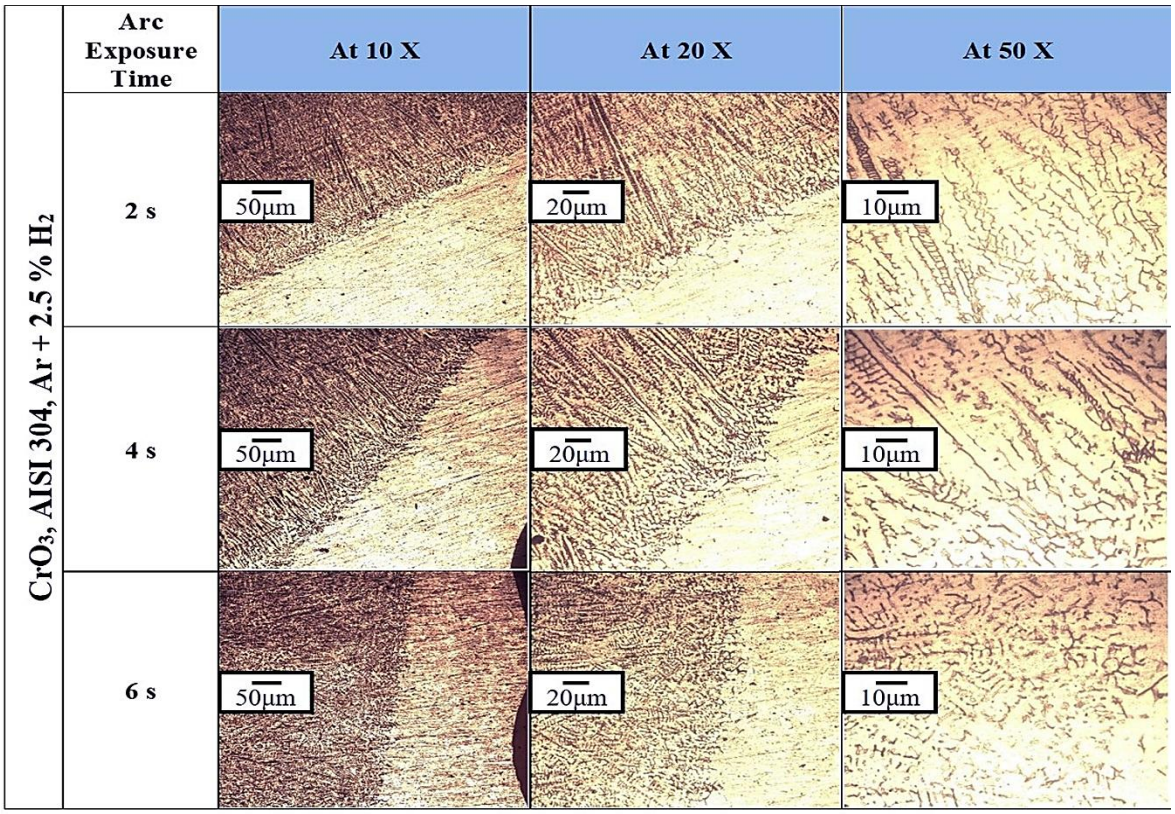


Figure 4.4: Microstructure of different arc exposure time (2s, 4s, and 6s) of A-TIG welding with $CrO_3$ flux on AISI 304 using150 A, Ar + 2.5 % $H_2$ shielding with 10 L/min gas flow rate

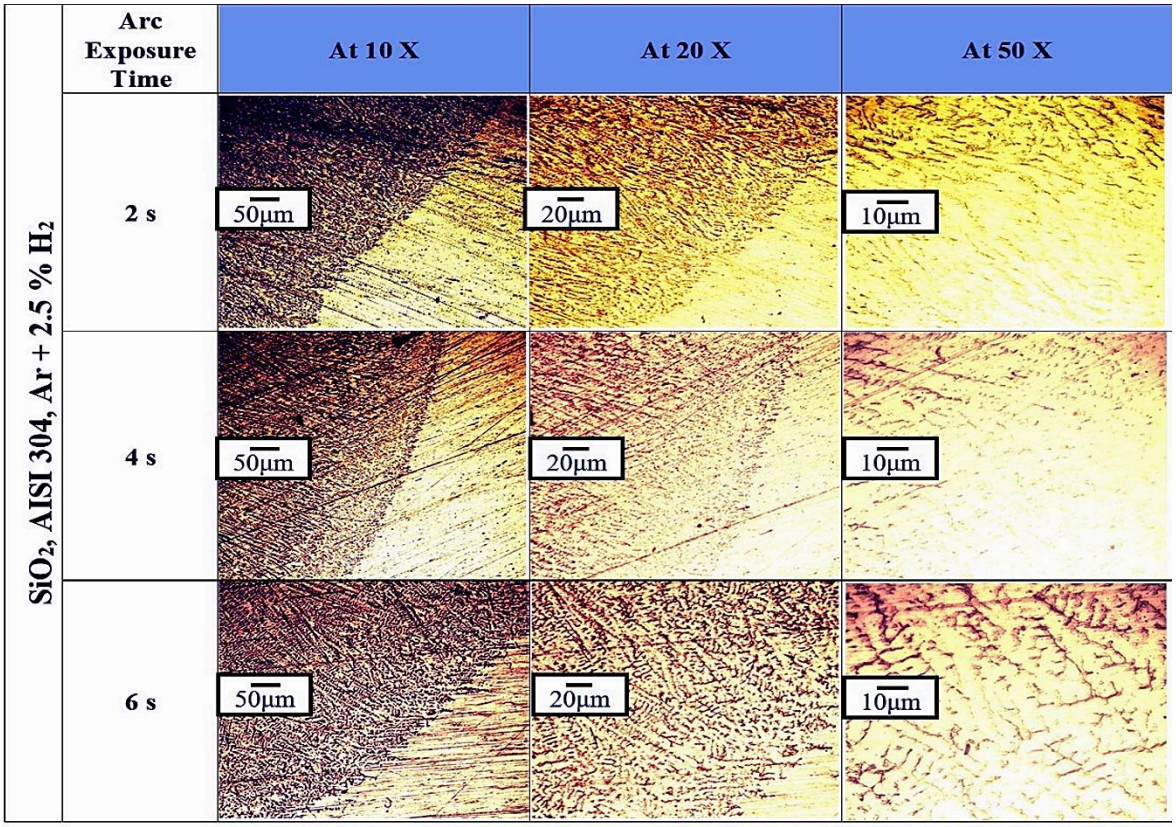


Figure 4.5: Microstructure of different arc exposure time (2s, 4s, and 6s) of A-TIG welding with $SiO_2$ flux on AISI 304 using150 A, Ar + 2.5 % $H_2$ shielding with 10 L/min gas flow rate

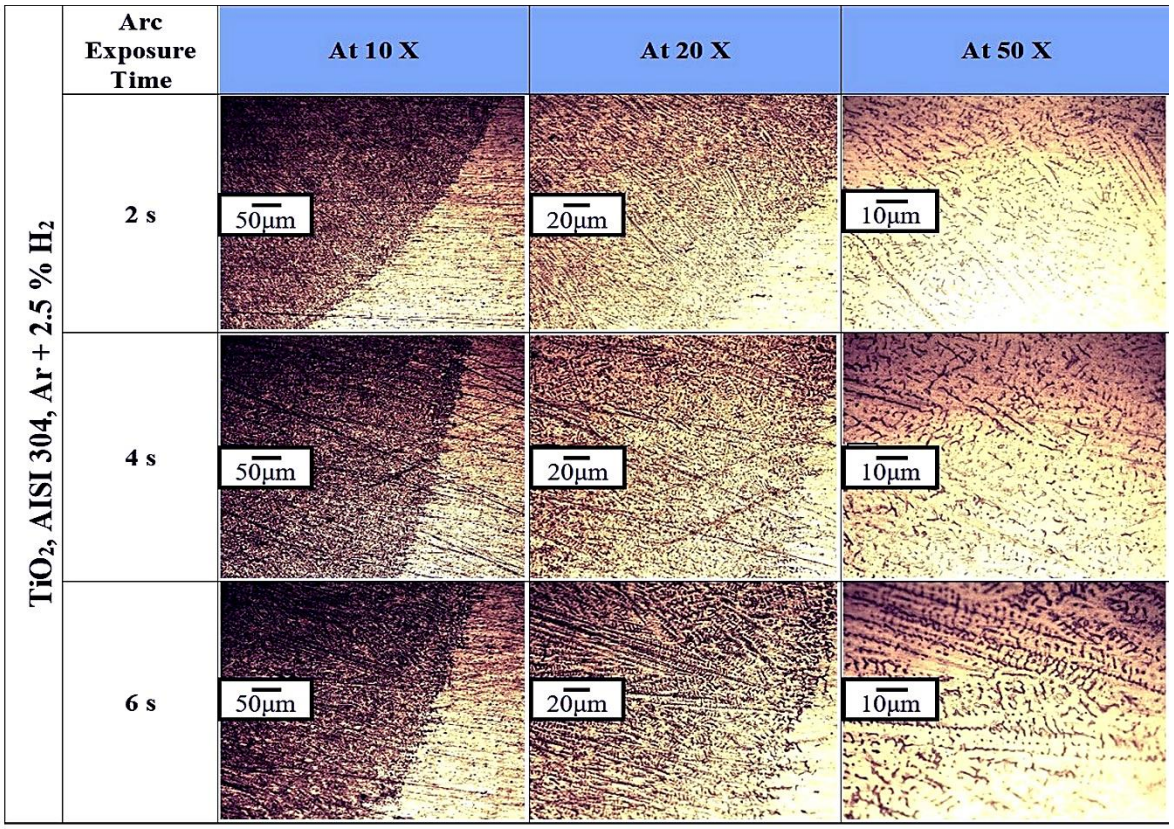


Figure 4.6: Microstructure of different arc exposure time (2s, 4s, and 6s) of A-TIG welding with $TiO_2$ flux on AISI 304 using150 A, Ar + 2.5 % $H_2$ shielding with 10 L/min gas flow rate

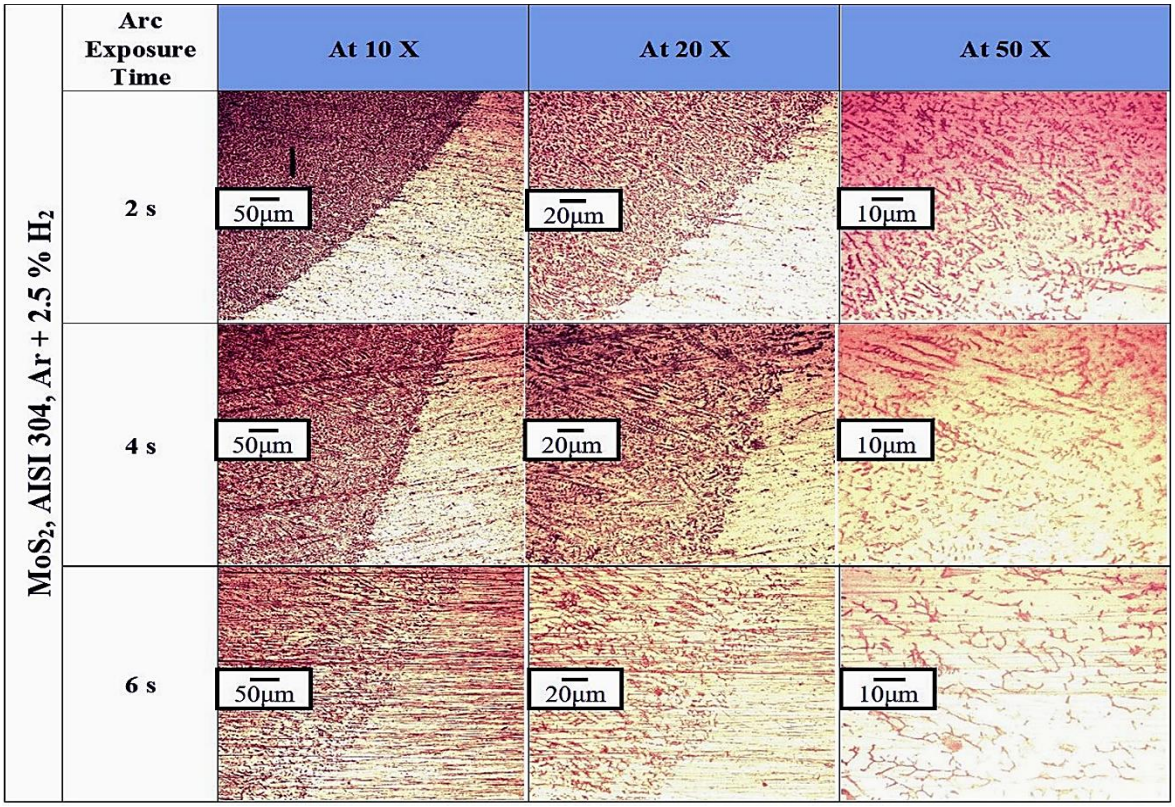


Figure 4.7: Microstructure of different arc exposure time (2s, 4s, and 6s) of A-TIG welding with $SiO_2$ flux on AISI 304 using150 A, Ar + 2.5 % $H_2$ shielding with 10 L/min gas flow rate

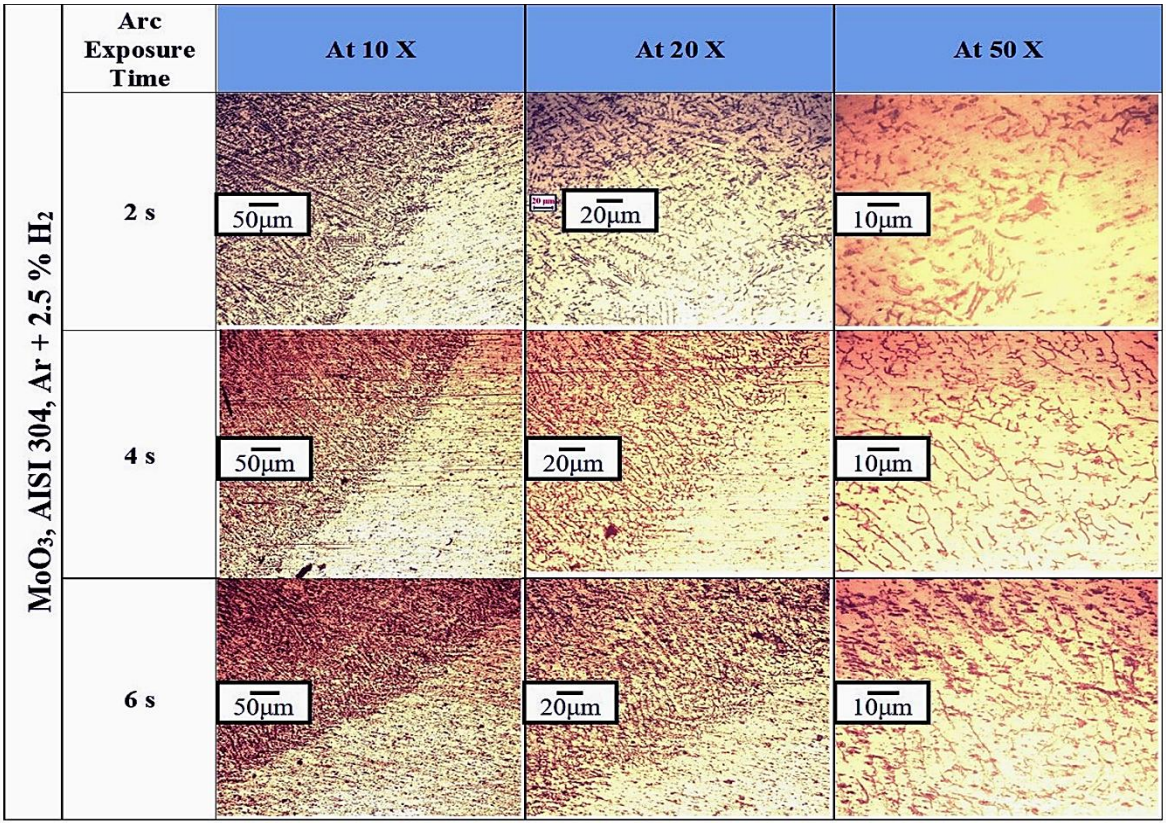


Figure 4.8: Microstructure of different arc exposure time (2s, 4s, and 6s) of A-TIG welding with $MoO_3$ flux on AISI 304 using150 A, Ar + 2.5 % $H_2$ shielding with 10 L/min gas flow rate

### 4.3.3 Effect of Activated Flux on Bead Appearance and Penetration on AISI 316:

The effect of activated flux and arc exposure time on the bead appearance and the associated penetration is shown in Fig. 4.9. The impact of arc exposure time and the mixed shielding environment was more significant in AISI 316 grade plates. In most cases of A -TIG welding, the penetration cross – over the thickness of the plates. The reverse Marangoni phenomenon was the most prominent cause for achieving the high DoP in this particular case. Some defects like crack and inclusion are also visible in the A – TIG welding at 6 sec arc exposure time in $CrO_3$, $MoS_2$, and $MoO_3$ fluxes. The main reason for crack may be due to a decrease in residual liquids at interdendritic regions with the decreasing temperature during solidification. Moreover, the maximum penetration was observed again in the $CrO_3$, $TiO_2$, and $SiO_2$ flux because of present oxygen elements and high arc temperature under the $H_2$ mix shielding environment.

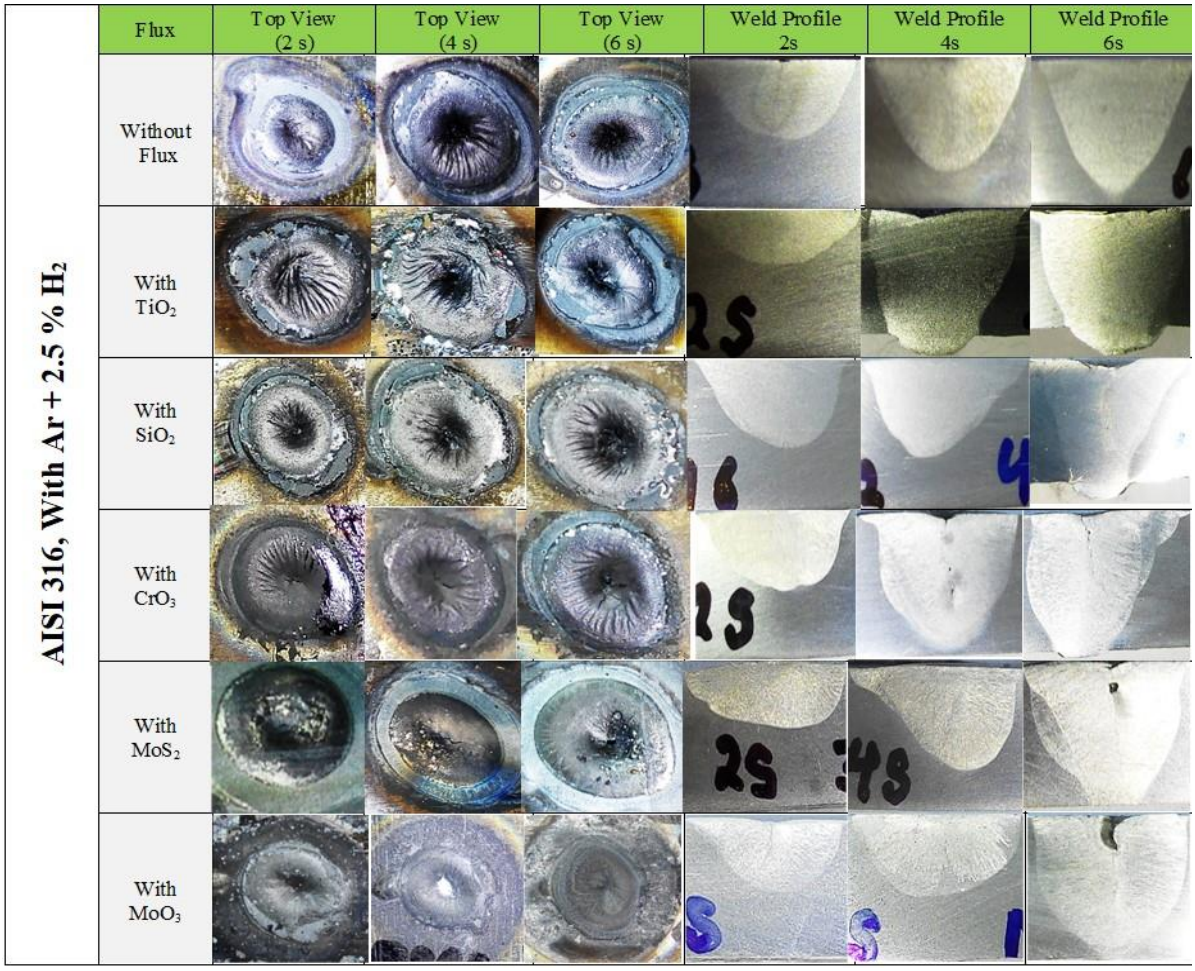


Figure 4.9: Showing the top surface and penetration of TIG and A-TIG welding of AISI 316 at different arc exposure times using Ar + 2.5 % $H_2$ shielding

### 4.3.4 Effect of Activated Flux on Microstructure of AISI 316:

Fig. 4.10 to Fig. 4.15 shows the microstructure of the interface region of all the TIG and A – TIG welding coupons at three magnification levels (i.e., 10 X, 20 X, and 50 X). No significant difference in terms of phase was observed in the microstructures of AISI 304 steel, but an increase in the concentration of resultant delta ferrite was observed. More concentration of resultant delta ferrite was observed in the case of without flux condition as compared to with flux condition. In the case of 2-sec arc exposure time, the delta ferrite was not fully developed due to fast cooling. Whereas, in the case of 6 sec fully developed ferrite matrix was observed to slow cooling rate. In some cases, the only change in the morphology/type of the resultant delta ferrite content was observed.

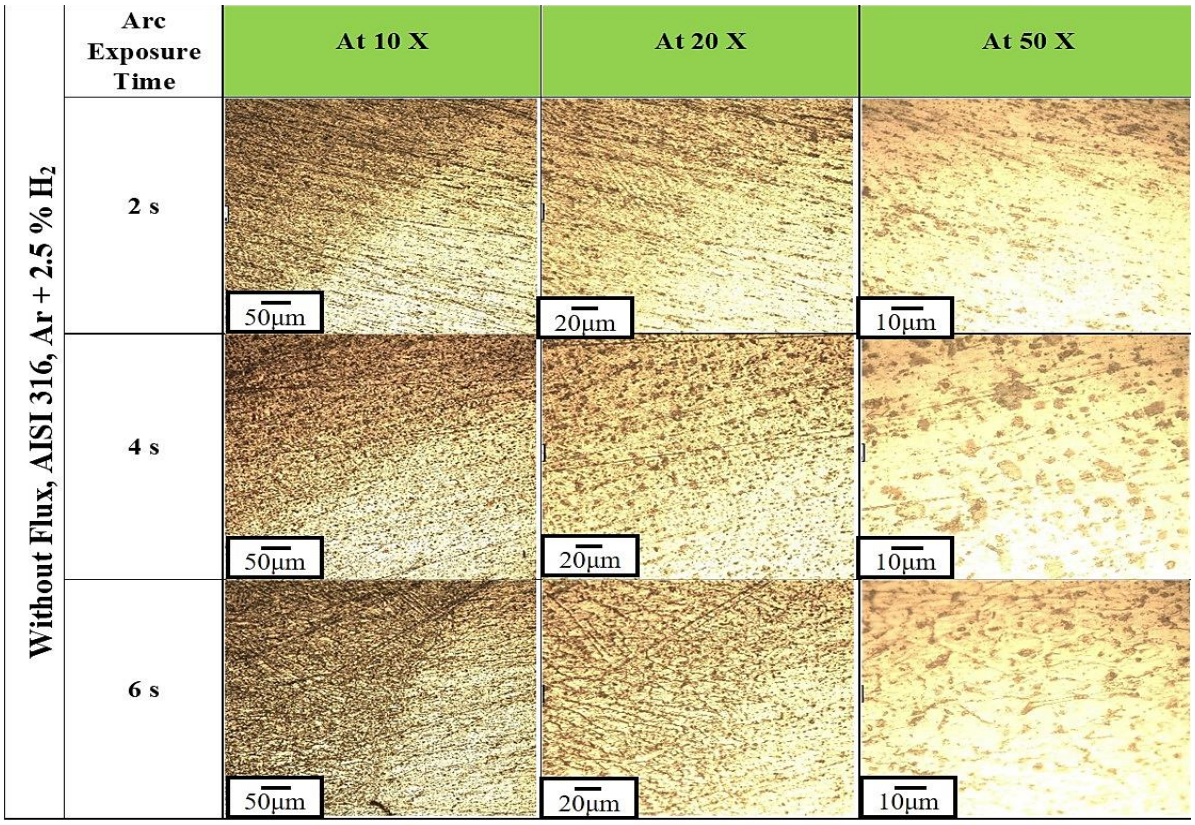


Figure 4.10: Microstructure of different arc exposure time (2s, 4s, and 6s) of conventional TIG welding on AISI 316 using150 A, Ar + 2.5% $H_2$ shielding with 10 L/min gas flow rate

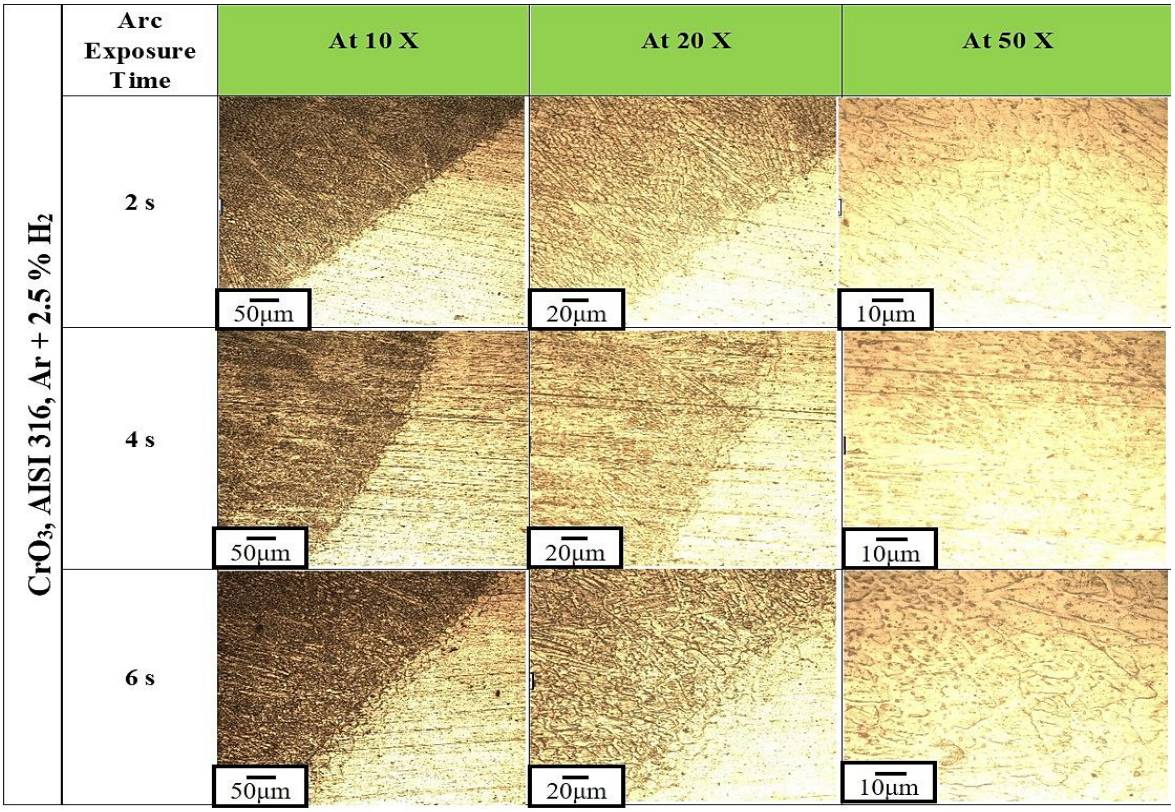


Figure 4.11: Microstructure of different arc exposure time (2s, 4s, and 6s) of A-TIG welding with $CrO_3$ flux on AISI 316 using150 A, Ar + 2.5% $H_2$ shielding with 10 L/min gas flow rate

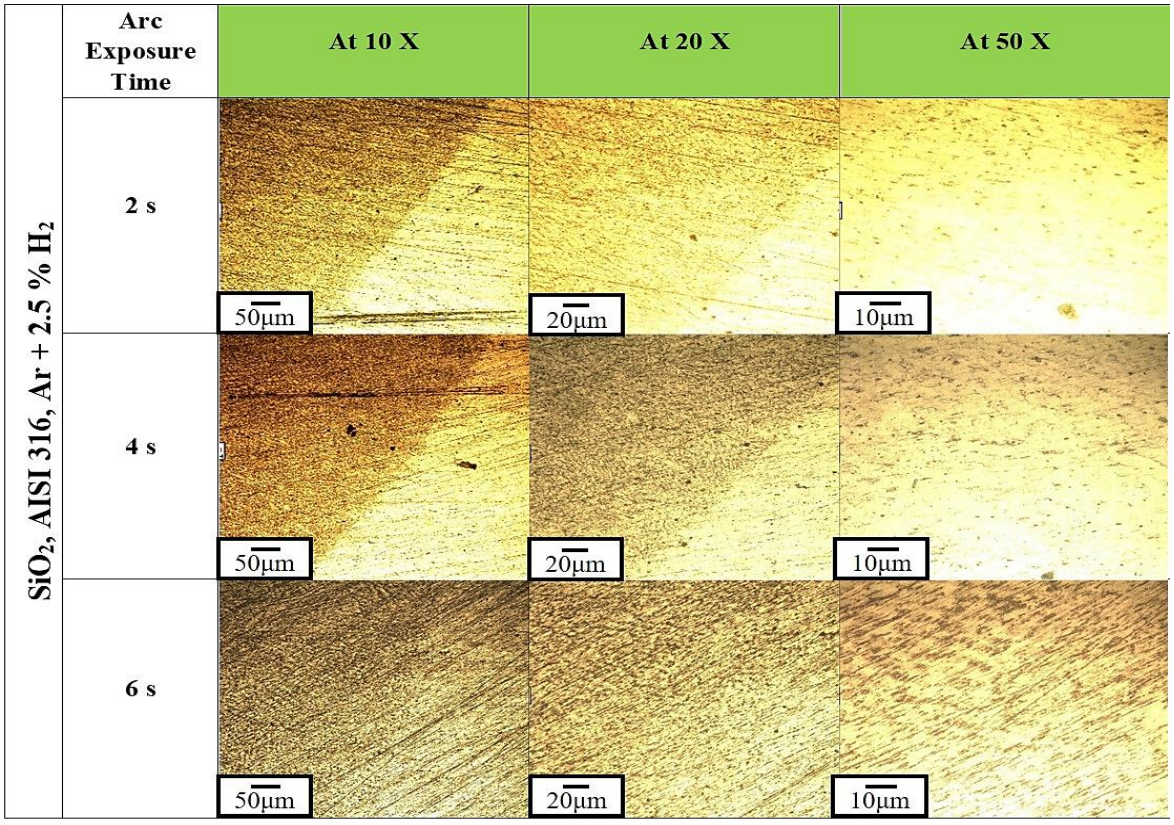


Figure 4.12: Microstructure of different arc exposure time (2s, 4s, and 6s) of A-TIG welding with $SiO_2$ flux on AISI 316 using150 A, Ar + 2.5% $H_2$ shielding with 10 L/min gas flow rate

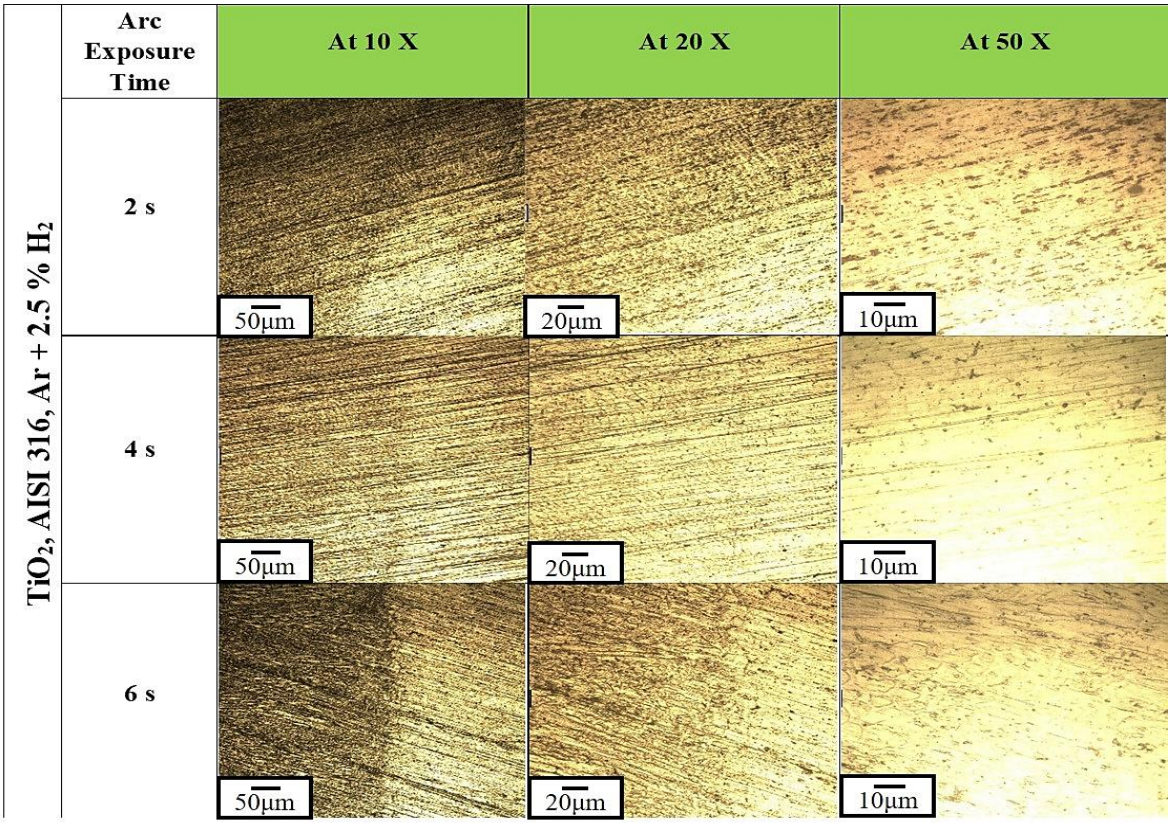


Figure 4.13: Microstructure of different arc exposure time (2s, 4s, and 6s) of A-TIG welding with $TiO_2$ flux on AISI 316 using150 A, Ar + 2.5% $H_2$ shielding with 10 L/min gas flow rate

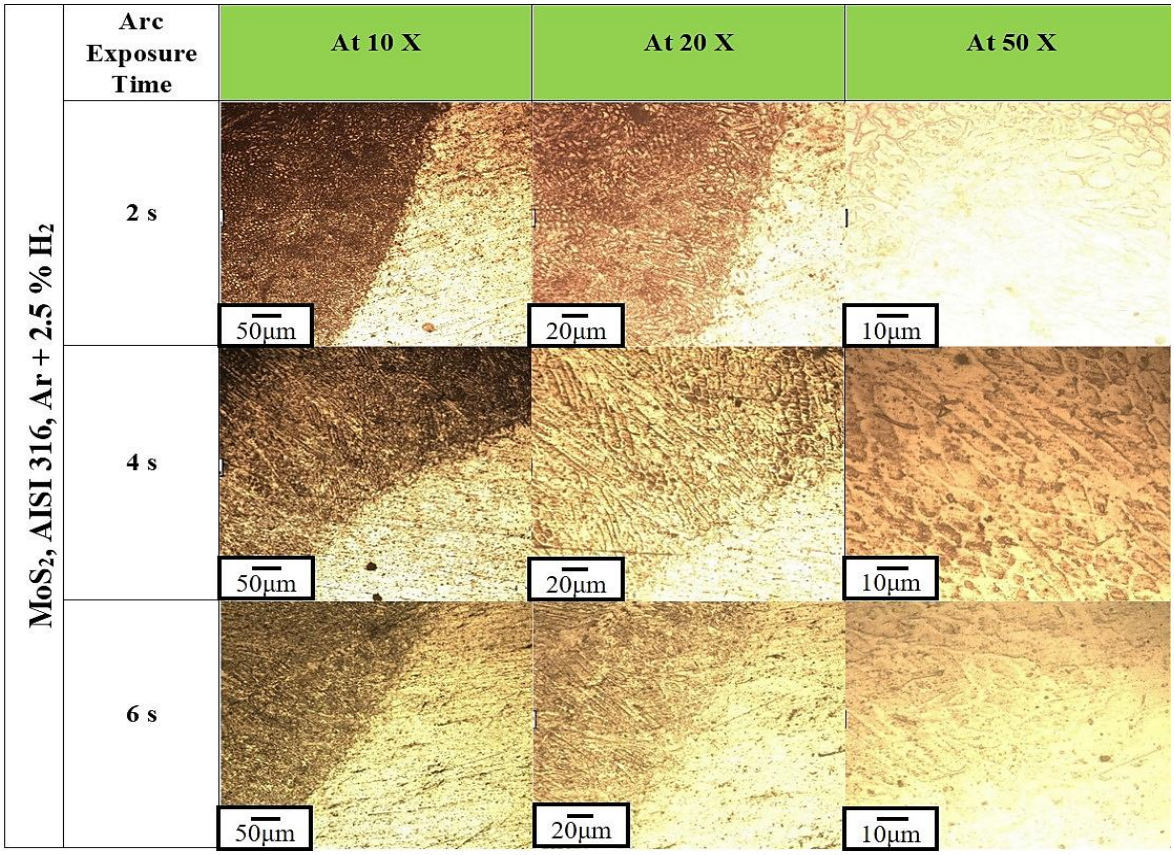


Figure 4.14: Microstructure of different arc exposure time (2s, 4s, and 6s) of A-TIG welding with $MoS_2$ flux on AISI 316 using150 A, Ar + 2.5% $H_2$ shielding with 10 L/min gas flow rate

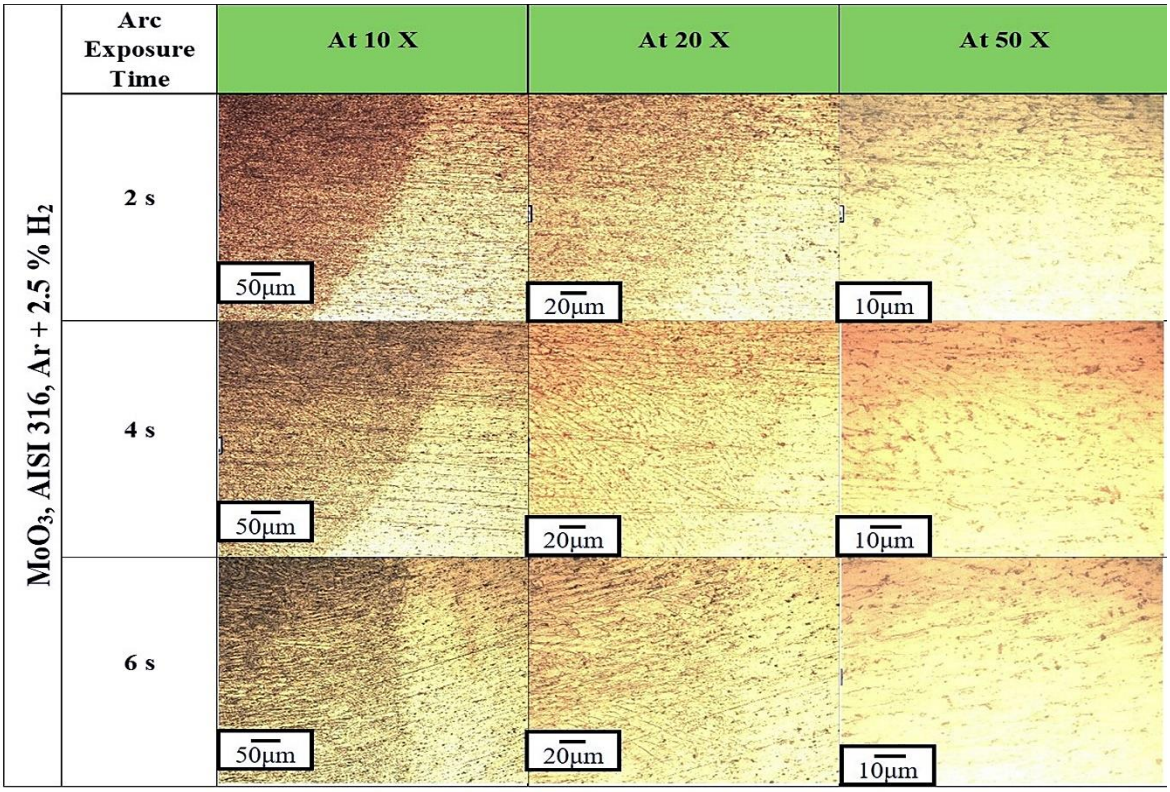


Figure 4.15: Microstructure of different arc exposure time (2s, 4s, and 6s) of A-TIG welding with $MoO_3$ flux on AISI 304 using150 A, Ar + 2.5% $H_2$ shielding with 10 L/min gas flow rate

### 4.3.5 Effect of Activated Flux on Bead Appearance and Penetration on DUP 2205

Similarly, in the case of DUP 2205, the top surface of weld and associated penetration is presented in Fig. 4.16, which also shows the effect of reverse Marangoni convection and Lorentz force. As DUP 2205 has two phases structure, i.e., ferrite and austenite in approximately in equal proportion. Hence, after etching of weld cross-section, two types of dendritic structure is appeared in fusion zone (FZ), all of the A – TIG welding and in conventional GTAW/TIG welding (Fig. 4.16). The flux residue is also visible in the case of all the A – TIG welds. The extra heat produced by the activated flux and associated cooling rate affects the directional growth of the dendrites. A hot crack was also observed in the case of $MoS_2$ flux. The detailed study about the influence of activated flux and $H_2$ shielding environment is elaborated in the subsequent sections, part of a second published research paper.

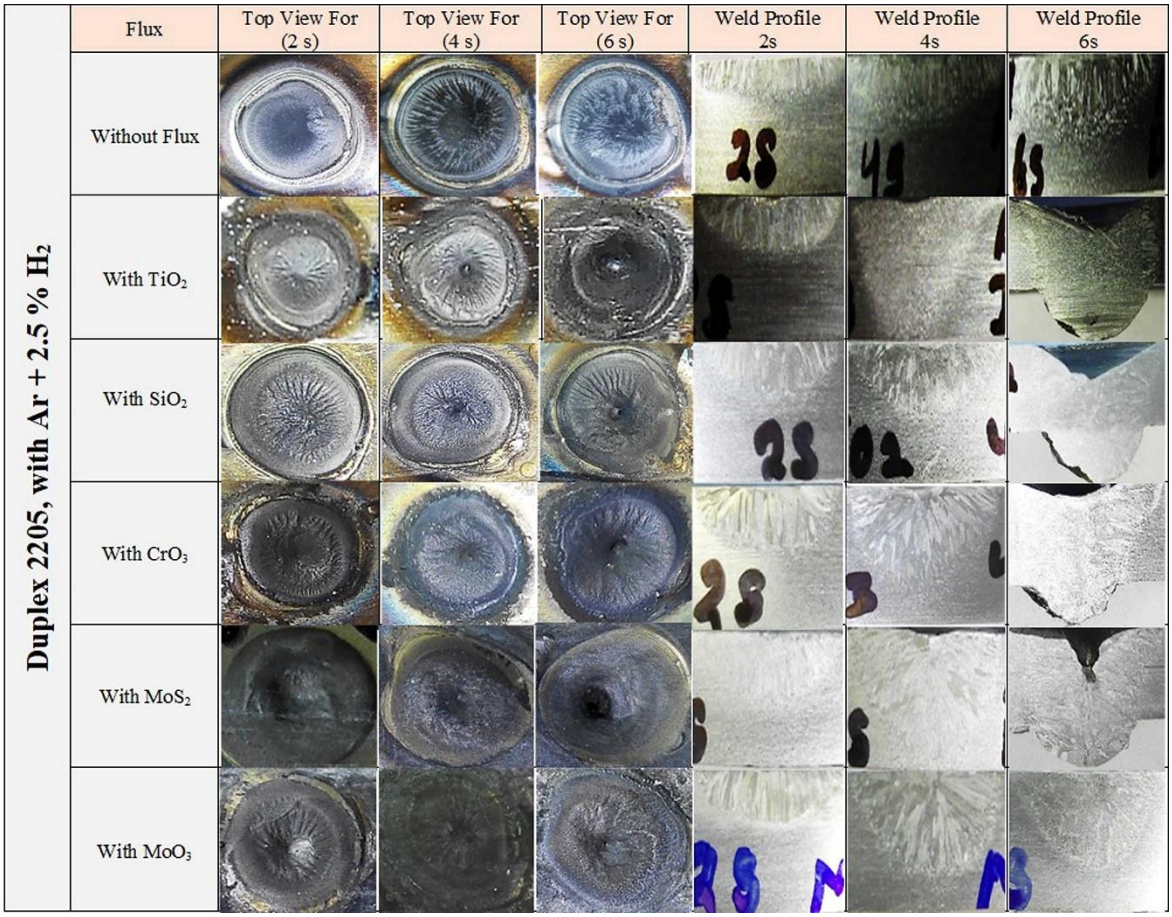


Figure 4.16: Showing the top surface and penetration of TIG and A-TIG welding of DUP 2205 at different arc exposure times using Ar + 2.5 % $H_2$ shielding

### 4.3.6 Effect of Activated Flux on Microstructure of AISI 316

The microstructure of the interface region of all the TIG and A – TIG welding coupons at three magnification levels (i.e., 10 X, 20 X, and 50 X) are presented in Fig. 4.17 to Fig. 4.22. A significant difference of two-phase dendritic structure was observed owing to Duplex structure. The growth of the dendrites depends on the net heat produced during A – TIG welding. The presence of $H_2$ also plays a significant role in the growth of the dendrites. The extra heat generated by the $H_2$ mixed shielding is also calculated and compared with the study of pure argon shielding (Chapter 3) in the subsequent pages.

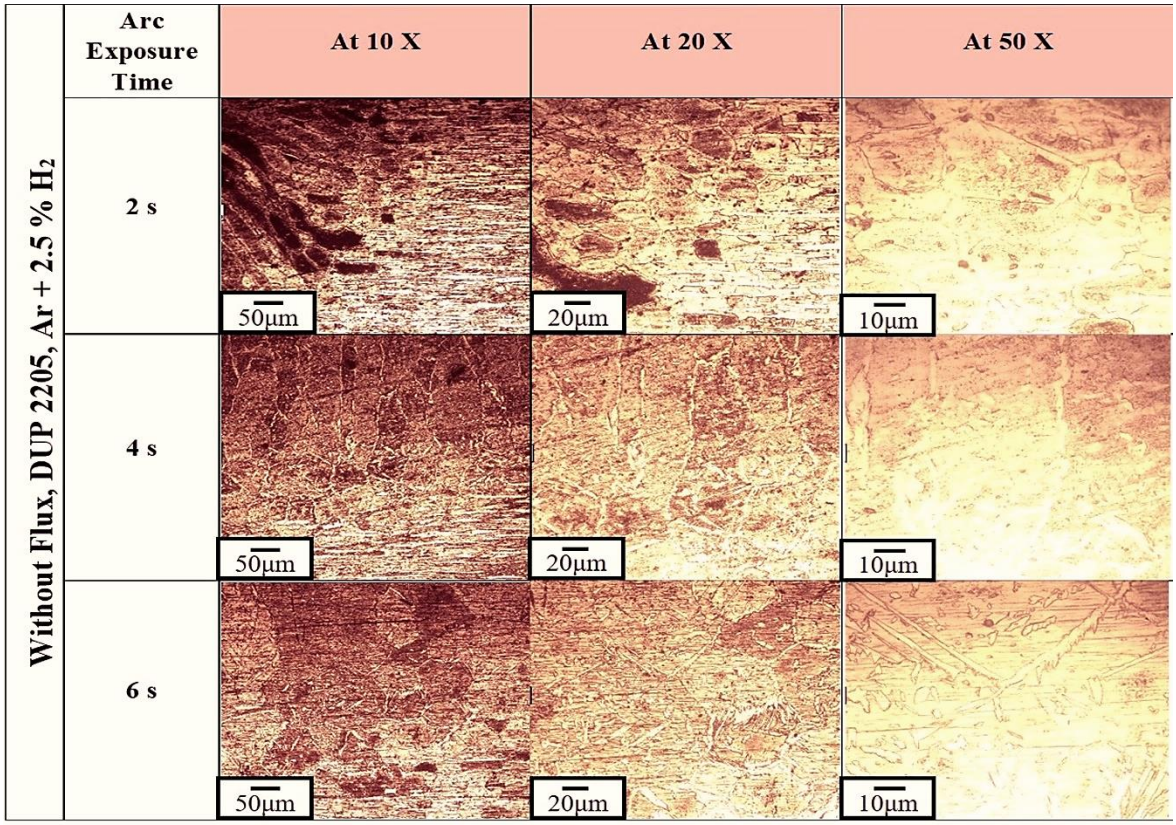


Figure 4.17: Microstructure of different arc exposure time (2s, 4s, and 6s) of conventional TIG welding on DUP 2205 using150 A, Ar + 2.5% $H_2$ shielding with 10 L/min gas flow rate

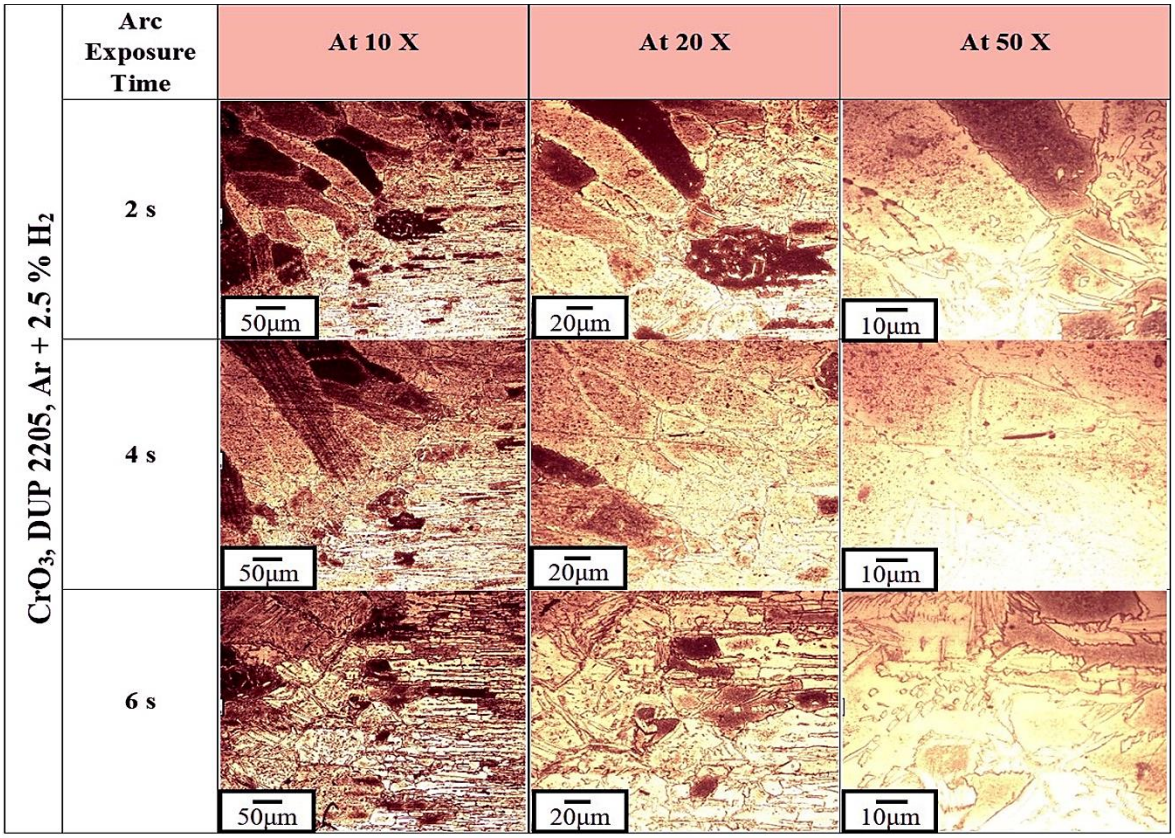


Figure 4.18: Microstructure of different arc exposure time (2s, 4s, and 6s) of A-TIG with $CrO_3$ welding on DUP 2205 using150 A, Ar + 2.5% $H_2$ shielding with 10 L/min gas flow rate

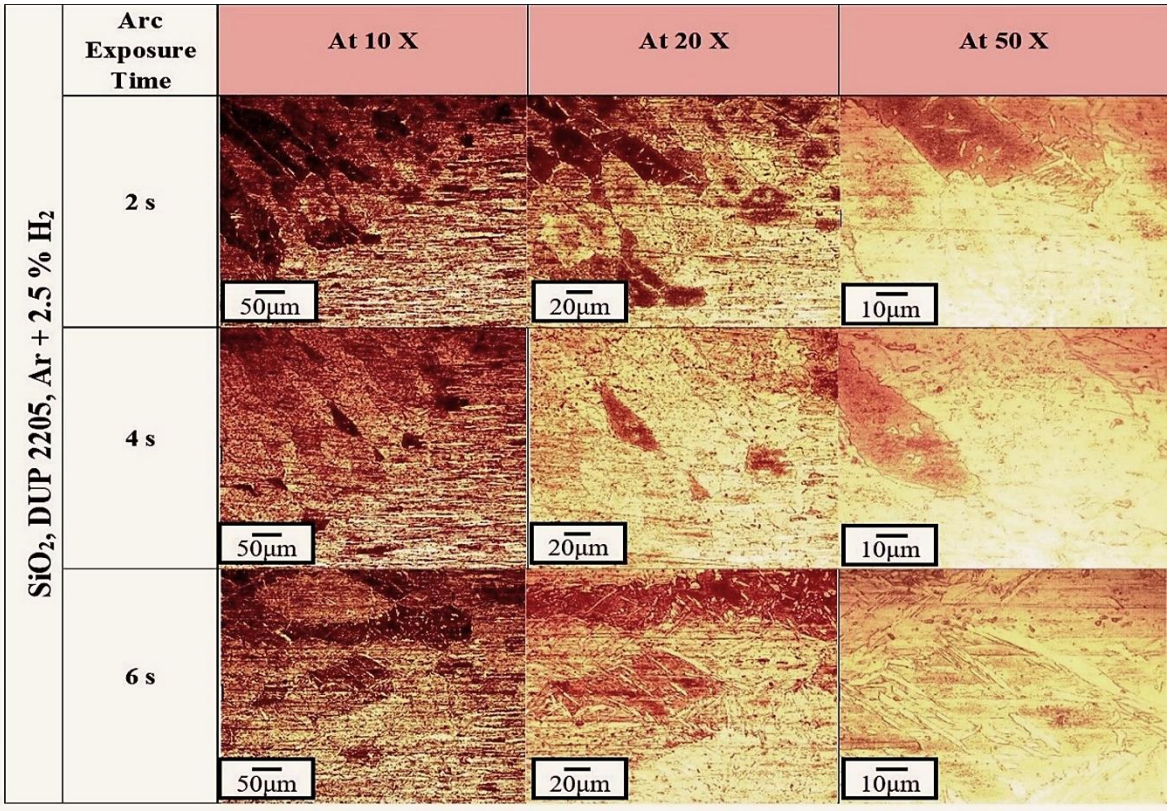


Figure 4.19: Microstructure of different arc exposure time (2s, 4s, and 6s) of A-TIG with $SiO_2$ welding on DUP 2205 using150 A, Ar + 2.5% $H_2$ shielding with 10 L/min gas flow rate

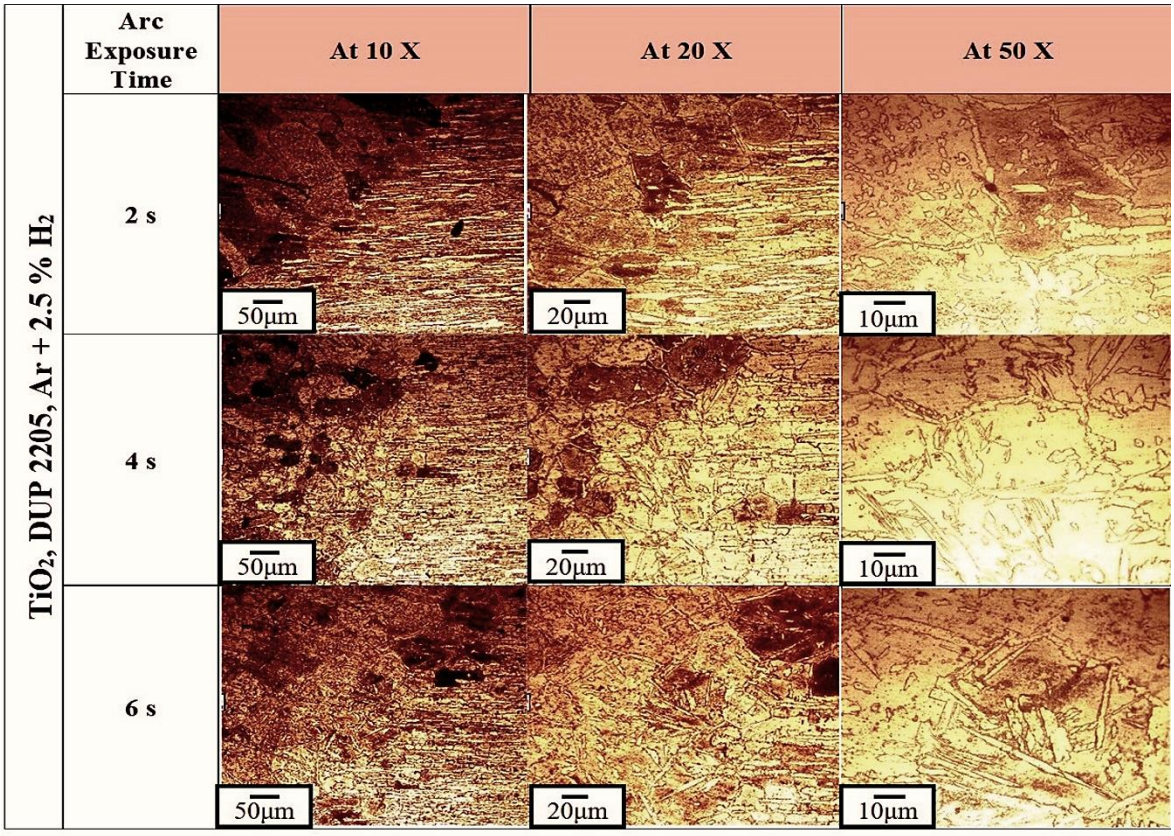


Figure 4.20: Microstructure of different arc exposure time (2s, 4s, and 6s) of A-TIG with $CrO_3$ welding on DUP 2205 using150 A, Ar + 2.5% $H_2$ shielding with 10 L/min gas flow rate

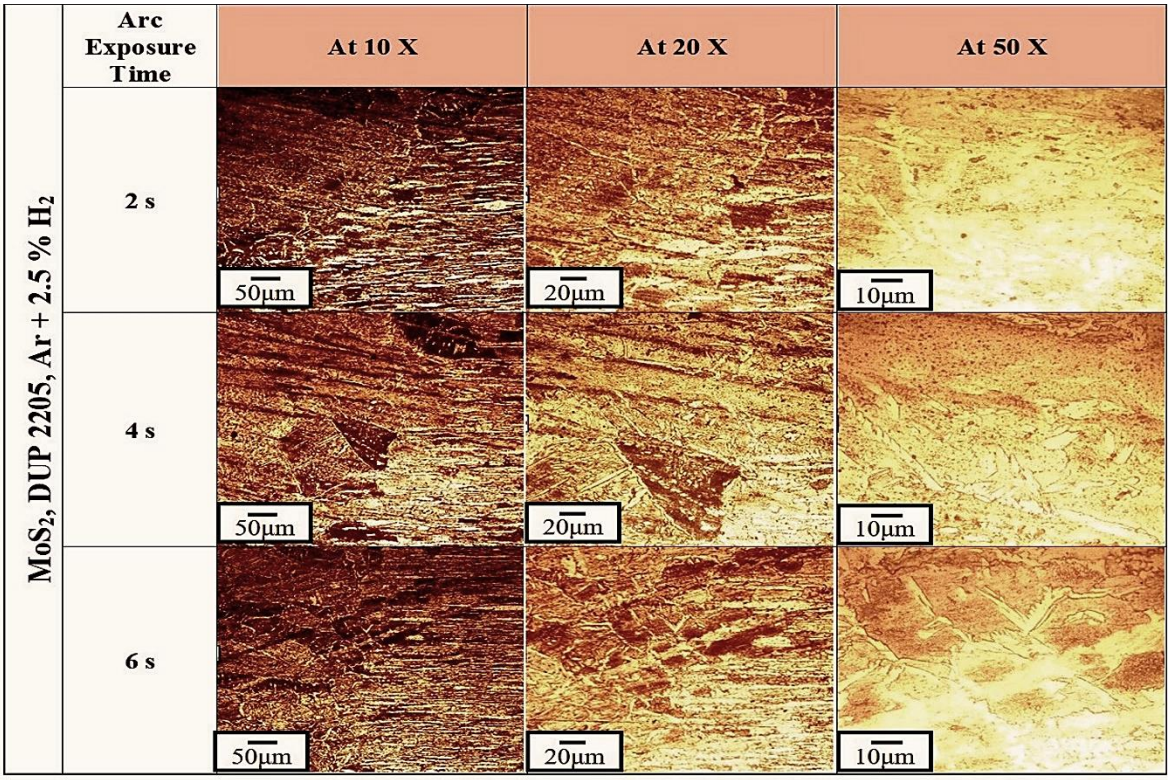


Figure 4.21: Microstructure of different arc exposure time (2s, 4s, and 6s) of A-TIG with $MoS_2$ welding on DUP 2205 using150 A, Ar + 2.5% $H_2$ shielding with 10 L/min gas flow rate

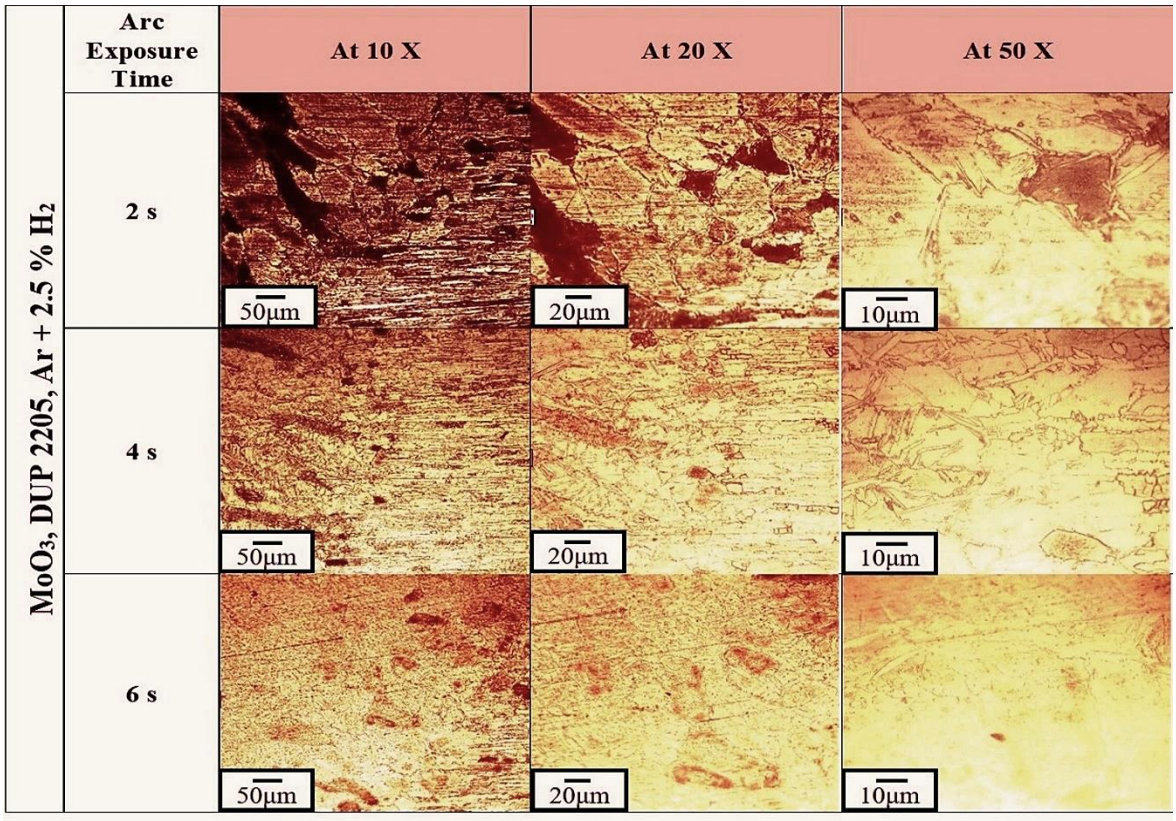


Figure 4.22: Microstructure of different arc exposure time (2s, 4s, and 6s) of A-TIG with $MoO_3$ welding on DUP 2205 using150 A, Ar + 2.5% $H_2$ shielding with 10 L/min gas flow rate

### 4.3.7 Effect of Activated Flux on Weld Profile and Aspect Ratio

The significant change in weld profile in terms of depth of penetration and weld width for Ar shielding environment is presented in Fig. 4.23 to 4.25. In the case of AISI 304, except for $CrO_3$ flux, the weld width increases with arc duration time. It shows the significant effect of the occurrence of Lorentz force and reverses Marangoni convection in the presence of more oxygen elements of the $CrO_3$ flux. Whereas in most of the cases of AISI 316 and DUP 2205, no significant change was observed in weld width. Most A – TIG welding shows a substantial shift in DoP compared to weld width. Whereas, in conventional GTAW/ TIG welding, a slight improvement in DoP was observed due to $H_2$ shielding. A-TIG welding with different fluxes showed a positive surface tension gradient and was found more prominent in DUP 2205 steel.

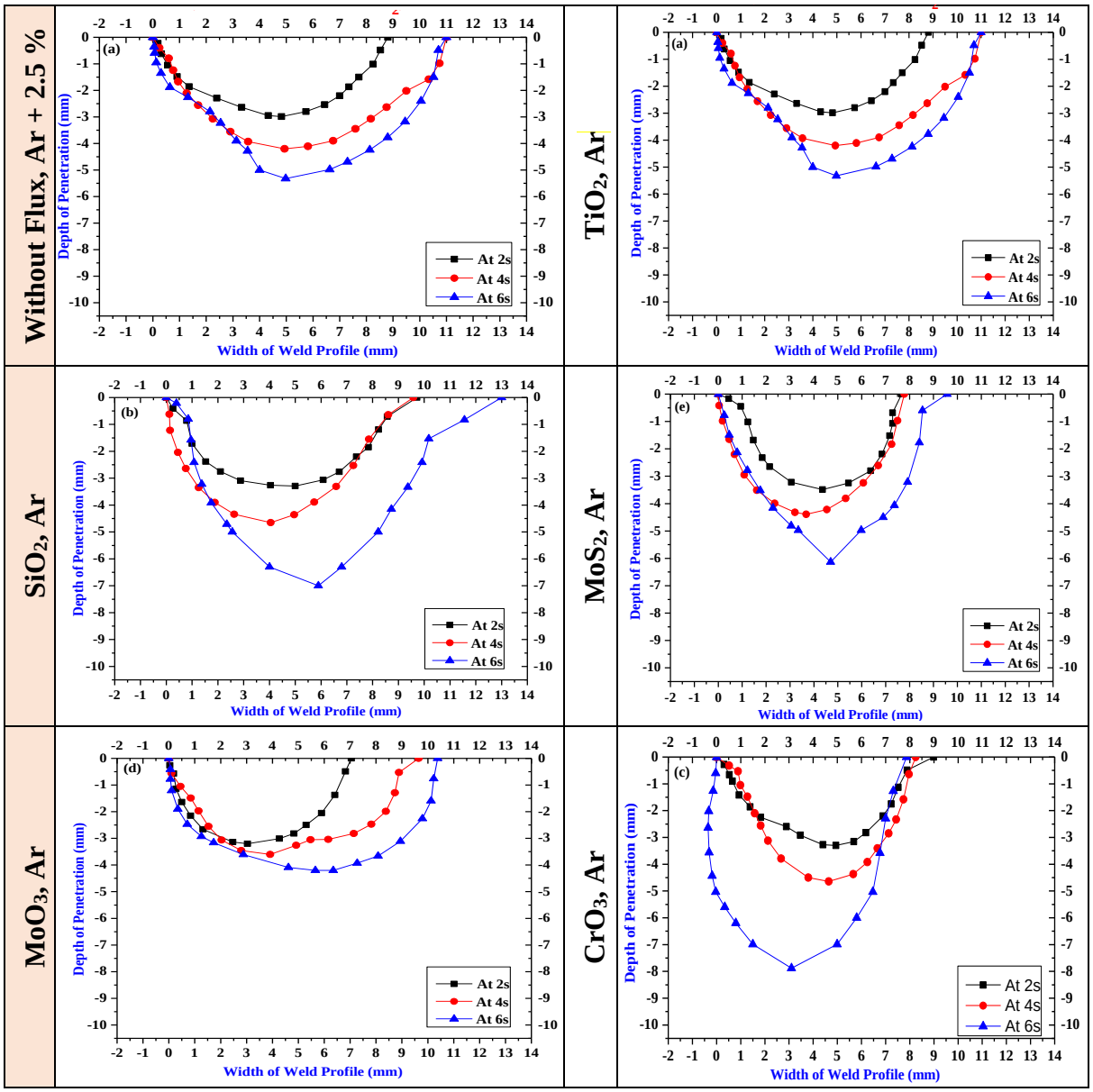


Figure 4.23: Weld profile of without flux and with flux with different arc exposure time and Ar + 2.5 % $H_2$ shielding on AISI-304

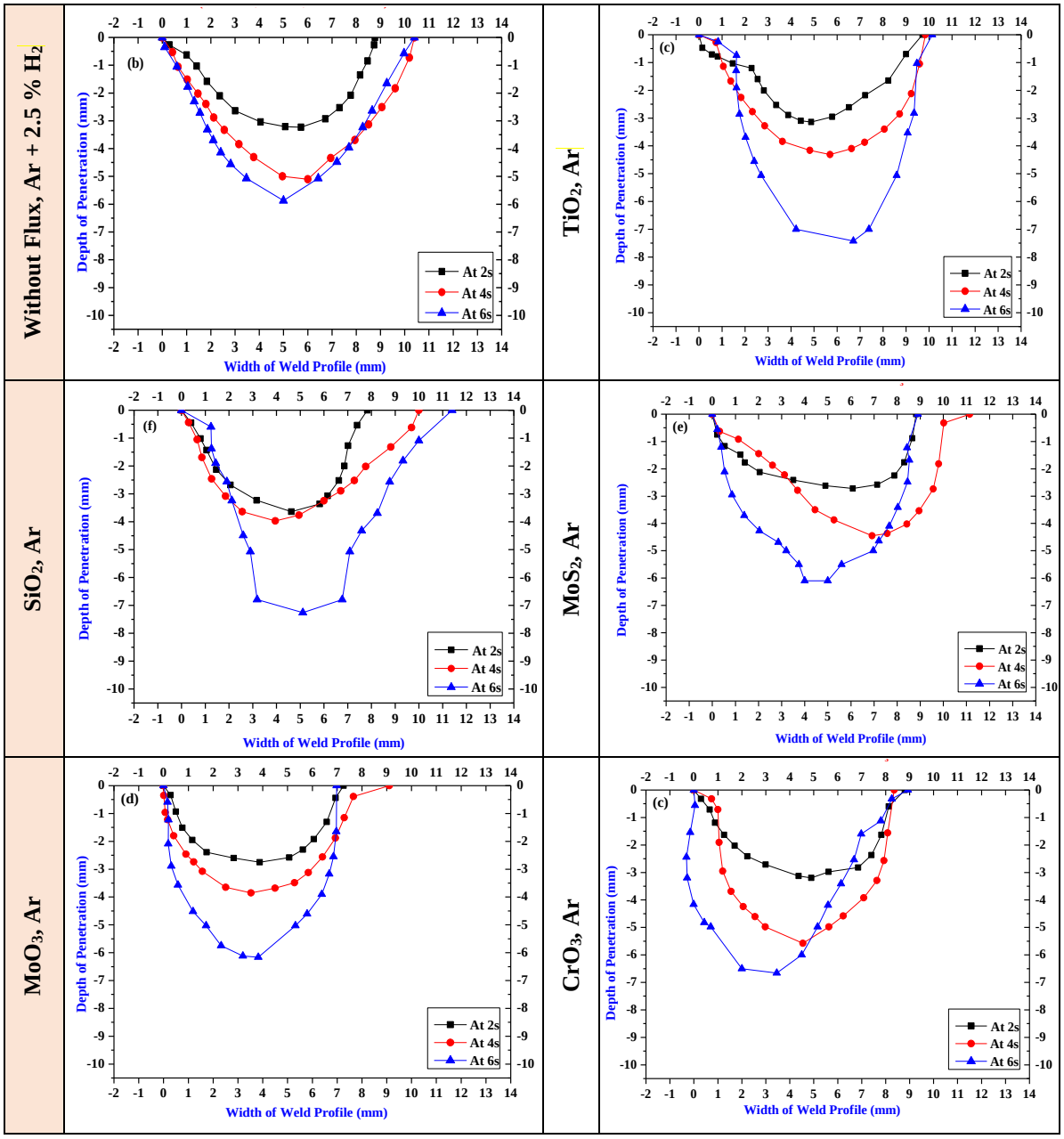


Figure 4.24: Weld profile of without flux and with flux with different arc exposure time and Ar + 2.5 % $H_2$ shielding on AISI 316

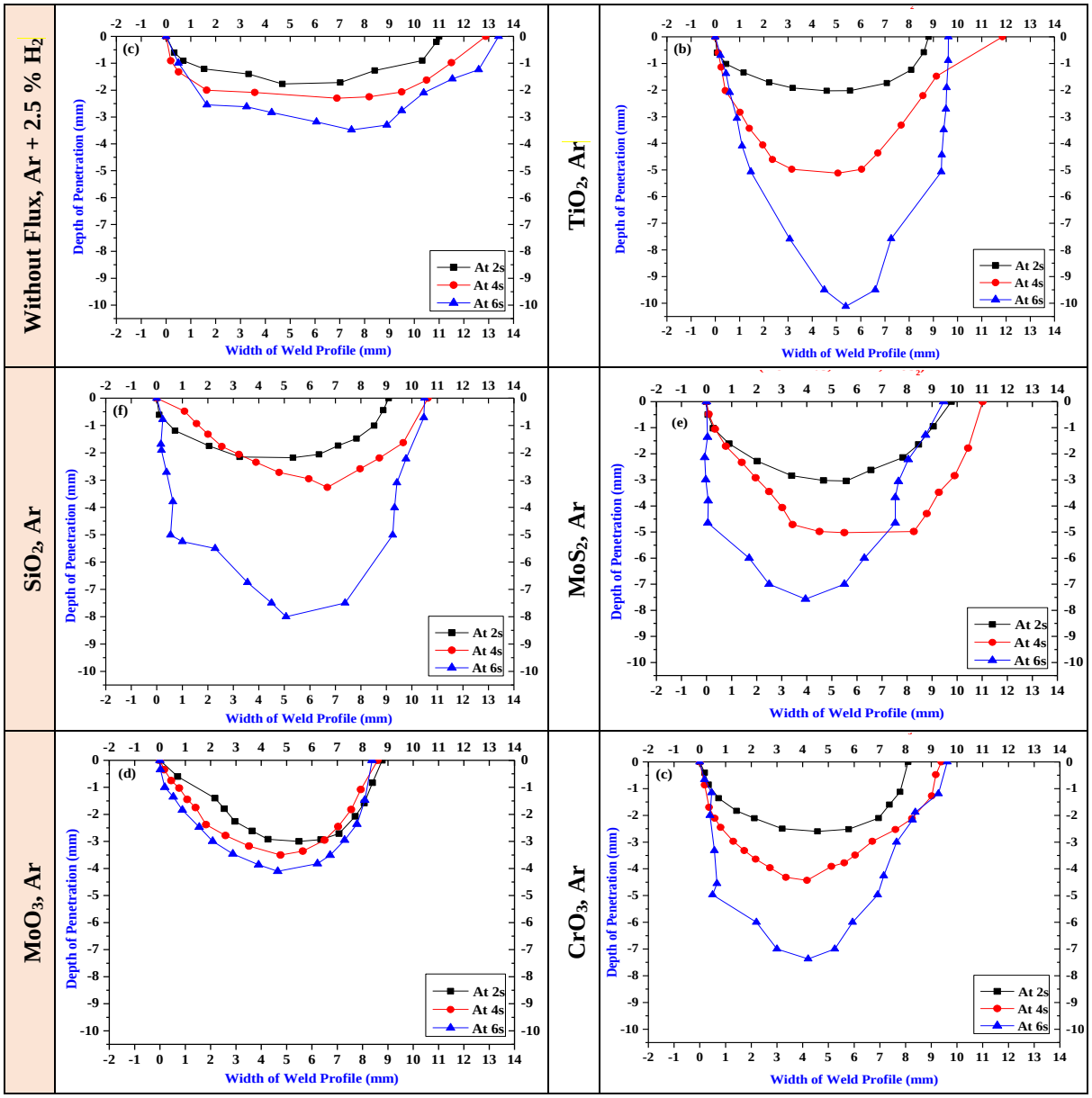


Figure 4.25: Weld profile of without flux and with flux with different arc exposure time and Ar + 2.5 % $H_2$ shielding on DUP 2205

Figure 4.25 compares the aspect ratio (i.e., width to penetration ratio) with argon shielding environment for all the three types of steel with a trend line (with $CrO_3$). The trend line shows that the aspect ratio decreases with the increase of arc exposure time, which is more significant in the case of duplex stainless steel (DUP 2205) stainless steel. Both the austenitic stainless steel and duplex stainless steel have some fluctuations for different fluxes. Therefore, these results generate further curiosity in the further investigation, which is presented in subsequent pages.

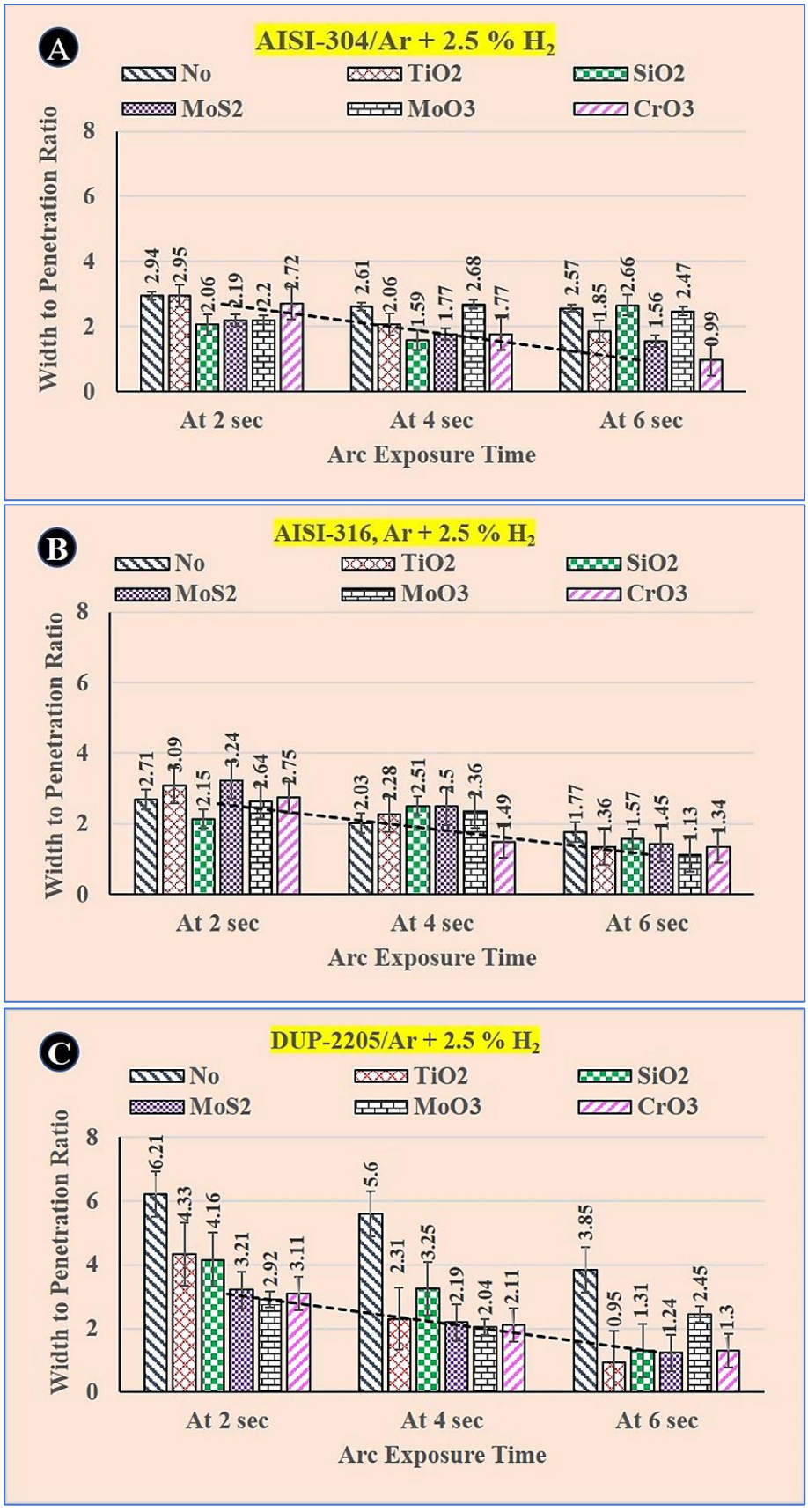


Figure 4.26: Comparison of an aspect ratio of width to penetration with Ar + 2.5 % $H_2$ shielding for no flux and with different fluxes on (A) AISI 304 (B) AISI316 (C) Duplex 2205 stainless steel

## 4.4 A-TIG Welding of Duplex Stainless Steel (2205) with Ar shielding [93]

For better understanding, the phenomena behind the higher depth of penetration by using $H_2$ mixed shielding environment and the decrease of aspect ratio in DUP 2205 stainless steel some weld coupon of A-TIG weld with unflux condition have been studied presented in subsequent pages. The most common process used for welding DUP 2205 and other stainless steel grades is gas tungsten arc welding (GTAW) [13, 46]. In a pure Ar shielding environment, S. Tathgir et al. [15] have investigated the oxygen-rich activated fluxes ($SiO_2$, $MoS_2$ and $CrO_3$). An activated flux could act as an insulator and may form a barrier [2, 14] in the path of the current flow direction. Therefore, various sulfur base and oxygen base fluxes have been studied to understand their behaviour in Ar [15] and Ar+$H_2$ environments. Hence, to understand the effect of $H_2$ in the shielding environment, the same set of oxide-based fluxes along with $TiO_2$ (oxygen-rich flux) are investigated for the $H_2$ mix (Ar + 2.5% $H_2$) shielding environment on the same set of welding parameters. The present study investigated the effects of four different fluxes of oxide and sulphur base in the presence of decomposed oxygen and 2.5 wt—% hydrogen in a shielding environment.

Hence, the investigation addresses the effect on weld pool behaviour, depth of penetration, weld pool chemistry, reverse Marangoni convection, Peclet number variation, and weld-pool microstructure evolution. Furthermore, heat input produced due to variables like the flux and the shielding environment has been discussed and compared with the un-fluxed condition. Finally, the distinctive observations are elaborated in the study with an associated mechanism, which explores the understanding of the process.

### 4.4.2 Materials and Methods

Duplex stainless steel (DSS)-2205 having a thickness of 5 *mm* had been used in the present study, and the chemical composition of as-received DSS is provided in Table 5.1. (Optical emission spectroscopy - Foundry Master, Germany).

Table 4.1: Chemical compositions of DSS-2205 sample

| Material | Percentage Composition (% wt.) | | | | | | | | | | | |
|---|---|---|---|---|---|---|---|---|---|---|---|---|
| | C | Mn | Si | Cr | Ni | S | P | Mo | Cu | W | Nb | Fe |
| Duplex 2205 | 0.03 | 1.83 | 0.39 | 25.1 | 4.68 | 0.005 | 0.02 | 3.08 | 0.18 | 0.02 | 0.002 | Bal |

Before welding, all the weld coupons were ground on the precision grinder (CHEVALIER, Model: FSG-2A1224) and ensured the clean workpiece surface. The samples of this study were welded with TIG and A – TIG welding using Ar + 2.5 % $H_2$ shielding environment, and the selected weld samples of 6 sec arc exposure time of DUP 2205 steel were welded with $CrO_3$,

$MoS_2$, $SiO_2$, and $TiO_2$, are used in the present study to justify the difference of shielding environment. A stationary arc welding method was selected despite a straight bead weld [20] to find out the significant effect of reverse Marangoni convection in terms of metal flow behaviour, Peclet number to find out the mode of heat transfer, and the heat source diameter or weld nugget diameter for determining the dilution rate.

TIG welding machine of 350 *Amp* capacity (Make Techno-Weld) used for Ar study (Chapter 4) to carry out the experiments. The rest of the process parameters were kept the same, which was used in the previous study of Ar welding (Chapter 4). The schematic of the process employed is shown in Fig.4.27.

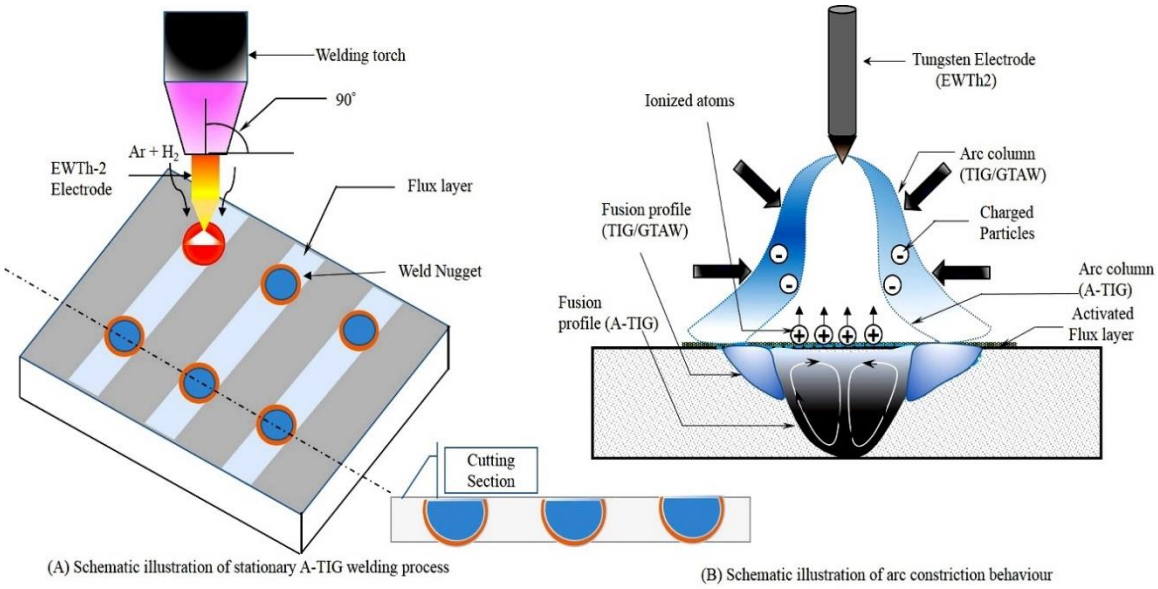


Figure 4.27: (A) Schematic representation of the process of stationary A-TIG welding (B) Arc constriction behaviour

The responses of the A-TIG welding process have been examined against the unflux condition (conventional TIG process). Hence, the investigation was conducted on all the TIG and A-TIG welding processes. The total thermal energy generated and used for welding, calculated as $V \times I \times t$, where *'V'* is the voltage (in volts), *'I'* is the current (in amperes), and 't' is the time in seconds (*s*). In conventional TIG, welding ($V \times I \times t$) could be 9000 ***J*** for 6 *seconds* for each welding spot [20]. The arc efficiency in this study is assumed to be 100 % as the stationary weld beads were performed by nullifying the speed and without any heat loss in the form of heat input to work material. Each TIG and A – TIG welding experiment was employed with three stationary spots/beads to ensure reproducibility in measurements. The measurements and subsequent analysis have been attributed to the average values taken from those three weld coupons. Test samples were extracted from the weld coupon by keeping the weld centre

exposed for investigation, and the standard metallurgical procedure was used for the preparation of samples for further investigations like optical emission spectroscopy (OES - Foundry Master, Make: World Wide Analytic System), Optical Microscopy (OM - DMILM, Make: Leica), Scanning electron microscopy (SEM - JEOL_JSM_6510LV), Energy Dispersive Spectroscopy (EDS), X-Ray diffraction analysis (XRD) and micro-hardness (Metatech_MVH-1) tests. The selected weld bead profiles were examined on a travelling measuring microscope and subsequent macrograph analysis by Image - J software.

### 4.4.3 Weld Pool Morphology

The heat input and the bead characteristics are critical phenomena which could govern the weld bead geometry [20]. Moreover, the oxygen and sulfur elements actively participate in weld pool reactions, leading to the varying weld pool behaviour through the reverse Marangoni convection and associated metal flow pattern. The top surface of as-welded TIG and A-TIG weld coupons are presented in Fig. 4.28. Some flux residue (in the form of slag) is clearly visible around the weld spots. In addition, the cone-type cavity formation due to the inward flow of metal is revealed due to reverse Marangoni convection.

The negative and positive surface tension gradient decides the flow of molten metal (i.e., outward and inward direction), which would ultimately control the shape of the weld pool. In the case of unflux condition, the pattern of liquid metal flow was found in an outward direction (along periphery), resulting in a wide weld pool with shallow penetration. However, in A-TIG welding, it was noticed to be inward (to the axis of weld pool), and that further results in a deep weld pool with a cone shape appearance (Fig. 4.28).

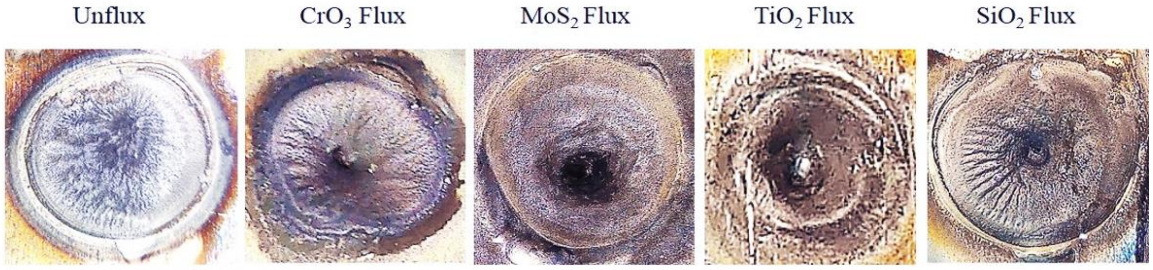


Figure 4.28: Top surfaces appearance of GTAW (unflux) and A-TIG weld coupons

The OM and SEM analysis specimens were polished on a disc polisher and etched using standard 'Carpenter Etchant.' The macrograph of unfluxed condition and with flux condition specimens of 6 sec arc exposure time is shown in Fig. 4.29. The process generates the extra arc thermal energy (Watt) due to more oxygen content in the oxide base fluxes. The addition of $H_2$ in shielding has been estimated and compared with the growth of dendrites, dendrite arm spacing, and grain size. The SEM, EDS, and OM locations have been encircled on

macrographs, as shown in Fig. 4.29. The yellow line shows the measurement path for micro-hardness with the 500-*gf* load.

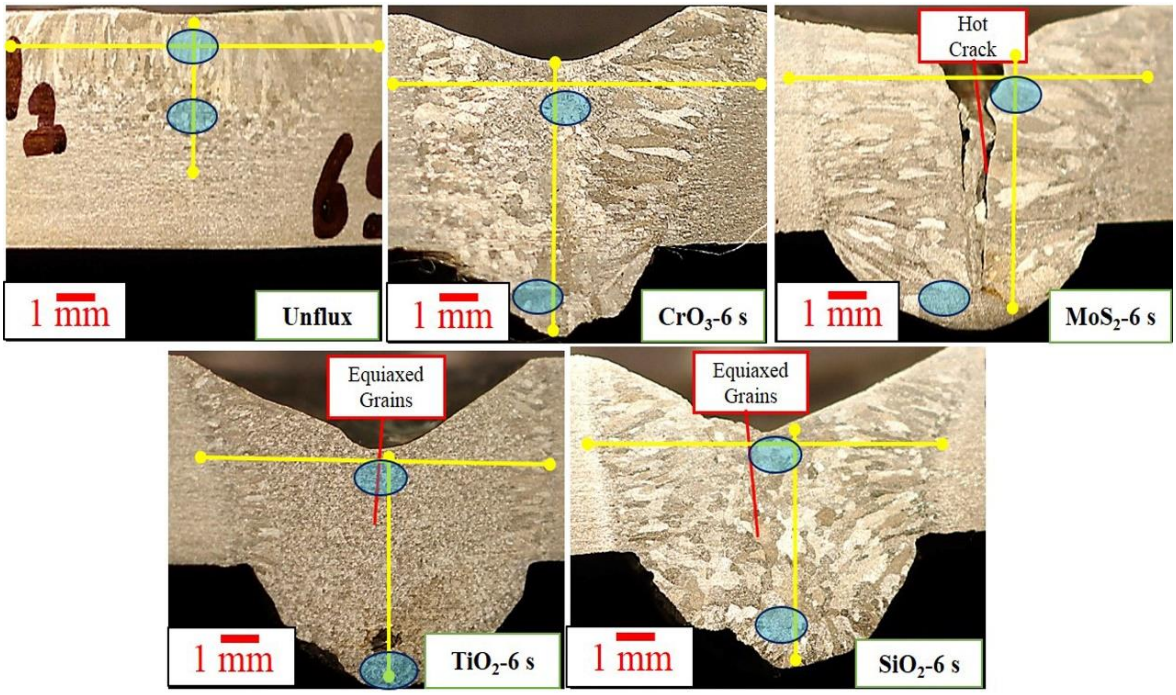


Figure 4.29: Macrographs of unflux, $CrO_3$, $MoS_2$, $TiO_2$ & $SiO_2$ welded coupons showing the dendritic structure, encircled area of observation for SEM, EDS and yellow lines of the micro-hardness path

Weld pool behaviour in TIG and A-TIG welding processes suggests that the surface tension gradient ($d\gamma/dT$) is negative in unflux conditions and positive in A-TIG welding conditions. Due to the presence of Lorentz force, the positive surface tension gradient helps in accelerating the liquid metal flow to the axis of the weld pool. In the present study, a stationary weld bead spot was performed to understand the effect of weld time, shielding environment, and different oxide base fluxes at a constant time without any weld speed factor on the weld pool properties. Therefore, the temperature gradient (G) and the growth rate (R) will remain consistent and will not be dependent on the welding speed [20] in the current investigation.

The macrograph of all the specimens (Fig. 4.29) shows the difference in weld pool morphology in terms of depth of penetration (DoP) and associated HAZ. Different weld morphology can be observed in all the micrographs due to different oxide-based fluxes and $H_2$ mixed shielding. The size of dendrite arms spacing is significantly varied in each flux condition. The dark shades represent the presence of the ferrite phase, and the white shades represent the austenite phase in the macrostructure of Fig. 4.29. Considering Fig. 4.29 for unflux condition (conventional TIG welding), the dendrite growth is almost vertical. At the same time, the dendrite growth in different A – TIG welding was observed to be horizontal. As in these fluxes (A-TIG), the

dendrite arm grows to the weld centre from the adjoining fusion interface. This suggests that less heat input (unflux) and high heat density (fluxed conditions) would directly govern the growth direction of dendrites according to the cooling rate. In the case of $CrO_3$ flux, the columnar types of dendrites were produced at the fusion interfaces due to higher arc temperature with lower G/R ratio, low-temperature gradient, and laminar flow of shielding gas. Higher arc energy (due to $H_2$) further affects the cooling rate and results in equiaxed grains in the centre of the weld zone.

In the present study, the dendrite growth was observed to be horizontal direction (In A – TIG) to weld centre axis, which agrees with the study [20] conducted without $H_2$ in shielding. The dendrite growth is the function of cooling direction, and this rate would govern the planes of grain. In the case of $MoS_2$ flux, a hot crack was observed during A-TIG welding. Ferrite grain boundaries with a decrease in the number of residual liquids at interdendritic regions with the decreasing temperature during cooling are found to be the main cause of hot cracking susceptibility in the case of Duplex Stainless Steel (DSS) [94].

In the case of $TiO_2$ flux, fine equiaxed grains were observed after welding in the centre of the fusion zone with small dendrites at the adjoining area of HAZ in the horizontal direction. Inclusion is also visible in Fig. 4.29 ($TiO_2$), which could be due to the entrapment of flux. The enhancement of equiaxed grains and the formation of the same may be attributed to increased heat input [32]. In the case of $SiO_2$ flux, a mixed microstructure of equiaxed grains and columnar dendrite was observed. The equiaxed grains nucleate in the centre part of the fusion zone. They further blocked the formation of the columnar dendrite, which justifies the effect of constitutional supercooling on solidification mode [32]. With a low-temperature gradient and higher growth rate, the equiaxed dendritic structure appeared in the case of $SiO_2$ flux. Both columnar dendrite and equiaxed grains co-existed in the mushy zone [32], and this zone is clearly visible in the case of $SiO_2$ flux.

### 4.4.4 Effect of $H_2$ on Thermal Energy Produced

The calculated thermal Energy for unflux welding was observed as 9000 *J* for 6 seconds (6 *s*) arc exposure time. However, the other factors responsible for thermal Energy are the activated fluxes and the shielding environment (Ar + 2.5 % $H_2$ mixture). The thermal Energy has been measured in watt (*W*) as suggested by Tathgir et al. [20], where the thermal Energy/heat (*V* * *I*) in unflux condition has been estimated to be1500 *W*, similar to the process parameters used in the present study. The total dilution area for conventional TIG and each A – TIG welding has been measured and can be seen in Fig. 4.29. Based on dilution area, in unflux welding

conditions with $H_2$ induced shielding, the energy required for 1 $mm^2$ dilution is estimated as 62.76 *W* (1500 W/23.9 $mm^2$). However, in the unflux condition of pure Ar-shielding, it was 201.32 *W* [20], which is almost three times more than the 2.5% $H_2$ in shielding. Hence, a small percentage of $H_2$ addition in argon shielding has a crucial role in total thermal Energy/heat produced and increases dilution area. The estimated thermal Energy/heat from the above relationships of dilution and associated thermal Energy/heat (W) is presented in Fig. 4.30.

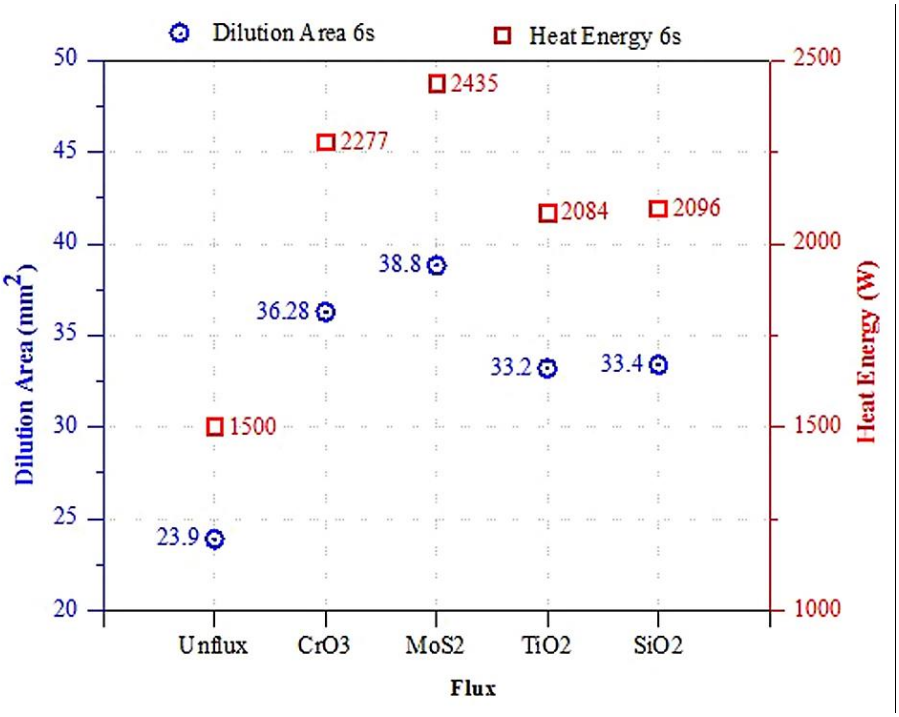


Figure 4.30: Comparison of dilution area versus and thermal Energy/heat energy of Ar and Ar + 2.5 % $H_2$

The dilution comparison in each case of fluxes with pure Ar [20] and Ar + 2.5 % $H_2$ has been presented in Table 4.2. In both types of shielding environments, the process parameters remained identical. Even though the dilution is significantly different, which is the result of $H_2$ present in the shielding environment and several flux compounds. The thermal Energy/heat energy required per unit dilution area is reduced considerably in $H_2$ induced shielding conditions based on the dilution.

As the A – TIG with $MoS_2$ flux condition has been noticed with the highest dilution, the estimated thermal Energy/heat energy produced in this case is observed to be 2435 *watts*, which is higher than the other flux conditions. Such a higher dilution area would also be responsible further for governing the weld strength of the joint [57, 74]. The total arc energy (heat energy) required in the welding is directly proportional to the dilution area [20]. Hence, the energy needed for this study is found significantly less than the Ar shielding study [20].

Table 4.2: Comparison between thermal Energy/heat energy and actual dilution area for 6 ***s*** arc exposure time

| **Flux Condition** | | **Unflux** | **$CrO_3$** | **$SiO_2$** | **$MoS_2$** | **$TiO_2$** |
|---|---|---|---|---|---|---|
| With pure Ar shielding (Tathgir et. al.) [20] | Dilution Area ($mm^2$) | 7.45 | 32.94 | 25.12 | 20.15 | -- |
| | Thermal Energy/heat energy (*Watt*) required per unit area | **1500** | **6632** | **5058** | **4057** | -- |
| With Ar + 2.5% $H_2$ | Dilution Area ($mm^2$) | 23.9 | 36.28 | 33.4 | 38.8 | 33.2 |
| | Thermal Energy/heat energy (*Watt*) required per unit area | **1500** | **2277** | **2096** | **2435** | **2084** |

The surface-active elements present in the fluxes help reduce the width-to-penetration ratio due to a significant increase in DoP and a reduction in the width of the fusion zone. The variations in DoP and width-to-penetration ratio for all weld coupons during TIG and A-TIG with different fluxes are shown in Fig. 4.31. From Fig. 4.31 (A), it can be observed that $TiO_2$ flux produced maximum DoP. However, the width-to-penetration ratio decreases.

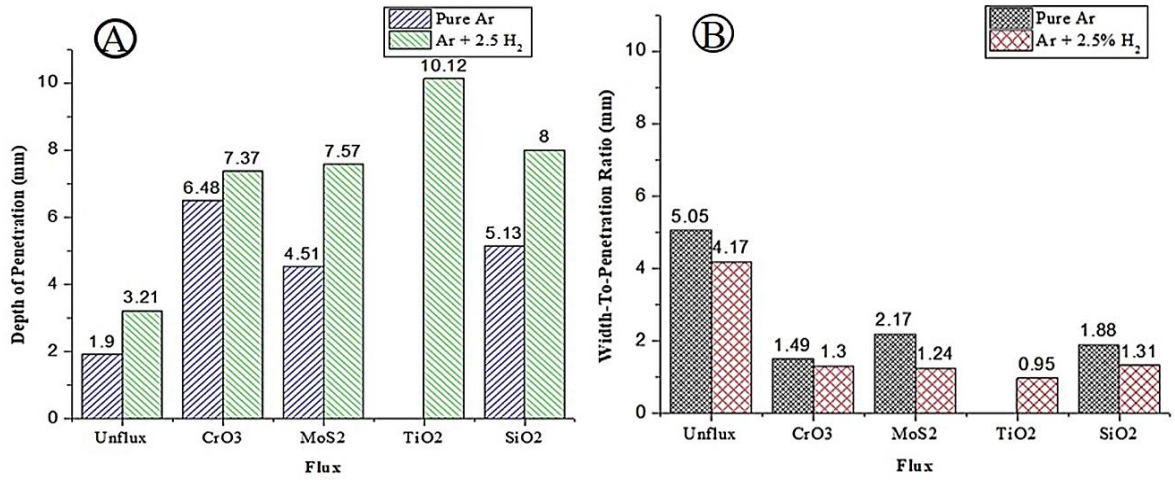


Figure 4.31: Comparison of (A) DoP and (B) width-to-penetration ratio of Ar and Ar + 2.5 % $H_2$

$H_2$ addition in shielding plays a significant role in achieving higher DoP by increasing the arc energy. Hydrogen in argon would increase the thermal conductivity and enthalpy of the gas mixture [49, 90]. The instances of increased enthalpy are evidenced in the present investigation owing to $H_2$ addition in shielding and subsequent variations in DoP and dilution.

### 4.4.5 Weld pool Chemistry and Weld Microstructure

Hydrogen in the shielding environment enriches the thermal Energy/heat energy of arc, which further enhances the decomposition of oxygen from the fluxes and some other elements. Such decomposed elements may get absorbed in molten metal [20]. The decomposition of flux promotes the absorption of other elements in the weld metal like Cr, Ti, Mo, S, and Si, and

these elements contribute to final weld chemistry. The saturated stage of cooling condition for a few seconds and the moderate percentage of carbon element present in the base metal could lead to carbide precipitation [95]. EDS, SEM, and XRD analysis are observed in agreement for the occurrence of second phase elements (Carbide) in the weld zone. SEM and EDS tests were performed on the top centre of the weld cross-section (Fig. 4.29).

#### 4.4.5.1 EDS Analysis of A – TIG weld

The region of the EDS spectrum taken from the specimen is shown (encircled) in Fig. 4.29. The SEM image of weld metal of $CrO_3$ flux is shown Fig. 4.32 A with associated EDS spectrum analysis for the highlighted region. The arrow indicates the region of intent, and from the spectrum analysis, the second phase was observed as chromium-rich carbide precipitate. Similarly, in $MoS_2$ fluxed weld metal, several instances of second phase particles of another kind of chromium carbide precipitate have been observed in Fig. 4.32 B. The EDS spectrum analysis has been used for understanding the effect of oxygen content (O) in the weld chemistry on metallurgical behaviour.

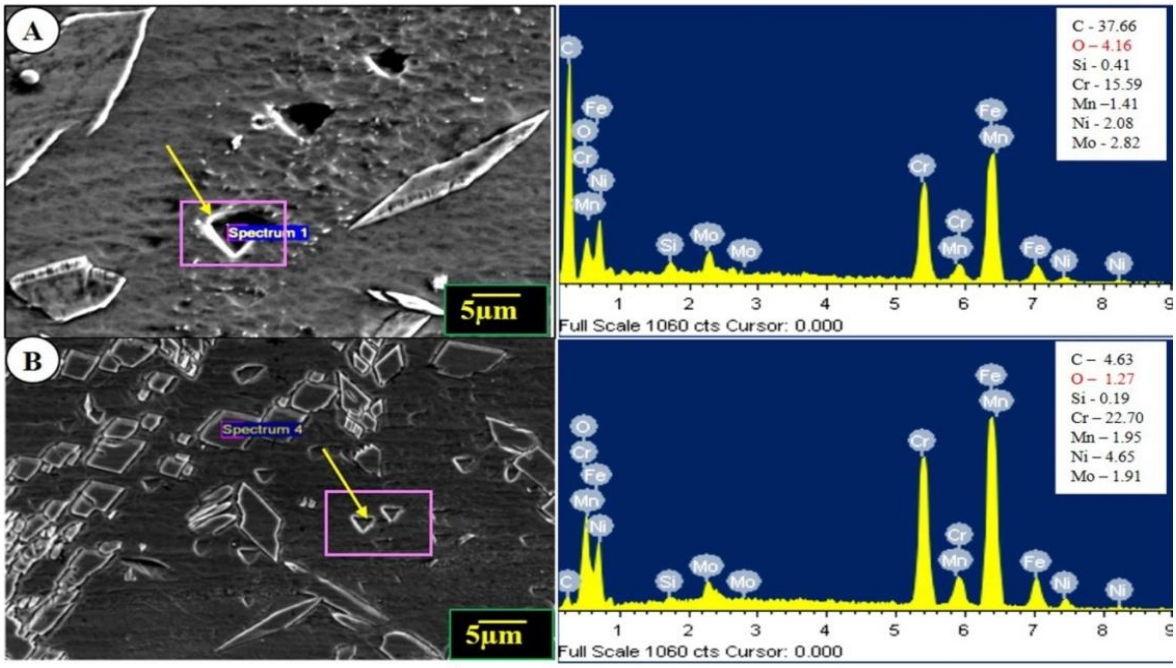


Figure 4.32: EDS spectrum of samples welded with (A) $CrO_3$ (B) $MoS_2$ activated flux

Figure 4.32 shows the $CrO_3$ and $MoS_2$ flux conditions. The EDS spectrum shows the elemental composition of the selected region, which agrees with the elemental composition of $M_{23}C_6$ - type Cr-rich carbide precipitate and other carbide precipitates ($Cr_3C_2$). The morphology of carbides is based on SEM microstructure. The elemental composition from EDS gives information on carbide presence, which is further confirmed by XRD analysis. The obtained results are further verified and validated using XRD analysis in subsequent sections to identify

and present the carbide particles. The phase quantification is a limitation of the current study. However, further phase confirmation has been accomplished using XRD analysis in the subsequent sections.

The weld metals were not observed with significant carbide precipitates (Fig. 4.33 A & Fig. 4.33 B) for the $TiO_2$ and $SiO_2$ fluxes. From the EDS spectrum analysis, shown in Fig. 4.32 & Fig. 4.33, the absorption of oxygen in the weld metal was observed to be significant in $CrO_3$ flux, $SiO_2$flux, and $TiO_2$ fluxes. However, comparatively least oxygen was noticed in $MoS_2$ flux. The observed result is found to agree, as, in $CrO_3$ flux, the decomposition of flux would ensure more amount of oxygen than other fluxes. In $TiO_2$ and $SiO_2$ flux conditions (Fig. 4.33), the EDS spectrums were focused on a particular grain (phase) showing the oxygen absorption in the weld metal. However, the small fraction of dissociated Ti and Si could be absorbed by weld metal. The rest would participate in burnt oxide residue on the top (Fig. 5.29) of weld metal owing to associated slag-metal, gas-metal reactions that occurred at the time of welding [20].

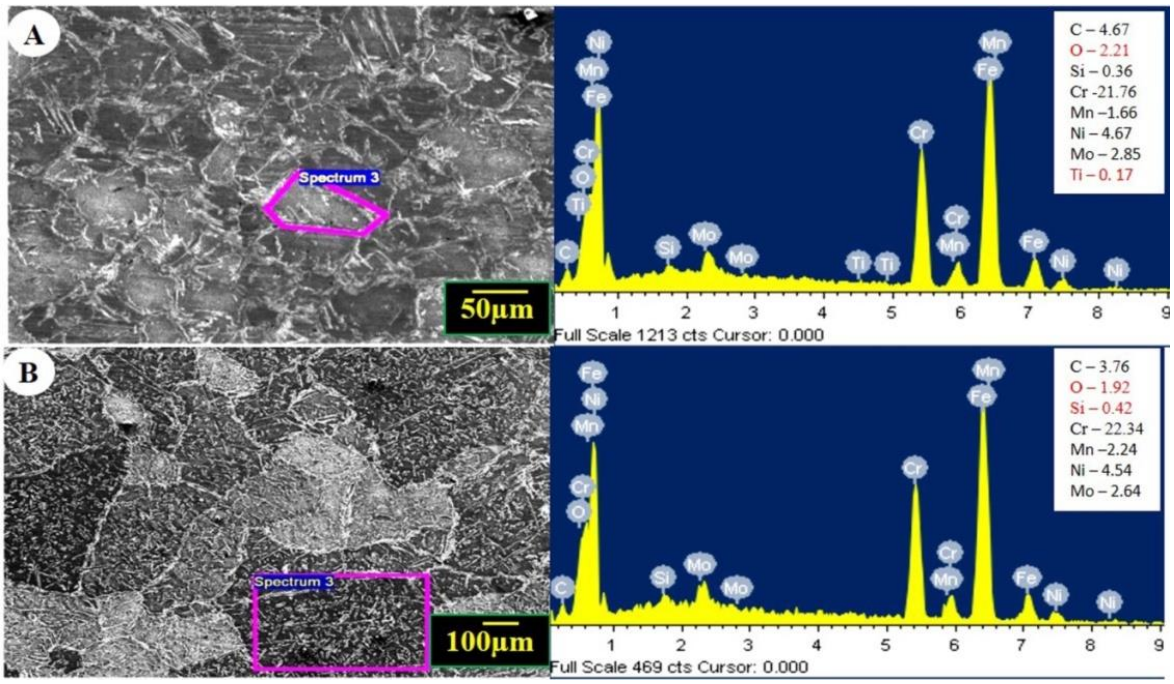


Figure 4.33: EDS spectrum of samples welded with (A) $TiO_2$ (B) $SiO_2$ activated flux

### 4.4.5.2 SEM Analysis of A – TIG weld

The general microstructure captured by SEM of A – TIG weld metal is shown in Fig. 4.34. The carbide precipitates [96] are indicated by the yellow arrow in Fig. 4.34 A and 4.34 B for $CrO_3$ and $MoS_2$ fluxes. Some instances of Widmanstatten austenite were observed at the grain boundaries (encircled red) in Fig 4.34 B and Fig. 4.34 D. Due to the complete decomposition of flux elements, the associated reaction of $H_2$ in the arc, heat density increased with the

reduction of the anode root area. It promotes the growth mechanism for austenite and ferrite grains. Considerable coursing of $\delta$- ferrite and Widmanstatten austenite is revealed in $SiO_2$ while comparing with the other fluxes and especially with $TiO_2$ flux. The same thing can be revealed from Fig. 4.29 and Fig. 4.34. Hence, the $H_2$ induced shielding with different flux elements could promote the higher arc energy, which further leads to the growth mechanism of austenite and ferrite in the weld metal.

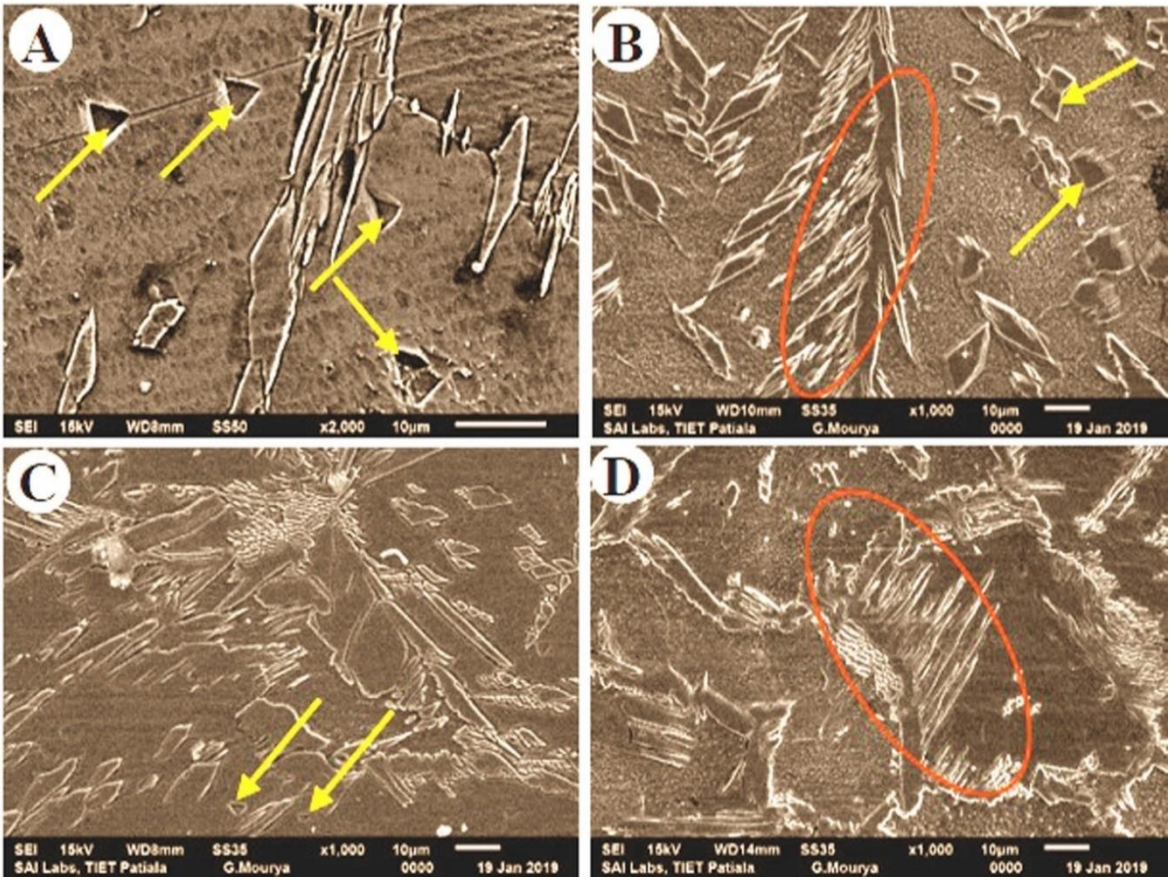


Figure 4.34: SEM image of A-TIG welded samples welded with (A) $CrO_3$ (B) $MoS_2$ (C) $TiO_2$ (D) $SiO_2$ flux

### 4.4.6 Grain Size and Dendrite Arm Spacing Measurement

The general microstructure of weld metal adjacent to the fusion interface is shown in Fig. 4.35. Fig. 4.35 A – E represents the microstructure for unflux, $CrO_3$, $MoS_2$, $TiO_2$, and $SiO_2$ fluxed weld metal, respectively. The dark shade represents the ferrite phase, whereas the light shade represents the austenite phase. The grain size measurement is elaborated in this section, and the representative microstructures are shown in Fig. 4.35, where 'F' stands for ferrite phase, and 'A' stands for austenite phase. The ferrite dendrite arm spacing (FDAS)is measured to be 87 $\mu m$, 116 $\mu m$, 111 $\mu m$, 77 $\mu m$ and 83 $\mu m$ in unflux, $CrO_3$, $MoS_2$, $TiO_2$, and $SiO_2$ fluxes respectively. However, the austenite dendrite arm spacing (ADAS)is measured to be 71 $\mu m$, 110 $\mu m$, 99 $\mu m$, 72 $\mu m$, and 77 $\mu m$ respectively in unflux, $CrO_3$, $MoS_2$, $TiO_2$, and $SiO_2$ flux

condition. The obtained results have been found in agreement due to the produced arc energy in the weld metal. The decomposition of flux elements causes more oxygen in $CrO_3$ flux, and the same has participated in a gas metal reaction where the $H_2$ is present. Hence, the intense heat produced in the $CrO_3$ flux is sufficient to grow the dendrite arms [20].

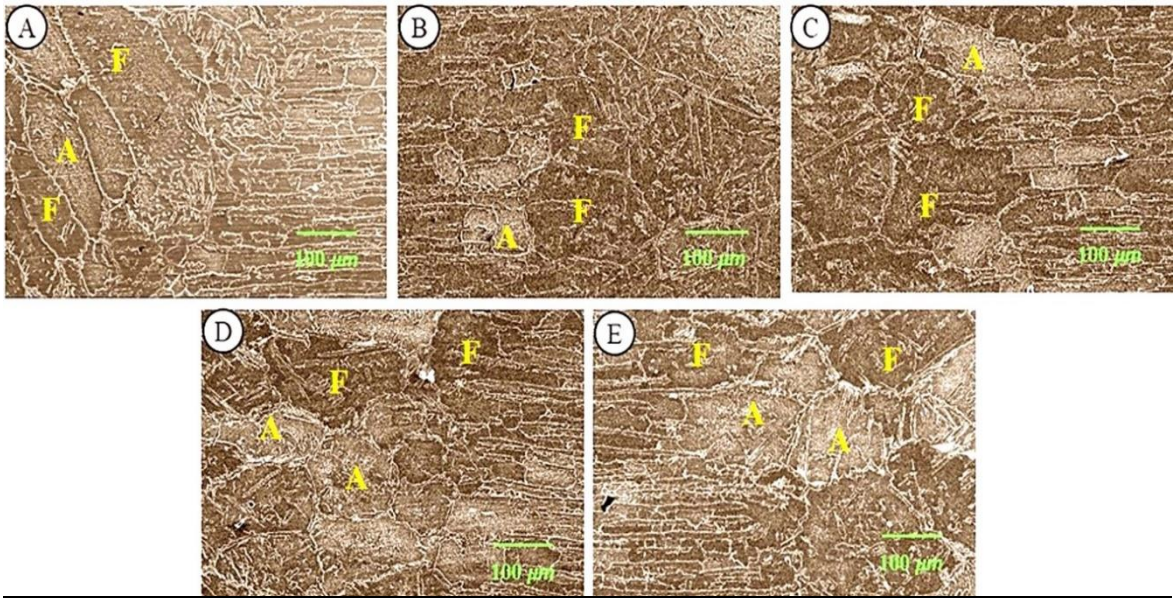


Figure 4.35: SEM image of HAZ of samples welded with (A) – (E) Unflux, $CrO_3$, $MoS_2$, $TiO_2$, and $SiO_2$ flux

The present study measured FDAS, ADAS, FGS, and AGS compared with values measured in pure Ar shielding by Tathgir et al. [20] for the same fluxes and process parameters. Hence, the effect of $H_2$ in shielding can be identified, and understanding would be clear. The measured values in Ar + 2.5% $H_2$ shielding and pure Ar shielding [20] are given in Fig. 4.36 for comparing the results. The FDAS and ADAS in both studies were observed with less scattering. However, considerable scattering in the values was observed with ferrite grain size (FGS) and austenite grain size (AGS), and the same thing is shown in Fig. 4.36, and further can be confirmed with Fig. 4.36. The amount of increased arc density or energy would lead to the growth of equiaxed grains. However, the dendrites are a function of cooling rate as well as composition. This is the reason for less scattering of data in FDAS and ADAS.

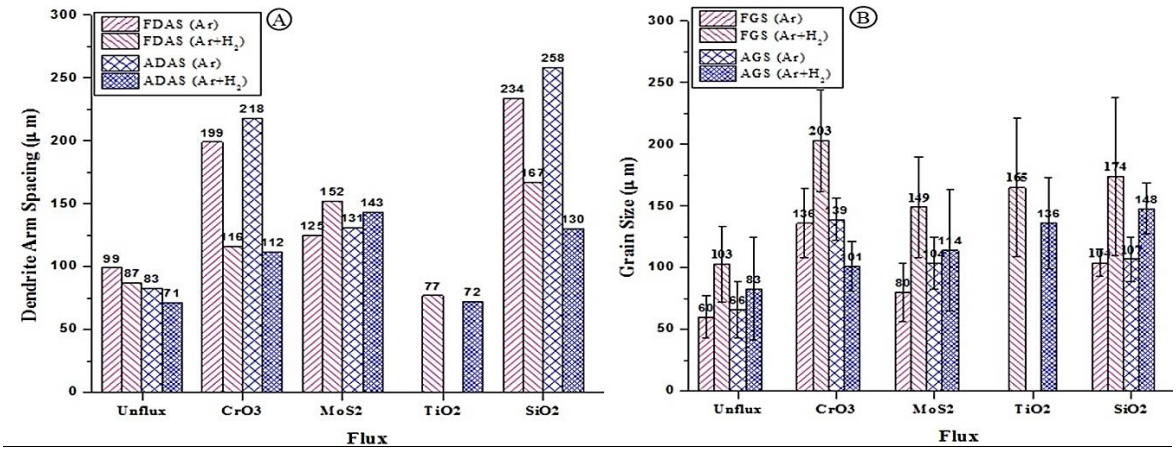


Figure 4.36: (A) Comparison of dendrite arm spacing and (B) comparison of average grain size

Figure 4.36 A represents the comparison of FDAS and ADAS for unflux, $CrO_3$, $MoS_2$, $TiO_2$, and $SiO_2$ fluxes in pure Ar shielding [20] and Ar + 2.5 % $H_2$ shielding. The average dendrite arm spacing in austenite is smaller than ferrite in unflux conditions. However, the ADAS is marginally lower than the FDAS in different flux conditions. While using the $H_2$ in shielding the FDAS and ADAS in unfluxed conditions are marginally reduced than pure Ar. However, a significant reduction is observed in the different flux conditions. Such variations are not significant in $MoS_2$ as there is no decomposition of oxygen during arc and associated reaction of $H_2$ and $O_2$ in the welding, directly governing the heat/energy produced in the weld metal.

While considering Fig. 4.36 B, it is observed that the mean grain size of ferrite and austenite grains in weld metal are coarsened (increased) in Ar + 2.5 % $H_2$ shielding in unfluxed and different flux conditions than the pure Ar shielding [20]. The trend is consistent in all conditions for FGS; however, in AGS of $CrO_3$, the mean grain size of AGS reduced than the pure Ar shielding [20]. It might be due to the diffusion of decomposed Cr into the weld metal, which is the strong ferrite stabilizer. Hence, the growth of austenite grains in the weld metal could be suppressed against ferrite grain growth. The mean FGS observed to be larger in the case of oxide-based fluxes. However, it is marginally reduced in $MoS_2$ flux in the Ar + 2.5 % $H_2$ shielding, and this is entirely different in pure Ar shielding [20]. Hence, the $H_2$ in shielding promotes the ferrite grain growth during the presence of oxygen, and the amount of oxygen in this environment decides the growth of ferrite grains. The size of AGS is smaller than FGS in Ar + 2.5 % $H_2$ shielding, which is the inverse case in pure Ar shielding. Hence, again, it is confirmed that the H2 in shielding promotes ferrite's growth compared to the austenite. The observed values and the results in the present study indicate the significant influences of $H_2$ in shielding on the mean grain size of ferrite and austenite as well as dendrite arm spacing of the

austenite and ferrite. The obtained results are in agreement with the results suggested by Gulenc et al. [50] for the grain growth with the addition of $H_2$ in shielding. The presence of $H_2$ in the shielding environment, along with the oxygen content and other active elements, would affect the thermal Energy/heat energy during arc and the respective arm spacing and grain growth mechanism. It could happen due to enhanced weld metal chemistry based on the varying slag-metal and gas-metal reactions [20] during the welding.

### 4.4.7 Peclet Number Analysis

The heat transfer largely governs the final weld pool shape and behaviour based on combined conduction & convection [20] in the molten weld pool. The combined effect of conduction and convection for heat transfer is different in different materials. However, it is quite possible to investigate them based on the Peclet number [20]. The Peclet number can predict the mode of heat transfer, and the same can be calculated by $Pe=L*Vmax / 2\alpha l$ [20, 83, 85, 86]. Where $V_{max}$ is the maximum surface velocity taken as 0.12 m/sec [20, 85, 86], $\alpha l$ is the thermal diffusivity of liquid, and $L$ is the characteristic length of the weld pool. This length (L) is measured as the radius of the weld pool in unflux condition, as the weld pool has a shallow depth of penetration. However, in increased penetration of fluxed conditions, it is estimated to be the depth of penetration [20, 83, 85]. The thermal properties of DSS are taken from the values suggested by Tathgir et. al.. [20].

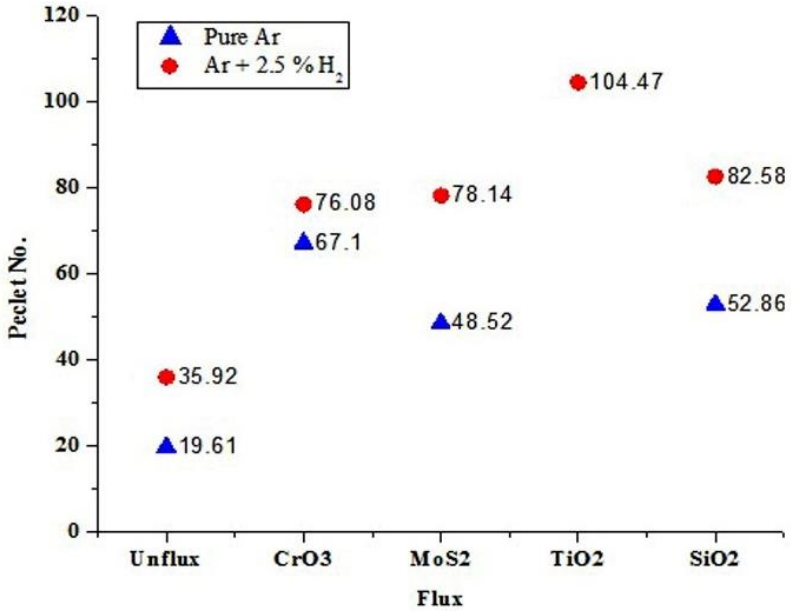


Figure 4.37: Comparison of Peclet number in Ar and Ar + 2.5% $H_2$ shielding

For a similar kind of study without $H_2$ induced shielding, the calculated Peclet numbers of the present study (Ar + 2.5% $H_2$) are compared with the pure Ar study [20] investigated by Tathgir et al. [20], and the same is presented in Fig. 4.37.

It is visible that the Peclet number is a function of heat transfer, and hence the values of Peclet Number (*Pe*) in Ar + 2.5% $H_2$ shielding environment is higher than pure Ar shielding environment [20]. Heat transfer in the weld pool is dominated by conduction for *Pe* << 1, While Pe >> 1, the heat transfer in the weld pool is dominated by convection [20]. The higher Peclet number in $H_2$ mix shielding suggests that the heat transfer in the molten pool for this study would be dominated by convection mode and due to the use of hydrogen gas. Moreover, the higher amount of thermal Energy/heat energy in an arc due to oxygen absorption and $H_2$ presence would increase heat transfer. The same thing has been evidenced while comparing Ar + 2.5% $H_2$ shielding with the pure Ar shielding Peclet numbers [20]. Tathgir et al. [20] reported the values of Peclet number in pure Ar shielding for different conditions, i.e., unflux, $CrO_3$, $MoS_2$, and $SiO_2$, as 19.61, 87.10, 48.52, and 52.86, respectively. The obtained Peclet numbers for the same flux condition in $H_2$ shielding are significantly larger than the without $H_2$ induced shielding environment [20]. Therefore, A-TIG weld pool behaviour in $H_2$ induced shielding environment along with weld pool shape mostly depends on the fluid flow mode in the weld pool. Such fluid flow in the weld pool is also governed by the combined effect of electromagnetic arc plasma and arc density [8, 12]. Hence, these features, oxide-based fluxes and $H_2$ in shielding could further govern the fluid flow behaviour, inverse Marangoni convection, and deeper penetration utilizing higher arc density.

### 4.4.8 XRD Analysis

Considerable metallurgical variations in weld chemistry could exist because several gas-metal and slag metal reactions occurred owing to oxygen, hydrogen, and surface-active elements in the activated fluxes. The obtained SEM, EDS, and optical microscopy analysis helps to understand the weld chemistry and associated phenomena of the enhanced penetration and dilution. However, further understanding about the phenomena based on formed phase structure is characterized using X-ray diffraction analysis. Figure 4.38 - A and 4.38 - B shows the characteristic reflexes of co-existing $\alpha$-Fe (BCC) and $\Upsilon$-NiFe (FCC) phases in the weld metal. The XRD pattern was obtained from the X'Pert PRO machine using 0.013 (2θ°) step size in 20° -90° position for all specimens. The subsequent analysis has been performed using 'X'- Pert High Score Plus software.

The XRD patterns for all the weld specimens are almost identical with varying peak intensity. The parent metal DSS has a significant amount of Cr, and the weld metal, owing to high heat density and associated cooling rate, may form the Cr-Carbide precipitates. Such precipitates have been evidenced in SEM, and it has been confirmed in the XRD analysis. After analyzing

peaks, more than one phase could exist at the same θ° position with different diffracted planes [97]. Such instances have been noticed in the present weld chemistry of DUP 2205. In case of $CrO_3$ flux very less intensity of $Cr_{23}C_6$ (Chromium carbide) with diffracted plane <531>at 50.623 (2θ°) (JCPDS file; 03-65-3132), [$Fe_3Ni_2$] austenite with diffracted plane <200> at 50.705 (2θ°) (JCPDS file; 03-65-5131) and $Cr_3C_2$ (Chromium carbide) with diffracted plane <223> at 81.974 (2θ°) (JCPDS file; 03-65-0897) phases have been confirmed. In the case of $MoS_2$ flux, $Cr_3C_2$(Chromium carbide) with diffracted plane <132>at 50.87 (2θ°) (JCPDS file; 03-65-0897) and [$Fe_3Ni_2$] austenite with diffracted plane <200> at 50.705 (2θ°) (JCPDS file; 03-65-5131) exists in the weld chemistry, which has also been evidenced in the microstructure (Fig. 4.32 B and Fig. 4.32 B). Whereas in case of $SiO_2$ flux $Cr_{23}C_6$ (Chromium carbide) with diffracted plane <531>at 50.623 (2θ°) (JCPDS file; 01-89-2724) and [Fe3$Ni_2$] was also found with diffracted plane <200> at 50.674 (2θ°) (JCPDS file; 03-65-5131) and $Cr_3C_2$ (Chromium carbide) with diffracted plane <223> at 81.974 (2θ°) (JCPDS file; 03-65-0897).Similarly, in $TiO_2$ flux, $Cr_{23}C_6$ (Chromium carbide) peak was found with diffracted plane <531> at 50.623 (2θ°) (JCPDS file; 03-65-3132) and at <911> at 82.354 (2θ°) (JCPDS file; 03-65-3132) and [$Fe_3Ni_2$] was also found with diffracted plane <200> at 50.705 (2θ°) (JCPDS file; 03-65-5131).

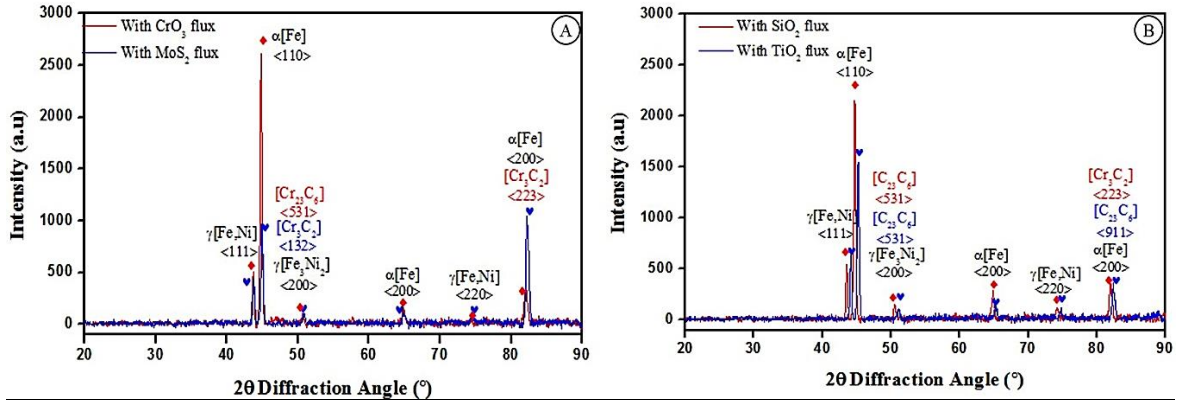


Figure 4.38: XRD Pattern of samples welded with (A) $CrO_3$ and $MoS_2$ flux (B) $SiO_2$ and $TiO_2$ flux

The phases like $\alpha$-Fe (BCC) with diffracted phases, <110> and <200> were observe along with $\Upsilon$-NiFe (FCC) with diffracted phases <111> and <220>. The obtained result of $\alpha$-Fe and Austenite [Fe, Ni] agrees with the data reported on XRD by other researchers [98, 99].

### 4.4.9 Micro-Hardness Analysis

The weld chemistry variations may cause the hardness to vary across the weld metal. Hence, the micro-hardness for all flux conditions with unflux conditions is presented in horizontal (transverse or width direction of weld) and vertical (depth or thickness direction of weld) regions in Fig. 4.39. In this study, the weld centre in most of the weld metal is observed with

approximately equiaxed grain structure with dendritic columnar structure growing inwards from the fusion boundary. Hence, the scattering in these regions could exist in the horizontal direction. The hardness variations in $SiO_2$ flux conditions are observed to be significant compared to $CrO_3$ and $MoS_2$. However, the distinctive variations in hardness compared to the unflux conditions have not been noticed. In thickness (vertical) direction, some instances of peak hardness in $CrO_3$ flux have been detected; however, the $TiO_2$ flux weld has shown consistent hardness moving towards the bottom fusion boundary of weld metal. The hardness associated with the microstructure is noticed in all hardness scans. Table 4.3 shows the comparative data of the $H_2$ induced shielding specimens with the pure Ar shielding specimens as reported by Tathgir et al. [20]. The table suggests that the marginal variation could be possible in average hardness owing to the use of $H_2$ induced shielding. However, the distinctive variation cannot be achieved in the hardness. Such minor variations could result from increased heat, as significant variations in the weld chemistry are not expected. The observed variations are a reflection of the heat input and the associated cooling rate, which could govern the nature of formed phases and associated hardness. The same thing is reflected in Table 4.3.

Table 4.3: Comparison of average micro-hardness for Ar and Ar + 2.5% $H_2$ shielding

| **Flux Condition** ⟶ | | **Unflux** | **$CrO_3$** | **$SiO_2$** | **$MoS_2$** | **$TiO_2$** |
|---|---|---|---|---|---|---|
| With Pure Ar (Tathgir et. al.) [20] | Horizontal direction | 293 | 287 | 271 | 275 | -- |
| With Ar + 2.5% $H_2$ | Horizontal direction | 290 | 274 | 279 | 265 | 280 |
| With Pure Ar (Tathgir et. al.) [20] | Vertical direction | 293 | 274 | 272 | 285 | -- |
| With Ar + 2.5% $H_2$ | Vertical direction | 287 | 282 | 282 | 291 | 310 |

Figure 4.39: Micro-hardness comparison for TIG and A-TIG welded samples (A) $CrO_3$, $SiO_2$, $MoS_2$ (B) $TiO_2$ and Unflux in the horizontal direction and (C) $CrO_3$, $SiO_2$, $MoS_2$ (D) $TiO_2$, and Unflux in the vertical direction

## 4.5 Summary

The significance of $H_2$ induced shielding in the different surface-active element fluxes for A-TIG processes has been investigated in the present study, along with detailed metallurgical characterization. The dendrites growth was found vertical in conventional TIG. However, In A-TIG ($H_2$ induced) was horizontal due to the high thermal Energy/heat energy and associated cooling rate. Due to a significant amount of Cr in the parent metal (DSS), there is a strong possibility of forming Cr-Carbide precipitates due to high heat density and associated cooling rate. Hydrogen in argon shielding increases the arc efficiency and decomposes oxides, which further generates high heat density due to oxygen. This was found to be highly significant in $CrO_3$ flux due to more oxygen than the other fluxes. Such a thing promotes the higher Peclet number. Hydrogen ($H_2$) in shielding promotes ferrite's growth than the austenite due to reactions of $H_2$ with decomposed oxygen in the weld pool.

# Chapter - 5
# Vertical Uphill A – TIG Welding

## 5.1 Introduction

It is already evidenced that the A – TIG welding could produce higher penetration, and it can be used to increase the productivity of conventional GTAW/TIG welding because of its requirement of edge preparation for higher thickness. Above 3 mm thickness, the edge preparation becomes even more critical. GTAW/TIG welding is generally preferred for high precision pipe welding for difficult positions, especially for root pass in the case of stainless steel. For welding higher thickness plates, edge preparation is necessary. Edge preparation of higher thickness pates or pipes of stainless steel is tough and adds extra cost, making the GTAW/TIG welding uneconomical.

The strength of the welding joint is a critical parameter. It is mainly a result of quality of the weld, which depends significantly on the operator skill in case of manual welding, especially for challenging positions. Furthermore, high tensile strength is the prime requirement of any welding joint. The gravity force mainly influences the quality of the vertical position welding or bead formation. Low current is used in the vertical upward/uphill position compared to e flat OR horizontal position, but the current is set higher than vertical downward/downhill position welding [100]. The range of stresses increases with concave front, which reduces fatigue life in case of both 2 G & 3 G welding positions [101]. During welding of steel pipe joints with 10 to 11% Cr in PC (pipe position for welding horizontal) and PJ positions (pipe position for welding downwards), fractures were observed in HAZ during tensile testing, while higher tensile strength was obtained in the PC position [102]. Higher toughness was observed from the HAZ region as compared to the weld zone and base metal [102].

The weld profile depends on the heat input value, called the shape factor. The shape factor is lower in case of vertical upward and overhead positions. The formation of acicular ferrite was found due to the use of high Mn content of filler in case of lower heat input values and primary ferrite with Widmanstatten/disturbed ferrite, and second phase ferrite was observed with higher heat input values [103]. Researchers also found out that the circumferential pipe welding by GMAW with root pass of TIG welding in vertical position has minimum dilution rate with more reinforcement than the flat position, which had minimum porosity [104]. The presence of delta ferrite in stainless steel weld promotes the presence of martensite, which further may deteriorate the mechanical properties, especially the joint's toughness [51].

Austenitic stainless steel has excellent corrosion resistance and better formability characteristics (available in different grades). It is used worldwide in chemical, nuclear, energy, fabrication, food, etc. [105, 106].

Compared to mild steel, austenitic stainless steel (ASS) is widely used in many manufacturing industries due to its good weldability and better mechanical properties. Additionally, it can be welded successfully with different welding techniques using both arc and resistance as a heat source, although resistance welding is better for thin sheets. For higher thicknesses, arc welding is used to weld.

In this study, to improve the capability of the A-TIG welding process and study its feasibility during difficult positions (Vertical/Up. hill), A-TIG welding with coated filler (with activated flux) was carried out on 5.74 mm thick austenitic stainless-steel plates (AISI 304). The experiments were conducted using Taguchi's L18 orthogonal array (Table 5.2). Three oxide-based fluxes, namely $CrO_3$, $SiO_2$, and $TiO_2$, were used to coat both filler and the base plates. The impact toughness (Charpy), microhardness, and bead geometry were analyzed, and results were compared with the conventional GTAW/TIG welded joints.

## 5.2 Experimental Methodology

Austenitic stainless-steel plates of 5.74 mm thick were cut to the size of 100 × 50 mm as coupon plates. After cutting, chemical composition was checked by the spectrometer and is presented in Table 5.1.

Table 5.1: Chemical compositions of base metal

| Material | % Composition | | | | | | | | | | | Thickness (mm) |
|---|---|---|---|---|---|---|---|---|---|---|---|---|
| | C | Mn | Si | Cr | Ni | S | P | Mo | Cu | W | Fe | |
| AISI 304 | 0.32 | 1.49 | 0.62 | 18.7 | 8.12 | 0.03 | < 0.003 | 0.24 | 0.43 | < 0.02 | Balance | 5.74 |

Vertical uphill A-TIG welding was performed using selected welding parameters using the L-18 orthogonal array listed in Table 5.2. Before welding, all work-piece edges were ground using a surface grinder (Falcon, Chevalier FSG 2A 1224, Taiwan) for square butt joint configuration and the top surface of base plates were cleaned by buffing. After grinding and buffing, all work-pieces were tacked at the back using the fixture (Fig.5.1). After tacking and cooling, the weld coupon joint area was properly cleaned by acetone to remove surface impurities/contaminations. Fine-grained 99.9 % pure oxide-based fluxes ($SiO_2$, $TiO_2$, $CrO_3$) were mixed individually with acetone to make an activated flux paste. The paste was applied with the help of a brush to form a thin layer of flux (20-25μm thick) on the weld area, and welding was completed after the complete evaporation of acetone. The filler was also coated

with the same activated flux to compensate for the loss of activated flux on the weld coupon in the vertical position. The experiments were completed using a conventional TIG welding machine (Make - Techno Weld, 350 A) with EWTh-2 (2% thoriated tungsten electrode) with a 3.2 mm diameter and a flat end conical tip and 60° vertex angle. All tacked coupons were welded one by one randomly as per the designed orthogonal array (L-18) with proper care, which is shown in Table 5.2.

Table 5.2: L-18 orthogonal array used for vertical A-TIG welding

| Sample No. | Gas | Gas Flow Rate (L/min) | Current (A) | Flux |
|---|---|---|---|---|
| 1. | Ar | 12 | 120 | $SiO_2$ |
| 2. | Ar | 12 | 140 | $TiO_2$ |
| 3. | Ar | 12 | 160 | $CrO_3$ |
| 4. | Ar | 14 | 120 | $SiO_2$ |
| 5. | Ar | 14 | 140 | $TiO_2$ |
| 6. | Ar | 14 | 160 | $CrO_3$ |
| 7. | Ar | 16 | 120 | $TiO_2$ |
| 8. | Ar | 16 | 140 | $CrO_3$ |
| 9. | Ar | 16 | 160 | $SiO_2$ |
| 10. | Ar+$H_2$ | 12 | 120 | $CrO_3$ |
| 11. | Ar+$H_2$ | 12 | 140 | $SiO_2$ |
| 12. | Ar+$H_2$ | 12 | 160 | $TiO_2$ |
| 13. | Ar+$H_2$ | 14 | 120 | $TiO_2$ |
| 14. | Ar+$H_2$ | 14 | 140 | $CrO_3$ |
| 15. | Ar+$H_2$ | 14 | 160 | $SiO_2$ |
| 16. | Ar+$H_2$ | 16 | 120 | $CrO_3$ |
| 17. | Ar+$H_2$ | 16 | 140 | $SiO_2$ |
| 18. | Ar+$H_2$ | 16 | 160 | $TiO_2$ |

The process steps for vertical A-TIG welding are shown in Fig. 5.1, including tacking arrangement, buffed coupon after tacking, holding of weld coupon and schematic diagram of vertical A-TIG welding. The novelty of vertical A-TIG welding is due to the use of coated filler to compensate for the loss of pasted activated flux. Because of gravitational force and axial flow of plasma force, the activated flux may detach the surface or fall during welding. A weaving technique was used to investigate the feasibility of A-TIG welding in a vertical uphill position on the square butt joint. Austenitic filler wire (316 L ) diameter 1.5 mm was used for welding the coupons. The 100 mm long plates were used for this study.

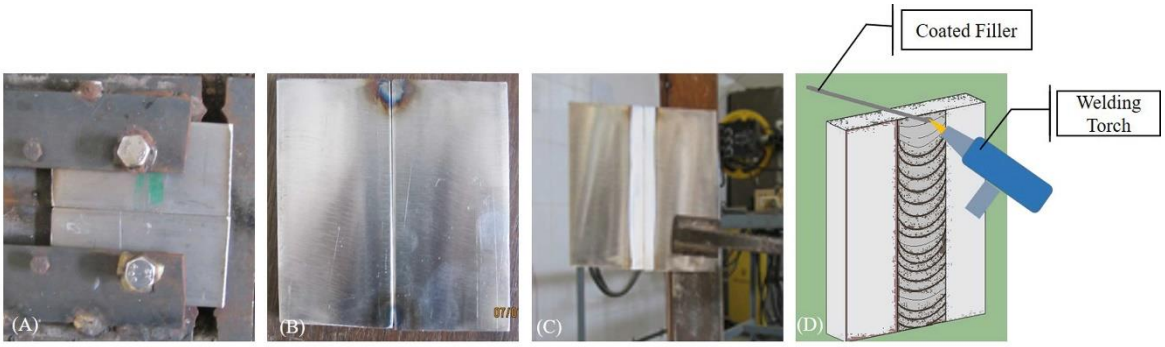


Figure 5.1: Vertical A-TIG welding process steps from left to right (Before tacking in a fixture, After tacking and buffing, Holding of test coupon after applying activated flux and last represent the process)

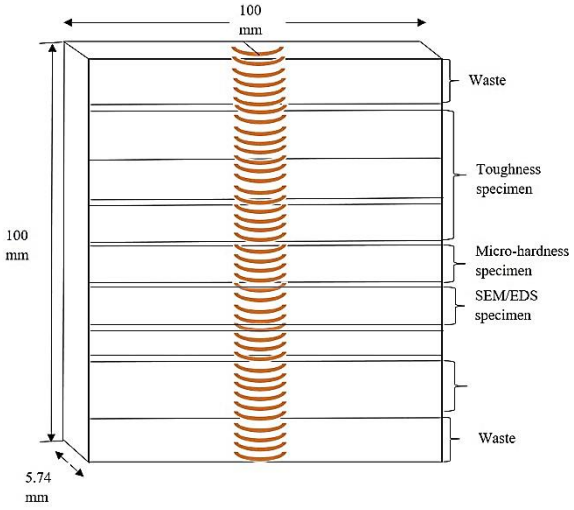


Figure 5.2: Schematic representation of extraction of samples

After vertical A-TIG welding, the samples were cut with a CNC wire cut EDM machine as per the schematic diagram shown in Fig. 5.2. The standard polishing technique was used to prepare micro-hardness, optical microscopy, and SEM samples using different emery papers on disc polisher. The polished samples were etched with "Ralph's" etchant, and weld profiles were also measured using a measuring microscope (AxioScope A1, Carl Zeiss, Gottingen, Germany), having an accuracy of 0.001 mm. A metallurgical study was also performed by a metallurgical microscope (make: Leica) for three magnification levels, i.e., at 10X, 20X, and 50X. Three samples were cut from each weld coupon for the toughness test and finally compared with the base TIG/GTA welded sample. Micro-hardness was also analyzed on a microhardness tester at a load of 500 g using a dwell time of 20 s.

The result of this study has been discussed based on dilution rate based on net thermal energy/heat energy and mechanical properties. The contribution of surface-activating elements in net thermal energy/heat energy, higher penetration and microstructural changes variations in the weld, and related mechanisms has also been studied.

## 5.3 Result and Discussion

It is already known that the weld quality strongly depends on the weld bead geometry parameters and the associated cooling rate. The cooling rate is responsible for the resultant weld microstructure. So, the heat input could greatly influence the resultant properties of the joint and its appearance. The type of shielding environment may also affect the associated cooling rate by increasing or decreasing the generated thermal Energy/heat energy (which is also discussed in the previous chapters). So, after analysing the success of A -TIG welding to achieve a higher depth of penetration, the influence of various welding parameters with different shielding environments is further elaborated using difficult position welding (Vertical uphill) in the subsequent sections. It was found that the heat input is responsible for the melting of base metal and filler metal melting rate. At minimum current, i.e., 120 A, the melting rate was lower than higher current, i.e., 160 A. The increased meting rate affects the actual welding time. The time taken to weld 100 mm length was observed to be 60 s, 45 s and 30 s for 120A, 140A and 160 A current settings, respectively.

### 5.3.1 Effect of Ar and Ar + 2.5 % $H_2$ Shielding on Weld Morphology

#### 5.3.1.1 Effect on Weld Appearance

Visual inspection of weld bead showed no undercut in the case of Ar shielding environment, for both conventional TIG welding (Fig. 5.3) and A-TIG welding at high current. (Fig. 5.4). Weld bead width was found more for high current, owing to higher melting of the base metal for both the shielding environment. In the Ar + 2.5 % $H_2$ shielding environment, some defects like undercuts were observed along with the weld bead and a deep undercut was observed for higher current (160 A) (Fig. 5.5 encircled by red). Similarly, porosity was also observed in some A- TIG welds (encircled by yellow) (Fig. 5.5).

Figure 5.3: Top surface and bottom surface of conventional TIG welding using 160 A and 16 L/min gas flow rate

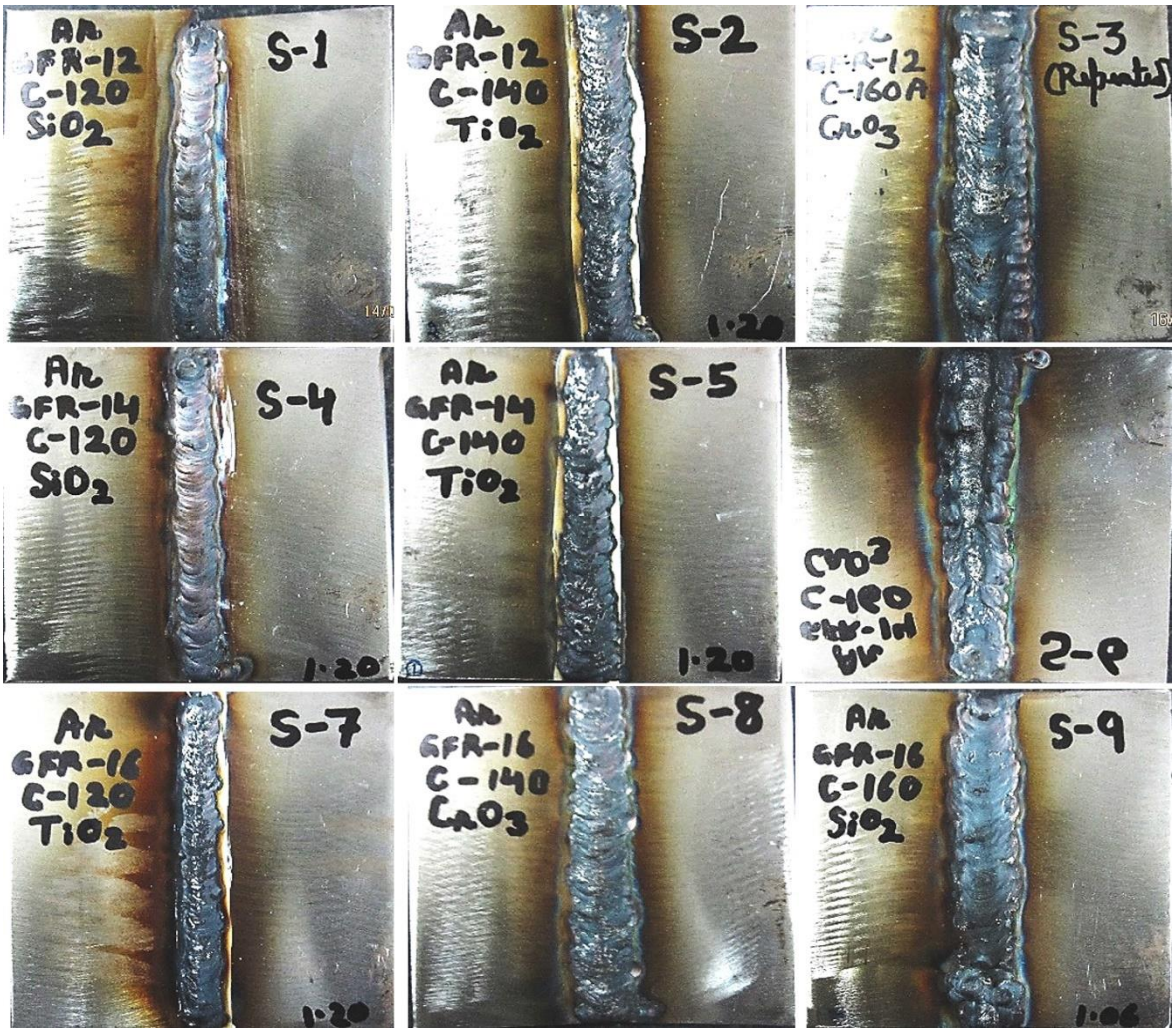


Figure 5.4: Weld bead appearance of Ar shielded weld coupon (S-1 to S-9)

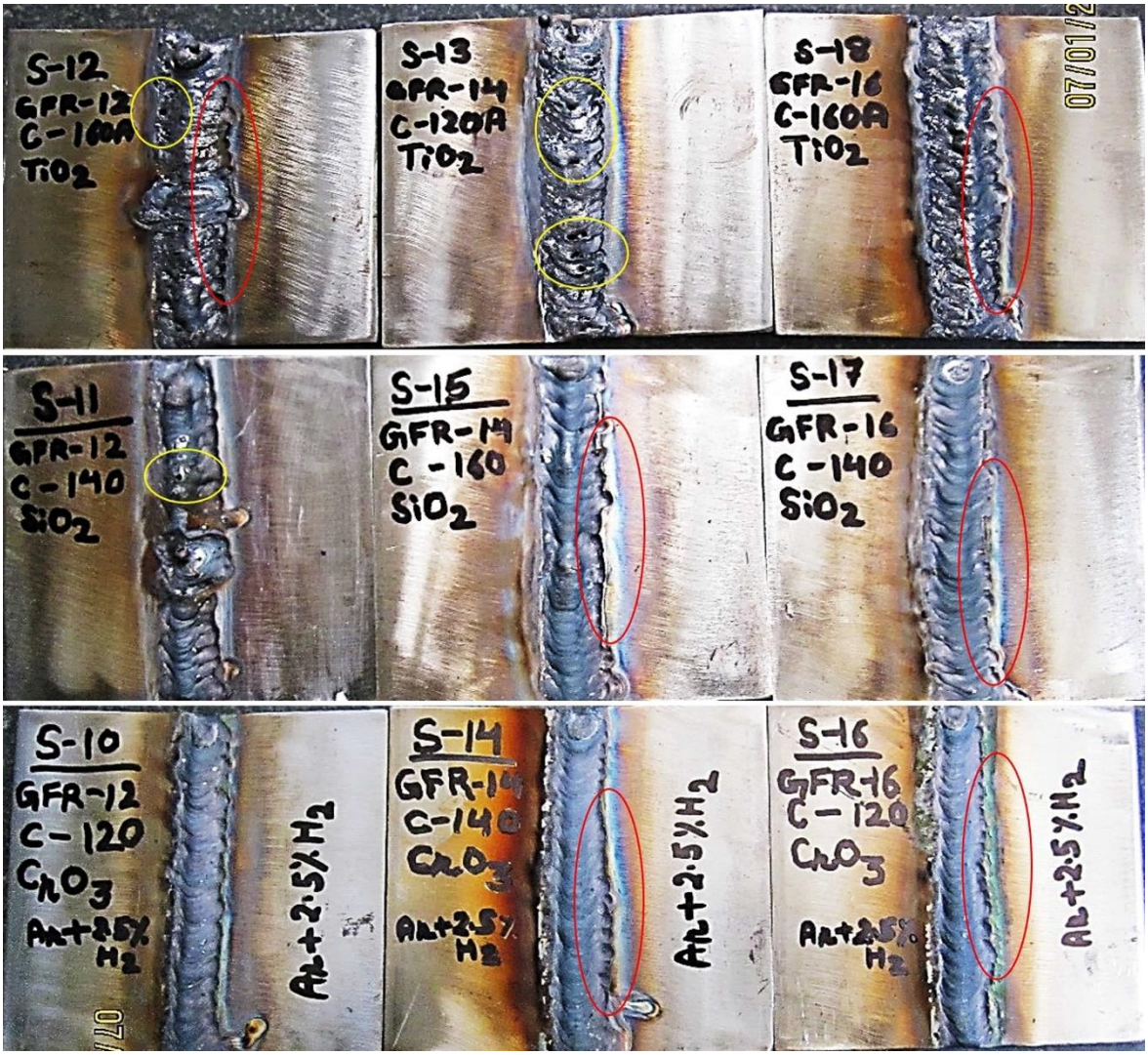


Figure 5.5: Weld bead appearance of Ar shielded weld coupon (S-10 to S-18)

### 5.3.1.2 Effect on Bead Geometry Parameters

In Table 5.3, sample 'A' and sample 'B' represent the conventional TIG welding with Ar and Ar + 2.5% $H_2$ shielding environment welding coupons. Both the weld coupons were welded at 160 A. Table 5.3 compares weld bead geometry and mechanical properties for both conventional TIG and A – TIG welding. The Charpy toughness of the parent metal was found as 90 J. High DoP with more dilution area was observed due to higher heat input and $H_2$ in the Ar gas, generating more heat. The difference in width of the weld may slightly differ due to electrode manipulation. The macrostructures of the etched samples are presented in Fig. 5.6. After etching, porosity was observed in some cases (S – 11 and S – 18) (Fig. 6.6), which could be due to the use of $H_2$ in shielding environment. In the case of the Ar shielded sample, no porosity was observed after cutting and etching.

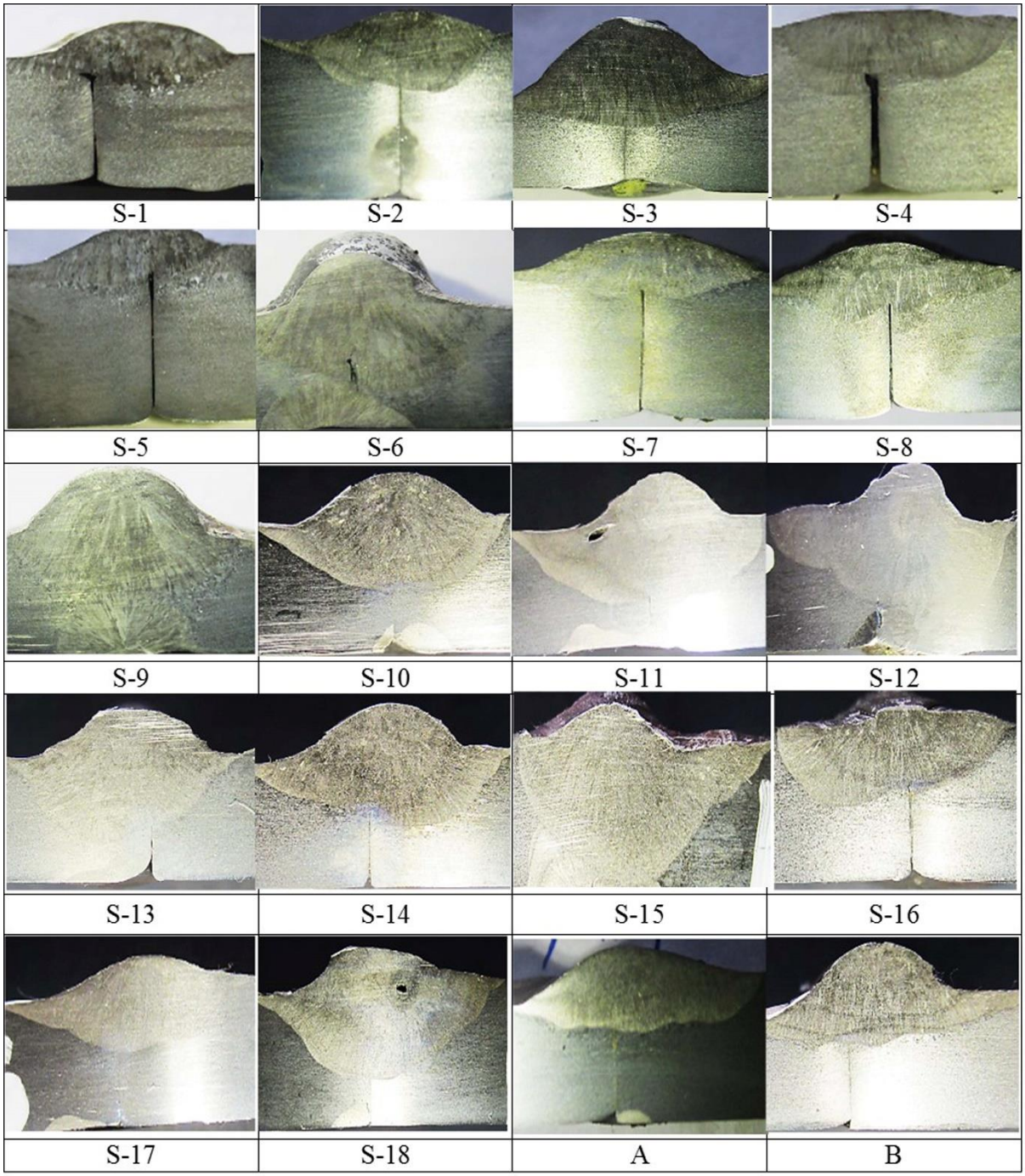


Figure 5.6: Macrograph of conventional TIG and A- TIG welding of vertical uphill position (S-1 to S-9 for Ar shielding, S-10 to S-18 with Ar +2.5 % $H_2$ shielding, 'A'- Without flux with Ar shielding and 'B'- Without flux with Ar +2.5 % $H_2$ shielding)

Despite the presence of undercut, the maximum depth of penetration (DoP), maximum dilution area and maximum toughness were found in sample 15 (S – 15), which was welded with $SiO_2$ flux using Ar + 2.5% $H_2$ shielding environment (Fig. 5.6). As silicon has a greater affinity towards the electron, it may attract more free electrons from the periphery of the arc and result in deeper penetration. By comparing the toe angle with penetration area (Fig. 5.7), it was observed that there is a strong relationship between toe angle and penetration area during Ar

shielding, whereas no significant relationship is found in the case of mixed shielding environment.

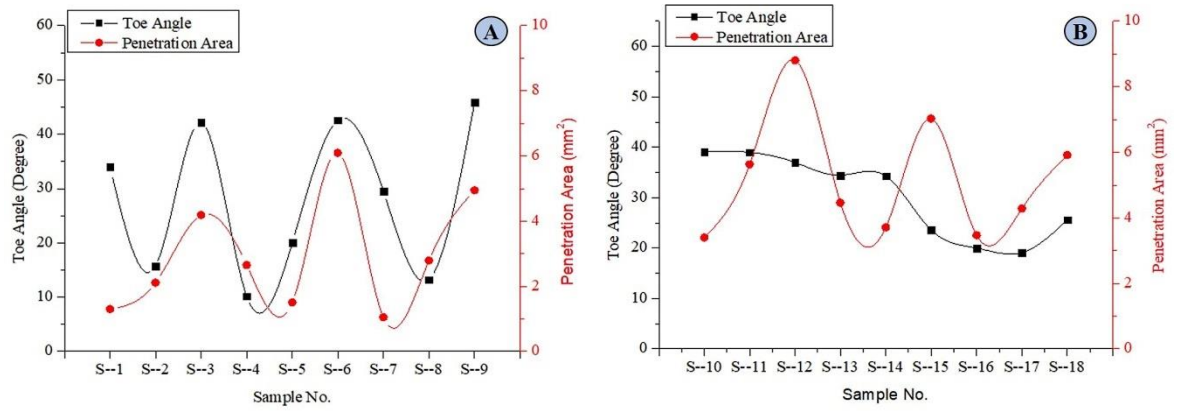


Figure 5.7: Comparison of DoP and bead height for the vertical uphill position (a) with Ar shielding (b) with Ar + 2.5 % $H_2$ shielding

Figure 5.8 shows the relationship between dilution and toe angle. Figure 5.8 A shows that when the toe angle decreases, then dilution increases, whereas Figure 5.8 B shows no relationship.

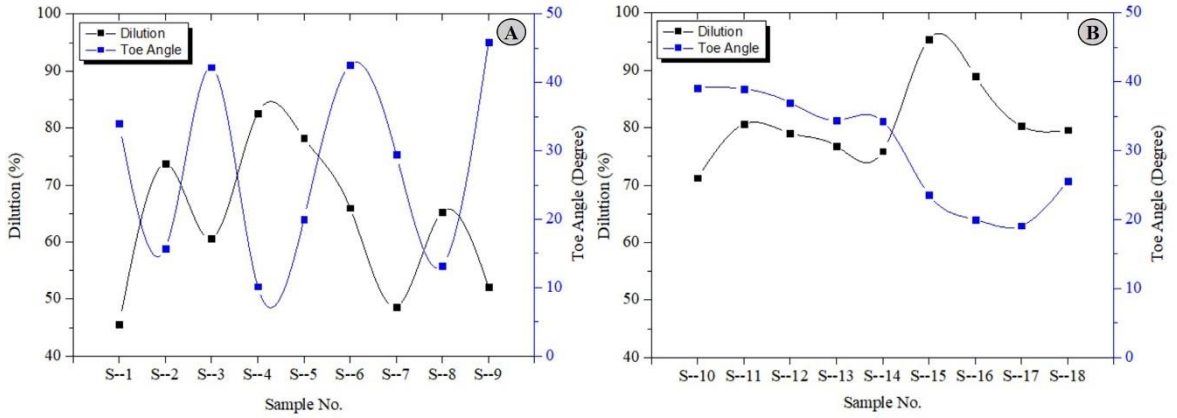


Figure 5.8: Comparison of dilution and toe angle for the vertical uphill position (a) with Ar shielding (b) with Ar + 2.5 % $H_2$ shielding

Table 5.3: Bead geometry parameters and mechanical properties

| Sample No. | Filler Deposit (gm) | Depth of Penetration (mm) | Bead Height (mm) | Average Toe Angle (Degree) | Penetration Area ($mm^2$) | Reinforcement Area ($mm^2$) | Dilution (%) | Average Toughness (Joule) |
|---|---|---|---|---|---|---|---|---|
| S--1 | 5 | 1.37 | 1.33 | 34.03 | 7.81 | 9.34 | 45.54 | 47.33 |
| S--2 | 6.5 | 2.18 | 0.93 | 15.74 | 12.64 | 4.51 | 73.70 | 45.33 |
| S--3 | 6.4 | 2.85 | 2.89 | 42.21 | 25.11 | 16.34 | 60.57 | 58 |
| S--4 | 5 | 2.57 | 0.44 | 10.16 | 15.91 | 3.35 | 82.60 | 35.33 |
| S--5 | 6.05 | 2.54 | 0.65 | 19.97 | 9.02 | 2.51 | 78.23 | 27.33 |
| S--6 | 7.1 | 3.91 | 3.12 | 42.58 | 36.56 | 18.85 | 65.98 | 58 |
| S--7 | 6.1 | 1.13 | 1.61 | 29.49 | 6.29 | 6.64 | 48.64 | 33.33 |
| S--8 | 6.1 | 2.22 | 1.13 | 13.2 | 16.73 | 8.88 | 65.32 | 24 |
| S--9 | 6.9 | 3.07 | 3.40 | 45.9 | 29.68 | 27.23 | 52.15 | 64 |
| S--10 | 5.1 | 2.5 | 1.61 | 39.13 | 22.1 | 8.91 | 71.26 | 47.33 |
| S--11 | 6.4 | 4.12 | 1.97 | 39 | 36.61 | 8.8 | 80.62 | 43.33 |
| S--12 | 7.4 | 2.26 | 2.3 | 36.98 | 57.25 | 15.17 | 79.05 | 67.33 |
| S--13 | 5.2 | 3.0 | 1.95 | 34.43 | 29.01 | 8.75 | 76.84 | 30.66 |
| S--14 | 6.2 | 3.74 | 1.78 | 34.28 | 24.12 | 7.65 | 75.92 | 48 |
| S--15 | 7.3 | 5.20 | 1.02 | 23.59 | 45.7 | 2.18 | 95.44 | 80 |
| S--16 | 5.3 | 3.03 | 0.68 | 20 | 22.55 | 2.78 | 89.02 | 47.33 |
| S--17 | 5.9 | 2.57 | 1.18 | 19.12 | 27.84 | 6.84 | 80.27 | 48 |
| S--18 | 7.2 | 4.02 | 1.56 | 25.59 | 38.46 | 9.85 | 79.61 | 71 |
| A | 6.9 | 2.49 | 1.07 | 15.08 | 25.03 | 9 | 73.55 | 25.33 |
| B | 7.1 | 2.51 | 2.06 | 37.65 | 25.58 | 7.25 | 68.60 | 43.33 |

The analysis of results revealed that welding at 160 **A** produces maximum penetration for both shielding conditions (pure Ar and Ar + 2.5 % $H_2$). It was also observed that the use of $H_2$ in a shielding environment produces more molten metal owing to higher arc temperature, which was difficult to handle and resulted in defects like undercut and impurities. The effect of the two shielding environments on penetration area, reinforcement area, and dilution rate are presented in Fig. 5.9 and Fig. 5.10.

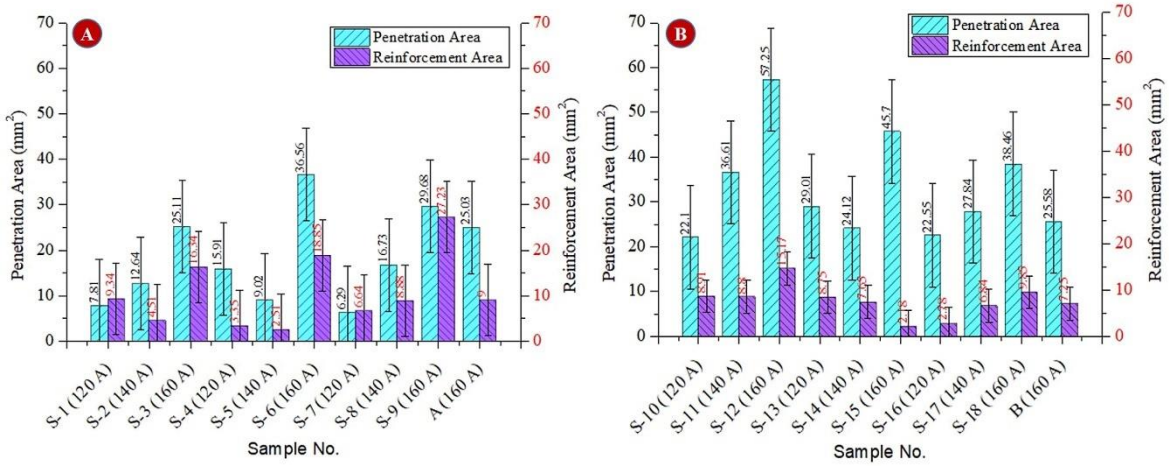


Figure 5.9: Comparison of Penetration area and Reinforcement area for the vertical uphill position (a) with Ar shielding (b) with Ar + 2.5 % $H_2$ shielding

After comparing the penetration area and reinforcement area (Fig. 5.9), it was concluded that the penetration area increases with the increase of current. This increase was found maximum

in a mixed shielding environment. In Fig. 5.10, the overall fluctuation of dilution area was observed in both cases, but it was found on the higher side in the case of mixed shielding environment. It was also observed that the amount of current did not affect the change in the dilution area.

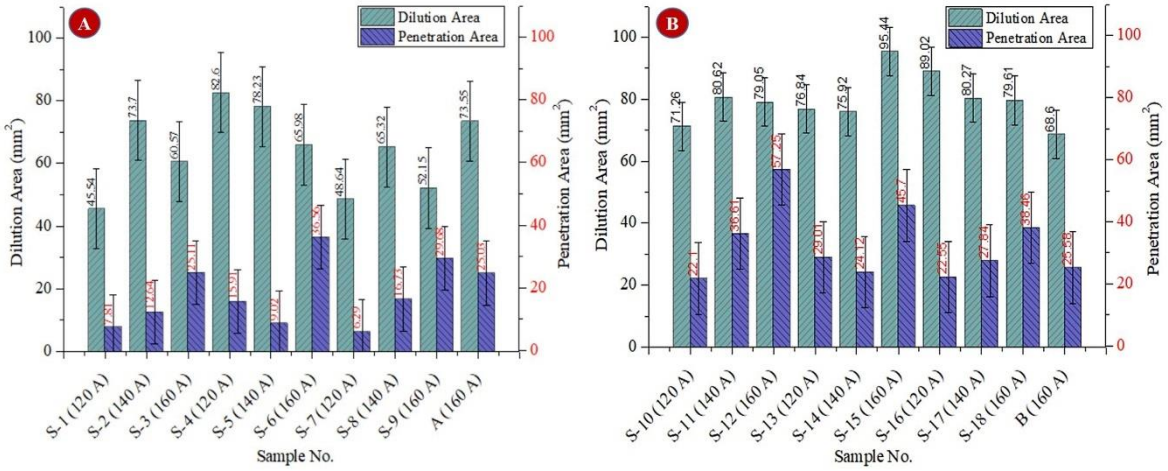


Figure 5.10: Comparison of dilution and Penetration area for the vertical uphill position (a) with Ar shielding (b) with Ar + 2.5 % $H_2$ shielding

### 5.3.2 Effect of Vertical Uphill A – TIG Welding on Weld Pool Chemistry:

In the case of conventional TIG welding, the weld pool chemistry changes only due to welding parameters and cooling conditions, whereas in the case of A-TIG welding, the weld pool chemistry is strongly influenced due to activated flux, shielding environment, cooling conditions and welding parameters. In Fig. 5.11(A) representing weld without flux condition (conventional TIG welding), the concentration of delta ferrite was observed to be less as compared to welding with mixed shielding environment shown in Fig. 5.11 (B). The dark phase (red) shows the ferrite phase in these figures. The presence of hydrogen ( 2.5 %) in Ar gas produced an abundant ferrite compared to pure Ar. This may be attributed to the net heat produced and the associated cooling rate of the weld.

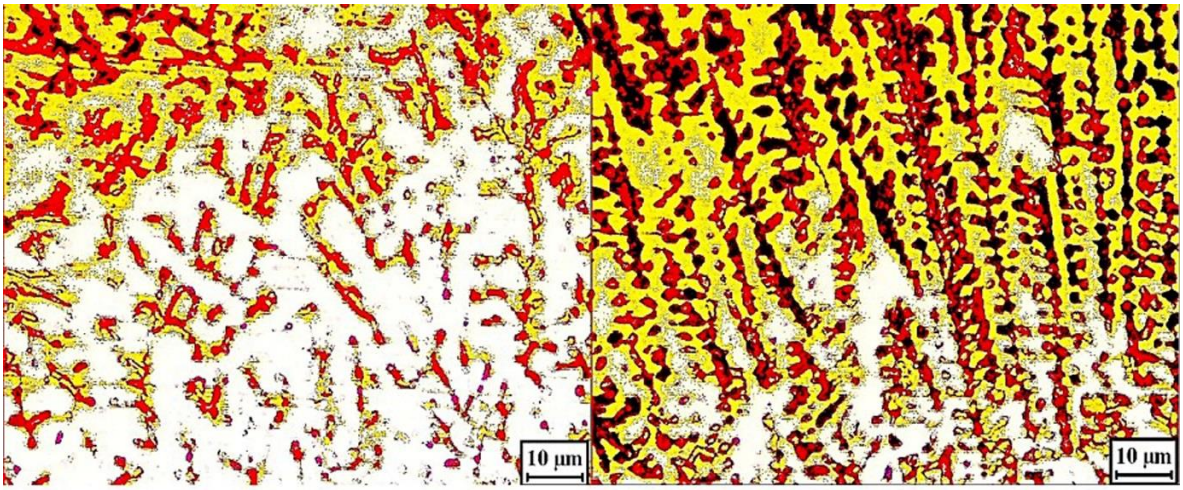


Figure 5.11: Microstructure of vertical uphill of conventional A – TIG (A) with pure Ar shielding using 160 A (B) with Ar + 2.5 % $H_2$ shielding using160 A

The microstructure of all vertical A – TIG welding coupons shows a mixed morphology of the remaining delta ferrite (Fig 5.12 and Fig. 5.13) in both shielding environments. The difference in the remaining delta ferrite in the microstructure was observed due to the difference in the cooling rate and owing to different heat inputs. The low level of current (i.e., 120 A) results in the closely packed delta ferrite compared to dispersed delta ferrite at higher current (i.e., 160 A) for both shielding environments. It may be due to the fast-cooling rate of the weld metal at low current, so it had less time available to convert the delta-ferrite to austenite [6]. It means the higher temperature at a high current improves the dispersion of delta ferrite in the case of conventional TIG welding with Ar shielding and A – TIG welding. This type of phenomenon was not present in the case of conventional TIG welding with a mixed shielding environment (Fig. 5.11 B). Hence, low ferrite content with the non-continuous network in the fusion zone of austenite stainless steel helps avoid brittle crack formation [107].

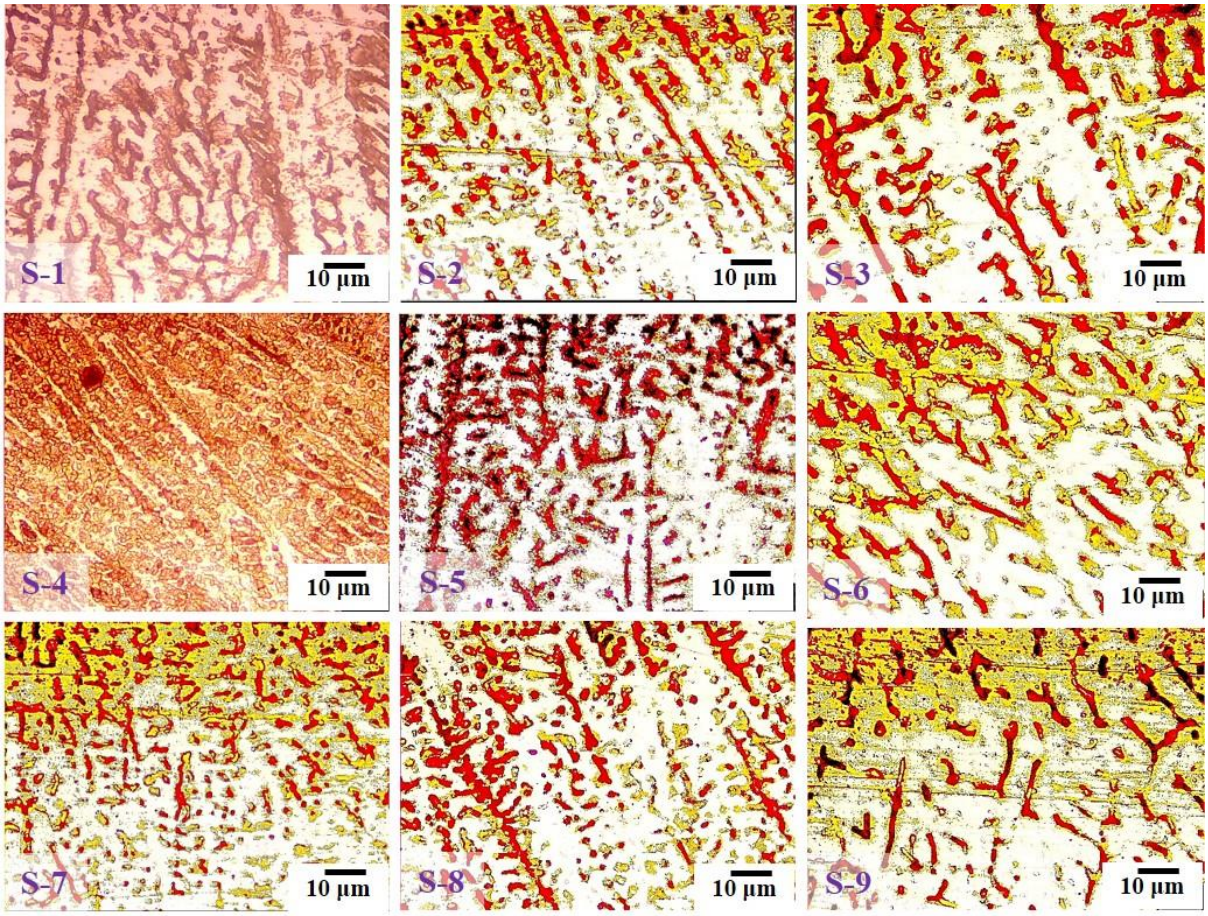


Figure 5.12: Microstructures of samples S – 1 to S – 9 obtained after A-TIG welding

When the microstructure of Ar shielded A – TIG welding (Fig.5.12) is compared with the Ar + 2.5 % $H_2$ shielded A – TIG welding (Fig.5.13), it was observed that the transformation of delta ferrite to austenite is more in case of $H_2$ mixed shielding owing to slow cooling rate. Hence, Ar + 2.5 % $H_2$ shielded A – TIG welding has a more diffuse delta ferrite structure due to the weld pool's higher temperature.

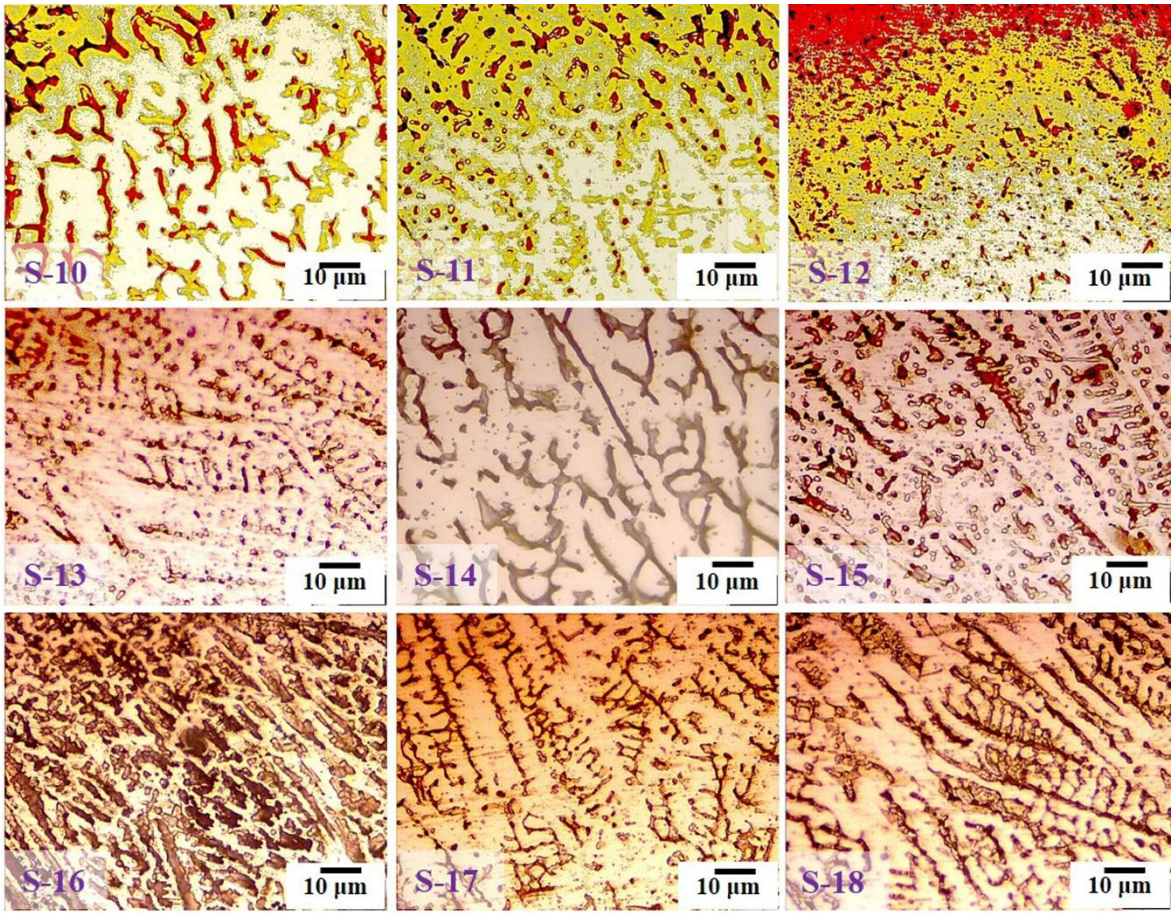


Figure 5.13: Microstructures of samples S – 10 to S – 18 obtained after A-TIG welding

## 5.3.3 Effect of Vertical Uphill A – TIG Welding on Mechanical Properties:

### 5.3.3.1 Microhardness Analysis

Microhardness variation of all vertical uphill A – TIG welding fusion zone, sample 'A' (conventional TIG welding with Ar shielding) and sample 'B' (conventional TIG welding with Ar + 2.5 % $H_2$ shielding) and base metal are presented in Fig. 5.14. It shows that the parent metal has a hardness of 222.27 (VHN). The variation in average microhardness in samples S 1 to S 18 is due to the different heat input (HI) and associated cooling rate, different shielding environments with different gas flow rates, and different oxide-based fluxes. The microhardness plot shows that the lowest hardness value corresponds to $CrO_3$ flux (VHN 161.36) for sample S-3. It is also less than the sample 'A' average microhardness (conventional TIG welding with Ar shielding). The maximum microhardness, i.e., VHN 240.74, was found for sample S – 12 (A – TIG weld with $TiO_2$ flux at 160 A). So, the total deviation of the microhardness is approximate VHN 39.

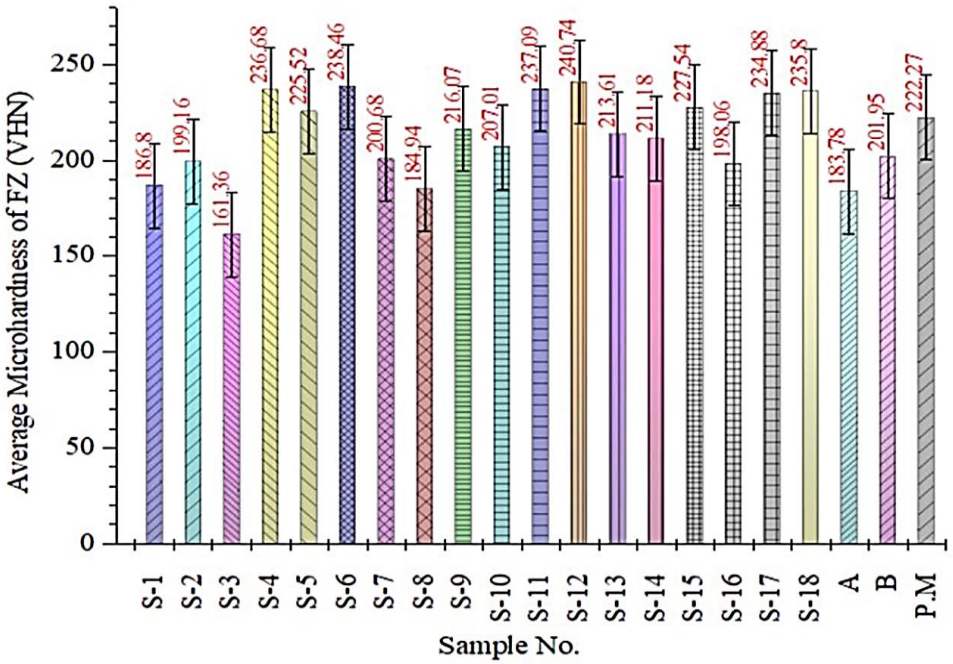


Figure 5.14: Variation of average micro-hardness of samples S-1 to S-18 including sample 'A' and sample 'B' and base metal

### 5.3.3.2 Toughness Analysis

The comparison of average fracture toughness (Impact Charpy test) at three current levels is shown in Fig. 5.15. Results show that sample S – 15 had maximum toughness, i.e., 80 **J** but less than the parent metal, which had a toughness of 90 **J**. The average toughness of without flux (no flux) and 'Ar' shielded sample was observed as 25.33 **J**, whereas it was measured as 43.33 J for mixed shielding environment. The average toughness was upsurging with the current value and was found maximum with a mixed shielding environment.

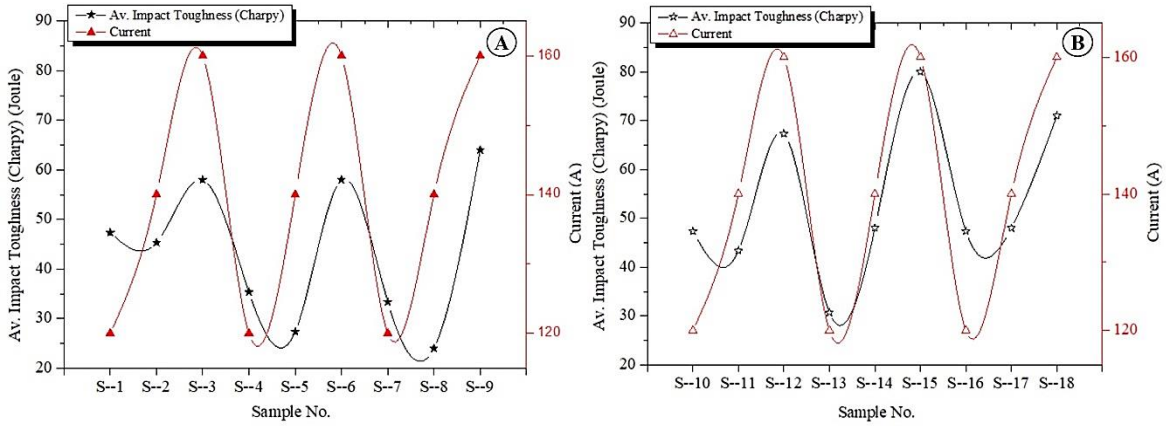


Figure 5.15: Comparison of average toughness and current for the vertical uphill position (a) with Ar shielding (b) with Ar + 2.5 % $H_2$ shielding

### 5.3.4 Taguchi Analysis

The main effect plots for diffusion, average toe angle, and toughness are presented in Fig. 5.16, Fig. 5.17, and Fig. 5.18. The X-axis represents the process parameters, and the Y-axis represents the dilution, average toe angle, and toughness value with the mean line. Fig. 5.16 reveals that Ar + 2.5 % $H_2$ gas with 14 L/min gas flow rate produces maximum dilution and is the most significant factor. Also, maximum current, i.e., 160 A and a flow rate of 12 L/min gas, is the most significant factor in achieving the weld bead's nominal toe angle (Fig. 5.17). The higher current setting is the most favourable factor for achieving a higher impact toughness value (Fig. 5.18).

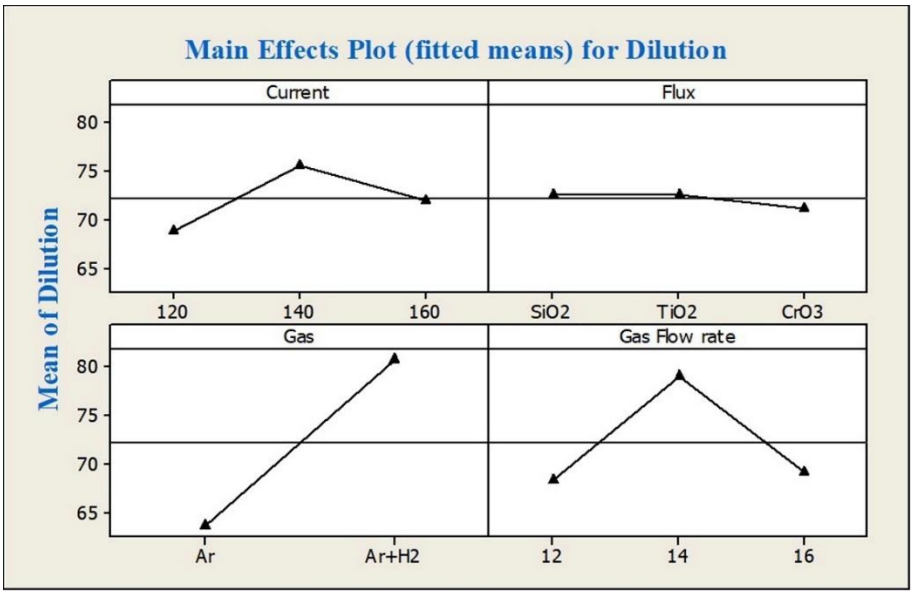


Figure 5.16: Main effect plot for dilution for vertical uphill A-TIG welding

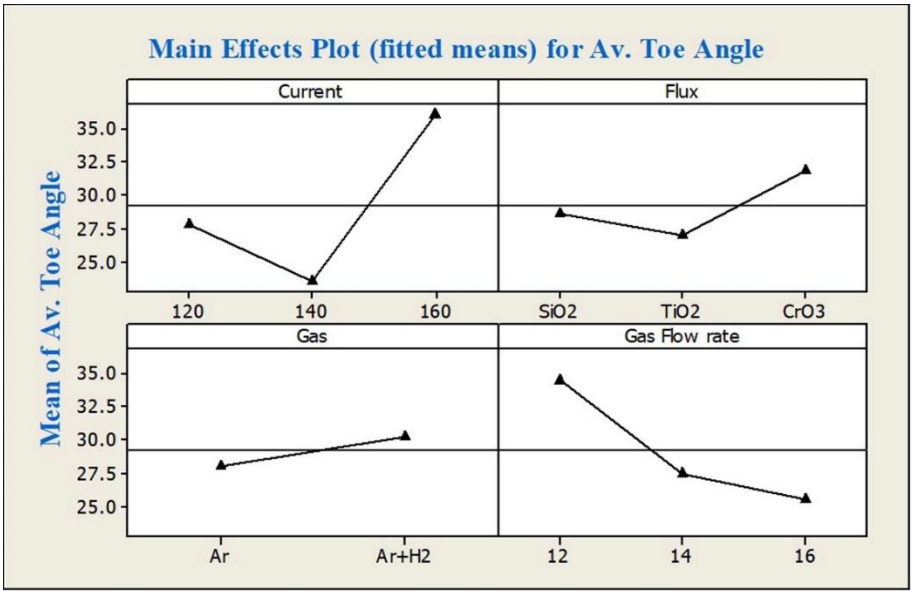


Figure 5.17: Main effect plot for toe angle for vertical uphill A-TIG welding

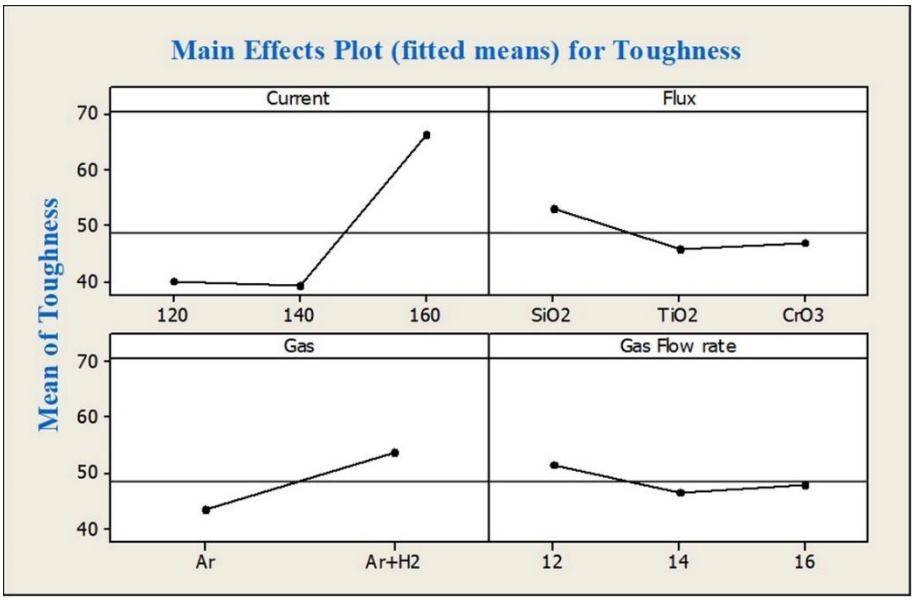


Figure 5.18: Main effect plot for toughness for vertical uphill A-TIG welding

## 5.4 Summary

The feasibility of vertical A – TIG welding was analysed by using different shielding environments. $H_2$ mixed shielding environment results in higher temperature owing to higher enthalpy rate, which leads to undercuts along the sides of the weld bead. It was also observed that A – TIG welding with $H_2$ mixed shielding is difficult to handle at high current due to the higher melting rate. The average penetration area and the dilution rate during vertical/uphill welding position significantly increased with an increase in current and as well as with $H_2$ mixed shielding environment. The simultaneous effect on reinforcement area (i.e., less reinforcement area) was also observed in the case of the $H_2$ mixed shielding environment. Toughness upsurges with high or low current value and $H_2$ mixed shielding with 14 L/min gas flow rate improve the dilution rate. Moderate current, i.e., 140 A, and higher gas flow rate were observed to be the most significant factors that decrease the average toe angle of the weld bead.

# Chapter - 6
# Parametric Study of Submerged Arc Welding (SAW)

## 6.1 Introduction

Submerged arc welding process (SAW) is widely used by heavy fabrication industries like shipbuilding, containers, bridges, pressure vessels, etc., due to the superior quality this process provides for [60, 108, 109]. The arc is hidden under the blanket of granular flux, making it more operator-friendly and is done mainly by semi-automatic or fully automatic machines. It may be performed with a single or multi spool, so a higher deposition rate is possible and is recommended for a long weld, increasing productivity [31, 110]. This process is mostly used for higher thickness and is generally completed by a multi-pass run.

The significant reduction in transverse stress is due to a narrower fusion zone profile which can be attained by using a small diameter electrode as the leading one in case of multiple electrode SAW. [111] Wire and flux combinations make the process suitable to achieve the desirable mechanical properties. Due to the significant content of Cr and Ni in austenitic stainless steel, it offers higher corrosion resistance. The weldability of these steels is very good due to the less sensitization problem [112]. The presence of $CaF_2$ in the flux improves the toughness properties, and $Al_2O_3$ significantly improves the grain refinement, which further enhances the presence of acicular ferrite (***AF***) in the weld metal [113]. Welding parameters are very important, especially when welding is completed in a single pass from the outside and inside surface of the material, like welding pipes by this process. In the case of SAW Pipes, as per ASTM and API standard [114], the welding should be defect-free and pass the radiography test, destructive test and hydrostatic testing (where water pressure is used to check to check any leakage and strength of joint). In the case of SAW pipes, the weld bead geometry plays a significant role, affecting the welding strength. The excess bead height and width of the weld is undesirable. The elements present in the flux in a compound strongly affect the weld metal chemistry [115, 116]. In mild steel welding with SAW, the basicity of flux plays showed a significant relationship in the remaining weight percentage of silicon, and other elements show no correlation with the basicity index of flux [117]. However, current and voltage influenced the element's transfer and weld metal composition [117]. A general trend of decreasing delta ferrite with an increasing cooling rate has been observed [118]. It was also observed that the percentage of $Cr_{eq}$ also influences delta ferrite (δ-ferrite); if it increases, δ -ferrite also increases and vice versa [119].

Many factors, such as current, arc voltage, stick-out, basicity index of flux, polarity, electrode diameter, preheating, joint geometry, welding speed, etc., are responsible for weld bead shape and size. All of these may influence the weld joint's microstructure, micro-hardness, and mechanical properties. Many researchers have carried out extensive research, but limited research has been reported on the use of highly basic flux with a higher basicity index of flux on welding of AISI 304 stainless steel, which is used in numerous applications during mass production.

In this study, the submerged arc welding (SAW) was carried out on thick austenitic stainless steel (ASS) plates (16 mm). Intentionally, this study uses a low pre-set value of current to see the effect of voltage, speed, stick-out and high basicity index flux on weld chemistry, bead geometry, weld quality, and its associated mechanical properties. The outcome from the experiments has been compared with the base metal properties. Taguchi experimental design methodology was used for analysis, and significant parameters have been identified by using the two-way ANOVA. This study has formed the basis for further use during hybrid arc welding (HAW) development.

## 6.2 Material and Method

In the present study, SAW was carried out by making a stringer bead on austenitic stainless steel (AISI 304) plates of 16 mm thick and of size 200 mm × 60 mm. The chemical composition of base metal was checked by optical emission spectroscopy (Foundry Master- Optical emission spectroscope, make: Germany), and the results are provided in Table 6.1.

Table 6.1: Chemical compositions of austenitic stainless steel (AISI 304) plates

| **Percentage Composition (% wt.)** | | | | | | | | | |
|---|---|---|---|---|---|---|---|---|---|
| **C** | **Mn** | **Si** | **Cr** | **Ni** | **S** | **P** | **Mo** | **Cu** | **Nb** |
| 0.03 | 1.14 | 0.47 | 19.4 | 8.26 | 0.01 | 0.04 | 0.15 | 0.237 | 0.008 |
| **Ti** | **Co** | **V** | **Fe** | | | | | | |
| 0.018 | 0.208 | 0.07 | Bal | | | | | | |

Table 6.2: Standard Chemical compositions of SAW filler wire (AISI 308L)

| **Percentage Composition (% wt.)** | | | | | | | | | | | |
|---|---|---|---|---|---|---|---|---|---|---|---|
| **C** | **Mn** | **Si** | **Cr** | **Ni** | **S** | **P** | **Mo** | **Cu** | **Nb** | **V** | **Fe** |
| 0.03 | 1.5 | 1 | 20 | 11 | 0.03 | 0.04 | 0.3 | - | 0.006 | - | Bal |

Before actual experiments, all the workpieces were properly ground by a precision surface grinder (Chevalier FSG 2A 1224). After tacking of side coupon plates and fixing the base plate on the SAW platform, they were cleaned with acetone to remove the residual impurities. Automelt S33 agglomerated flux (Make: Ador Welding Limited), with a basicity index of 3.1 (having a chemical composition, $SiO_2$ + $TiO_2$ – 10 %, $Al_2O_3$ + MnO – 35 %, $CaF_2$ – 50 %)

which conforms to ER 308 L wire (Refer Table 6.2) was used in the present study, and after baking at 300° C for two hours before welding. The flux used in the present study had a grain size between 0.25-1.60 mm. The schematic diagram of the SAW process is also shown in Fig. 6.1(a).

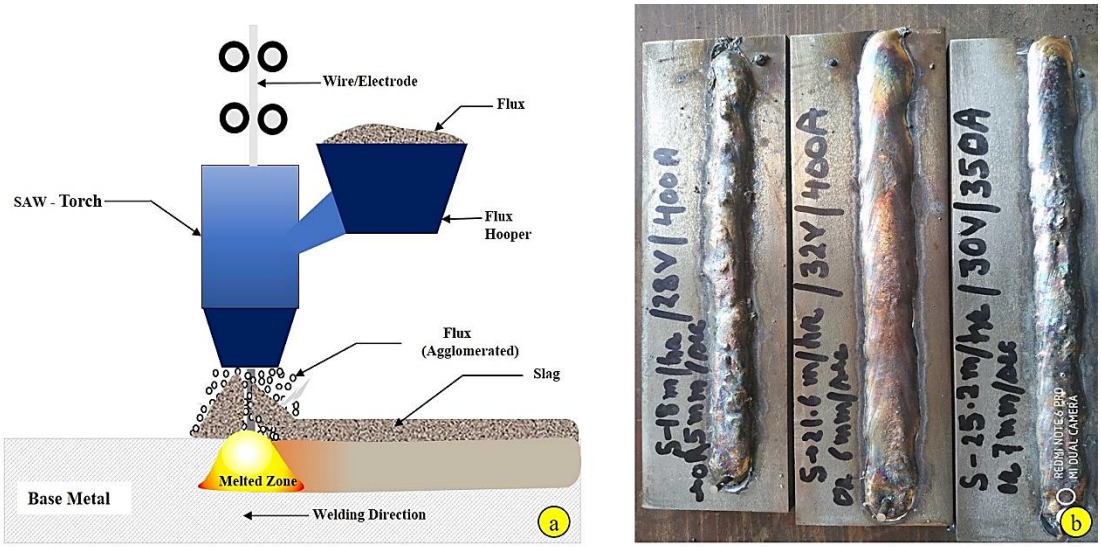


Figure 6.1: (a) Schematic representation of SAW process (b) Trials of SAW

The choice of welding parameter is imperative to achieve the best weld quality, as the weld quality strongly depends on the welding parameters. So, to choose the significant parameters, some initial trials of SAW were performed on the same material, and the trial runs are shown in Fig. 6.1 (b). After the preliminary investigation of SAW, the three prominent factors, (i) voltage (V), (ii) travel speed of trolley (mm/s), and (iii) electrode stick-out (mm), were identified and varied at three levels as given in Table 6.3. The constant parameters are provided in Table 6.5. Taguchi's orthogonal array (L-9) using constant voltage (CV) was used for the study (Table 6.4), and the responses are presented in Table 6.6.

Table 6.3: Variable process parameters and levels for the welding of AISI 304

| S. No. | Parameters | Unit | Levels |
|---|---|---|---|
| 1. | Voltage | V | 30, 32, 34 |
| 2. | Travel Speed | mm/s | 4, 4.5, 5 |
| 3. | Stick-out | mm | 25, 30, 35 |

Table 6.4: L-9 Orthogonal array for SAW of austenitic stainless steel

| Exp. No. | Voltage (V) | Travel Speed (mm/s) | Stick-out (mm) |
|---|---|---|---|
| 1 | 30 | 4.0 | 25 |
| 2 | 30 | 4.5 | 30 |
| 3 | 30 | 5.0 | 35 |
| 4 | 32 | 4.0 | 30 |
| 5 | 32 | 4.5 | 35 |
| 6 | 32 | 5.0 | 25 |
| 7 | 34 | 4.0 | 35 |
| 8 | 34 | 4.5 | 25 |

| | | | |
|---|---|---|---|
| 9 | 34 | 5.0 | 30 |

Table 6.5: Constant parameters for the experiments

| S. No. | Power Source | Constant Parameter | Set value/Type |
|---|---|---|---|
| 1. | SAW<br>(Tornado SAW, M-800)<br>Make: Ador Fontech Ltd. | Polarity | DCEP (Direct current electrode positive) |
| | | Mode | CV (Constant voltage) |
| | | Initial Current Setting | 380 A |
| | | Electrode/Filler wire size | 3.15 mm |
| | | Electrode Specification | AWS A 5.9 ER308L |
| | | Wire Feeding Position | Vertical (90°) |
| | | Flux | Agglomerated (Automelt S33) |

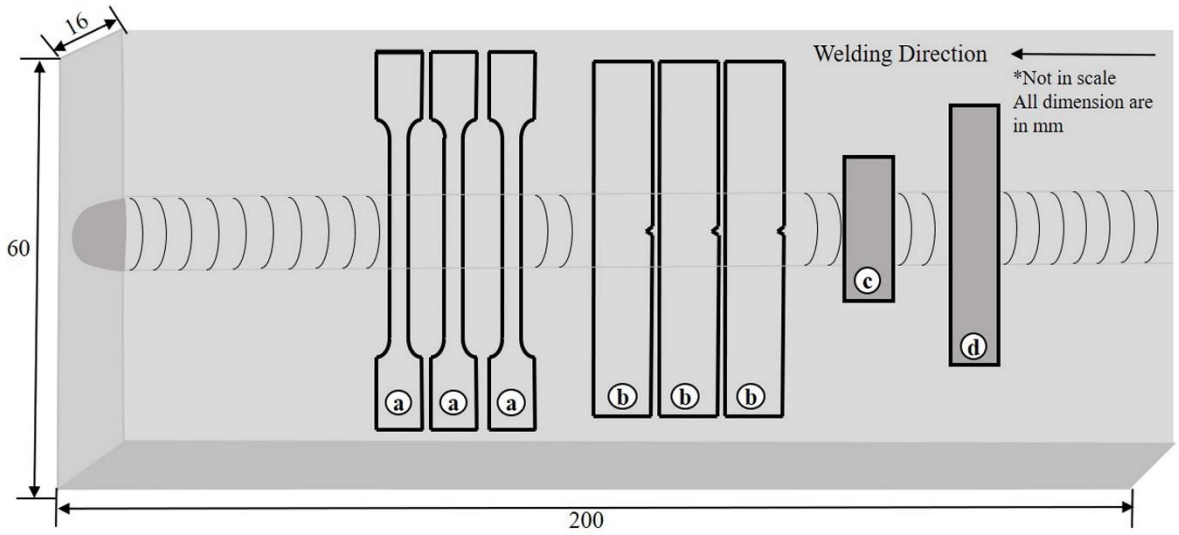


Figure 6.2: Schematic representation of extraction location of samples (a) transverse tensile test (b) transverse impact toughness samples (c) microstructural analysis, and (d) for microhardness

After trials on 200 mm long and 59-60 mm-wide plates, samples were taken for further study. The weld samples were cut across the weld bead (cut transversally) for microstructure analysis, micro-hardness, tensile, and toughness test (Charpy), as shown in Fig. 6.2. For determining bead geometry parameters, the cut samples were further prepared by grinding, polishing, and etching for metallurgical examination. To study the microstructure and depth of penetration (DoP), a metallurgical and a measuring microscope with 1 µm least count (Axio-Scope A1 of Carl Zeiss, Germany) was used. Out of nine experiments, the sample that achieves maximum DoP was selected to determine the mechanical properties, namely toughness (Charpy) and tensile strength. The bead geometry parameters, i.e., reinforcement height and area of reinforcement and dilution area, were measured by image-J software and mentioned in Table 6.6. The change in the chemical composition of weld metal was also analysed for all the weld coupons by optical emission spectroscopy. Finally, Microhardness was measured in both vertical and horizontal directions.

## 6.3 Results and Analysis

### 6.3.1 Effect of Welding Variables on Bead Shape and Appearance

All weld coupons were first analysed by visual inspection, and from the first look of Fig. 6.3, the weld coupon SAW-1, 2, and 3 (welded with 30 V) showed a poor bead appearance/uneven bead with porosity. The main cause of poor bead appearance and porosity may be the welding speed because, at higher speed, heat input per unit length decreases, and the fast-cooling rate of weld-metal provide less time for the escape of gases. The samples SAW - 4, 5, and 6 (welded with 32 V) appeared significantly better as compared to SAW - 1, 2, 3. Carefully examination of weld bead surface showed some amount of porosity (Fig. 6.3) in SAW- 6 (welded with maximum speed, i.e., 5 mm/s), and less porosity was found in SAW- 5 coupon (welded with medium speed). Minimum porosity was observed in the SAW – 4 (welded with minimum speed 4 mm/s speed). More bead height was observed in the case of SAW - 1 to SAW – 6 weld coupons (Table 6.5 and Fig. 6.4) due to low voltage. In case of SAW – 7 to SAW – 9 coupons, weld beads were found smooth with less porosity in the SAW 7 and SAW 8 (Fig. 6.3).


Figure 6.3: Weld-bead appearance of SAW coupons (1 To 9)

### 6.3.2 Weld Profile Measurement and analysis

The responses related to bead geometry parameters is provided in Table 6.6. The penetration increased when heat input increased, affecting the dilution. Higher voltage and low-speed help achieve the average toe angle measured from both sides of the weld. Better butt joint properties of submerged arc welded joint are possible if it satisfies the following condition.

$$\mathbf{R_w / P \geq 2, \text{ and } R_w / R_h \geq 6}$$

Where $\mathbf{R_w}$ is the reinforcement width, **P** is the penetration, and $\mathbf{R_h}$ stands for reinforcement height. Only trial no. 7 had justified the bead geometry relationship, i.e., $\mathbf{R_w/P \geq 2}$ **and** $\mathbf{R_w/R_h \geq 6}$.

Table 6.6: Orthogonal array for SAW and responses

| Exp No. | Voltage (V) | Travel Speed (mm/s) | Stick -out (mm) | DoP (mm) | Dilution (%) | Heat Input (KJ/mm) | Reinf. Height (mm) | Reinf. Width (mm) | Av. Toe Angle (°) | $R_w/P$ | $R_w/R_h$ |
|---|---|---|---|---|---|---|---|---|---|---|---|
| 1 | 30 | 4.0 | 25 | 5.88 | 42.06 | 2.85 | 5.47 | 17.32 | 101.20 | 2.94 | 3.16 |
| 2 | 30 | 4.5 | 30 | 5.39 | 47.32 | 2.53 | 5.21 | 15.90 | 56.42 | 2.94 | 2.90 |
| 3 | 30 | 5.0 | 35 | 4.57 | 47.61 | 2.28 | 4.15 | 16.55 | 49.65 | 3.62 | 3.98 |
| 4 | 32 | 4.0 | 30 | 6.67 | 48.15 | 3.04 | 5.22 | 19.60 | 70.03 | 2.93 | 3.75 |
| 5 | 32 | 4.5 | 35 | 5.75 | 50.26 | 2.70 | 4.65 | 16.83 | 63.72 | 2.92 | 3.61 |
| 6 | 32 | 5.0 | 25 | 5.88 | 47.56 | 2.43 | 4.82 | 20.13 | 50.54 | 3.42 | 4.17 |
| 7 | 34 | 4.0 | 35 | 8.00 | 61.08 | 3.23 | 3.12 | 20.35 | 54.54 | 2.54 | 6.52 |
| 8 | 34 | 4.5 | 25 | 6.92 | 56.95 | 2.87 | 4.03 | 20.22 | 50.82 | 2.92 | 5.01 |
| 9 | 34 | 5.0 | 30 | 5.38 | 54.52 | 2.58 | 3.81 | 21.62 | 43.62 | 4.01 | 5.67 |

### 6.3.3 Relationship between Heat input, Voltage, and Average toe angle

The bead geometry relationship parameter needs to be controlled through process parameters for higher joint strength. From Fig. 6.4, the average toe angle shows a significant relationship with heat input. It was analysed that the average toe angle also decreases when voltage increases. The low toe angle confirms that the welding will have good mechanical properties. The weld travel speed may also influence the desired mechanical properties because it influences the bead geometry relationship.

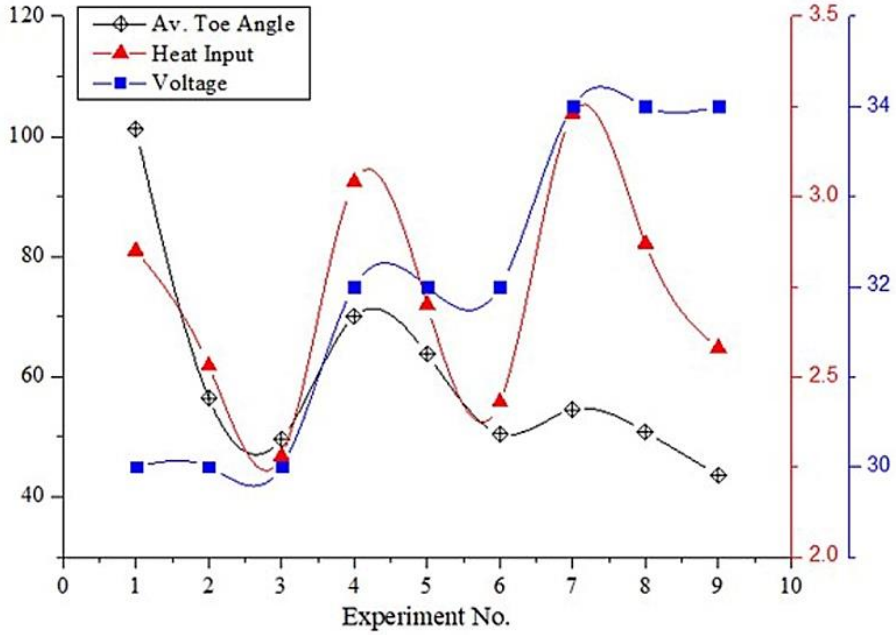


Figure 6.4: Relationship between voltage, heat input, and average toe angle of SAW samples

### 6.3.4 Macrostructure and Microstructure Analysis

From Fig. 6.5, SAW – 1 to SAW – 9 shows that the directional solidification pattern of delta ferrite is mostly emerging from the parent metal, and all columnar grains show an upward pattern (approximately making 45$^{o}$ to the weld centre line in the opposite direction). So, their solidification pattern is less prone to cracking. One slag inclusion/cavity was observed in the case of the extracted sample of coupon SAW – 1 (Fig. 6.5).

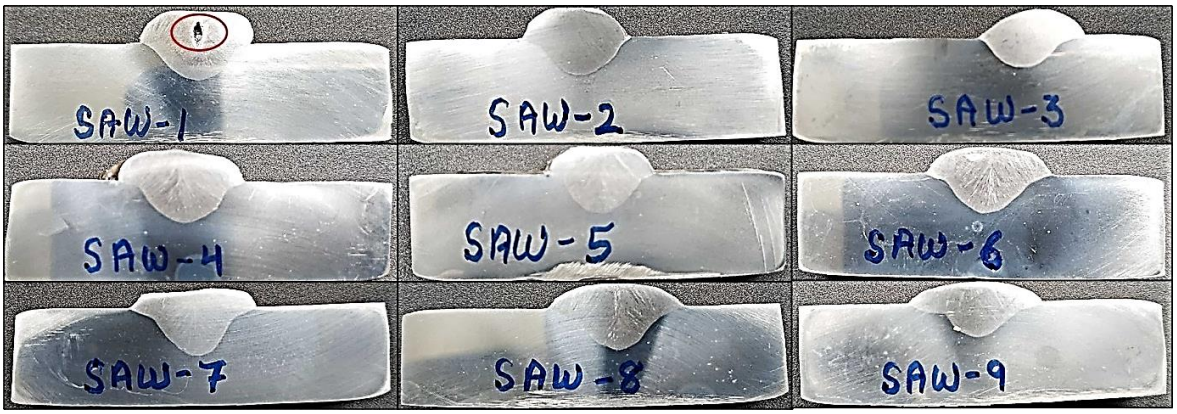


Figure 6.5: Macrostructure of SAW coupons (1 To 9)

The microstructures of different weld zones are shown in Fig. 6.6, Fig. 6.7, and Fig. 6.8 (SAW – 1 To SAW – 9). It exhibited a mixed morphology of retained ferrite, such as skeletal delta ferrites, lacy ferrite, and vermicular ferrite in the upper central region of the fusion zone. Figure 6.6 shows the microstructure of samples that were welded at 30 **V at** different welding speeds, i.e., 4, 4.5, and 5 mm/s. In the upper central part of the fusion zone, no such significant difference was observed in the resulting pattern. All the samples of 30 **V** of different speed welded samples have a lacy ferrite structure matrix in the central zone. The lathy ferrite was found in the root and interface regions with skeletal delta ferrite.

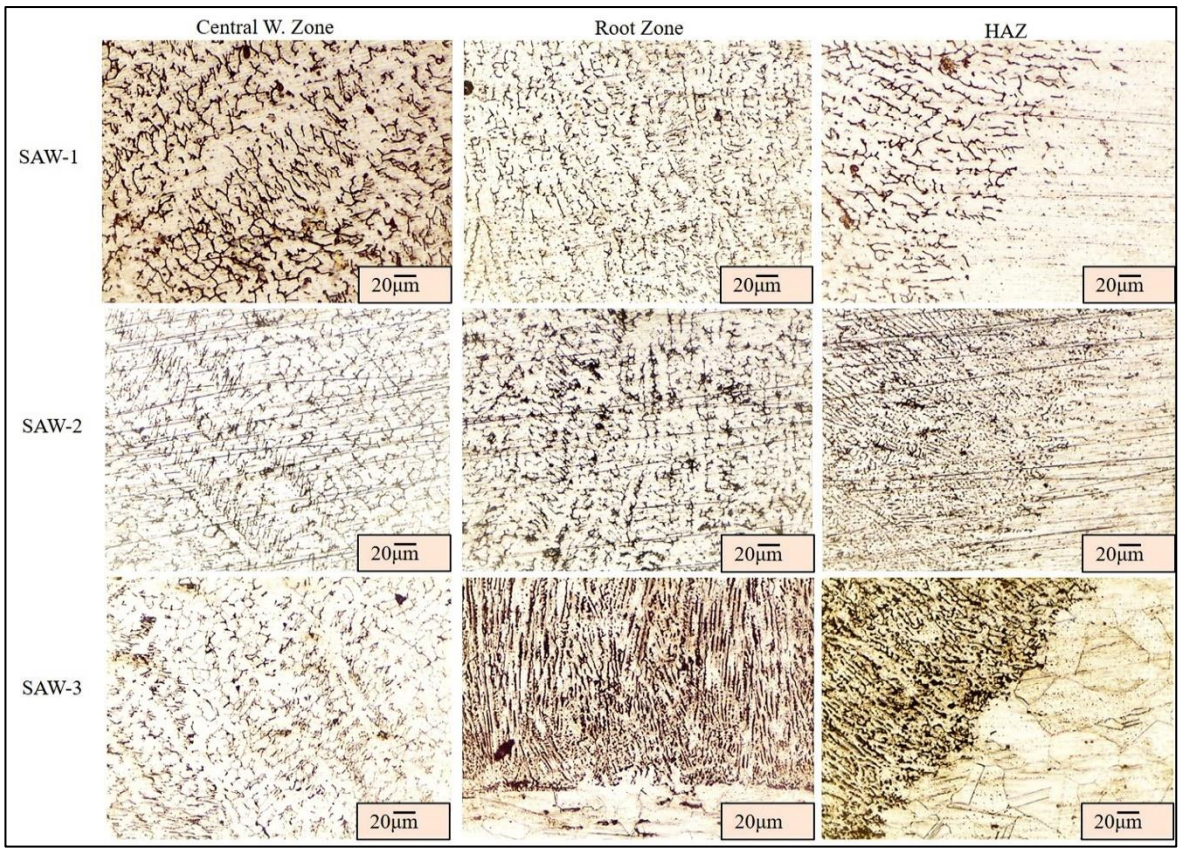


Figure 6.6: Microstructure of upper central region, root and HAZ of SAW coupons (1 To 3) which are welded at 30 **V**

The only difference in percentage concentration of ferrite content in the fusion zone may be possible due to variation of the heat input and associated cooling rate. The microstructure observed that the sample which was welded at 5 mm/s welding speed has more ferrite content due to the short time available for the transformation of delta ferrite to austenite.

Similarly, the same microstructure pattern was also detected in the case of SAW using 32 **V** and 34 **V** at different welding speeds (Fig. 6.7 and Fig 6.8). No significant change in the resultant microstructure was observed.

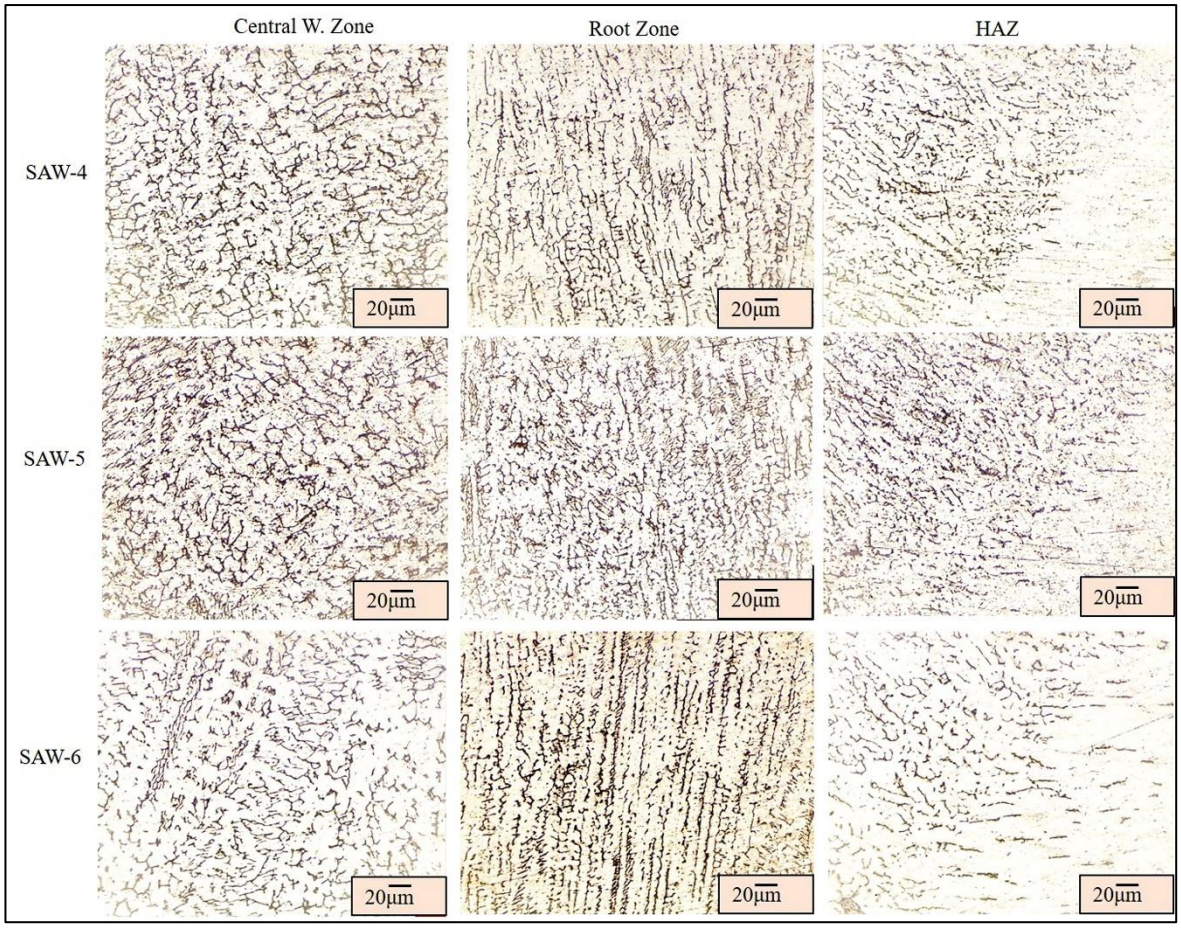


Figure 6.7: Microstructure of upper central region, root and HAZ of SAW coupons (4 To 6) which are welded at 32 **V**

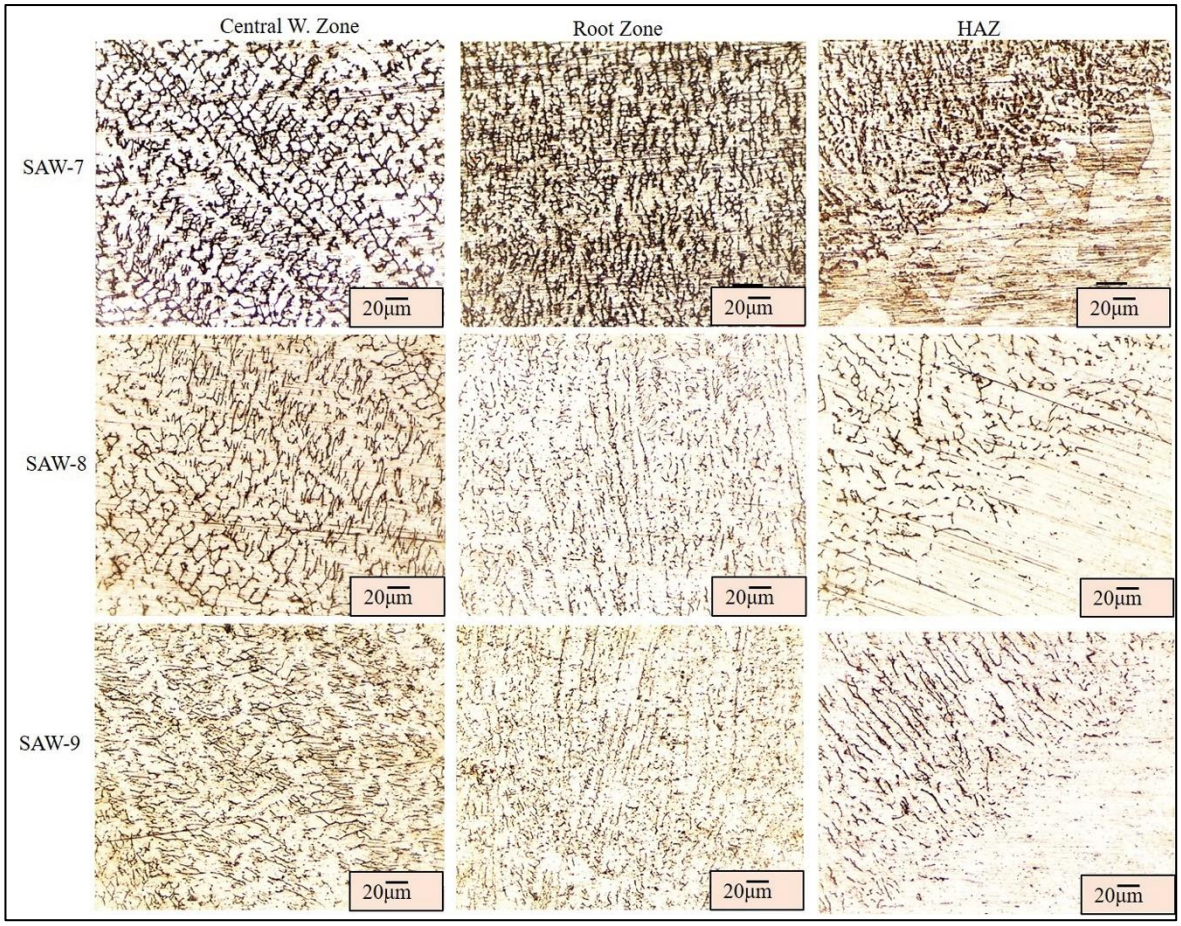


Figure 6.8: Microstructure of upper central region, root and HAZ of SAW coupons (7 To 9)

### 6.3.5 Effect of Heat Input on the Chemical Composition and the Ratio of $Cr_{eq}/Ni_{eq}$

The variation of heat input and wire-flux combination result in the variation of some alloying elements. The test samples of spectroscopy are shown in Fig. 6.9 and the result of a change in the percentage of the element are presented in Fig. 6.10.

Figure 6.9: Tested sample of spectroscopy

Small variation was found in the "Ni" percentage in the welded samples. Still, it was higher than the parent metal, and this variation may have been due to the dilution rate owing to the higher percentage present in the filler metal. The variation of the "Cr" percentage was found very little in all specimens. Similarly, the variation of "Mo" and "Si" percentages was found less in both cases than the filler metal percentage. In comparison, the retained content of "C" and "Mn" elements shows a decreasing trend with the increase of arc voltage and dilution rate.

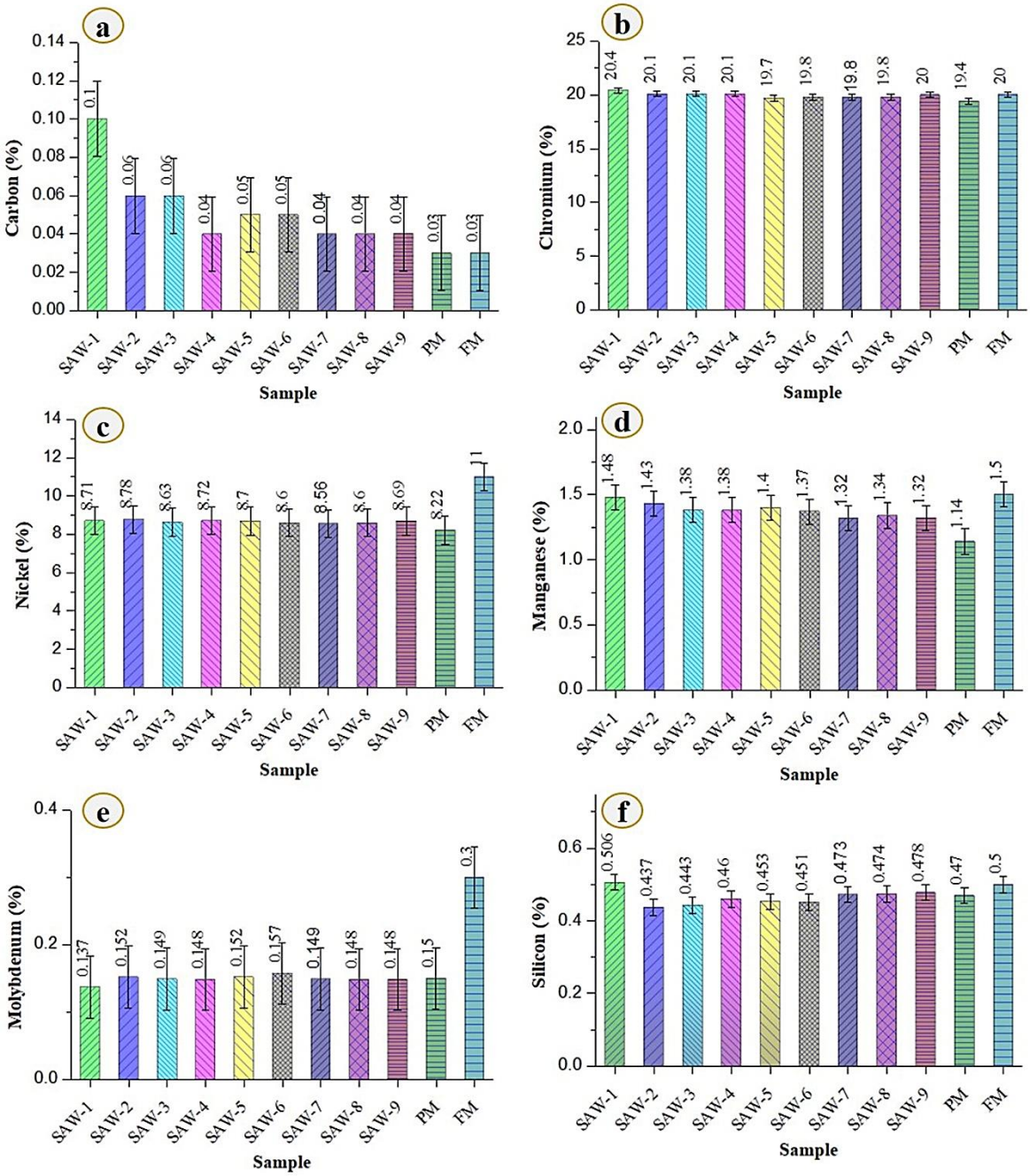


Figure 6.10: Comparison of essential elements (a) C, (b) Cr, (c) Ni, (d) Mn, (e) Mo and (f) Si (%) of the base metal, filler metals and fusion zone of all weld coupons

In welding of austenitic stainless steels, the resultant delta (δ) ferrite content significantly influences the chemistry of the fusion zone by decomposing it to a brittle phase called the sigma phase, especially at higher temperatures. [120] The delta (δ) ferrite content may be evaluated from the different constitution diagrams like Schaeffler, Delong, and WRC – 92 diagrams. In the present study, no nitrogen is found in the base metal and filler metal and the resultant chemical composition of the fusion zone, so the delta ferrite content can be predicted and evaluated by plotting the $Cr_{eq}$ and $Ni_{eq}$ on Scheffler diagram. Fig. 6.11 shows that the samples ferrite percentage range is from 8 % to 15 %.

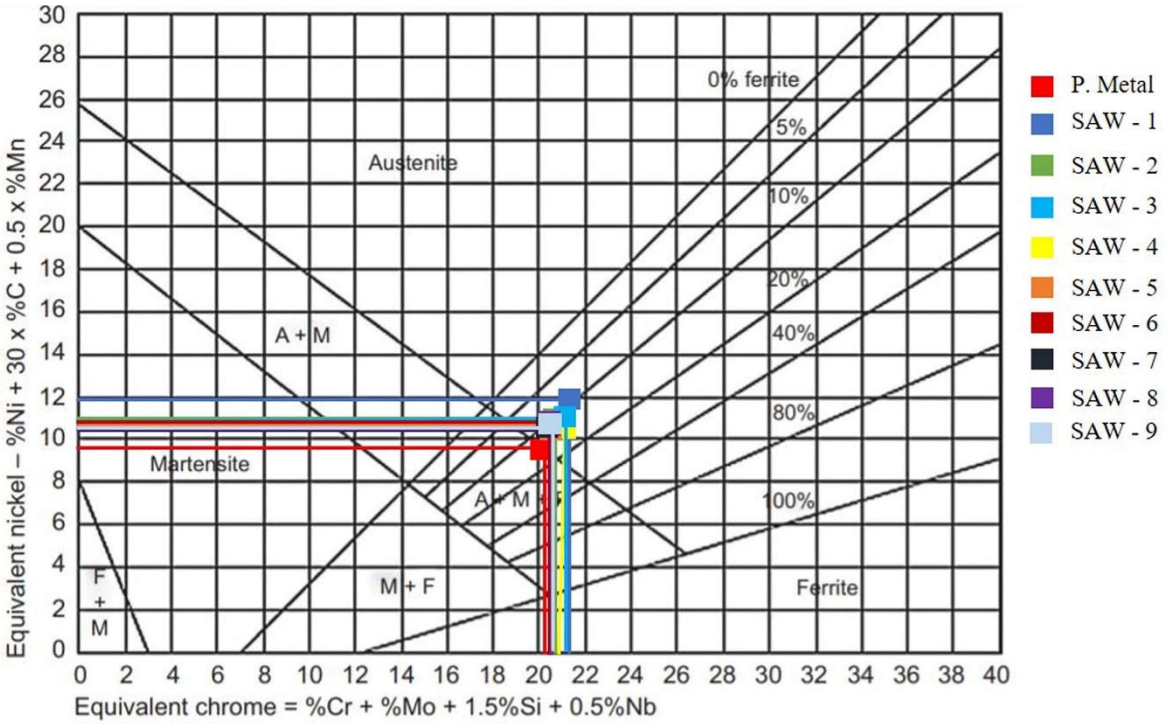


Figure 6.11: Plot of $Cr_{eq}$ and $Ni_{eq}$ on Scheffler diagram

From Fig. 6.12, it can be analysed that the ratio of $Cr_{eq}/Ni_{eq}$ increases with the increase in the voltage, followed by speed. If the ratio of $Cr_{eq}/Ni_{eq} < 1.5$, the mode of solidification will be austenitic or the austenitic-ferritic. Similarly, when the ratio is between 1.5 - 2.0, the mode solidification will be ferritic – austenite. Whereas, when the $Cr_{eq}/Ni_{eq}$ ratio is > 2.0, the mode of solidification will be ferritic (mode IV) [121]. In the present study, the ratio of $Cr_{eq}/Ni_{eq}$ is between1.5 - 2.0, so the solidification mode is ferritic – austenite.

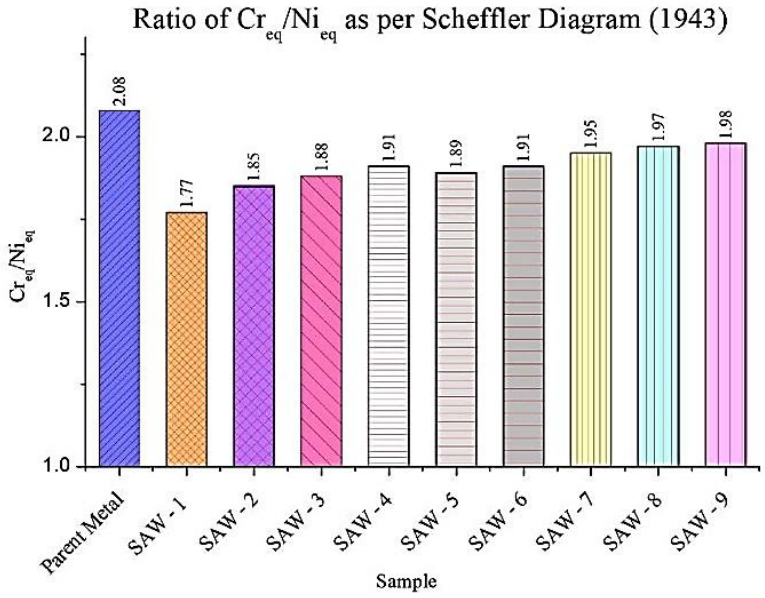


Figure 6.12: Plot of the calculated $Cr_{eq}/Ni_{eq}$ ratio

### 6.3.5 Effect of Voltage (V) and Welding speed on Impact Toughness

In this study, SAW – 7 samples achieved the maximum depth of penetration (DoP). So, three specimens from parent metal and three samples from the SAW-7 coupon (maximum DoP) were cut out for both Charpy and tensile test. The weld coupon's start and end parts (1") were treated as rejected parts for all the welded coupons. The non-standard Charpy 'V' notch test specimens of transverse weld specimen (for the welded samples) and the base plate were cut out using wire-cut EDM. Three samples were taken from the SAW – '7' coupon, which had maximum penetration among all the specimens and the other three samples were cut out from the parent metal. The term non-standard refers to the position of the extracted sample to find the influence of the variable parameters on the related mechanical properties. The result for toughness is presented in Table 6.7. The schematic positions of extracted Charpy samples and the notch position is shown in Fig. 6.13. Notch positions were kept perpendicular to the longitudinal direction of the weld bead (Fig. 6.13). It shows the specimen was extracted from a region covering half of the weld penetration profile and half the area covering the HAZ and parent metal area.


Figure 6.13: (A) Extracted specimens show different regions, and position, notch position and dimensions (B) Parent metals Charpy specimens and (C) SAW – 7 specimens

The extracted specimens were tested as per the ASTM E23 standard at room temperature (30°C) after confirming the notch size and position of the notch. The extracted specimens for the Charpy test are shown in Fig. 6.13 (B) and Fig. 6.13 (C). A comparison of the resultant value of toughness (Joules) is presented in Fig. 6.14 (a). The average toughness value for the parent metal was found as 152 **J**, whereas in SAW – '7' coupon samples were found to be 158.33 **J**. It suggested that the welding heat improves the toughness owing to small grains during recrystallization. The maximum toughness was found in sample number '3' of the SAW – '7' coupon due to the maximum region/area of penetration covered by the penetrating region available for the test. In the case of parent metal (AISI 304), the average toughness value (153.33 **J**) is in the area below the notch, which is equal to 80 $mm^2$ (10 mm × 8 mm). In the present study, the area available below the DoP for SAW – 7 (1) sample was measured and found equal to 38.4 $mm^2$ and the rest 41.6 $mm^2$ area left for the FZ, HAZ and for the parent metal (unaffected area). The toughness observed for this sample was 155 **J**. Similarly, for the SAW – 7 (2) sample, the area measured up to DoP was evaluated and measured as 38.1 $mm^{2,}$ and the rest was 41.9 $mm^2$. The difference of area of sample SAW – 7 (2) from the sample SAW – 7 (1) is very small, so it causes a minimum difference in toughness. In the SAW – 7 (3) sample, the area up to DoP was measured as 43.4 mm2, and the rest as 36.6 $mm^2$. From these measurements, the maximum area (up to DoP) of the fusion zone was available in the case of sample SAW – 7 (3), which took maximum energy to break it. Hence, the heat of conventional SAW improves the toughness, and it justified the increased impact toughness in the case of sample SAW – 7 (3) as shown in Fig. 6.13. The dotted lines in Fig. 6.14 (c) show the fusion zone depth in the extracted samples, and it was measured by a measuring microscope.

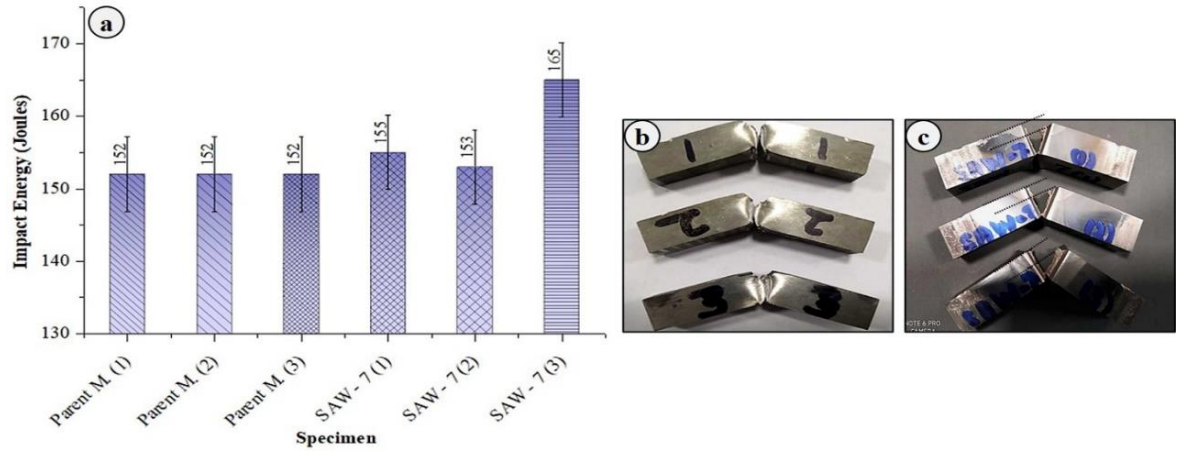


Figure 6.14: (a) Comparison of Impact toughness of base metal and SAW – '7' specimens (b) Tested parent metals specimens and (c) Tested Charpy SAW – '7' specimens

From the result of the toughness test (Fig. 6.14 a), it can be said that impact toughness increases at higher heat input owing to slow welding speed. Because at low-speed, penetration increases, and it also influences the grain refinement [122]. So, in the present study, higher penetration helps to increase the toughness. Moreover, the change in the available area of fusion profile in the toughness sample results in different toughness values of the SAW – '7'.

### 6.3.5 Effect of Voltage (V) and Welding speed on Tensile Strength

The tensile tests were performed for the as-received parent metal, and the sample which had the maximum DoP after the SAW process was SAW – '7'. Three samples were extracted from each sample/weld coupon for this test. The tensile test was conducted using TINIUS OLSEN (Model HK50S) machine using a standard procedure (ASTM E8M). The **2 mm/min** crosshead velocity was employed during all the tensile tests. The samples were extracted using wire-cut EDM, and the samples of SAW – '7' were polished and etched by using 'carpenter etchant' to show the region of fusion profile and are shown in Fig. 6.15. The detailed dimensions of the tensile test specimens are shown in Fig. 6.15 (a). The measurements of the fabricated tensile samples were completed as per the standard. The subsize tensile specimen gauge length was maintained as per the standard (ASTM E8M) without compromising the proper grip. As the available width of the base metal plate was in the range of 58 to 60 mm, so done accordingly. All the tensile tests were performed at the ambient temperature ensuring proper clamping.

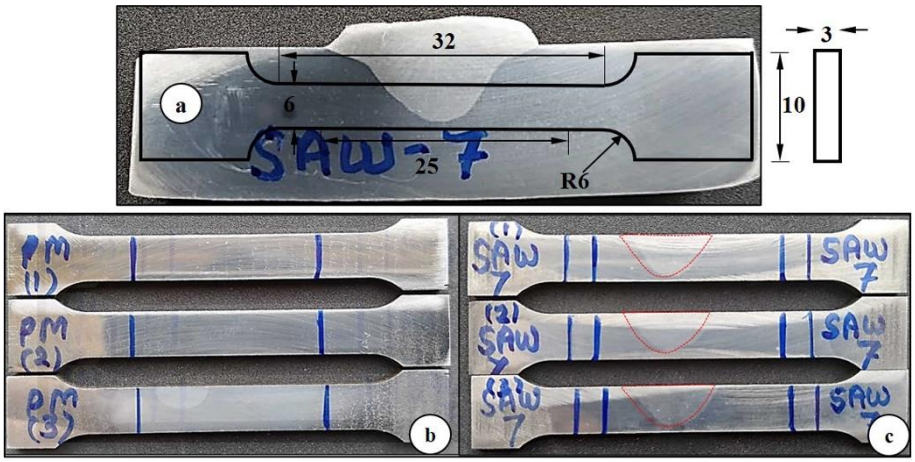


Figure 6.15: (a) Schematic illustration and location of subsize tensile specimen (b) Extracted parent metals tensile specimens and (c) Extracted specimens from SAW – '7' coupon

The fusion zone profile is visible in Fig. 6.15 (c) after polishing and etching of samples. The tensile test results in the form of tensile stress – tensile strain are presented in Fig. 6.16, and the mechanical properties are summarized in Table 6.7. The tensile test result revealed that the

parent metal performed better than the conventional SAW weldment under tensile loading (Fig. 6.16). For SAW weldments (SAW – '7' coupon), the average UTS (Ultimate Tensile Strength), average YS (Yield Strength), and the average elongation were obtained as 677.33 **MPa**, 425 **MPa**, and 78.63 %, respectively (Table 6.7). Higher values were obtained for the parent metal (UTS = 739.66 MPa, YS = 446.66 MPa and elongation = 108.16 %).

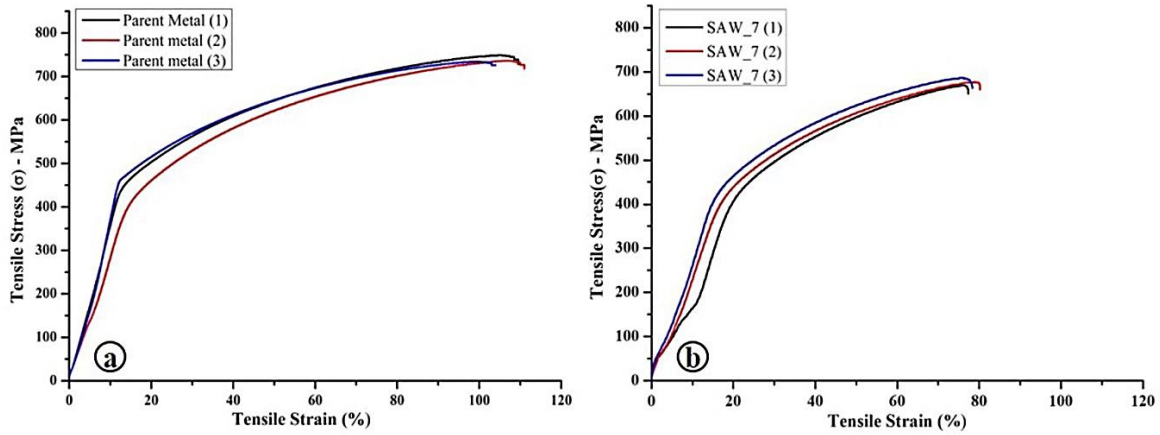


Figure 6.16: Tensile stress v/s tensile strain curve for both (a) Parent metal and (b) SAW – '7'

It was observed that the fracture took place within the gauge length in the case of the parent metal, whereas in SAW – '7' coupon samples, the fracture took place also within the gauge length but from the fusion zone (Fig. 6.17 B). The zone of fracture is encircled with yellow colour. This may be due to the presence of coarse grain structure in the fusion zone. The fusion zone of the SAW – '7' sample has a columnar dendrite structure, and the orientation of the dendrites is approximately 45$^{o}$ to the vertical centre axis. It was also observed that the parent metal is more ductile than the welded sample owing to maximum percentage elongation (Fig. 6.17). The gauge length of the transverse tensile specimen of the SAW – '7' coupon has different zones like fusion, HAZ, and the parent metal, so a difference in strain was observed in this case. In other words, it obtained less strain value than the base metal.

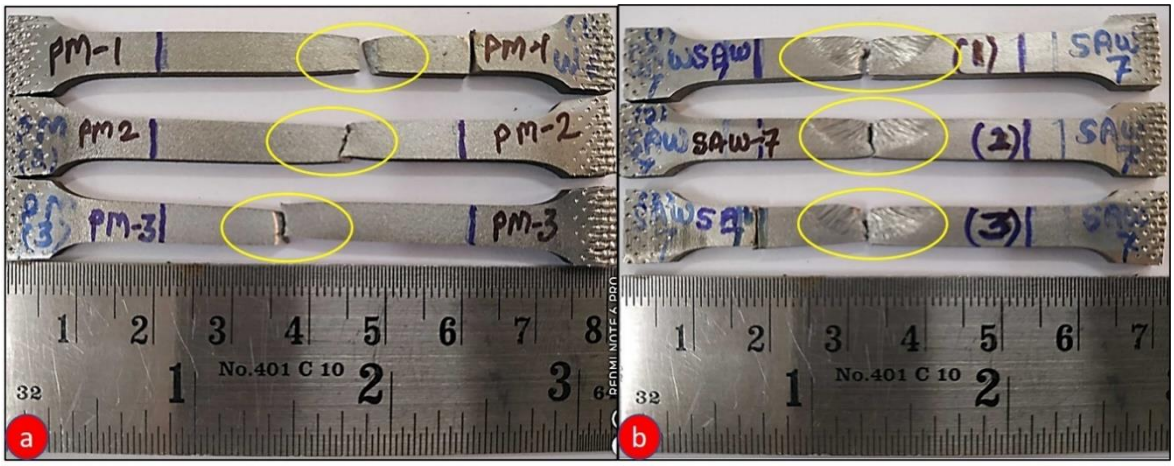


Figure 6.17: Fractured/Tested samples (a) Parent metal and (b) SAW – '7'

Table 6.7: Mechanical properties of SAW

| S. No. | | Specimen | Impact Energy (Joule) | Average Impact Toughness (Joule) | Tensile Strength (MPa) | Average Tensile Strength (MPa) | Yield Strength (MPa) | Average Yield Strength (MPa) | Percentage Elongation (%) |
|---|---|---|---|---|---|---|---|---|---|
| 1. | I. | Parent Metal | 152 | 152 | 749 | 739.66 | 460 | 446.66 | 109.5 |
| | II. | Parent Metal | 152 | | 736 | | 450 | | 111 |
| | III. | Parent Metal | 152 | | 734 | | 430 | | 104 |
| 2. | I. | SAW – 7 | 155 | 157 | 669 | 677.33 | 420 | 410 | 77.4 |
| | II. | SAW – 7 | 153 | | 677 | | 410 | | 80.2 |
| | III. | SAW – 7 | 165 | | 686 | | 400 | | 78.3 |

### 6.3.6 Fractography Analysis

The SEM micrographs of tensile strength tested samples of parent metal (1 No. sample) and SAW – 7 (2 No. sample) were studied to understand the type of fracture-related morphology, and the same is presented in Fig. 6.18. Small size impurities are present in the case of SAW – 7 samples (Fig. 6.18 C), whereas no impurity was observed in the parent metal sample at lower magnification. Higher magnification micrographs of both parent metal and SAW – 7 samples revealed dimples [123] and microvoids of different sizes. The flawless fibrous microstructure (Fig. 6.18 B) had a dimple of 2 – 4 μm, revealing that the parent metal had a ductile fracture, which is also validated by Fig. 6.16 it has more value of strain. On the other hand, SAW – 7 also has a uniform dimple structure, proving that it had undergone a ductile fracture. But some impurities were also observed in the toughness specimen, which is shown in Fig. 6.18 C.

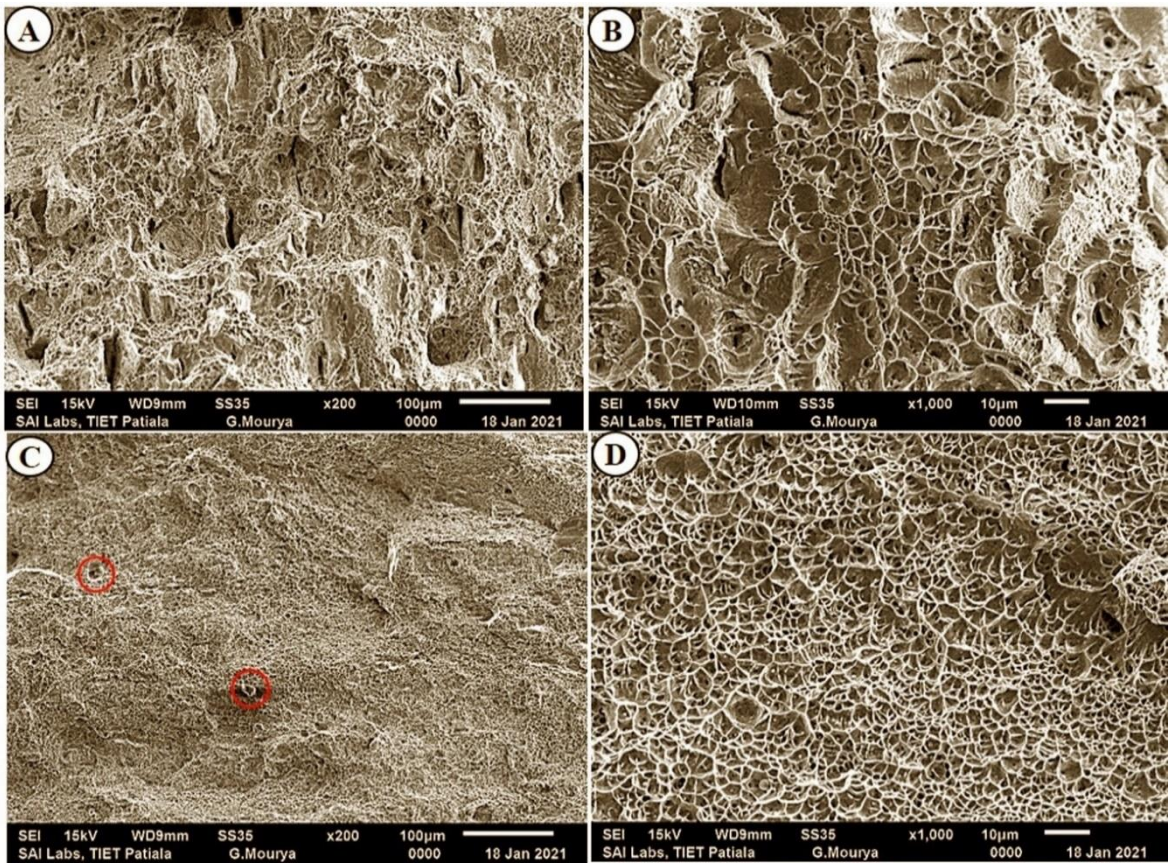


Figure 6.18: SEM micrographs of tensile test fractured surface with different magnification and at a different location: (A) and (B) Base metal (AISI 304 steel), (C) and (D) SAW – 7 samples

The fractured surface of the toughness sample (iii sample) of the SAW – 7 coupon (Fig. 6.19) shows the presence of dimples and a cavity, whereas no cavity was found in the parent metal specimen. The presence of austenite at the grain boundaries is also visible in Fig. 6.19, which justified that the toughness of this sample would be high, and the result of toughness values are also presented in the bar graph of Fig. 6.14 A.

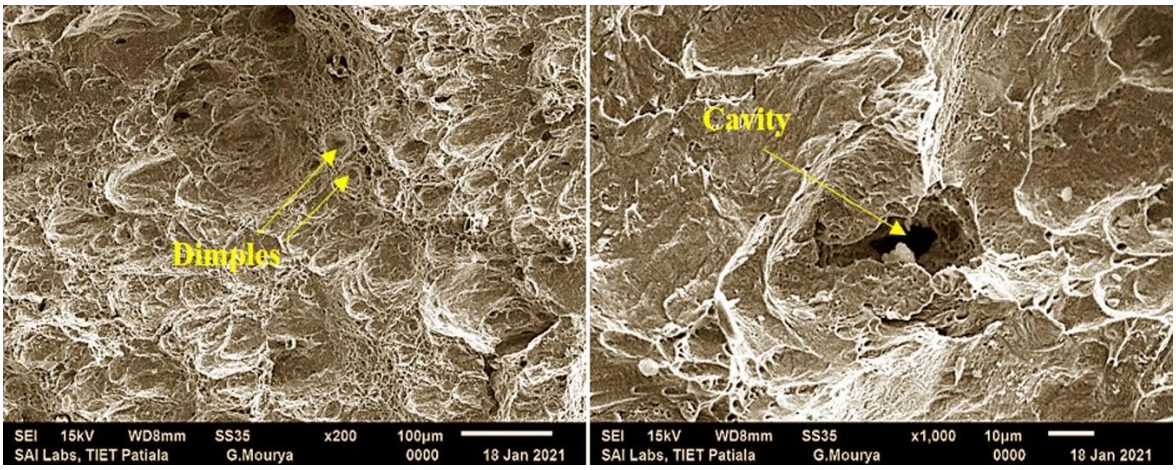


Figure 6.19: SEM micrographs of toughness test fractured surface of SAW – 7 (Sample No. 3) of different magnification at a different location

### 6.3.7 EDS Analysis

The EDS analysis of the toughness sample for SAW – 7 is presented below. The highlighted region spectrum of a fractured SAW – 7 sample specimen is shown in Fig. 6.20.

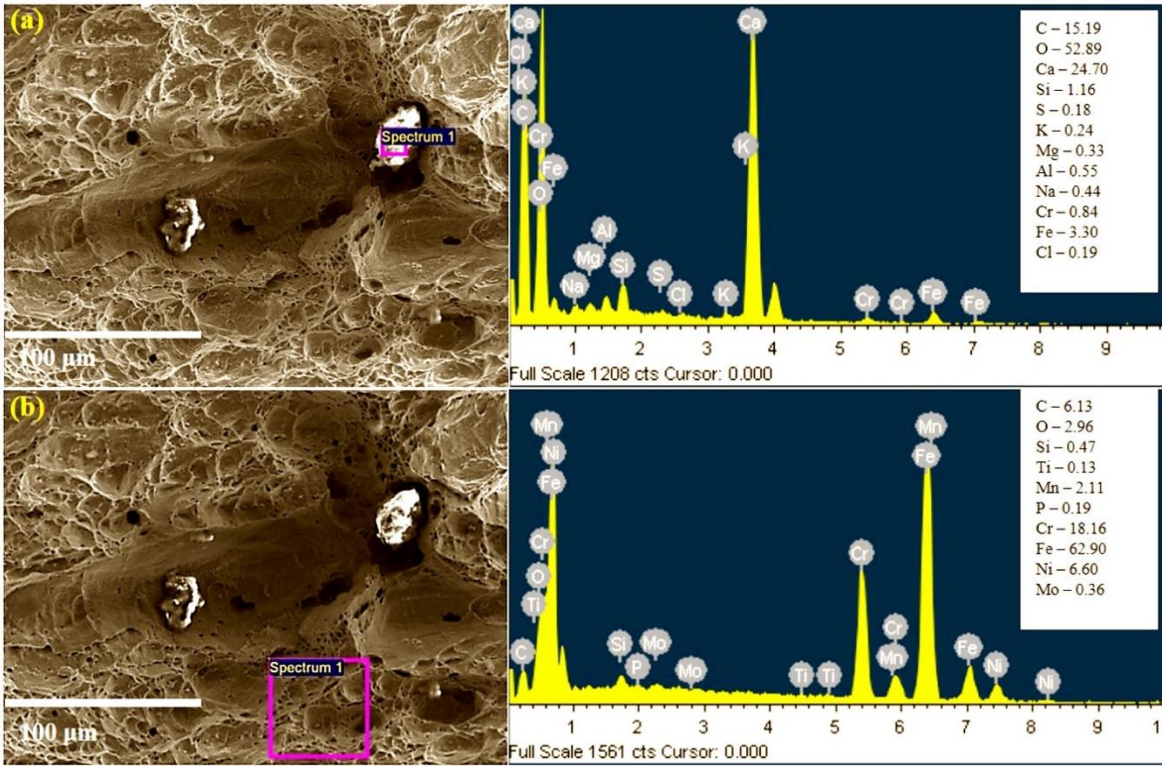


Figure 6.20: SEM micrographs with EDS spectrum of toughness test fractured surface of SAW – 7 sample

Another SEM micrograph of a different region of toughness sample of SAW -7 (Fig. 6.20 'a' and 'b') clearly shows the inclusion took place in the weld metal. The EDS analysis (Fig. 6.20 'a') was performed on the inclusion, and the spectrum result revealed a high weight percentage of oxygen which is an oxide. The other spectrum was taken adjacent to this inclusion representing the composition of AISI 304 stainless steel.

### 6.3.8 Microhardness Analysis

The Vickers hardness of all the weld coupons was measured along the X-X direction (line across the width), and Y-Y movement (Line across the thickness) is shown in Fig. 6.21. The microhardness test was performed below 1.5 mm distance from the top surface of the parent metal and at a constant distance of 0.5 mm from each point in case of X – X direction. Similarly, in the case of the Y – Y direction, the microhardness point crossed the thickness of the weld profile.

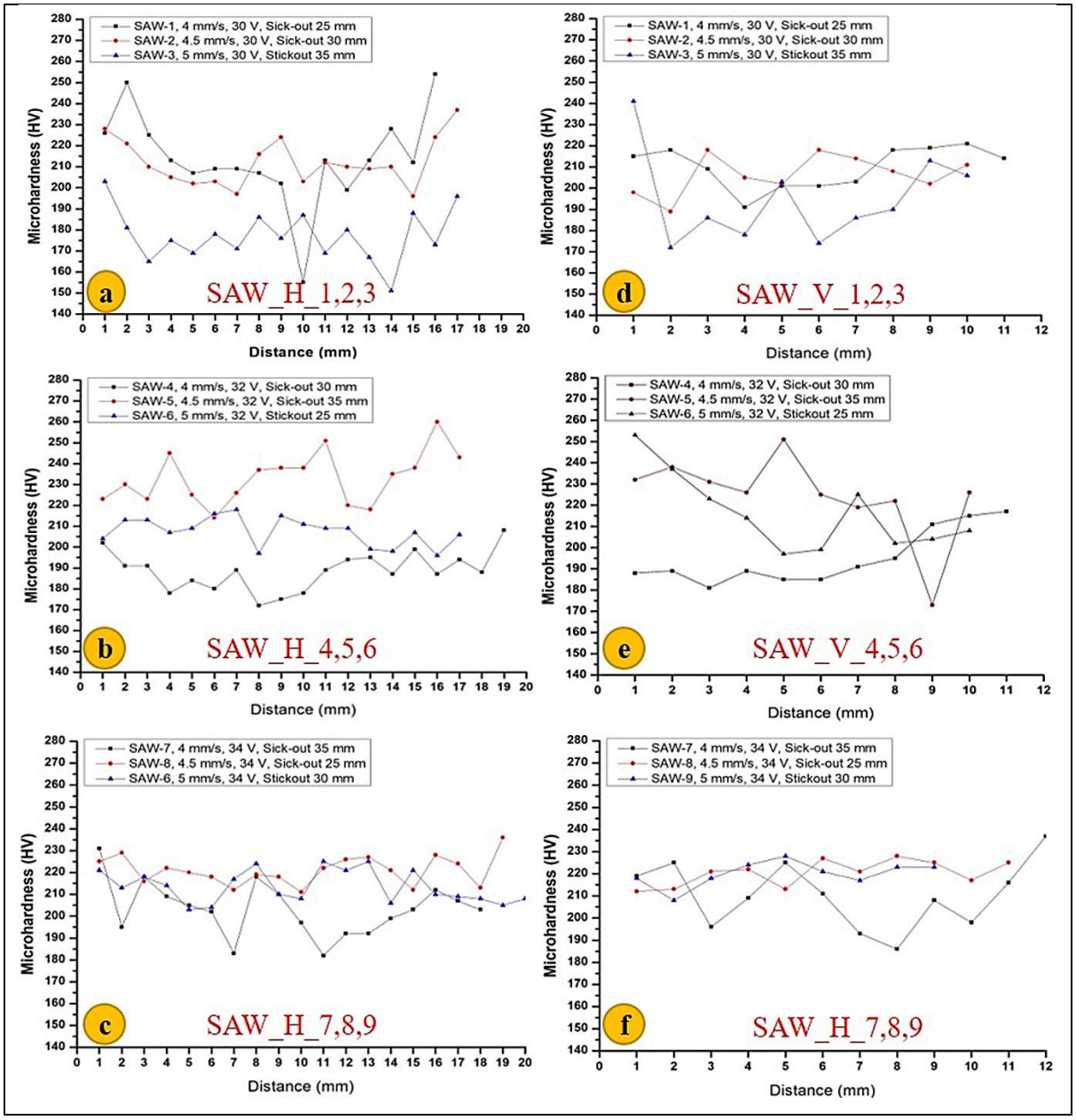


Figure 6.21: Microhardness distribution plot (a), (b) and (c) for X – X direction and (d), (e) and (f) for Y – Y direction

The Vickers hardness of the base metal was found in the range of 205-225 HV, while microhardness for the coupon 1 – 3 (using 30 '**V**') was found in the range of 150 HV to 255 HV and for coupon 4 – 6 (using 32 '**V**') vary from 170 HV to 260 HV, and for coupon 7 – 9 (using 34 '**V**') was found in the range of 180 HV to 235 HV. Similarly, after measuring microhardness in the Y – Y direction, the variation found minimum for the samples/coupons welded with higher voltage. The variation of microhardness in a particular order may be due to the presence of the ferrite phase in the austenitic structure. So, it can be said that the microhardness range varied, conferring to the voltage used in the study.

### 6.3.9 Analysis of Variance for Depth of Penetration (DoP)

To find out the significance of process parameters like welding voltage, travel speed, and stick-out on the DoP, ANOVA was performed with a 95 % confidence level. F-test value was used to find out the most significant factor corresponding to each process parameter value. It is based on the principle that the larger the F value, the greater the effect of that parameter, and the P-value should be less than 0.05 for the significant factor. The result obtained from the ANOVA table and response table for the DoP is shown in Tables 6.8 and 6.9. From Table 6.8, it is clear that the maximum percentage contribution is obtained for speed and the least percentage contribution of electrode stick-out.

Table 6.8: Analysis of Variance for DoP(mm), using Adjusted SS for Tests

| Source | Unit | DOF | Seq. SS | Adj. MS/ Variance | F-value | P-Value | Percentage contribution |
|---|---|---|---|---|---|---|---|
| Voltage | V | 2 | 3.3270 | 1.6635 | 3.91 | 0.204 | 40.74 |
| Speed | mm/s | 2 | 3.7168 | 1.8584 | 4.37 | 0.186 | 45.51 |
| Stick-out | mm | 2 | 0.2713 | 0.1356 | 0.32 | 0.758 | 3.32 |
| Error | - | 2 | 0.8514 | 0.4257 | | | 10.43 |
| Total | - | 8 | 8.1665 | | | | 100 |

The response table for process parameters with their rank in terms of significance is shown in Table 6.9. After comparing the F-value from the '**F table**,' i.e., 4.459 and calculated F-value (ANOVA Table), all factors are not statistically significant. Similarly, the P-value is greater than 0.05. It means that we would fail to reject the null hypothesis, or all the population means are equal. Moreover, the speed of welding is at rank 1 with 45.51 %.

Table 6.9: Response Table for DoP

| Level | Voltage | Speed | Stick-out |
|---|---|---|---|
| 1 | 5.280 | 6.850 | 6.227 |
| 2 | 6.100 | 6.020 | 5.813 |
| 3 | 6.767 | 5.277 | 6.107 |
| Delta | 1.487 | 1.573 | 0.413 |
| Rank | 2 | 1 | 3 |

The main effect plot of the process parameters for the DoP of SAW is shown in Fig. 6.21. The X-axis represents the process parameters, and the Y-axis represents the DoP with the mean line.

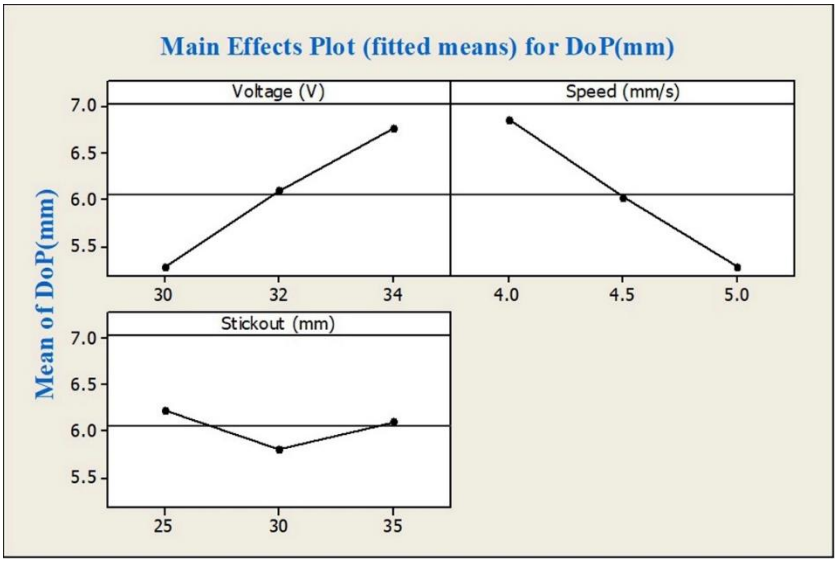


Figure 6.22: Main effect plot showing the influence process parameters on DoP

From Fig. 6.22, the maximum welding voltage (34 V) at minimum welding speed (4.0 mm/s) produced maximum DoP. But the stick-out value did not influence the DoP and was found to be an insignificant factor.

### 6.3.10 Analysis of Variance for Dilution

Similarly, to determine the significance of the same process parameters (welding voltage, travel speed, and stick-out) on the dilution, ANOVA was performed at 95 % confidence level. The result obtained from the ANOVA table and response table for the dilution is presented in Table 6.10 and Table 6.11. The ANOVA table shows that the maximum percentage contribution is of speed, and the least percentage contribution is of electrode stick-out.

Table 6.10: Analysis of Variance for dilution (%), using Adjusted SS for Tests

| Source | Unit | DOF | Seq. SS | Adj. MS/ Variance | F-value | P-Value | Percentage contribution |
|---|---|---|---|---|---|---|---|
| Voltage | V | 2 | 227.961 | 113.981 | 16.00 | 0.059 | 83.35 |
| Speed | mm/s | 2 | 4.054 | 2.027 | 0.28 | 0.778 | 1.48 |
| Stick-out | mm | 2 | 27.249 | 13.625 | 1.91 | 0.343 | 9.96 |
| Error | - | 2 | 14.244 | 7.122 | | | 5.21 |
| Total | - | 8 | 273.508 | | | | 100 |

The response table for process parameters with their rank in terms of significance is shown in Table 6.11. Voltage is statistically significant after comparing the F-value from the ‘F table’ , i.e., 4.459, and calculated F-value (ANOVA Table). The other factors were found as insignificant. Similarly, the ‘P-value is approximately equal to 0.05. It means that we would fail to reject the null hypothesis in the case of travel speed and stick-out. Voltage significantly contributed to dilution and is at rank 1 with 83.35 %.

Table 6.11: Response Table for the dilution

| Level | Voltage | Speed | Stick-out |
|---|---|---|---|
| 1 | 45.66 | 50.43 | 48.86 |
| 2 | 48.66 | 51.51 | 50.00 |
| 3 | 57.52 | 49.90 | 52.98 |
| Delta | 11.85 | 1.61 | 4.13 |
| Rank | 1 | 3 | 2 |

The main effect plot of the process parameters for the dilution is shown in Fig. 6.23. The X-axis represents the process parameters, and the Y-axis represents the dilution rate with the mean line.

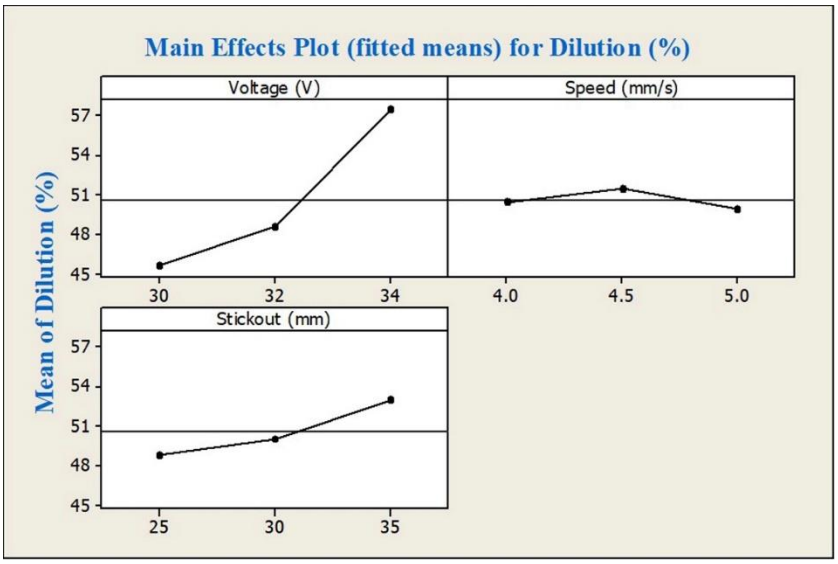


Figure 6.23: Main effect plot showing the influence process parameters on dilution

From Fig. 6.23, it is analysed that the maximum welding voltage (34 V) produced maximum dilution. But the other parameters, i.e., stick-out and speed, did not influence the dilution.

## 6.4 Summary

The present study addresses the key factors such as welding voltage and high basicity index of flux. These are responsible for metallurgical changes and the associated mechanical properties of SAW for AISI 304 stainless steel. Though conventional SAW may produce a higher deposition rate and good mechanical properties, less voltage and higher welding speed may lead to many defects. The most significant parameters found were voltage and travel speed which were responsible for the change in bead profile parameters and mechanical properties. In the present study, the ratio of $Cr_{eq}/Ni_{eq}$ is between1.5 - 2.0, so the solidification mode is ferritic – austenite. Maximum penetration was achieved with maximum voltage and minimum speed, i.e., 34 **V** and 4 mm/s. Only SAW-7/experiment no. 7 justifies the relationship of $R_w/D_p$ and $R_w/R_h$. No significant change in the remaining delta ferrite type in the centre of the fusion zone. Due to less voltage (30 **V**), the weld bead height increases, and the weld bead appearance was uneven, leading to visible defects like porosity. However, higher welding voltage and higher welding speed produced a smooth welding bead with no flaw.

# Chapter - 7
# Autogenous A – TIG Welding (AA-TIG)

## 7.1 Introduction

In the previous study of stationary A – TIG welding, it was observed that the A – TIG welding is responsible for a higher depth of penetration (DoP). It increases the productivity of conventional GTAW/TIG welding by increasing welding speed and achieving high DoP due to reverse Marangoni convection. Therefore, AA – TIG welding optimisation is necessary to study the ideal welding speed during submerged arc welding (SAW) before proceeding to hybrid arc welding (HAW). In this chapter, the mechanical properties of AA – TIG were found to justify the contribution in a hybrid welding process.

## 7.2 Material and Method

For this study, automatic A – TIG welding (AA -TIG) was performed by forming a stringer bead on the material used in SAW (i.e., AISI 304 plates of 16 mm thick) of size 200 mm × 60 mm. The chemical composition of base metal material was analysed by optical emission spectroscopy (Foundry Master- O.E.S, make: Germany), and the analysed data of the essential elements are presented in Table 7.1. An investigation was conducted to find the optimal parameters contributing to the hybrid arc welding process in the present study.

Table 7.1: Chemical compositions of austenitic stainless steel (AISI 304) plates

| Percentage Composition (% wt.) | | | | | | | | | |
|---|---|---|---|---|---|---|---|---|---|
| **C** | **Mn** | **Si** | **Cr** | **Ni** | **S** | **P** | **Mo** | **Cu** | **Nb** |
| 0.03 | 1.14 | 0.47 | 19.4 | 8.26 | 0.01 | 0.04 | 0.15 | 0.237 | 0.008 |
| **Ti** | **Co** | **V** | **Fe** | | | | | | |
| 0.018 | 0.208 | 0.07 | Bal | | | | | | |

In this study, to find the optimum welding speed and current. Before experiments, all workpieces were properly ground and buffed by a precision surface grinder. After cleaning the workpiece surface, activated flux (made by mixing powder-based oxide of high purity and acetone) was pasted on the surface of base plates using a paintbrush. Three oxide-based fluxes, i.e., $TiO_2$, $SiO_2$, and $CrO_3$, were used as activated fluxes. The variable process parameters are also shown in Table 7.2. An L – 9 orthogonal array was used to find the main factor effect for initial investigation, presented in Table 7.3.

Table 7.2: Variable process parameters and levels for the welding of AISI 304

| S. No. | Parameters | Unit | Levels |
|---|---|---|---|
| 1 | Current | Ampere | 250, 280, 310 |
| 2 | Travel Speed | mm/s | 4, 4.5, 5 |
| 3 | Flux | -- | $TiO_2$, $SiO_2$, $CrO_3$ |

The AA – TIG welding was performed using a SAW trolley for the constant movement of the torch at a fixed gap of 3 mm for the stability of the process and shown in Fig. 7.1. The welding was accomplished at a flow rate of 10 L/min using EWTh - 2 and Ar shielding.

Table 7.3: L-9 Orthogonal array for AA - TIG of austenitic stainless steel

| Exp. No. | Current (A) | Travel Speed (mm/s) | Flux |
|---|---|---|---|
| 1 | 250 | 4.0 | $CrO_3$ |
| 2 | 250 | 4.5 | $SiO_2$ |
| 3 | 250 | 5.0 | $TiO_2$ |
| 4 | 280 | 4.0 | $SiO_2$ |
| 5 | 280 | 4.5 | $TiO_2$ |
| 6 | 280 | 5.0 | $CrO_3$ |
| 7 | 310 | 4.0 | $TiO_2$ |
| 8 | 310 | 4.5 | $CrO_3$ |
| 9 | 310 | 5.0 | $SiO_2$ |

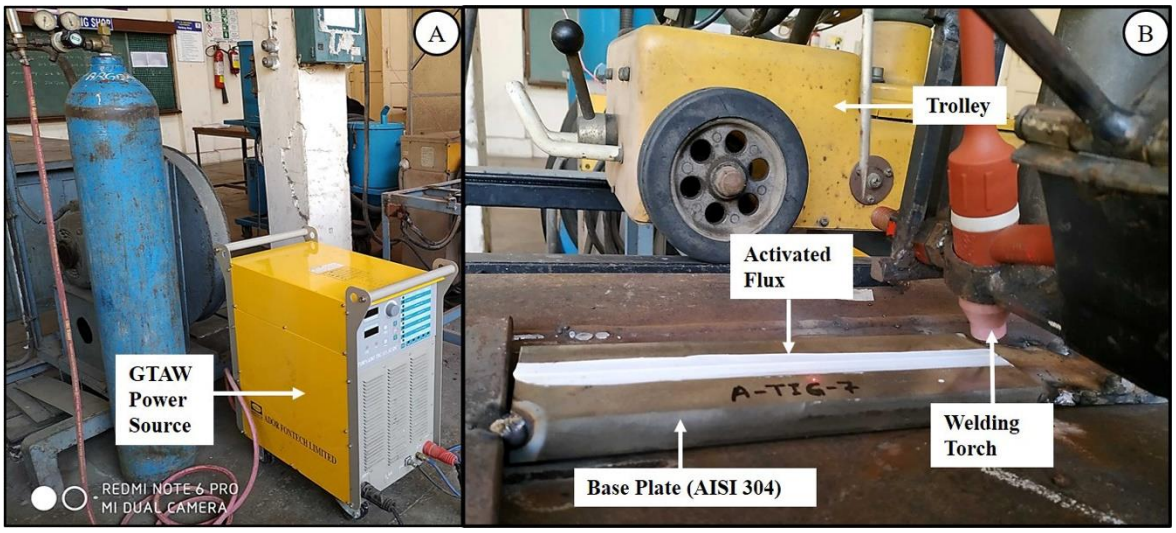


Figure 7.1: (A) Showing power source (B) AA – TIG process

During visual inspection, it was observed that AA-TIG welding produced a flat weld bead at low travel speed, whereas the bead height increases with an increase in travel speed. In the case of samples 7, 8, and 9, maximum depth of penetration (DOP) was achieved at a higher current, i.e., 310 **A** (Fig. 7.3). So, it was concluded that a higher current produced maximum DOP and it was tried for three oxide-based fluxes at the same current and same travel speed. So, AA - TIG was further accomplished at 310 **A** with three fluxes using two-speed levels, i.e., 4 mm/s and 5 mm/s. A tunnel hole was observed in the case of sample 8 (Fig. 8.3), which was welded with $CrO_3$ flux.

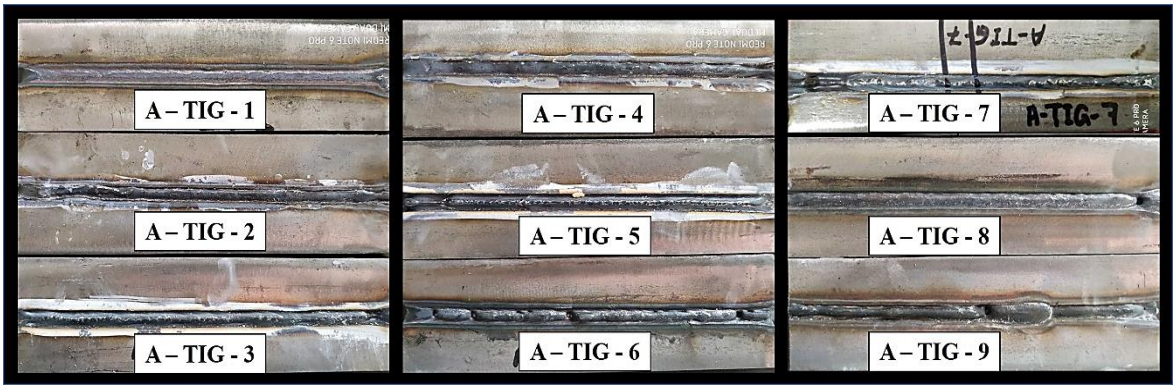


Figure 7.2: Weld-bead appearance of AA – TIG welding (1 To 9)

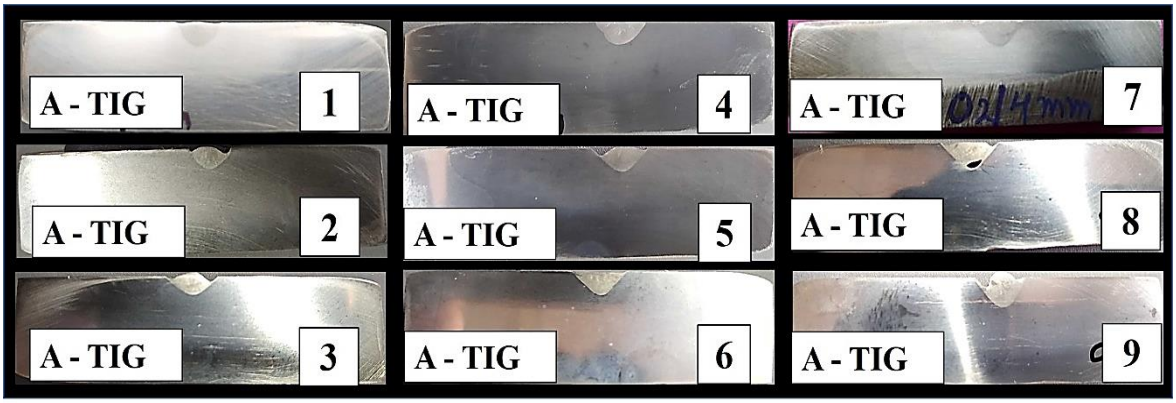


Figure 7.3: Macrograph of AA – TIG welding (1 To 9)

## 7.3 Results and Discussion

### 7.3.1 Macrostructure Analysis

The AA – TIG welding macrograph corresponds to all the three fluxes, i.e., $CrO_3$, $SiO_2$, and $TiO_2$, shown in Fig. 7.4. Higher DoP was observed in case of slow arc travel speed, i.e., 4 mm/s. The travel speed can be further reduced to achieve higher DoP, but the slower speed will not be productive for a hybrid process (i.e., A – TIG + SAW). The microstructure analysis of AA – TIG welding samples was not done because it is already present in Chapter 3 and Chapter 4.

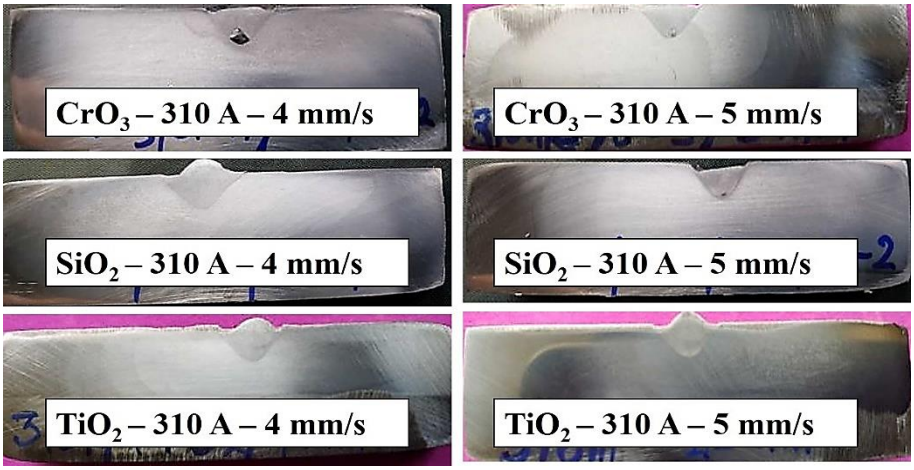


Figure 7.4: Macrograph of AA – TIG welding of different welding speed and different activated flux welded at 310 A

After analysing the macrostructure of the welded sample of Fig. 7.4, no significant difference in DOP was observed for three different fluxes at two different welding speeds. The DoP of 4 mm/s welding speed was found marginally higher than 5 mm/s welding speed. In the case of $CrO_3$ flux, a tunnel porosity was observed at 4 mm/s welding speed, which is visible in Fig. 7.4, and a similar defect was observed in Fig. 7.3, with the same flux.

### 7.3.2 Effect of AA – TIG Welding Parameters on Toughness

Due to the low variation in DoP, a toughness test for $CrO_3$ flux was performed to find the individual contribution of AA - TIG welding in further study of HAW. Therefore, to explore the effect of current and welding speed on toughness, three Charpy 'V' notch test samples of the transverse weld (from sample CrO3_4mm/s_310 **A**) were extracted using wire-cut EDM process (Fig. 7.5). The toughness specimens were etched after polishing and tested as per the ASTM E23 standard at room temperature (30°C) after confirming the notch size dimensions and position of the notch. The extracted specimens for the Charpy test are shown in Fig. 7.5.


Figure 7.5: Showing extracted, the polished and etched specimen of toughness test (Charpy) (A) AA – TIG_$CrO_3$_4 mm/s and (B) AA – TIG_$CrO_3$_5 mm/s

The values of toughness are presented in Table 7.5. Notch positions were kept perpendicular to the longitudinal direction of the weld bead, as mentioned in (Chapter 7). The specimens were tested as per the ASTM E23 standard at room temperature (30°C) after confirming the notch dimensions and position of the notch. A comparison of the resultant value of toughness (Joules) is presented in Fig. 7.6. The variation in toughness at a speed of 4 mm/s was due to the presence of a tunnel hole. At the same speed, sample no. 3 (AA – TIG_CrO3_4 mm/s) produced maximum toughness, i.e., 150 Joules, close to the parent-metal toughness. If this tunnel hole did not exist, the toughness would differ, and it may exceed the hardness of the base metal. In the case of 5 mm/s welding speed, the maximum toughness was observed as 140 Joules for sample 3 (AA – TIG_$CrO_3$_5 mm/s).

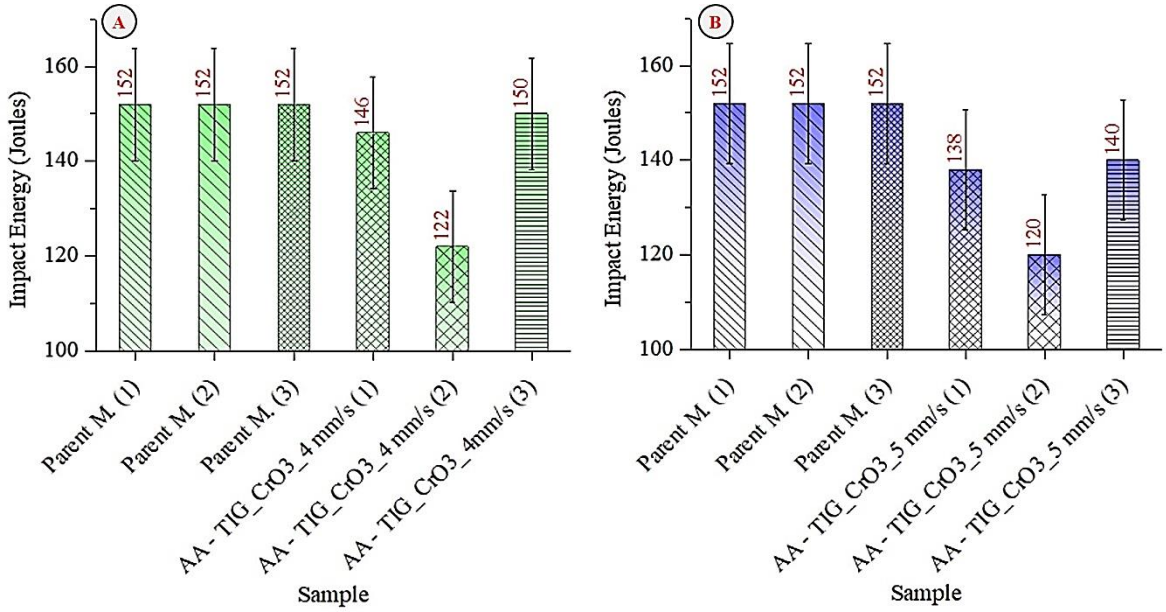


Figure 7.6: Comparison of Impact toughness of base metal and AA – TIG_$CrO_3$ for two welding speeds (A) 4 mm/s (B) 5 mm/s

### 7.3.3 Effect of AA – TIG Welding Parameters on Tensile Strength

The tensile tests were also performed for both the welding speed, i.e., 4 mm/s and 5 mm/s of AA – TIG welding, which was welded with $CrO_3$ flux. The location and dimension of the subsize tensile specimen were kept the same as mentioned in the previous study of SAW in Fig. 6.14 of Chapter 6. The dimensions of the fabricated tensile specimens were maintained as per the ASTM E8M standard and shown in Fig. 7.7. The subsize tensile specimen gauge length and reduced section length were maintained as per standards with a bit of compromise of the grip length because the available width of the base metal plate was in the range of 58 to 60 mm. But, the tensile tests were performed by ensuring a strong grip of the sample. Before testing, the samples were polished and etched to see the fusion profile, presented in Fig. 7.8.

The tensile tests were conducted using the standard procedure at the TINIUS OLSEN (Model HK50S) machine. The 2 mm/min crosshead velocity was employed during all the tensile tests. All the tensile tests were performed at the ambient temperature with ensuring proper grip.

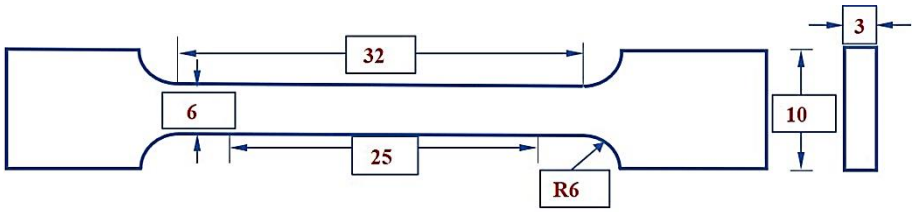


Figure 7.7: Showing schematic illustration of the sub-size tensile specimen as per ASTM E8M

Since the width of the extracted tensile sample shows complete fusion zone/DoP and due to the low penetration in 5 mm/s welding speed, a minor region of the fusion zone profile (Fig. 7.8 B) appeared in the etched sample. Hence, higher tensile strength was observed in the case of 5 mm/s welding speed than 4 mm/s welding speed due to the availability of more area of an unaffected zone (parent metal).


Figure 7.8: Extracted specimen from AA – TIG welding (A) AA – TIG_$CrO_3$_4 mm/s (B) AA – TIG_$CrO_3$_5 mm/s

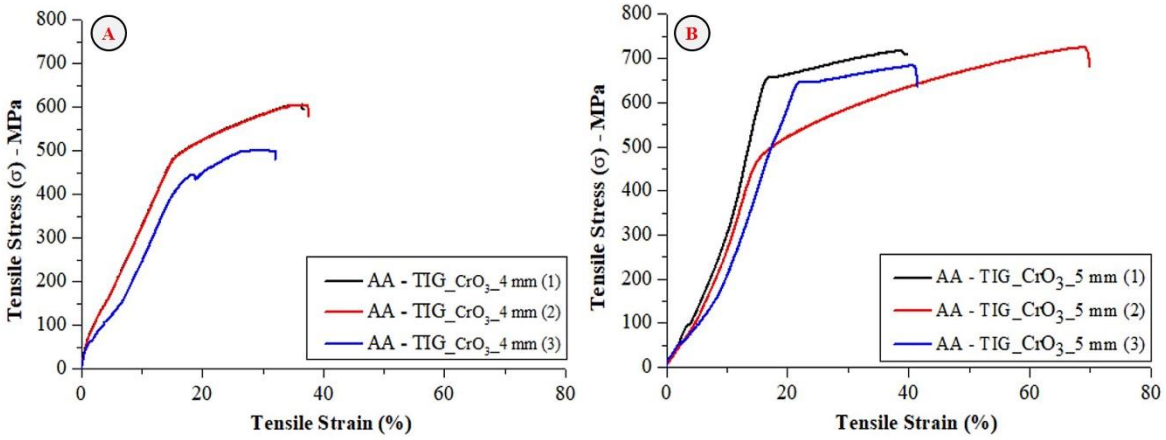


Figure 7.9: Tensile stress v/s tensile strain curve for (A) AA – TIG_$CrO_3$_4 mm/s

(B) AA – TIG_$CrO_3$_5 mm/s

The tensile test results in the form of stress-strain are presented in Fig. 7.9, and the mechanical properties are summarized in Table 7.4. The result of the tensile test of the parent metal is already presented in the previous study of SAW, i.e., Chapter 6 (Fig. 6.15). In the present study, the maximum ultimate tensile strength (i.e., 605 MPa) was observed from sample no. – 1 of 4 mm/s welding speed. In comparison, the maximum tensile strength of 725 MPa was observed for sample no. – 2 of 5 mm/s welding speed due to the presence of minimum weld profile and minimum HAZ in the extruded sample number – 2 (Fig. 7.8 B). So, the tensile strength of sample no. 2 of 5 mm/s speed may be considered the parent metal's strength. A low tensile strength was obtained in the case of 4 mm/s welding speed samples due to tunnel hole porosity, compared to 5 mm/s welding speed. Hence, the presence of any defect in the weld metal reduces the weldment strength and may affect elongation [124].

Table 7.4: Mechanical properties of AA – TIG welding

| S. No. | | Specimen | Impact Energy (Joule) | Average Impact Toughness (Joule) | Tensile Strength (MPa) | Yield Strength (MPa) | Percentage Elongation (%) |
|---|---|---|---|---|---|---|---|
| 1 | i. | AA – TIG_ $CrO_3$_4 mm/s | 146 | 139.33 | 605 | 490 | 36.7 |
| | ii. | AA – TIG_ $CrO_3$_4 mm/s | 122 | | 604 | 490 | 37.5 |
| | iii. | AA – TIG_ $CrO_3$_4 mm/s | 150 | | 502 | 450 | 32 |
| 2 | i. | AA – TIG_ $CrO_3$_5 mm/s | 138 | 132.66 | 717 | 650 | 39.7 |
| | ii. | AA – TIG_ $CrO_3$_5 mm/s | 120 | | 725 | 480 | 69.8 |
| | iii. | AA – TIG_ $CrO_3$_5 mm/s | 140 | | 684 | 640 | 41.4 |

## 7.4 Summary

This study revealed the influence of current and welding speed on the mechanical properties of AA – TIG welding. Though AA – TIG may produce higher penetration and good mechanical properties, higher welding speed may create tunnel porosity in the presence of activated flux. Both the welding parameter were found responsible for the change in bead profile and mechanical properties. Though higher tensile and yield strength are also possible through AA – TIG welding, the recrystallization process may affect the percentage elongation.

# Chapter - 8
# Hybrid Arc Welding (HAW)

## 8.1 Introduction

The approach to meet the demand for higher productivity during welding has been made by various researchers, which led to the development of hybrid processes. The productivity/ effectiveness of a hybrid welding process can be measured by considering the significant improvement in welding speed and depth of penetration. The other way of evaluating the process is to consider welding quality, mechanical properties, and microstructural characteristics.

Most efforts have been made by using a high energy source like a laser beam with other arc welding processes like gas metal arc welding (GMAW), plasma arc welding (PAW), submerged arc welding (SAW), and gas tungsten arc welding (GTAW) as a hybrid process [23–27]. SAW is a modified arc welding process where an arc is completely hidden under a thick flux layer, making it operator-friendly. Previously SAW was considered a highly productive welding technique to achieve a higher deposition rate in the case of thicker steels [31]. It could also be used for welding austenitic stainless steel. Higher heat input is required to enhance the process productivity and make it economical, which leads to other problems. Generally, higher thicknesses are welded by multiple passes using groove joint geometry, which may lead to distortion. Thus edge preparation requirement is still a challenge in the case of stainless steel which makes it an uneconomical and more time-consuming. On the other hand, high power laser beam welding (LBW) has unique features of high energy density which make it useful for single-pass welding of thick steels up to 20 mm. However, it may lead to the formation of brittle phases and aptness to porosity due to the fast cooling rate of weld metal [29]. Also, high power laser welding is costly, and proper joint fit-up is required for best results. Moreover, the LBW is also more prone to cracks than an electric arc power source. The LBW is also more prone to porosity/ contamination than an electric arc power source [125].

Many types of laser sources are now being used in different manufacturing industries. It was found that the plume produced by the $CO_2$ laser interacts with the pulsed GMAW arc under a particular set of welding variables which further reduces the intensity of the laser [23]. The depth of penetration in the laser-arc hybrid process may be influenced by the type of gas or gas mixture and its flow rate [23, 126]. There is a need to synchronize the angle between a Plasma Arc Welding (PAW) torch and laser gun to establish the interaction of the arc and laser to achieve the combined effect of both processes [25]. This requirement is also required in the

laser-arc (Laser + GMAW) hybrid process, which makes it more complex. So, to overcome all these issues, a new hybrid arc welding process has been developed by combining A-TIG and SAW. Both A-TIG welding (Activated Tungsten Inert Gas Welding) and the SAW (submerged arc welding) come under arc welding and were combined in a hybrid process. The A – TIG welding provides for higher penetration at low heat input using oxide-based fluxes [8, 9, 20] and SAW results in a higher deposition rate [60, 127, 128].

This hybrid (A-TIG + SAW) process was carried out on 16 mm thick austenitic stainless steel (ASS). This study was undertaken with an aim to assess the effect of process parameters on the weld profile, weld chemistry, grain growth, microhardness, and the toughness of combined HAZ and base metal samples. The combined effect of both process arcs provides a smooth weld bead with a defect-free weld in the presence of $TiO_2$, $SiO_2$ and $CrO_3$ activated flux. This study was completed after a parametric study of both A-TIG and SAW welding on the same material and same thickness. A low pre-set value of current (in SAW) was used in this study to see the overall effect of the welding parameters on the outcomes of this new hybrid process and validated by measuring its mechanical properties.

## 8.2 Material and Method

The standard AISI 304 stainless steel plates of 200 × 60 × 16 mm thickness were used in the present study for conventional submerged arc welding (SAW) and autogenous A-TIG welding. The chemical composition was analyzed by optical emission spectroscopy (Foundry Master, Germany) and is shown in Table 8.1.

Table 8.1: Chemical compositions of AISI 304 plates

| Material | Percentage Composition (% wt.) | | | | | | | | | | | |
|---|---|---|---|---|---|---|---|---|---|---|---|---|
| | C | Mn | Si | Cr | Ni | S | P | Mo | Cu | Ti | V | Fe |
| AISI 304 | 0.03 | 1.14 | 0.47 | 19.4 | 8.22 | 0.012 | 0.04 | 0.15 | 0.23 | 0.01 | 0.07 | Bal |

Before hybrid welding, all the coupon surfaces were properly ground and buffed using a precision surface grinder, polishing machine, and cleaned with acetone. The coupon was tacked on the base plate of the platform with a side coupon of the workpiece. The present study was performed by maintaining the minimum gap between the SAW and GTAW electrodes (as shown in Fig. 8.1). Activated flux was prepared by mixing the oxide in the acetone and was applied on the weld surface before tacking. Before welding, it was ensured that the flux was completely dried. In the present work, A-TIG welding led the SAW while maintaining the adjusted gap of 35 mm between two electrodes. For A-TIG welding, 310 **A** current was used with straight polarity and an arc force setting of 100 (0.9 g-f approximately) [129]. A thoriated

tungsten electrode (EWTh-2) of diameter 3.18 mm having vertex angle of 60$^{o}$ and pure 'Ar' shielding were used in the present study. For submerged arc welding (SAW), the agglomerated flux was preheated at a temperature of 300$^{o}$ C for two hours to remove the retained moisture. This hybrid arc welding was conducted using Taguchi's OA (L – 9) for SAW and autogenous A – TIG welding. All the coupons were welded at room temperature conditions, and the schematic diagram of the hybrid arc process is shown in Fig. 8.1(a). This study's detailed constant and variable parameters are provided in Table 8.2 and Table 8.3.

The arc produced by the hybrid process provided a smooth weld bead and a defect-free weld in the presence of $TiO_2$, $SiO_2$ and $CrO_3$ activated flux. A preset value of 380 **A** current (for SAW) was used in this study and validated by comparing mechanical properties before and after the welding. The welded coupons after HAW are shown in Fig8.3. The heat input for A-TIG welding was of the order of 0.775 **KJ/mm** at a speed of 4 mm/s and 0.620 **KJ/mm** for the welding speed of 5 mm/s. The thermal efficiency for both the A-TIG welding and SAW was taken as 1. Similarly, 3.230 **KJ/mm** heat input rate was used at a welding speed of 4 mm/s with 34 **V**, and 2.280 KJ/mm at a welding speed of 5 mm/s with 30 **V** for submerged arc welding (SAW). Hence, the combined heat input rate at the speed of 4mm/s and 5 mm/s was of the order of 4.005 KJ/mm and 2.9 KJ/mm, respectively. The parameters of this study were chosen based on a parametric study of SAW on the same base metal of the same thickness.

The outline of the new hybrid process that combines A – TIG with conventional SAW is presented in Fig. 8.1. Hybrid arc welding (HAW) was performed on the same 16 mm thick austenitic stainless steel (ASS) at two different voltage settings (i) 30 volts and (ii) 34 volts at two speeds (i) 4 mm/s and (ii) 5 mm/s. The purpose of this study was to find out the effect of these factors on the weld profile, bead geometry, weld chemistry, grain growth, microhardness, tensile strength, and impact toughness of partition zone (50 % fusion area and 50 % base metal). This study also explores the use of A-TIG welding to enrich the SAW and its associated outcomes/results. The responses of this study are the comparison of two welding speeds (i.e., 4 mm/s and 5 mm/s) and voltage used for SAW (i.e., 34 **V** and 30 **V**).

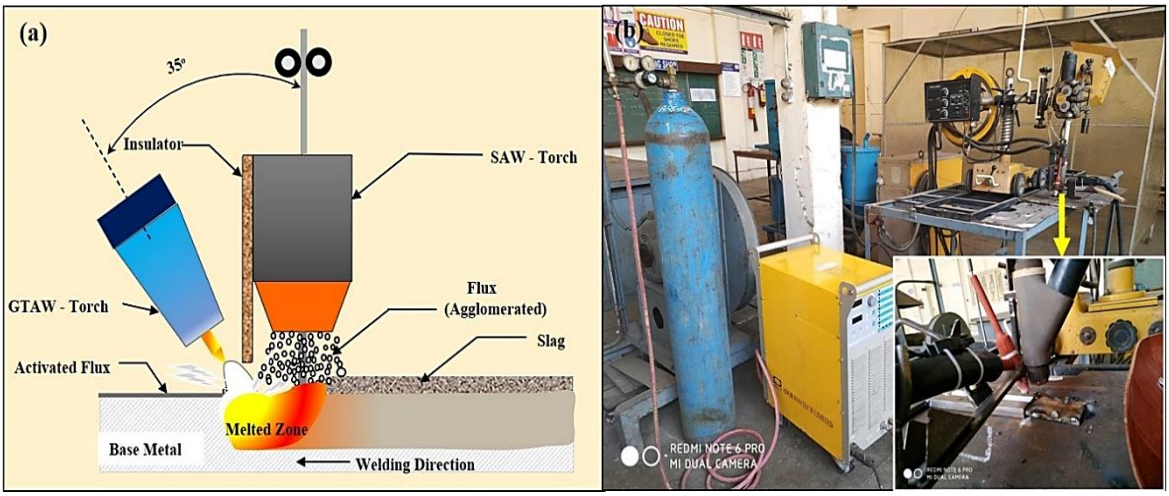


Figure 8.1: (a) Schematic representation of hybrid arc welding (HAW) (b) Actual Setup

The terminology of the weld profile is shown in Fig. 8.2. Different parameters of weld profile such as reinforcement width ($R_w$), reinforcement height ($R_h$), penetration area ($P_a$), reinforcement area ($R_a$), penetration (P) were calculated after polishing and etching by using calibrated measuring microscope and using image J software.

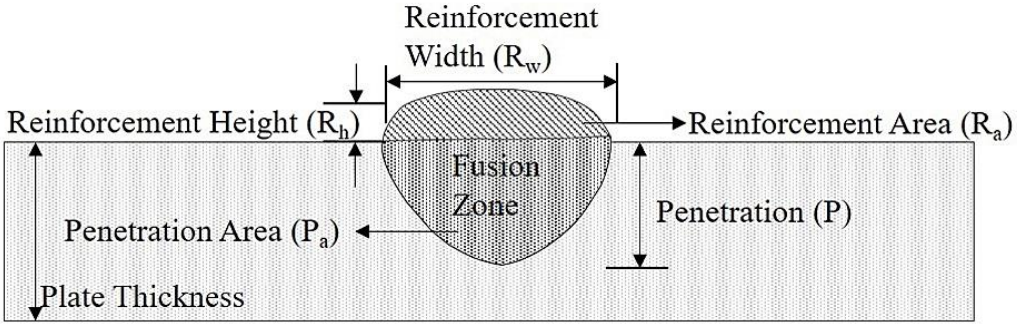


Figure 8.2: Weld profile nomenclature for a bead on plate

Table 8.2: Constant parameters of the hybrid process (SAW + A- TIG)

| S. No. | Power Source | Constant Parameter | Set value/Type |
|---|---|---|---|
| 1. | **SAW** (TORNADO SAW, M-800) Make: Ador Fontech Limited | Polarity | DCEP (Direct current electrode positive) |
| | | Mode | CV (Constant voltage) |
| | | Initial Current Setting | 380 A |
| | | Electrode/Filler wire size | 3.15 mm |
| | | Electrode Specification | AWS A 5.9 ER308L |
| | | Electrode Feeding Position | Vertical (90°) |
| | | Flux | Agglomerated |
| | | Workpiece Thickness | 16 mm |
| | | Stick out | 25.4 mm |
| | | | |
| 2. | **GTAW (For A – TIG)** (TORNADO TIG 315 AC/DC) Make: Ador Fontech Limited | Polarity | DCEN (Direct current electrode negative) |
| | | Electrode Size | 3.18 mm |
| | | Electrode | Tungsten (2% Th) |
| | | Current | 310 A |
| | | Gas | Pure Ar |
| | | Gas Flow rate | 10 L/min |
| | | Vertex Angle of electrode | 60° |
| | | Torch Angle | 55° from ground level or 35° from Saw torch |
| | | The gap between electrodes tip (between SAW wire and GTAW electrode) | 35mm |

Table 8.3: Variable parameters of HAW process (SAW + A- TIG)

| S. No. | Activated Flux | Welding Speed (mm/s) | Voltage (V) for SAW | Level |
|---|---|---|---|---|
| 1. | **$CrO_3$** | 4, 5 | 30 and 34 | 2 |
| 2. | **$SiO_2$** | 4, 5 | 30 and 34 | 2 |
| 3. | **$TiO_2$** | 4, 5 | 30 and 34 | 2 |

To examine the microstructure, measuring the DoP, and weld profile, a measuring microscope having 1 µm least count (Axio-Scope A1 of Carl Zeiss, Germany) was used. The schematic diagram for the location of extraction of samples to perform the destructive and non-destructive test is presented in Fig. 8.15.

## 8.3 Results and Discussion

### 8.3.1 Effect of Welding Variables on Bead Shape and Appearance

The melting rate increased by combining the two arcs, and the weld appearance was found satisfactory. The leading arc of the A-TIG process was found to be a perfect source to cause the annealing effect, successfully preheated the metal, and delayed the cooling rate of the weld

puddle. All hybrid arc welding (HAW) coupons were kept at room temperature, and after cooling, they were analysed for visual Inspection (Fig. 8.3). In visual inspection, no surface defect was observed after welding. The only difference in weld bead width was observed. It was due to the welding voltage difference. The bead appearance of HAW is shown in Fig. 8.3. The effect of voltage and speed was accessed from bead appearance. The value of current (initial current setting) was kept same in each case. The difference in weld width is provided in Table 8.3. By comparing with conventional SAW (Chapter 6), it could be concluded that the appearance of HAW was observed better for both welding speeds and found to be flawless.

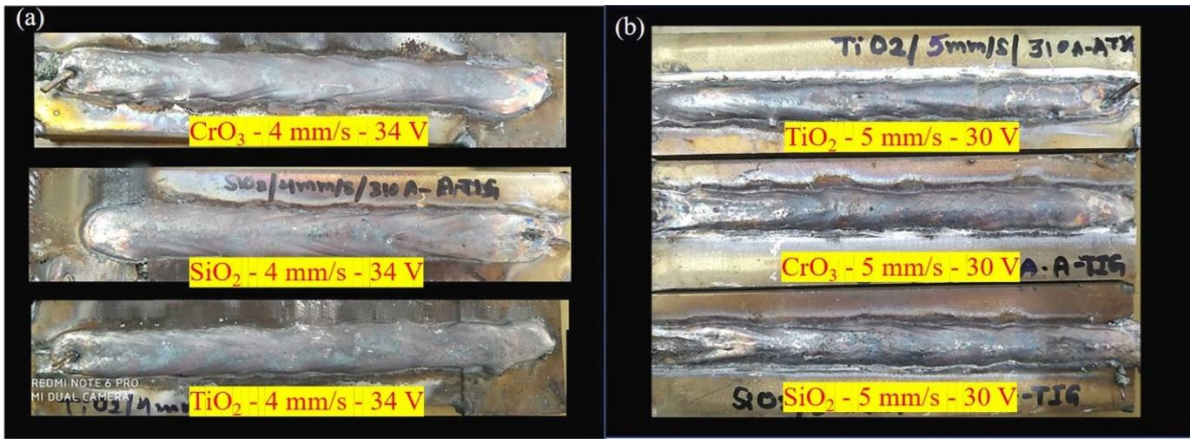


Figure 8.3: Welded coupons of hybrid arc welding (HAW) welded at two different voltages (i.e., 34 V and 30 V) and with two different welding speeds (i.e., 4 mm/s and 5 mm/s)

## 8.3.2 Weld Metal Morphology and Effect of Primary Ferrite

The net heat applied for a welding process, and the cooling rate may be sufficient to change the chemistry of the resultant weld bead and its associated structure. In the case of austenitic stainless steel (ASS), the weld bead comprises retained delta ferrite embedded in the austenite matrix. The cooling rate decides the shape/type of retained ferrite during the transformation phase of primary ferrite. The presence of an activated flux may also influence the retained ferrite structure and its associated metallurgy. The appearance of retained ferrite may be of vermicular ferrite, lathy ferrite, and lacy ferrite. The presence of oxygen elements in the oxide-based fluxes increases the molten pool temperature. The welding speed affects the cooling rate, which further influences the grain growth and its associated mechanical properties. The welding process heat input and the bead characteristics govern the weld bead geometry [127].

### 8.3.2.1 Hybrid Arc Welding (HAW) with CrO3

Figure 8.4 (a) shows a hybrid arc welded (HAW) coupon (A - TIG + SAW), which was performed at 4 mm/s welding speed at 34 V and a transverse cut etched specimen with weld bead microstructures of different weld regions. The HAW with $CrO_3$ flux produced a clean,

smooth weld bead, and no surface defect was observed in the visual inspection. This coupon's measured weld profile parameters are also given in Fig 8.4 (b) and Table 8.4. By comparing the weld bead with the conventional SAW bead of the previous chapter (Chapter 6), no porosity was observed during the hybrid process due to the annealing effect and slow cooling rate of the hybrid process. A cluster of vermicular delta ferrite networks microstructure was observed in the upper central region of the weld bead Fig 8.4 (c). This structure would have good mechanical properties. The **lathy ferrite** was observed near the interface/boundary of the fusion zone (Fig 8.4 (d)), and a network of **lacy ferrite** networks (Fig. 8.4 (e)) was observed in the root, which represents the direction solidification pattern of weld metal.

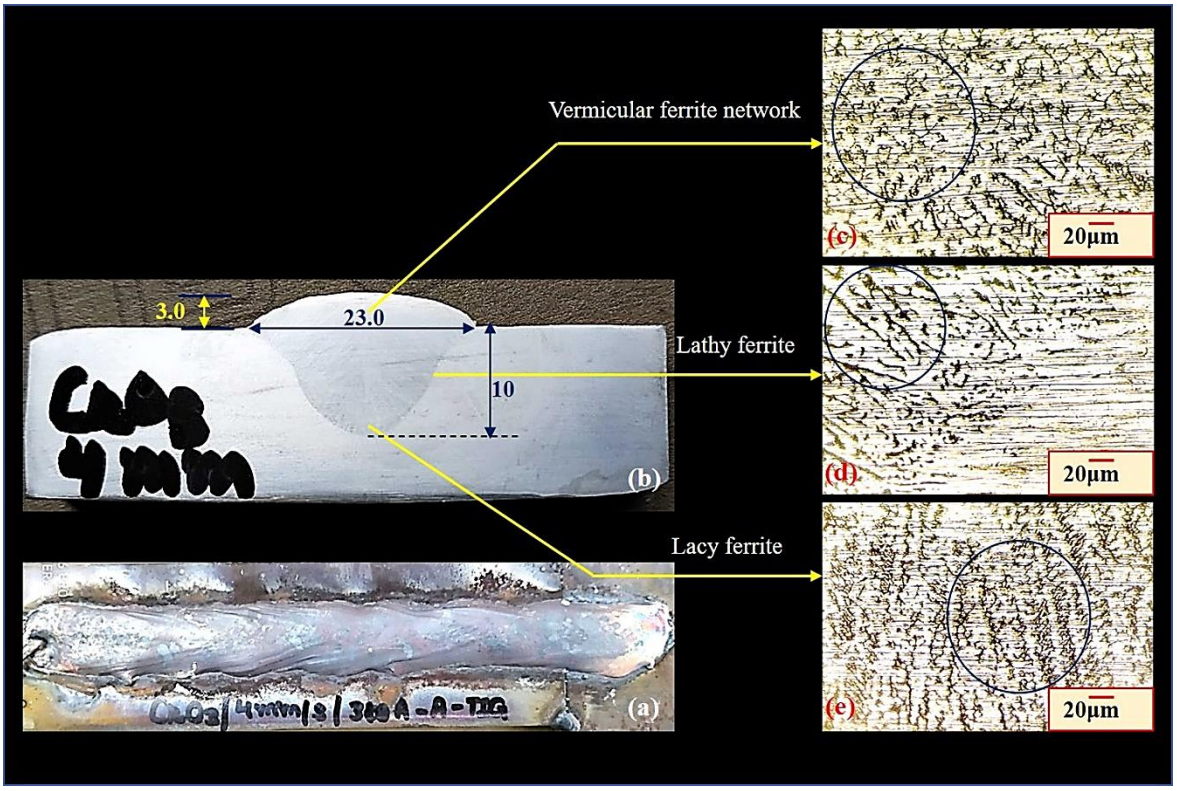


Figure 8.4: Photograph contains (a) Hybrid welded coupon using $CrO_3$ flux at 4 mm/s welding speed (b) Macrograph of the etched specimen (c), (d), and (e) showing the microstructure of different regions of weld bead

A study of "S David - 1981 [130] is found in agreement with the present study that ASS weld produced a mixed morphology of delta ferrite was found after solidification (using AISI 308 steel filler wire). It was observed that the delta ferrite exists in the austenite matrix due to the incomplete transformation of $\delta - \gamma$ [130]. The point of interest is the formation of **vermicular ferrite** in the upper middle part of the weld profile. The study of "S David" reported that this type of ferrite (Vermicular ferrite) had been found in the microstructure with a ferrite number of 5 – 15 FN, and the Lacy ferrite morphology had been found with 13 – 15 FN. A significant DoP, i.e., 10 mm, was achieved by using 4 mm/s welding speed.

In the case of 5 mm/s welding speed, the maximum DoP achieved was 7.6 mm (Fig. 8.5), and the reinforcement height was observed more due to less voltage. A considerable difference in weld bead width and overall dilution was noticed while using two different welding speeds and two different voltages in Table 8.5. Figure 8.5 (c), (d) shows the presence of **acicular ferrite** (*AF*) in the upper central region of the weld profile and near the fusion zone boundary. Lacy ferrite was observed in the root site of the weld profile, and this type of ferrite morphology was found during the transformation of primary δ – ferrite to Widmanstatten austenite and ferrite [130].

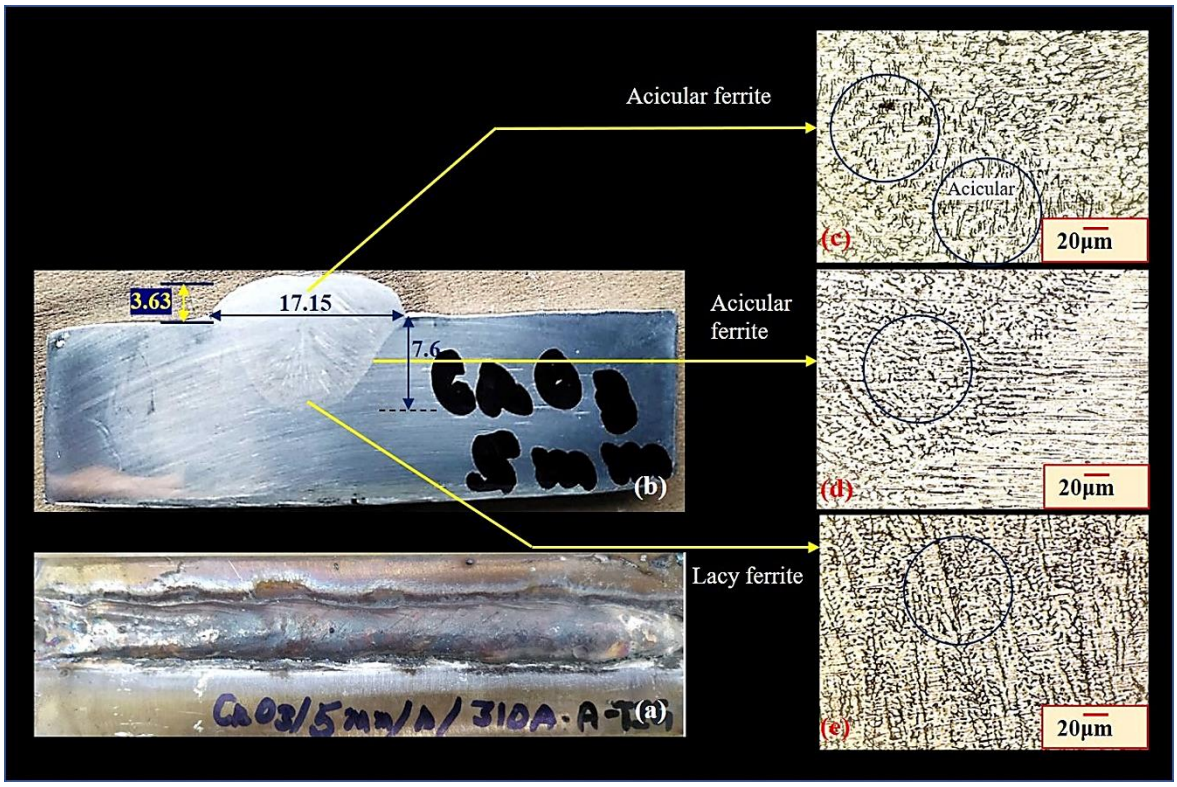


Figure 8.5: Photograph contains (a) Hybrid welded coupon using $CrO_3$ flux at 5 mm/s welding speed (b) Macrograph of the etched specimen (c), (d), and (e) showing the microstructure of different regions of weld bead

### 8.3.2.2 Hybrid Arc Welding (HAW) with $SiO_2$

The same study was also performed with $SiO_2$ flux. The as-welded weld coupon with cross-sectional cut sample and its related microstructures of different regions are shown in Fig. 9.6. The same penetration depth was achieved as in the case of welding with $CrO_3$ flux. The upper zone of the weld was observed with the presence of vermicular and acicular ferrite matrix. And concentrated vermicular ferrite morphology was observed near the fusion zone boundary. The presence of vermicular ferrite in the weld metal minimizes the occurrence of hot cracking of weld metal [131].

In contrast, dense lacy ferrite was observed in the root part of the weld profile. A significant increase in bead width was found with $SiO_2$ flux as compared to welding with $CrO_3$ flux (As Si has a greater affinity towards electrons). No welding defect was observed on the surface of the weld bead.

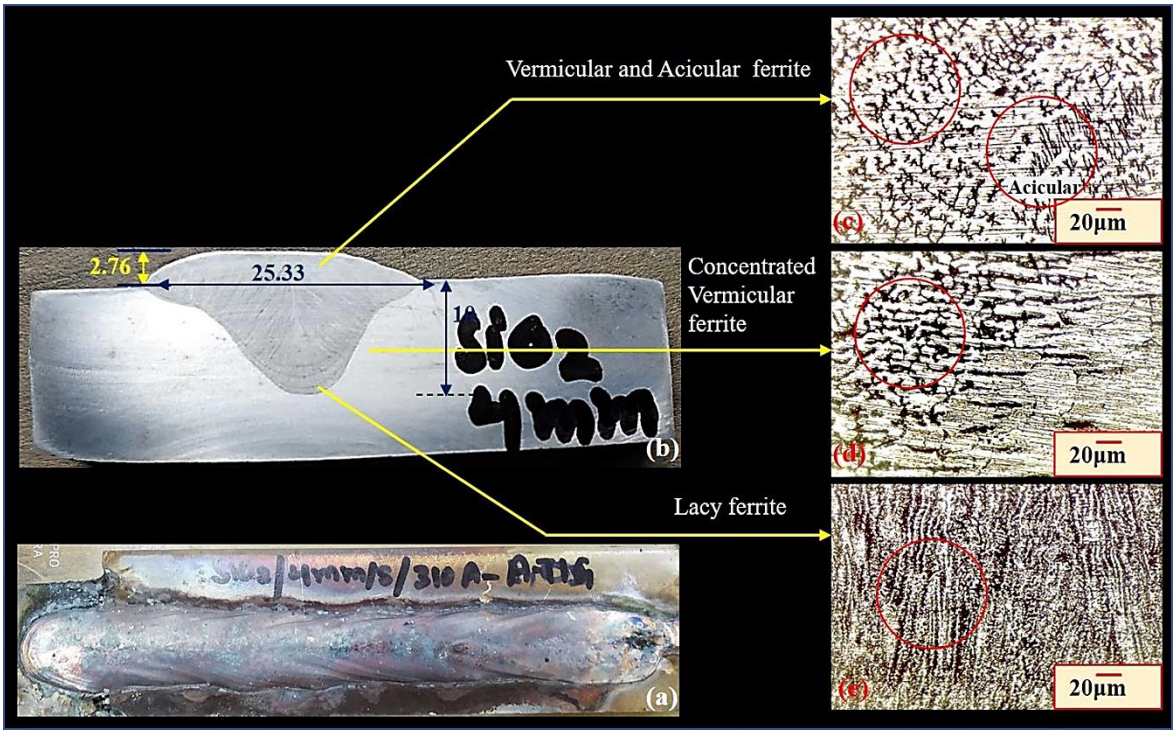


Figure 8.6: Photograph contains (a) Hybrid welded coupon using $SiO_2$ flux at 4 mm/s welding speed (b) Macrograph of the etched specimen (c), (d), and (e) showing the microstructure of different regions of weld bead

When the same flux ($SiO_2$) was used with other speeds (i.e., 5 mm/s), the reinforcement height increased, and DoP decreased. An inclusion was observed after cutting of the sample, and the same is represented in Fig. 8.7. At the speed of 5 mm/s with $SiO_2$ flux, the upper central region had a mixed morphology of vermicular and interlaced ferrite. The globular ferrite morphology was observed near the fusion zone boundary and lathy ferrite morphology at the root side.

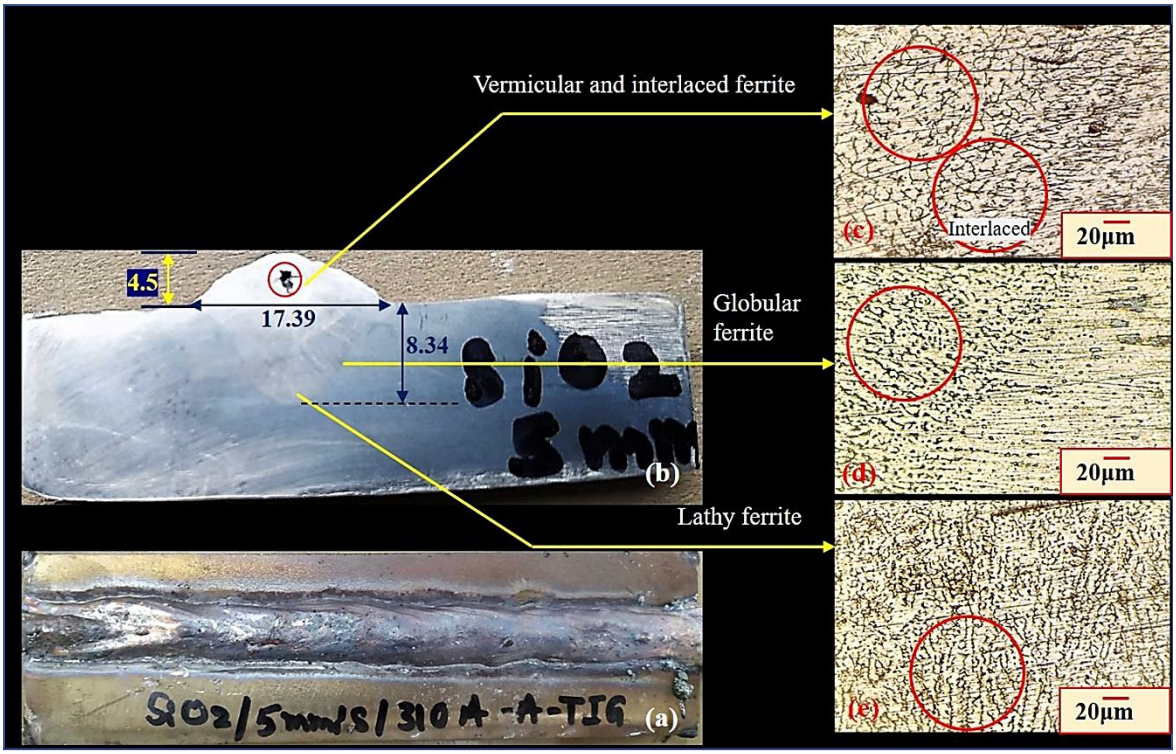


Figure 8.7: Photograph contains (a) Hybrid welded coupon using $SiO_2$ flux at 5 mm/s welding speed (b) Macrograph of the etched specimen (c), (d), and (e) showing the microstructure of different regions of weld bead

Globular ferrite may be present due to the instability of another type of ferrite in the molten pool. During solidification, it may break down/transform into a disconnected globule of the particular type of network [130].

### 8.3.2.3 Hybrid Arc Welding (HAW) with $TiO_2$

Hybrid Arc Welding (HAW) with $TiO_2$ flux produced a mixed morphology of vermicular and interlaced ferrite in the upper central part of the weld zone (Fig. 9.8 (c)). A vermicular ferrite network was observed near the fusion zone, and Lacy ferrite was detected at the root of the weld. The weld profile is similar to the weld profile of HAW with $CrO_3$ flux. No defect was observed on the surface of the weld bead. All the weld coupons show the vertical direction of the lacy or lathy ferrite in the root of the weld, which represents the directional cooling of the molten metal. In the case of 5mm/s welding speed, $TiO_2$ assisted HAW produced the mixed morphology of vermicular and interlaced ferrite in the upper part of the fusion zone (Fig. 8.9 (c)). A transformation of lacy to globular ferrite was observed near the fusion boundary, and a lathy ferrite matrix was observed at the root of the weld.

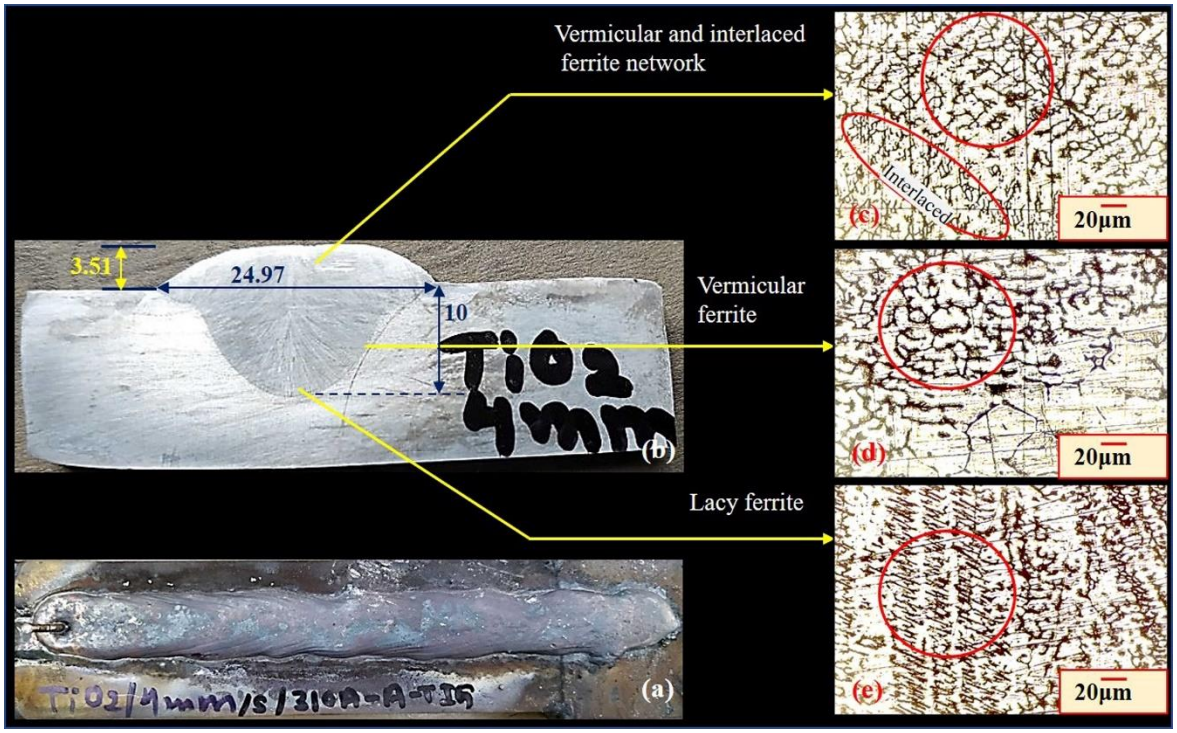


Figure 8.8: Photograph contains (a) Hybrid welded coupon using $TiO_2$ flux at 4 mm/s welding speed (b) Macrograph of the etched specimen (c), (d), and (e) showing the microstructure of different regions of weld bead

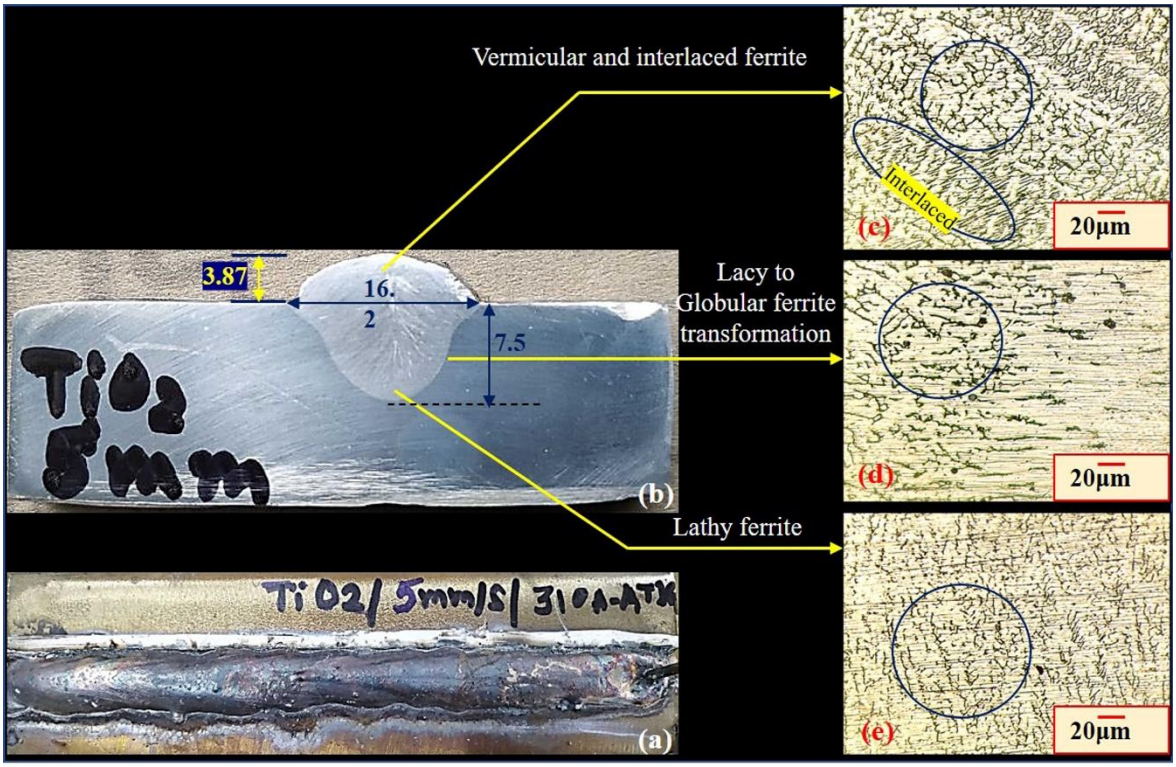


Figure 8.9: Photograph contains (a) Hybrid welded coupon using $TiO_2$ flux at 4 mm/s welding speed (b) Macrograph of the etched specimen (c), (d), and (e) showing the microstructure of different regions of weld bead

### 8.3.3 Weld Profile Measurement and analysis

According to Table 8.4, penetration increases when heat input increases, affecting the dilution. Higher voltage helps to increase the average contact angle, which was measured from both sides of the weld. In general, and in SAW welding, the welding quality is considered good if it satisfies the following condition. The

$$\mathbf{R_w/P \geq 2}$$
$$\mathbf{R_w/R_h \geq 6}$$

So, this study (HAW), which was performed at a welding speed of 4 mm/s and with 34 volts (V), satisfied both the condition and another. Whereas with 5 mm/s welding speed using 30 volts (V) met only one condition, i.e., $\mathbf{R_w/P \geq 2.}$

Table 8.4: Process parameters and their outcomes in terms of bead geometry

| Exp. | Speed (mm/s) | Voltage (V) | Heat Input (KJ/mm) (A-TIG + SAW) | DoP (mm) | Dilution (%) | Reinf. Height $R_h$ (mm) | Reinf. Width $R_w$ (mm) | Average Toe Angle (°) | $R_w/P$ | $R_w/R_h$ |
|---|---|---|---|---|---|---|---|---|---|---|
| **HAW with $CrO_3$** | 4 | 34 | 0.775 + 3.230 | 10 | 70.58 | 3 | 23 | 45.171 | 2.3 | **7.66** |
| HAW with $CrO_3$ | 5 | 30 | 0.620 + 2.280 | 7.6 | 64.168 | 3.63 | 17.15 | 56.81 | 2.25 | 4.72 |
| **HAW with $SiO_2$** | 4 | 34 | 0.775 + 3.230 | 10 | 68.58 | 2.76 | 25.33 | 36 | 2.53 | **9.17** |
| HAW with $SiO_2$ | 5 | 30 | 0.620 + 2.280 | 8.34 | 64.43 | 4.5 | 17.39 | 42.82 | 2.08 | 3.86 |
| **HAW with $TiO_2$** | 4 | 34 | 0.775 + 3.230 | 10 | 67.52 | 3.51 | 24.97 | 37.92 | 2.49 | **7.11** |
| HAW with $TiO_2$ | 5 | 30 | 0.620 + 2.280 | 7.5 | 62.96 | 3.87 | 16.2 | 56.76 | 2.6 | 4.18 |

Figure 8.10 represents the variation of average toe angle of reinforcement with dilution rate in case of both the welding speed, i.e., 4 mm/s and 5 mm/s with 34 and 30 volts of arc. Fig. 8.10 (a) observed that the average toe angle decreases with a decrease in dilution rate in HAW with $CrO_3$ and $SiO_2$ flux using 34 Volts and 4 mm/s welding speed.

A different trend was observed with $SiO_2$ flux at 30 Volts and using 5 mm/s welding speed (Fig 8.10 b). The same trend for HAW with $TiO_2$ flux for both welding speeds was observed in Fig. 8.10 a and b.

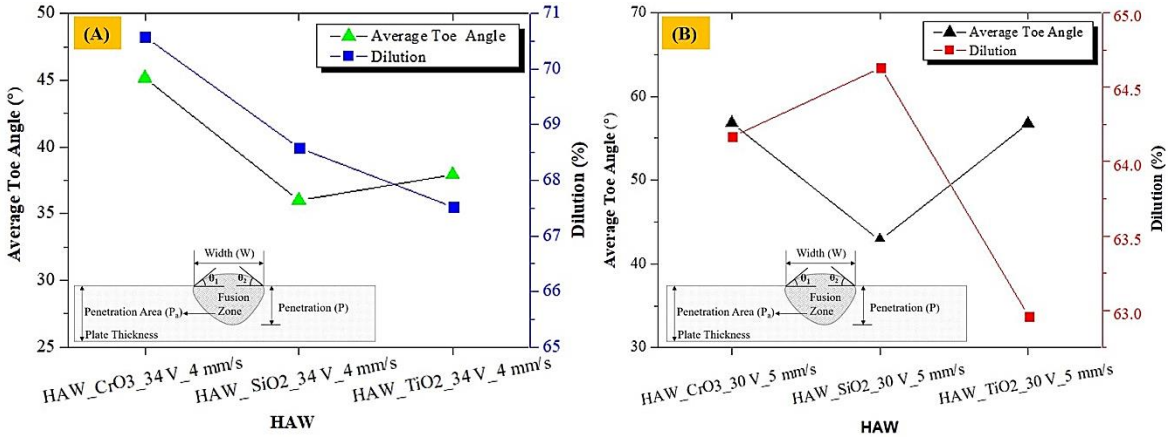


Figure 8.10: Calculated average toe angle of reinforcement and dilution rate variation w.r.t different flux (a) using 4 mm/s welding speed and 34 volts (b) using 5 mm/s welding speed and 30 volts

From Fig. 8.11(a), it was observed that the reinforcement area also increases with the increase of penetration area. It means there had been an increase in overall dilution, and this increase was found different in different types of fluxes. Hybrid arc welding with $TiO_2$ flux produced maximum penetration, so an overall increase in dilution rate had been found [8, 9, 93]. But the ratio of $\mathbf{R_w/R_h}$ is found maximum in the case of $SiO_2$ flux preceding by $CrO_3$ and $TiO_2$ flux, whereas this trend was different for 5 mm/s speed using 30 Volts (**V**) (Fig. 8.11 b).

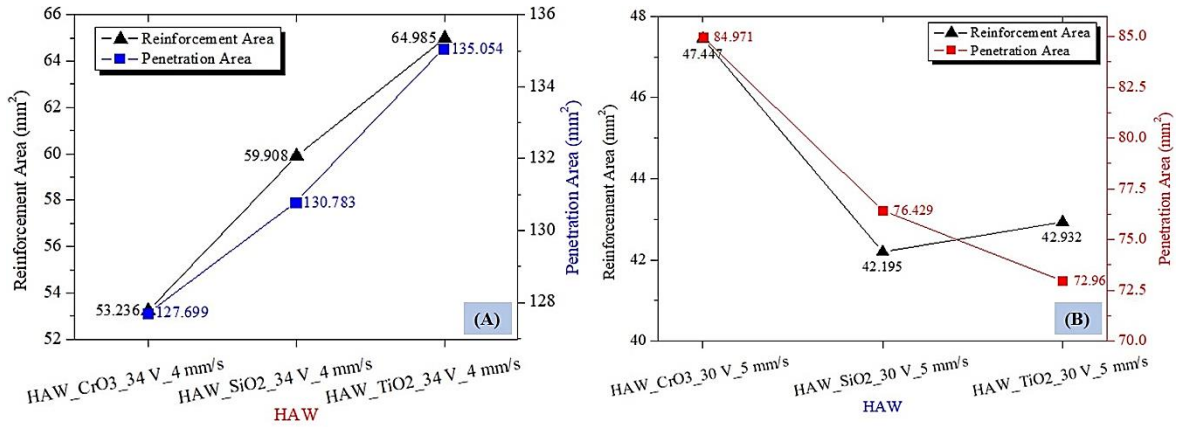


Figure 8.11: Calculated reinforcement area and penetration area variation (a) using 4 mm/s welding speed and 34 volts (b) using 5 mm/s welding speed and 30 volts

The effect of welding speed and welding voltage on the penetration area is visible from Fig. 8.12, but it could not influence the dilution area. A slight increase in the dilution area was noticed using 4 mm/s welding speed and 34 V. But, a slight increase in penetration area was observed in the case of $SiO_2$ and $TIO_2$. It may be due to the presence of 10 % of $SiO_2$ + $TiO_2$ in agglomerated flux (AUTOMELT S33). Hence, more oxygen elements present in the flux were attributed to higher heat, which eventually increased the overall penetration area.

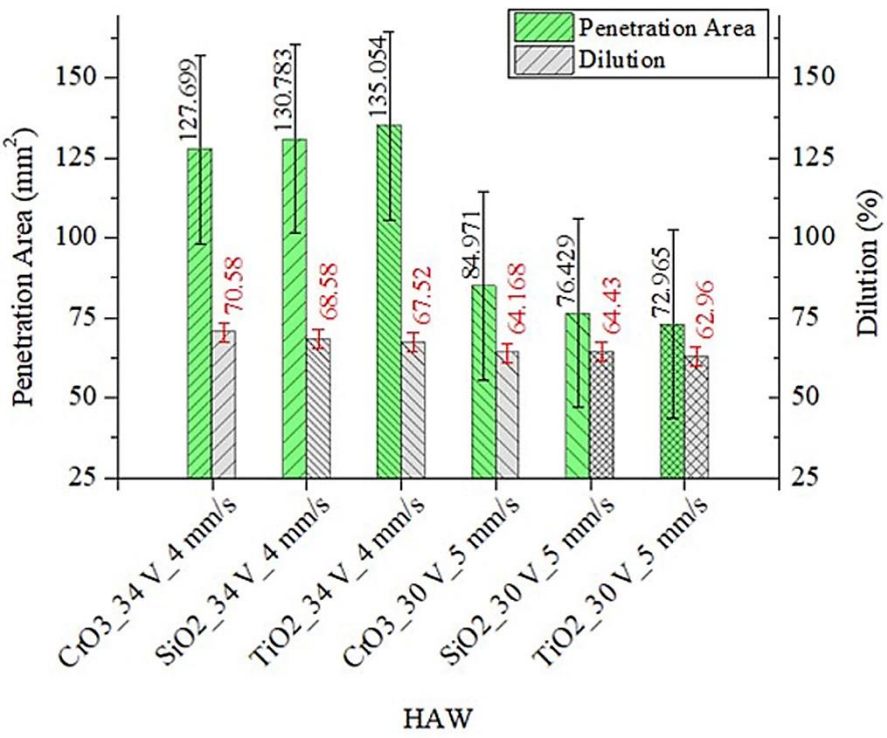


Figure 8.12: Comparison of penetration area and dilution rate

### 8.3.4 Effect of Hybrid Process on Retained Chemical Composition and the Ratio of $Cr_{eq}/Ni_{eq}$:

The variation of heat input of the hybrid process and the chemical composition of filler wire and flux may affect the retained chemical composition of weld metal alloying elements. The tested sample of spectroscopy test is presented in Fig. 8.13.

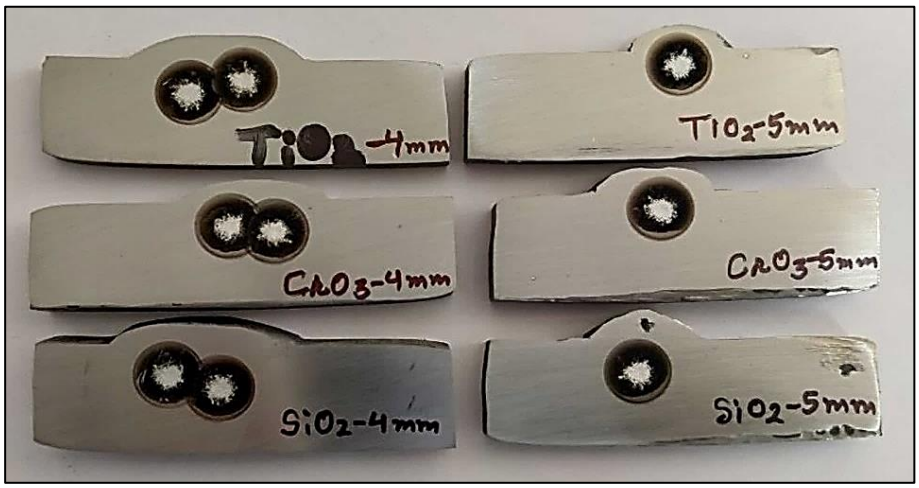


Figure 8.13: Represents tested specimens of chemical composition by spectroscopy

Observing the bar graph of Fig. 8.14 (a), the variation in element "C" was found more in the HAW process, especially in the case of $TiO_2$ using 34 Volts and found above the parent and filler metal, while minute variation was found in the case of "Cr" and "Si" (Fig. 8.14 b and f).

The retained “Ni” and “Mo” percentage was found to be less as compared to filler metal composition (Fig. 8.14 c). Some variation in “Mn” content in the weld-metal was also observed (Fig. 8.14 d).

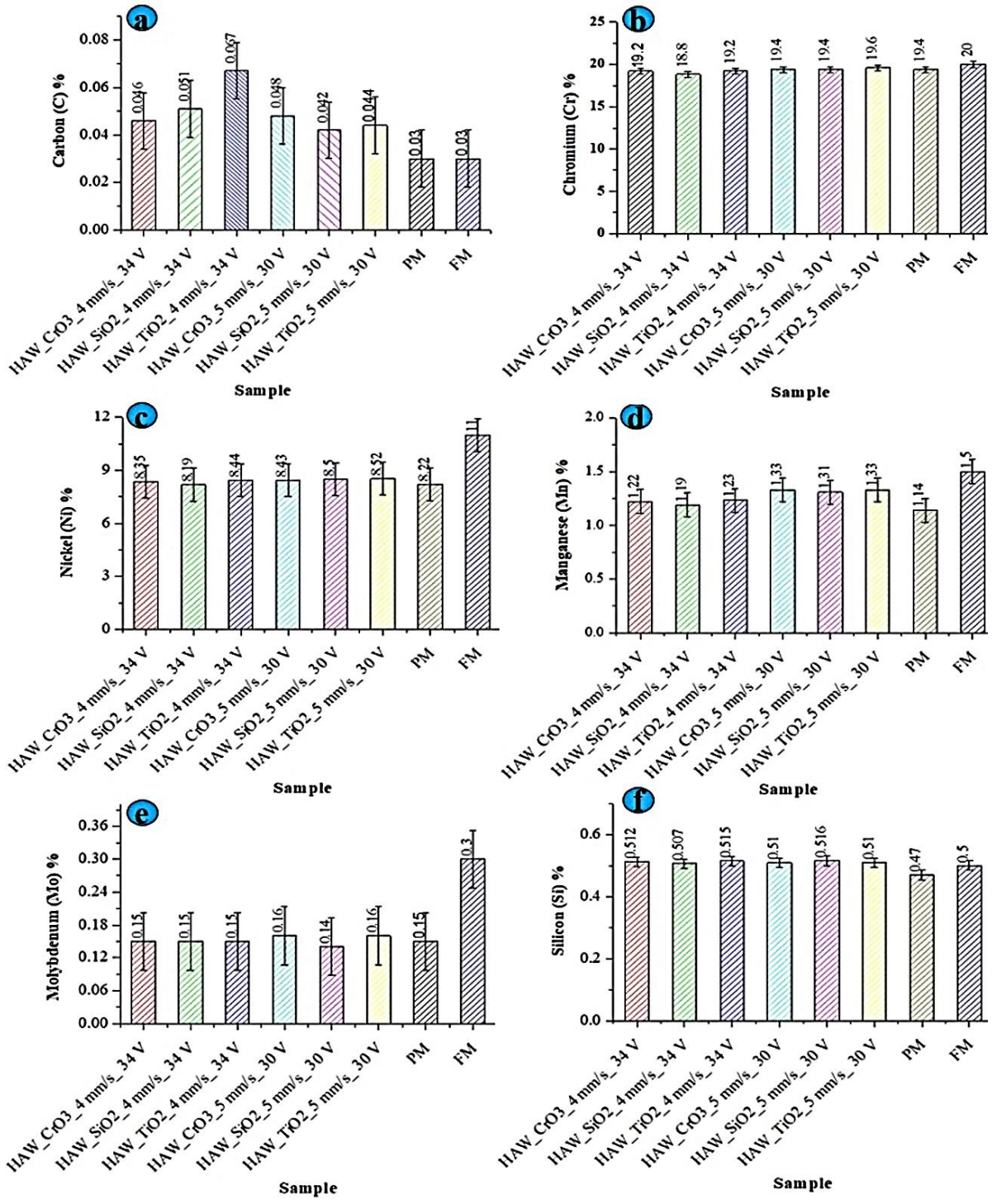


Figure 8.14: Represents variation of significant elements of tested specimens by spectroscopy (a) C, (b) Cr, (c) Ni, (d) Mn, (e) Mo and (f) Si percentage of the base metal, filler metals and fusion zone of all weld coupons

The resultant variation of these elements led to the variation of the ratio of $Cr_{eq}/Ni_{eq}$. If the ratio of $Cr_{eq}/Ni_{eq}$ is found to be less than 1.5, then the mode of solidification will be austenitic or austenitic-ferritic. Similarly, when this ratio lies between 1.5 - 2.0, then it will be ferritic – austenite mode. The solidification mode could be ferritic if it is more significant than 2.0 (mode IV) [121].

The bar chart in Fig. 8.15 shows the variation of the ratio of $\mathbf{Cr_{eq}}$ / $\mathbf{Ni_{eq}}$ for both the welding speed (i.e., 4 and 5 mm/s). The ratio of $\mathbf{Cr_{eq}}$ / $\mathbf{Ni_{eq}}$ was found in the range of 1.5 – 2. Hence, the present study suggests the ferrite to austenite solidification mode. Similar results were found in the conventional SAW study (previous chapter, i.e., Chapter 6).

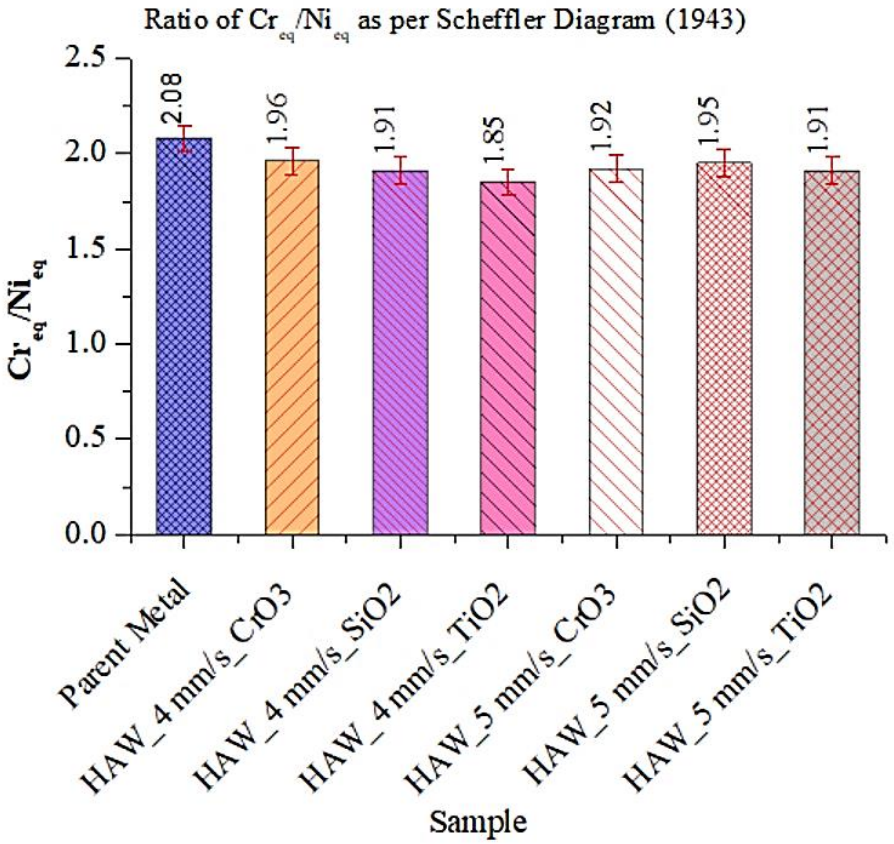


Figure 8.15: The plot of the calculated $Cr_{eq}$ / $Ni_{eq}$ ratio for the HAW samples

### 8.3.5 Effect of Hybrid Process (HAW) on Impact toughness

After welding, samples were extracted for further study. The samples were cut across the weld bead for microstructure analysis, micro-hardness, tensile, and toughness (Charpy), as shown in Fig. 8.16. The cut samples were further processed by grinding, polishing and etching to meet standard metallurgical procedures.

The schematic positions of extracted samples with the notch position justified the aim of this test. The 'V'- notch was intentionally kept perpendicular to the longitudinal direction of the

weld bead Fig. 8.16. It shows the specimen was extracted from a region covering half of the weld penetration profile, and half the area covers the HAZ and the parent metal area. The start and end parts (25.4 mm) were treated as rejected parts for all the welded coupons. The toughness of Charpy specimens was tested as per the ASTM E23 standard at room temperature (30°C) after confirming the notch size dimensions and position. Another view of non-standard extracted samples for the Charpy 'V' notch test is presented in Fig. 8.17 which were extracted using a wire-cut EDM. The term non-standard refers to the position of the extraction of the sample. The same samples were used to find the influence of HAW on the mechanical properties. The ready samples for the impact test (Charpy) are shown in Fig. 8.18, and the tested and etched specimens of the Charpy test are presented in Fig. 8.19. A comparison of the mechanical properties, including toughness test results, is shown in Table 8.5.

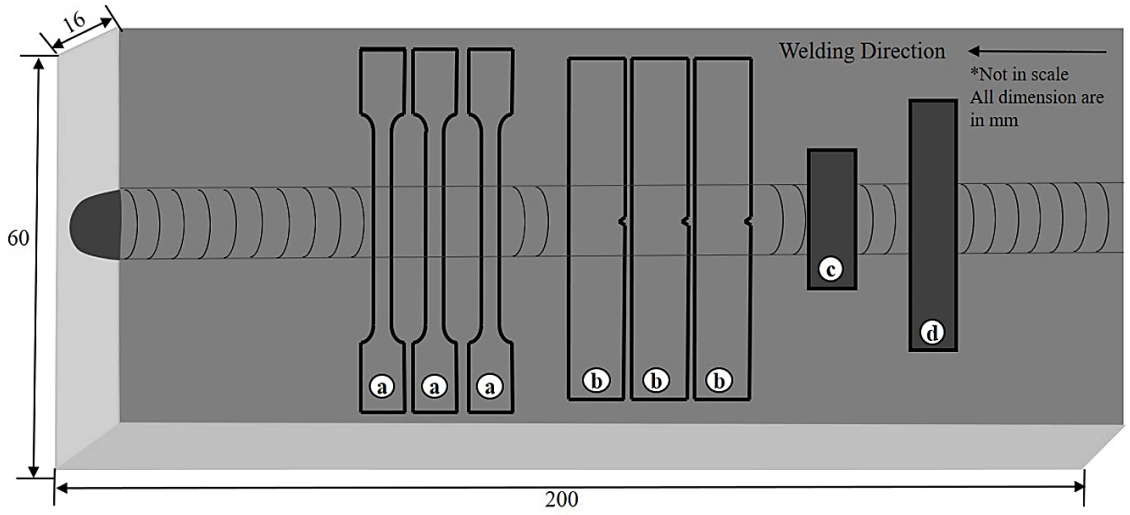


Figure 8.16: Schematic representation of extraction location of samples (a) transverse tensile test (b) Charpy impact toughness (c) microstructural analysis, and (d) for microhardness analysis

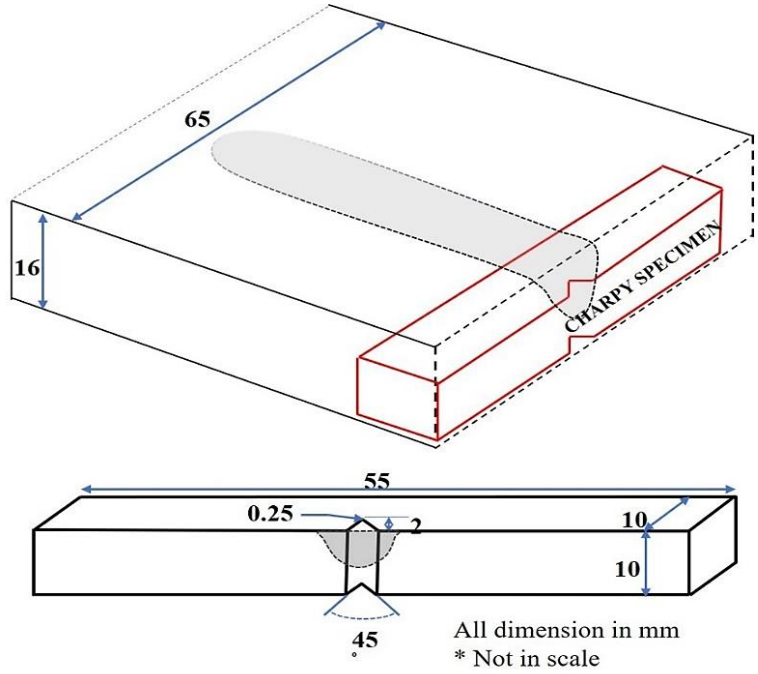


Figure 8.17: Schematic representation of the exact location of Charpy specimen with dimensions


Figure 8.18: Fabricated samples of Charpy "V" – notch specimens of HAW

Figure 8.19: Etched and Tested samples of toughness test (Charpy) show the penetration profile

Table 8.5: Comparison of calculated toughness and tensile strength of parent metal, SAW and HAW

| S. No. | | Specimen | Impact Energy (Joule) | Average Impact Toughness (Joule) | Tensile Strength (MPa) | Average Tensile Strength (MPa) | Yield Strength (MPa) | Average Yield Strength (MPa) | Percentage Elongation (%) |
|---|---|---|---|---|---|---|---|---|---|
| 3. | IV. | Parent Metal | 152 | 152 | 748 | 743.66 | 445 | 446.66 | 108.5 |
| | V. | Parent Metal | 152 | | 736 | | 450 | | 110 |
| | VI. | Parent Metal | 152 | | 747 | | 445 | | 109.5 |
| 4. | IV. | SAW – 7 | 155 | 157 | 669 | 675 | 420 | 410 | 77.3 |
| | V. | SAW – 7 | 153 | | 677 | | 410 | | 80 |
| | VI. | SAW – 7 | 165 | | 679 | | 400 | | 77 |
| 5. | I. | HAW_$CrO_3$_4 mm/s_34 V | 170 | **170** | 665 | **664.33** | 440 | **436.66** | 78.55 |
| | II. | HAW_$CrO_3$_4 mm/s_34 V | 168 | | 665 | | 440 | | 81 |
| | III. | HAW_$CrO_3$_4 mm/s_34 V | 172 | | 663 | | 430 | | 74.15 |
| 6. | I. | HAW_$SiO_2$_4 mm/s_34 V | 164 | 166 | 659 | 660.66 | 400 | 403.33 | 72.5 |
| | II. | HAW_$SiO_2$_4 mm/s_34 V | 168 | | 656 | | 400 | | 72.4 |
| | III. | HAW_$SiO_2$_4 mm/s_34 V | 166 | | 667 | | 410 | | 78.5 |
| 7. | I. | HAW _$TiO_2$_4 mm/s_34 V | 160 | 163.66 | 595 | 618.33 | 420 | 406.66 | 53.1 |
| | II. | HAW _$TiO_2$_4 mm/s_34 V | 168 | | 630 | | 400 | | 65 |
| | III. | HAW _$TiO_2$_4 mm/s_34 V | 162 | | 630 | | 400 | | 64.5 |
| 8. | I. | HAW_$CrO_3$_5 mm/s_30 V | 150 | 161.33 | 620 | 620 | 400 | 400 | 66.8 |
| | II. | HAW_$CrO_3$_5 mm/s_30 V | 150 | | 621 | | 400 | | 65.9 |
| | III. | HAW_$CrO_3$_5 mm/s_30 V | 184 | | 619 | | 400 | | 63.3 |
| 9. | I. | HAW_$SiO_2$_5 mm/s_30 V | 168 | 169.33 | 646 | 657 | 410 | 403.33 | 72.3 |
| | II. | HAW_$SiO_2$_5 mm/s_30 V | 170 | | 677 | | 400 | | 81 |
| | III. | HAW_$SiO_2$_5 mm/s_30 V | 170 | | 648 | | 400 | | 76.9 |
| 10 | I. | HAW _$TiO_2$_5 mm/s_30 V | 146 | 146.66 | 658 | 647 | 410 | 403.33 | 73.5 |
| | II. | HAW _$TiO_2$_5 mm/s_30 V | 152 | | 651 | | 400 | | 71.3 |
| | III. | HAW _$TiO_2$_5 mm/s_30 V | 142 | | 632 | | 400 | | 75.2 |

After analysis of the toughness test (Table 8.5) of the HAW process, it was concluded that all the HAW samples except the $TiO_2$_5mm_30 V sample took higher impact energy to break even from the parent metal sample and SAW sample (SAW – 7). The notch of all the samples of 5 mm/s welding speed, which were welded with 30 Volts, covers the maximum area of HAZ.

### 8.3.6 Effect of Hybrid Process (HAW) on Tensile Strength

For finding the weld strength, tensile tests were performed for all the extracted samples of HAW. For the tensile test, three samples were extracted from each weld coupon. The tensile test was conducted using TINIUS OLSEN (Model HK50S) machine using a standard procedure (ASTM E8M). The **2 mm/min** crosshead velocity was employed during all the tensile tests. The schematic diagram with a dimension of the sample preparation and machine used for this test is shown in Fig. 8.19. The samples were extracted using wire-cut EDM, and all-welded samples were polished and etched by using 'carpenter etchant' to show the region of weld profile and are presented in Fig. 8.19.

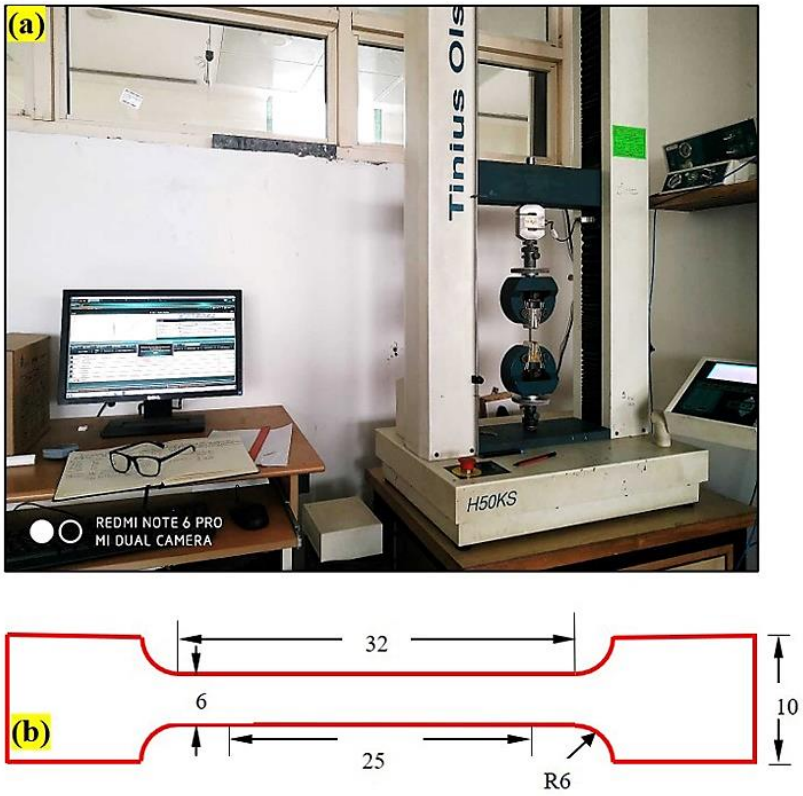


Figure 8.20: (a) Tensile testing machine (Courtesy: IIT Ropar Campus, Ropar)
(b) Schematic illustration of subsize tensile specimen

The subsize tensile specimen gauge length and reduced section length were maintained as per standards (Fig. 8.20 b) without compromising the grip length because the available width of the base metal plate which was in the range of 58 to 60 mm. All the tensile tests were performed

at room temperature ensuring proper grip. The extracted samples of tensile testing, unpolished and polished with etching for both the welding speed (i.e., 4 mm/s and 5 mm/s) are presented in Fig. 8.21 (A – D). The weld profile is visible in the polished samples. This was intentionally done to ensure the location of the fracture during the test and for further analysis. The tested samples (after fracture) are presented in Fig. 8.22, which shows the fracture took place from the weld centre in all the specimens. After comparing the tensile specimen of the HAW and SAW study (Chapter 6, Fig. 6.13), it was found that the middle part of the tensile samples of HAW consist/exhibit a whole fusion zone. Whereas the tensile samples of the SAW study (Fig. 6.13) had both fusion and some part of the unaffected heat zone, and the SAW – 7 tested tensile samples exhibit some marginal increase in tensile strength.

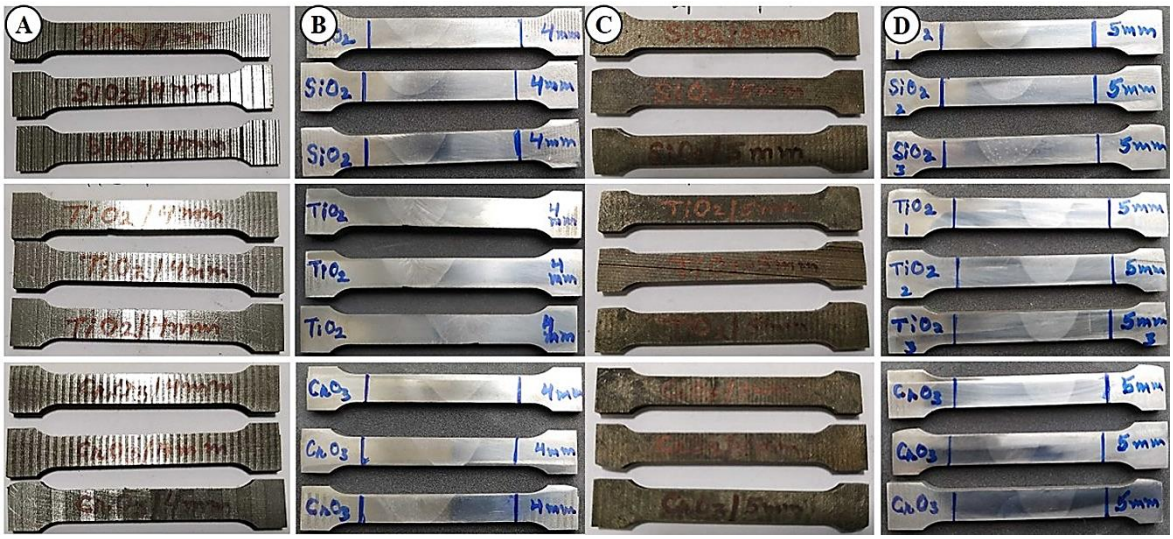


Figure 8.21: Extracted samples for tensile testing, unpolished and polished (A) and (B) For 4 mm/s welding speed (C) and (D) For 5 mm/s welding speed

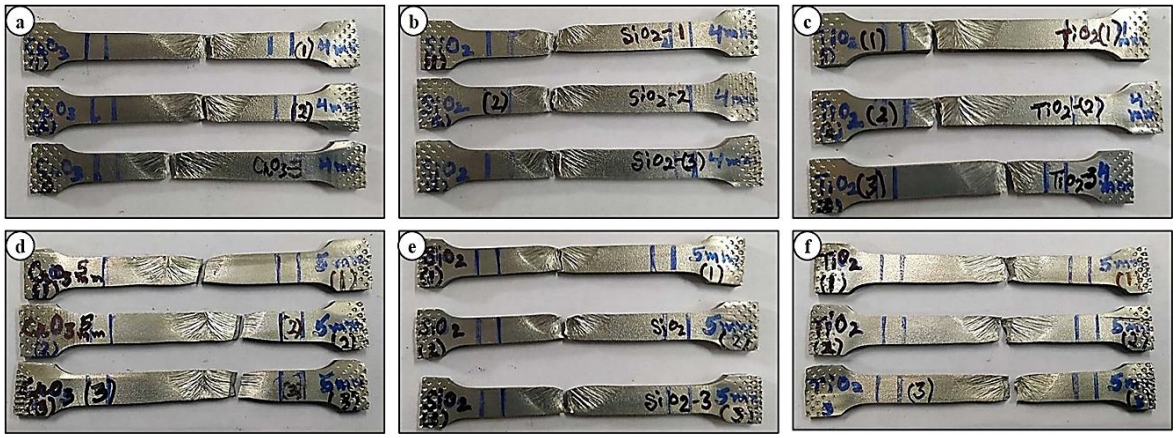


Figure 8.22: Fractured/Tested samples of HAW (a) – (c) of 4 mm/s welding speed and (d) – (f) of 5 mm/s welding speed

Figure 8.23 shows the stress-strain curve for all the HAW samples. From the tensile testing results represented in Table 8.5, the coupon welded with CrO3 flux produced more yield strength than the conventional SAW – 7 sample.

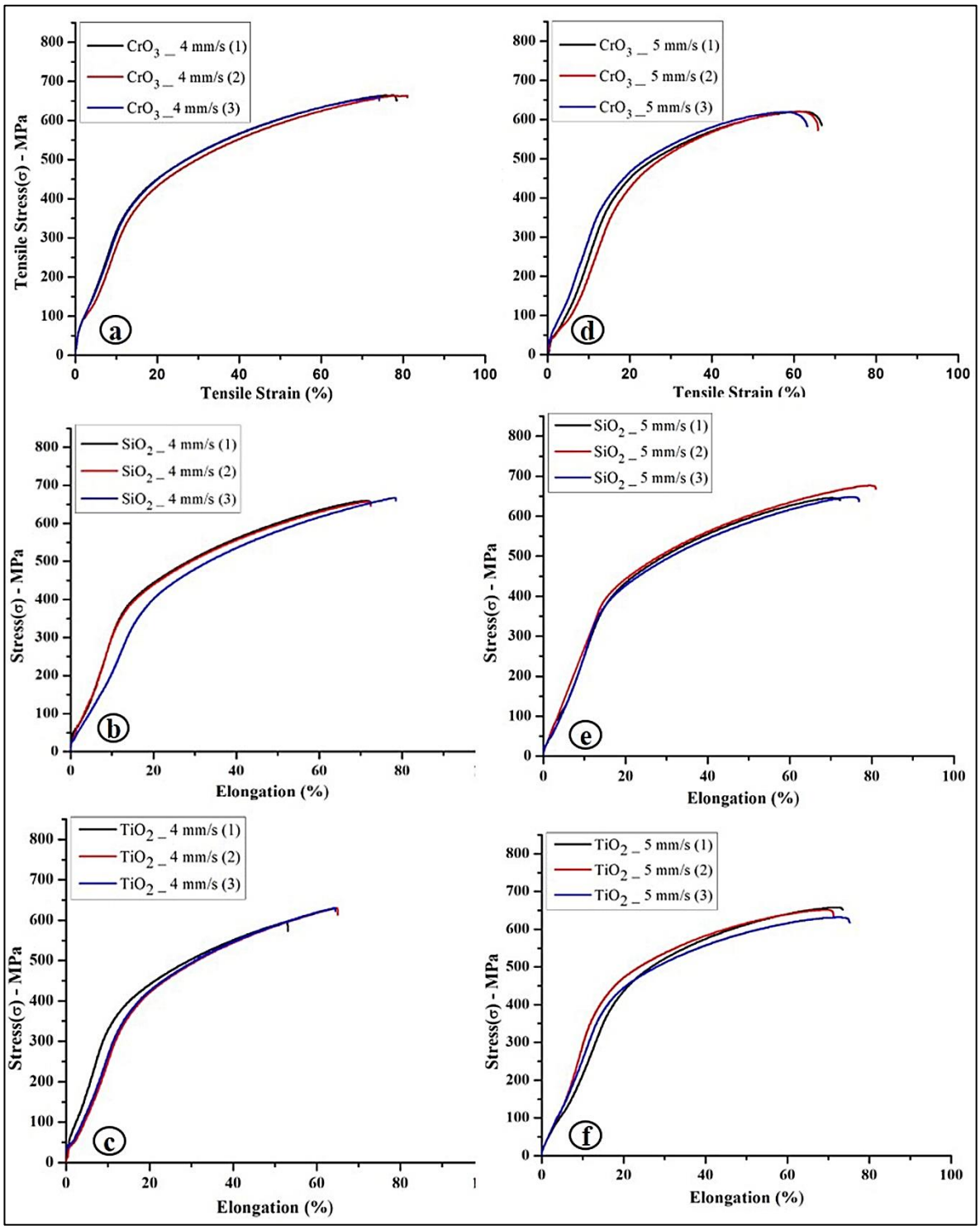


Figure 8.23: Tensile stress v/s tensile strain curve for HAW (a-c) for 4 mm/s welding speed and (d-f) for 5 mm/s welding speed

### 8.3.7 Fractography Analysis

Fractography analyses were performed to observe the surface of all the fractured Charpy specimens and tensile test specimens of HAW samples. SEM was used to take images of different magnification at different locations to analyze fractured surfaces. Figure 8.24 represents HAW_$CrO_3$_4 mm/s of sample no. **1**. The fibrous structure of austenite on the grain boundary is visible with dimples (Fig. 8.24 A, B, and D), which formed after the plastic flow of microvoids and coalesced into larger voids. The varied dimples size was found in the case of HAW with $CrO_3$ flux, and from 2 – 20 µm size (Fig. 8.24 A and B). The significant necking of material produced these types of dimples, and this type of fracture produced a ductile fracture. The highest value of average impact energy (170 ± 2 Joule) was observed in HAW_$CrO_3$ (iii) samples which were welded with 34 volts and 4 mm/s welding speed.

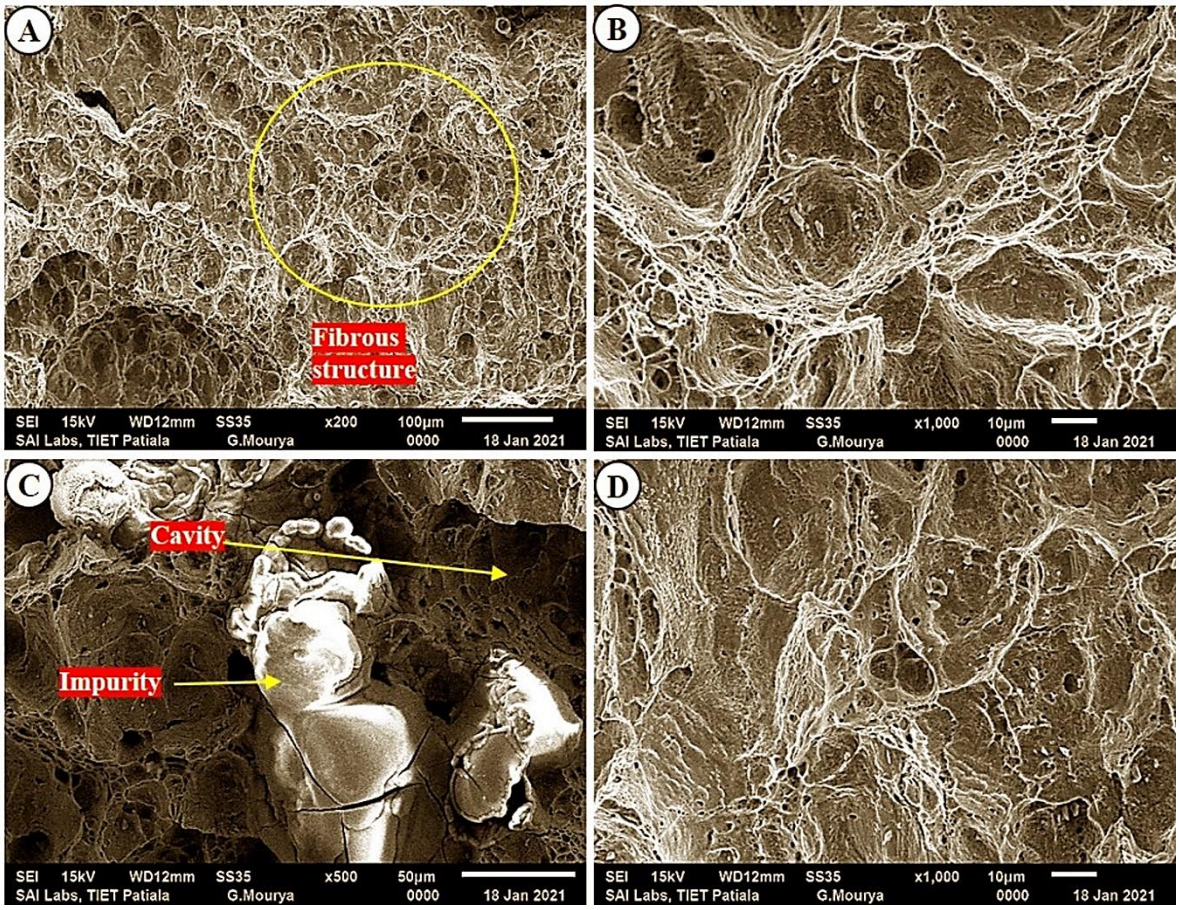


Figure 8.24: SEM micrographs of toughness test fractured surface of different magnification of HAW_$CrO_3$_4 mm/s sing 34 volts

An oxide formation was also observed at one place, which is shown in Fig. 8.24 C, and the validation of the observed impurity was done using EDS analysis, which is shown in Fig. 8.27 (a).

Figure 8.25 represent HAW_$SiO_2$_4 mm/s of sample no. **3**. In this case (Fig. 8.25), some microvoids (white arrow) were observed in the SEM microstructure. A fracture path is also observed within ferrite grain (Fig. 8.25 D), leading to a cavity. The presence of such crack evidenced the presence of some large columnar grain structure.

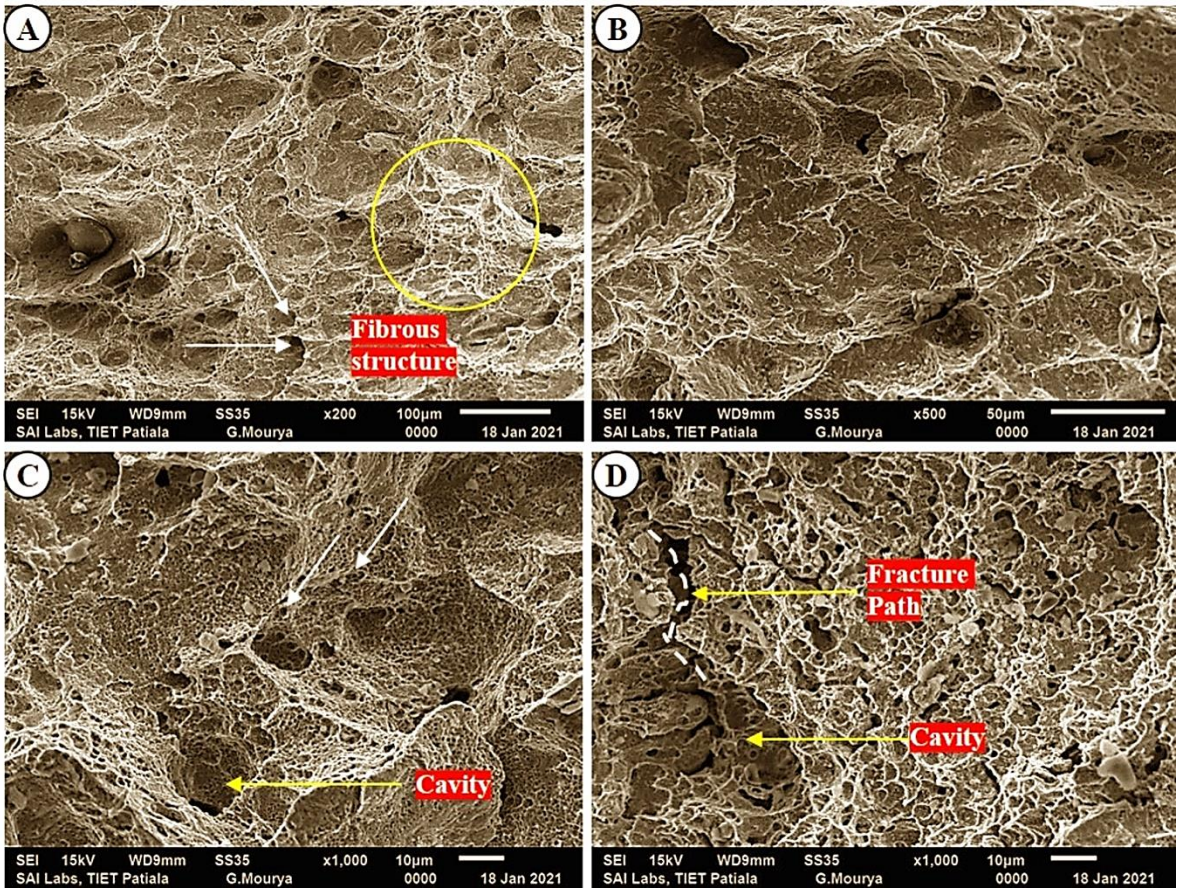


Figure 8.25: SEM micrographs of toughness test fractured surface of different magnification of HAW_$SiO_2$_4 mm/s using 34 volts

Figure 8.26 represents the micrograph of toughness sample no. 1 of HAW_TiO2_4 mm/s study, in which porosity and a cavity were observed (Fig. 8.26 A and D). Some microvoids were also observed in the micrograph with a sufficient amount of austenite distribution having a fibrous structure. Minute-sized oxides were also observed in the cavity (Fig. 8.26 A) and were further analysed by EDS analysis (Fig. 8.29). No traces of carbide precipitation were found during fractography of fractured toughness samples of the HAW process. The toughness value or the energy absorbed during the **V – notch** Charpy test was observed more than the toughness value of parent metal except for the samples welded with $TiO_2$_30 V_5 mm/s (Table 8.5).

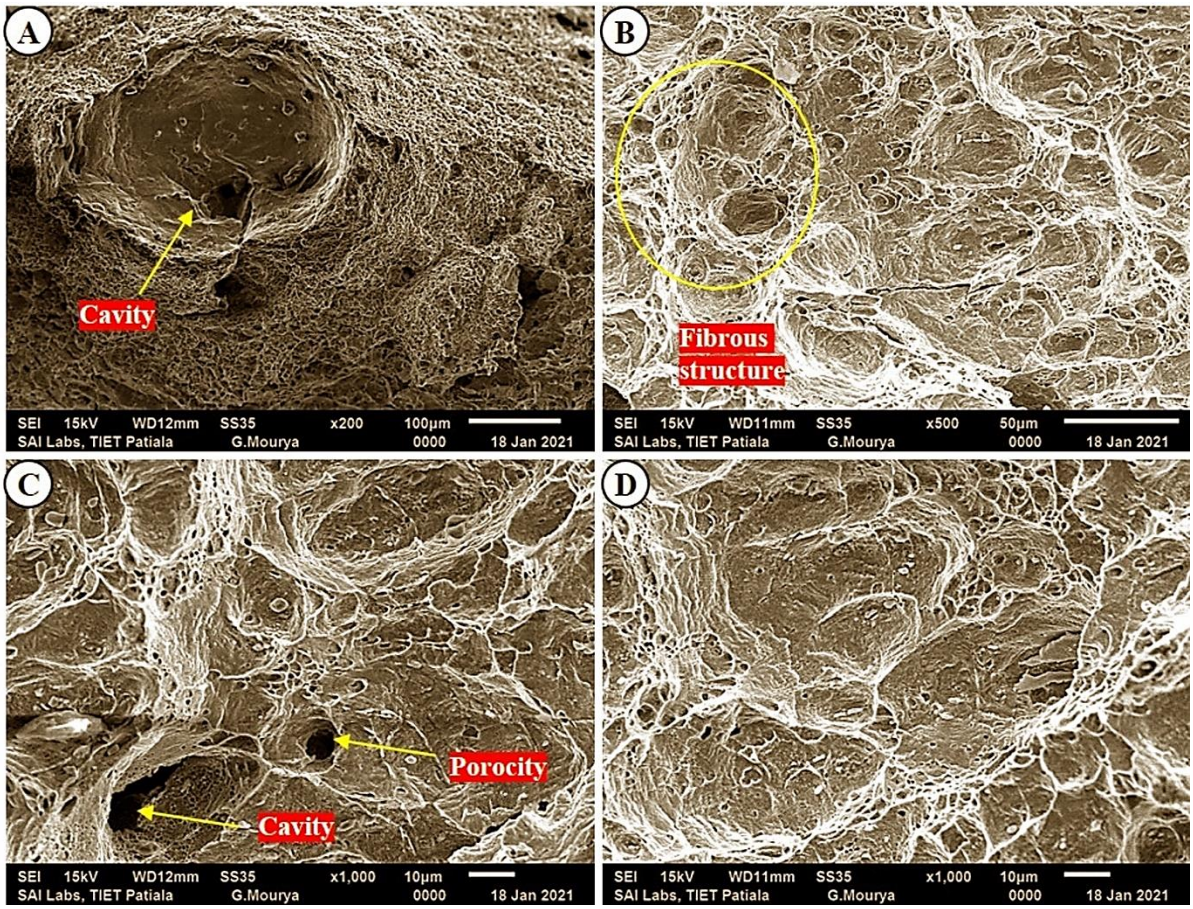


Figure 8.26: SEM micrographs of toughness test fractured surface of different magnification of HAW_$TiO_2$_4 mm/s using 34 volts

Similarly, the fractured analysis of all the tensile samples (fractured samples) was performed for both the welding speeds, i.e., 4 mm/s and 5 mm/s (Fig. 8.27 – Fig. 8.29). The SEM micrographs were taken at three magnification levels, i.e., 200 X, 100 X, and 500 X of different locations. Figure 8.27 (a) – (c) represents HAW_$CrO_3$ of sample 1, which was welded at 4 mm/s welding speed, and Fig. 8.27 (d) – (f) represent HAW_$CrO_3$ of sample no.1, which was welded at 5 mm/s welding speed. After analysis, no impurities were found on the fractured surface. Both welding speed samples produce a ductile fracture and have a dimple (pit) structure. The only difference is the size of dimples observed in both samples. The average size of dimples was measured as 2.5 - 3 µm in the case of 4 mm/s welding speed samples and 2 - 2.5 µm in the case of 5 mm/s welding speed samples. But some microvoids were found in the 5 mm/s welding speed samples, which results in low average tensile strength.

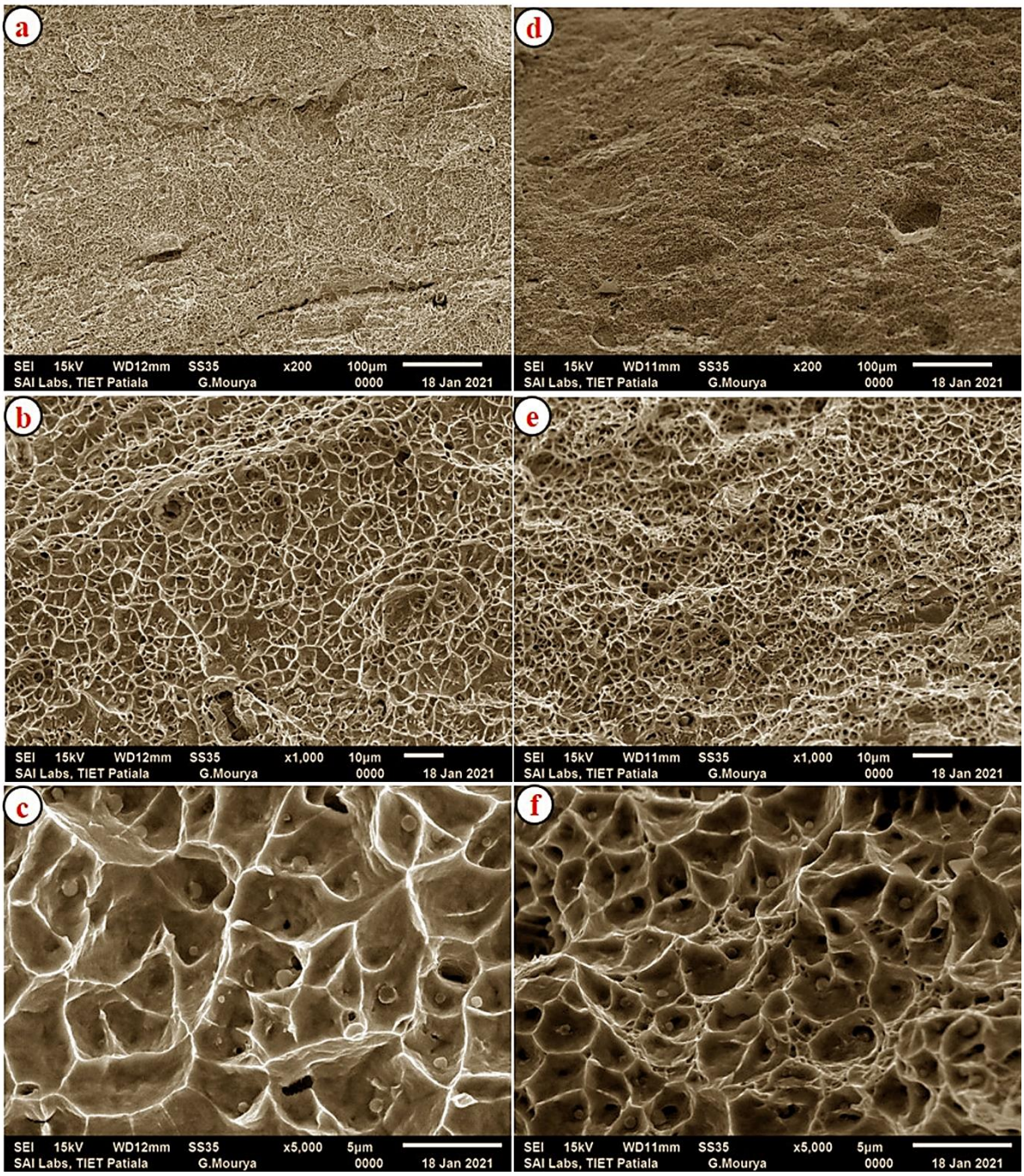


Figure 8.27: SEM micrographs of tensile test fractured surface of different magnification of (a) – (c) HAW_$CrO_3$_4 mm/s using 34 volts (d) – (f) HAW_$CrO_3$_5 mm/s using 30 volts

Similarly, Figure 8.28 (a) – (c) represent to HAW_$SiO_2$ of sample 3, which was welded at 4 mm/s welding speed, and Fig. 8.28 (d) – (f) illustrate HAW_ $SiO_2$ of sample no. 3, which was welded at 5 mm/s welding speed. No impurity was observed in both the samples and the average size of dimples were also equal i.e., 2 – 5 µm. But a small difference in average tensile strength was noticed due to the existence of some microvoids in the case of sample welded with 5 mm/s (Table 8.5).

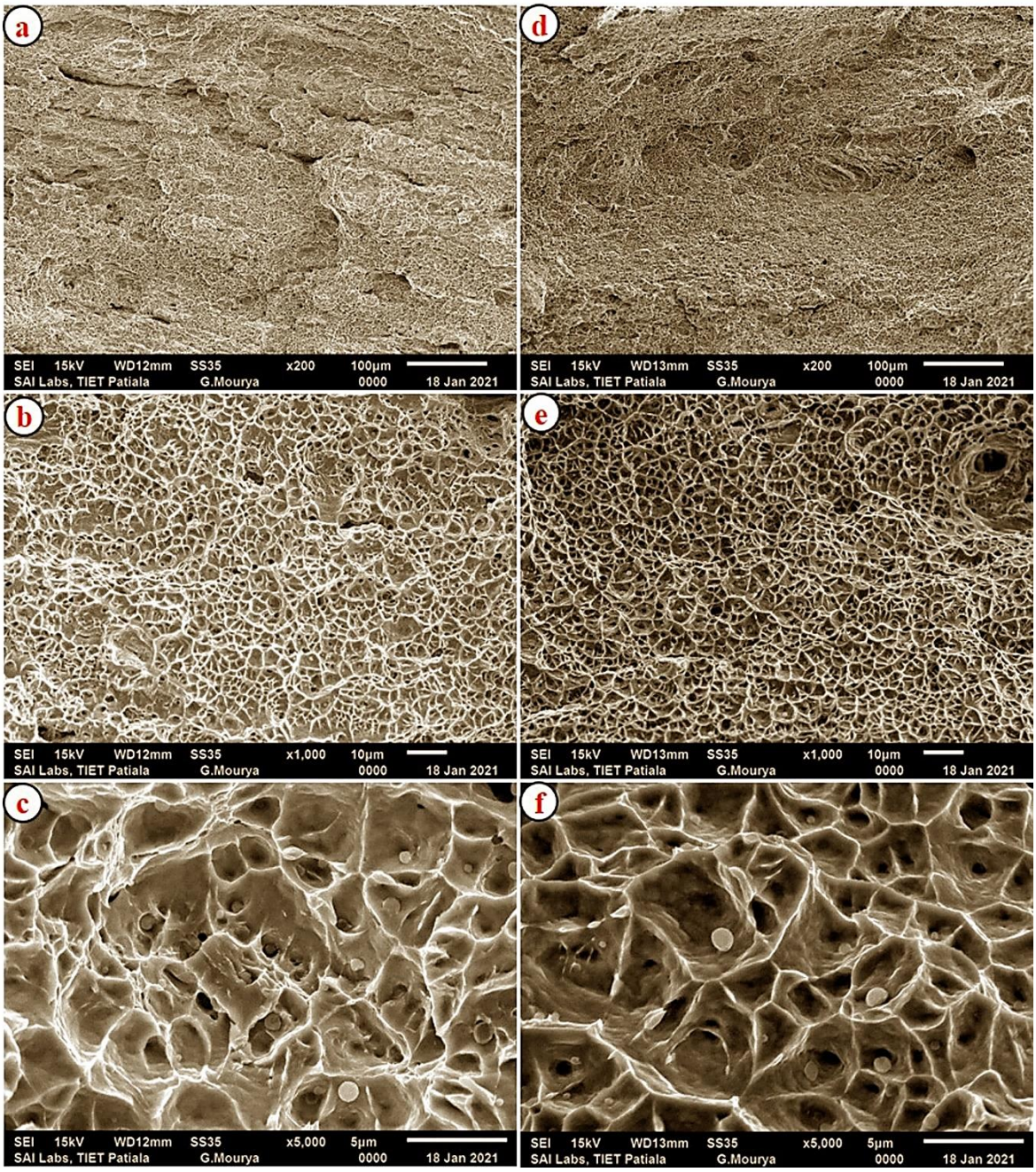


Figure 8.28: SEM micrographs of tensile test fractured surface of different magnification of (a) – (c) HAW_$SiO_2$_4 mm/s using 34 volts (d) – (f) HAW_ $SiO_2$_5 mm/s using 30 volts

Similarly, Figure 8.29 (a) – (c) represent to HAW_$TiO_2$ of sample 1, which was welded at 4 mm/s welding speed, and Fig. 8.29 (d) – (f) represent HAW_ $TiO_2$ of sample 3, which was welded at 5 mm/s welding speed. An impurity with microvoids was observed in the sample which was welded at 4 mm/s welding speed (Fig 8.29 a-c), and some inclusion (Fig 8.29 d) with a porosity (Fig 8.29 e) of size 45.416 µm was also observed in case of the sample which was welded using 5 mm/s welding speed. Hence, the presence of inclusion and porosity ultimately reduced the tensile strength for these particular samples (Table 8.5).

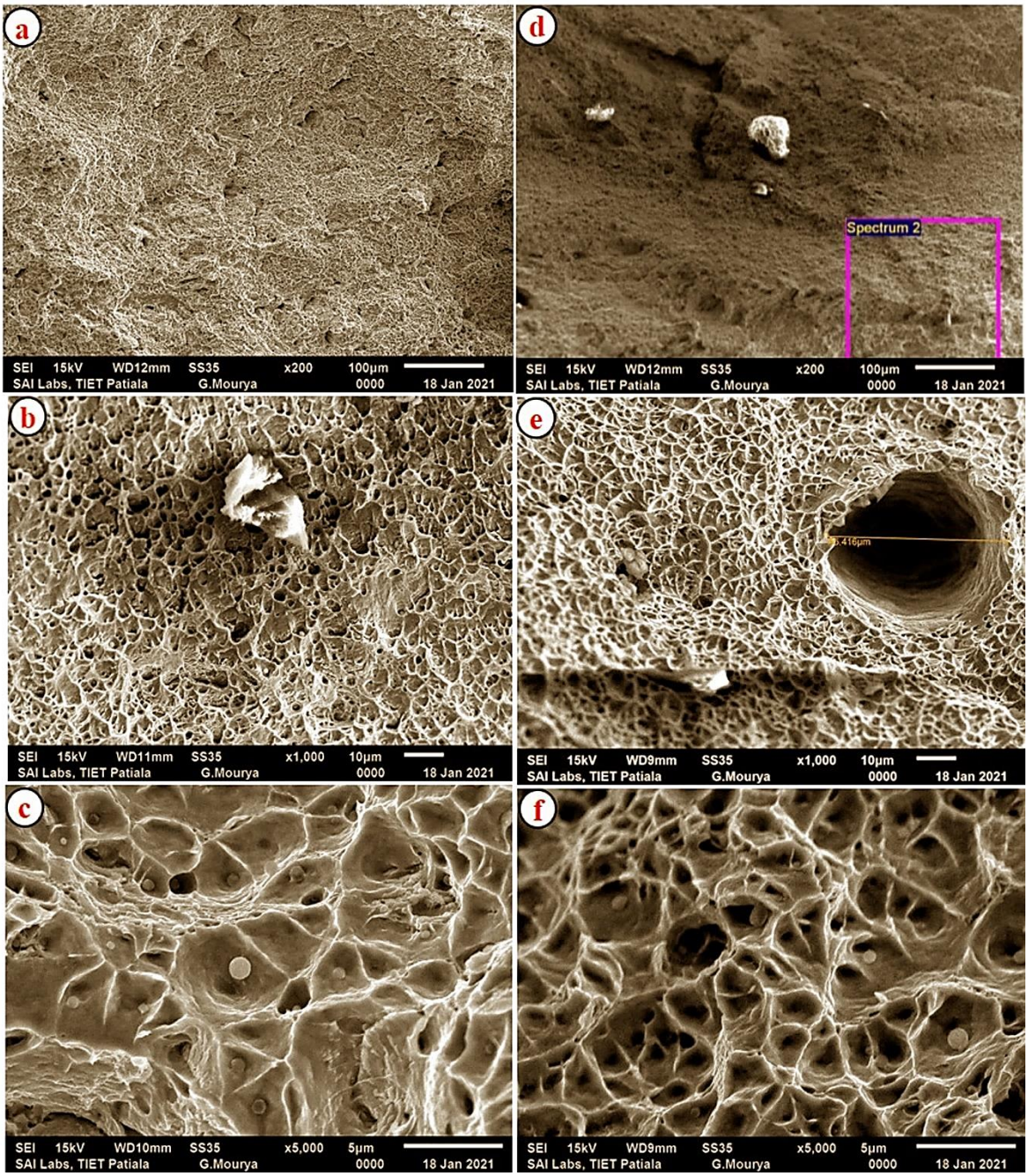


Figure 8.29: SEM micrographs of tensile test fractured surface of different magnification of (a) – (c) HAW_$TiO_2$_4 mm/s using 34 volts (d) – (f) HAW_ $TiO_2$_5 mm/s using 30 volts

### 8.3.8 EDS Analysis

The EDS analysis of the toughness sample for the 4 mm/s study is presented in Fig. 8.30. The highlighted region spectrum of a fractured specimen of HAW_$CrO_3$_4 mm/s is also shown in Fig. 8.30. The SEM image of the particular region is also shown with the result of EDS. The high amount of oxygen with iron element indicates that it is an iron oxide (Fig. 8.30 a). The rest is austenite stainless steel, which was found near this impurity, and the resultant elements are shown in Fig. 8.30 (b).

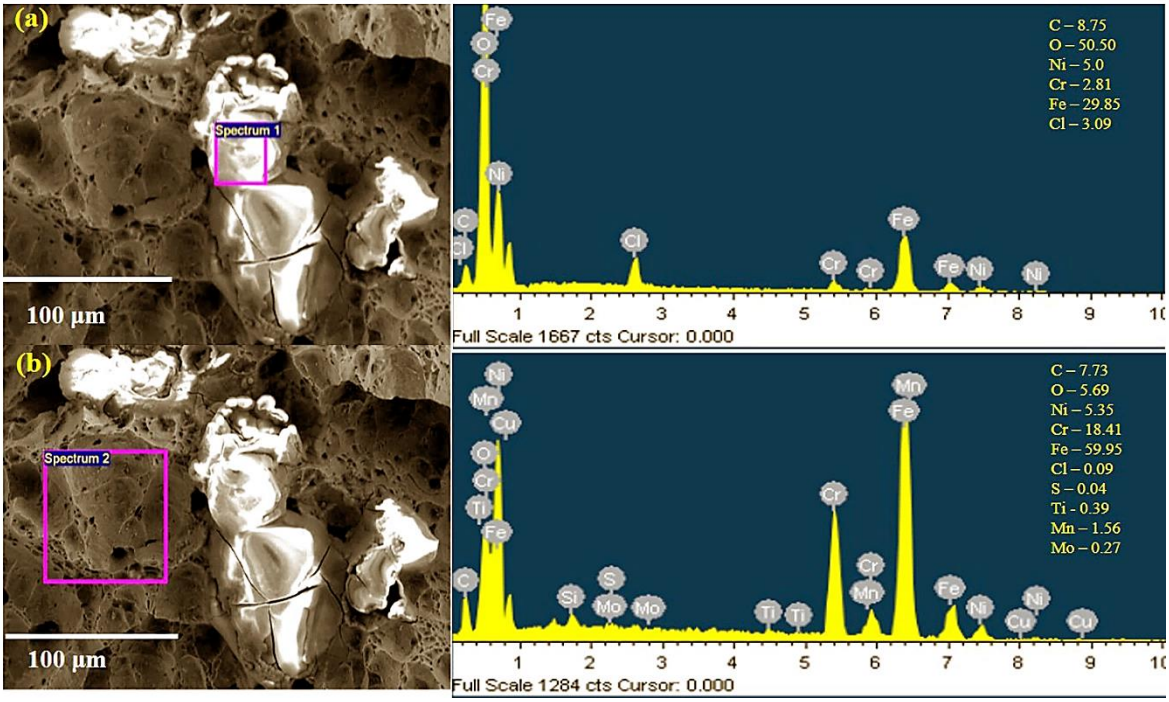


Figure 8.30: EDS spectrum of toughness sample of HAW_$CrO_3$_4 mm/s (a) Impurity region (b) metal region

In the case of the HAW_$SiO_2$_ 4 mm/s sample, a small impurity of iron oxide was found, and the corresponding spectrum is also presented in Fig. 8.31 (a), and spectrum 2 of the nearby region shows the chemical composition of austenitic stainless-steel Fig. 8.31 (b).

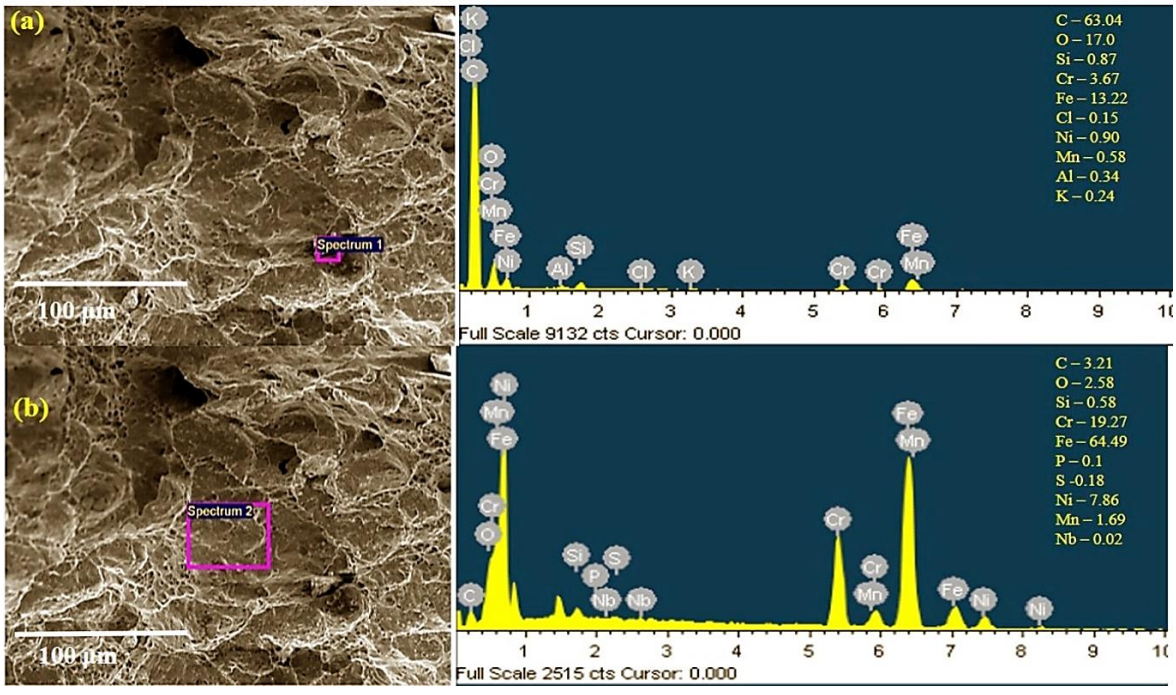


Figure 8.31: EDS spectrum of toughness sample of HAW_$SiO_2$_4 mm/s (a) Impurity region (b) metal region

A big size cavity was formed after the fracture in HAW_$TiO_2$_4 mm/s sample, shown in Fig. 8.32 (a), in which some parted chromium-rich oxide was noticed, which could be confirmed through the EDS spectrum (Fig. 8.32).

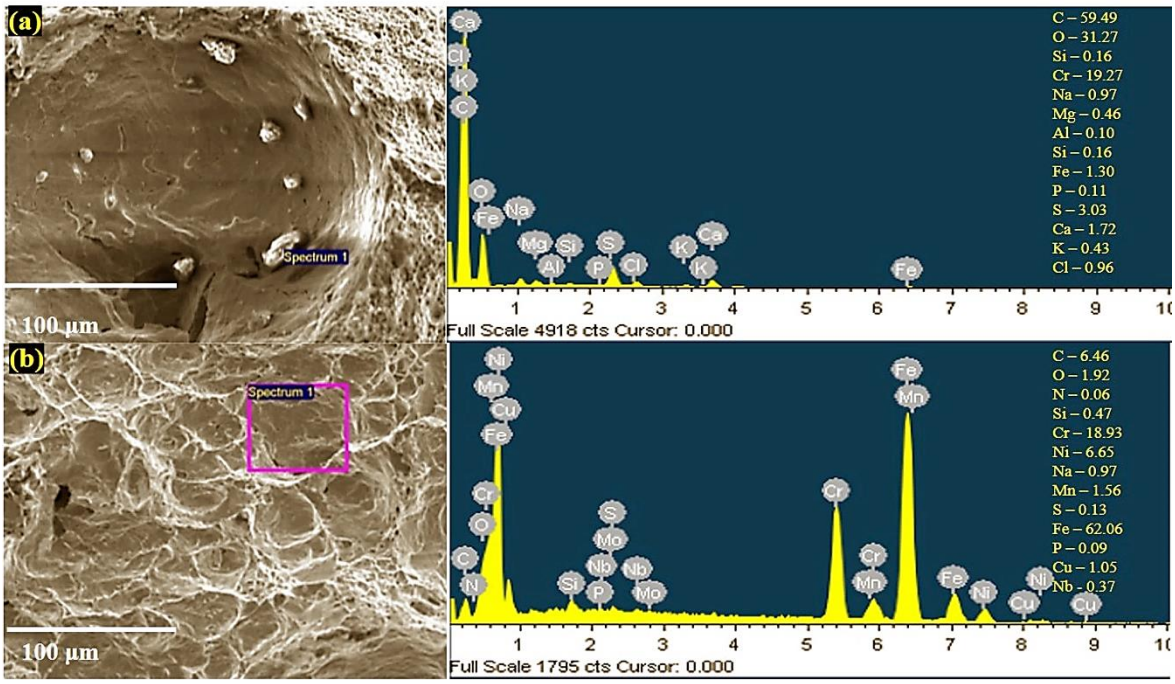


Figure 8.32: EDS spectrum of toughness sample of HAW_$TiO_2$_4 mm/s (a) Impurity region (b) metal region

### 8.3.9 Microhardness Analysis

The microhardness of HAW samples was measured along the horizontal axis (across the width) and vertical axis (across the thickness) of the weld bead and presented in Fig. 8.33. The microhardness test was performed by keeping a 1.5 mm distance below the surface of the parent metal and by maintaining a constant gap of 0.5 mm in each reading point for both directions of measurement. HV measurement was taken from the unaffected heat area, then crossed HAZ, fusion zone, and finally finished at unaffected heat area. A similar gap of 0.5 mm was maintained in the vertical axis direction. For vertical direction, the microhardness point starts from the fusion zone and then crosses the weld profile's thickness. The direction of microhardness measurement and the observed microhardness is presented in Fig. 8.33. The average microhardness of parent metal was observed as **271 ± 3 HV**. More variation of HV range was observed in 5 mm/s welding speed samples as compared to 4 mm/s welding speed samples. The main cause of the fluctuation of HV in the case of 5 mm/s welding speed is the fast cooling of weld metal compared to 4 mm/s welded samples. For the vertical axis measurement (centre of fusion zone), the range of HV for both the welding speed was observed on the lower side. The average HV of HAW samples of both the welding speed was found to

be less as compared to the parent metal. The sufficient heat input and the slow cooling of molten metal produced fine grains after recrystallization in the fusion zone which ultimately increased the toughness of the weld.

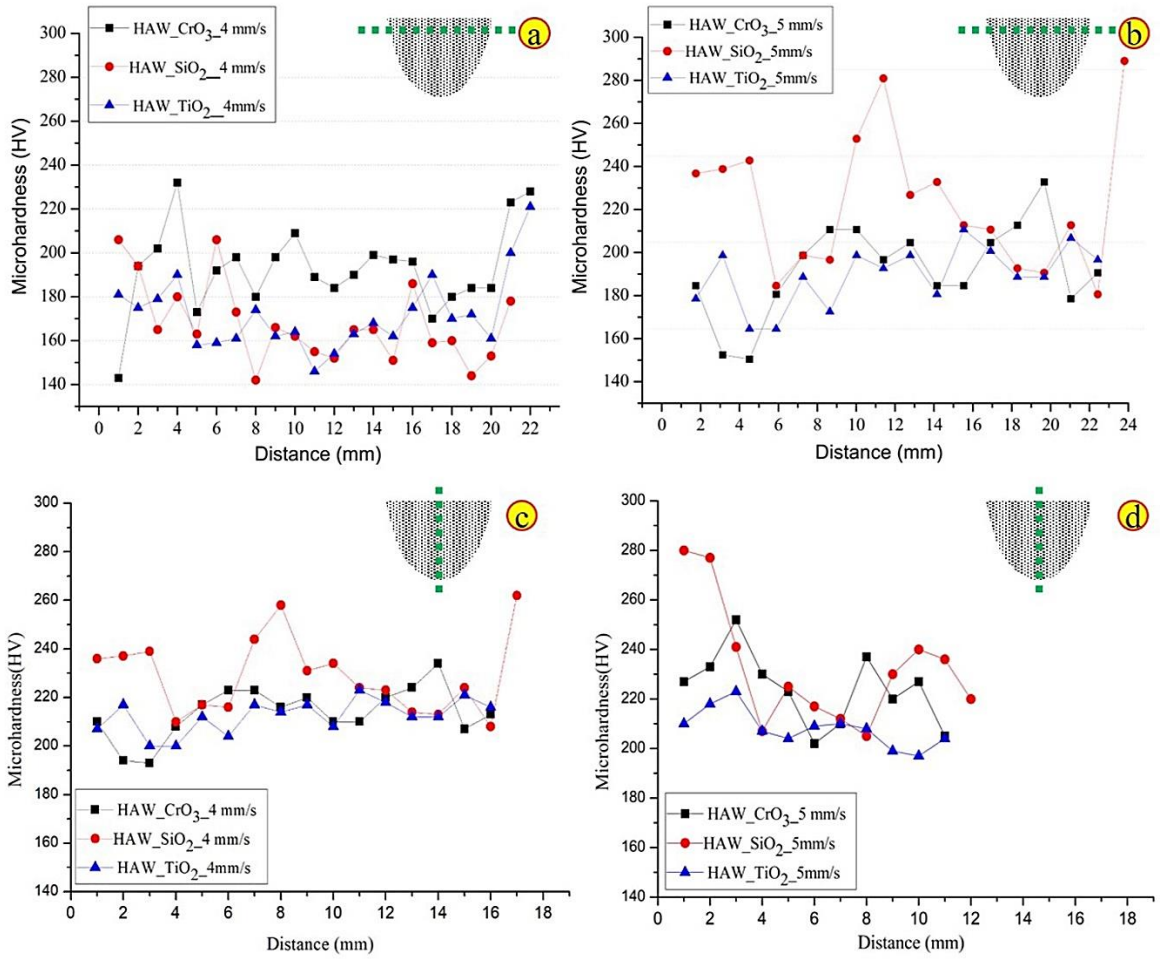


Figure 8.33. Microhardness variation along with horizontal and vertical axis (a) – (c) samples of HAW welded at 4 mm/s using 34 V (d) – (f) samples of HAW welded at 5 mm/s using 30 V

## 9.4 Summary

The combined effect of both the A-TIG and SAW process arc provided a smooth weld bead in the presence of $TiO_2$, $SiO_2$ and $CrO_3$ activated flux. So, All the HAW coupons were observed defect-free during the visual inspection. The coupons that were welded at 4 mm/s welding speed using 34 **V** produce the highest and similar depth of penetration. The average fracture toughness of HAW samples was found more as compared to conventional SAW welding samples and parent metal samples except for one sample, i.e., the HAW_$TiO_2$_5mm/s welding speed sample. The tensile properties of the HAW_$CrO_3$_4 mm/s sample were found more favourable as compared to other HAW samples, and the average yield strength was found to be greater than the conventional SAW welding sample. All the toughness and fractured tensile samples showed a ductile fracture, and during SEM analysis of the fractured surface, impurity/porosity was observed in some cases. The average microhardness of all the HAW samples was found to be lower than the parent metal.

# Chapter - 9
## Conclusions and Future Scope

## Conclusions

The objective of the present study was to explore the use of A – TIG welding and the development of a hybrid process to improve the mechanical properties of stainless-steel welded joints without edge preparation thereby improving the productivity of the process. The present study investigated the effect of different types of oxide-based activated flux on penetration depth, depth-to-width ratio, metallurgical changes, slag metal and gas metal reaction, mechanical properties with varying shielding environments. The investigation was carried out on different graded steels like austenitic stainless steels (AISI 304 and AISI 316) and duplex stainless steel (Duplex 2205) using conventional TIG and A – TIG welding, SAW, and HAW. A comparison between traditional TIG and A – TIG welding and a comparison of SAW and HAW in a different study was also accomplished.

The conclusions drawn from the investigation of A - TIG welding, SAW and HAW are summarized below.

### Objective 1: Study the weld profile development during Activated TIG (A-TIG) welding for different grades of stainless steel at the different exposure time

1. In A-TIG welding, the oxygen-rich fluxes interact with the arc's outer region electrons, which lead to redistribution of charge carrier. This phenomenon was found to be the primary cause of arc constriction.
2. Maximum influence of low aspect ratio was observed in case of A – TIG welding of Duplex Stainless Steel (DSS).
3. Heat transfer in the molten pool was dominated by convection mode due to activated fluxes, which was reflected from the higher Peclet number (*Pe*).
4. Oxide-based flux governs the dendrite arm spacing and length of dendrites due to the effect of heat produced, which is influenced by oxygen content in the weld. More oxygen content with higher heat generation dominates the larger grain size, long dendrite length, and higher dendrite arm spacing in case of A-TIG welding with $SiO_2$ and $CrO_3$ flux.
5. The presence of oxygen / oxide-based fluxes leads to the formation of CO / $CO_2$ in the weld, and that could be the main reason for void/cavity formation and associated

cracking due to the volumetric expansion of gas. The activated flux did not affect the hardness behaviour of the weld significantly.

6. The dendrite growth rate is directly governed by the thermal Energy of arc produced owing to surface-active elements along with the $H_2$-induced shielding. The dendrites growth is vertical in conventional TIG. However, it is horizontal in A-TIG ($H_2$ induced) owing to the high thermal Energy of arc and associate cooling rate.

## Objective 2: To evaluate the performance of A-TIG welded joints for difficult positions with different shielding environment

1. A – TIG in the vertical position using Ar shielding environment produced flawless weld and no significant change in the microstructure and the microhardness was observed.
2. The use of $H_2$ mixed shielding causes higher temperature owing to a higher enthalpy rate, which further leads to undercutting along the sides of the weld bead. The A – TIG welding using $H_2$ mixed shielding environment at high range of current is difficult to handle due to the high melting rate.
3. The average penetration area and the dilution rate during vertical/uphill welding position is significantly increased with an increase in current and as well as with $H_2$ mixed shielding environment. The simultaneous effect on reinforcement area (i.e., less reinforcement area) was also observed in the case of the $H_2$ mixed shielding environment.
4. Toughness upsurges with high current and $H_2$ mixed shielding with 14 L/min gas flow rate improve the dilution rate. Whereas moderate current, i.e., 140 A, and higher gas flow rate, were observed to be the most significant factors that decrease the average toe angle of the weld bead.

## Objective 3: To study the profile of the weld bead during the SAW for AISI 304

1. The most significant parameters found were welding voltage and travel speed responsible for the change in bead profile characteristics and mechanical properties.
2. SAW at 34 **V** and 4 mm/s speed justifies the relationship of $\mathbf{R_w / P \geq 2}$, **and** $\mathbf{R_w/R_h \geq 6}$.
3. At lower voltage (30 **V**), the weld bead height increases, and the weld bead appearance is uneven, leading to defects like porosity. However, higher voltage and low speed produce a smooth welding bead with no flaw.
4. Maximum penetration was achieved with high voltage and low speed, i.e., 34 V and 4 mm/s. No significant change in the remaining delta ferrite type was observed in the middle of the fusion zone.

5. The result shows that the ratio of $Cr_{eq}/Ni_{eq}$ is between1.5 - 2.0, so the solidification mode is ferritic – austenite.

### Objective 4: To develop a hybrid welding process (A-TIG + SAW) and study of weld bead profile obtained on AISI 304

1. The average fracture toughness of HAW samples was found to be higher than conventional SAW and parent metal samples except for in one case (HAW_$TiO_2$_5mm/s).
2. The tensile properties of the HAW_$CrO_3$_4 mm/s sample are more favourable as compared to other HAW samples, and the average yield strength of the same sample was found to be greater than the conventional SAW welding sample.
3. All the toughness and fractured tensile samples showed a ductile fracture, and during SEM analysis of the fractured surface, some impurity with porosity was observed in some cases.
4. The average microhardness of all the HAW samples was found lower than the parent metal, and some variation in the hardness value was observed in the case of 5 mm/s welding speed samples.

Finally, it can be concluded that the new HAW process provides better weld quality as compared to stand-alone A-TIG or SAW with minimum edge preparation for high thickness welding. It significantly increases the material deposition rate resulting in enhanced productivity of the process.

## Future Scope:

Suggested future scope of work includes:

- Development of numerical simulation of HAW.
- HAW by using higher heat input of A – TIG welding.
- It may be tried using constant current characteristics.
- It may also try with a higher output source of conventional GTAW/TIG welding.
- HAW may also try with the acidic nature of agglomerated flux.

# List of Publication:

| Sr. No. | Title of Paper | Authors' Name | Journal | Volume, Year, Page no. | Impact Factor |
|---|---|---|---|---|---|
| 1. | A-TIG welding process for enhanced-penetration in Duplex stainless-steel: effect of activated fluxes | **Surinder Tathgir, Dinesh W. Rathod & Ajay Batish** | Materials and Manufacturing Processes (Taylor & Francis, SCI Journal) | 34, 2019, 1659 – 1670 | **4.616** |
| 2. | Process enhancement using hydrogen-induced shielding: $H_2$-induced A-TIG welding process | **Surinder Tathgir, Dinesh W. Rathod & Ajay Batish** | Materials and Manufacturing Processes (Taylor & Francis, SCI Journal) | 35, 2020, 1084 – 1095 | **4.616** |
| 3. | Emphasis of Weld Time, Shielding Gas and Oxygen Content in Activated Fluxes on the Weldment Microstructure | **Surinder Tathgir, Dinesh W. Rathod & Ajay Batish** | Mechanical Engineering for Society and Industry (Universitas Muhammadiyah Magelang) | 1, 2021, 86 – 95 | **-- (Scopus)** |

**1st Research Paper – DOI:** 10.1080/10426914.2019.1666990

**2nd Research Paper – DOI:** 10.1080/10426914.2020.1765251

**3rd Research Paper – DOI:** https://doi.org/10.31603/mesi.5903

# References:


[1] McGuire, M. F. *Stainless Steels for Design Engineers*; 2019. https://doi.org/10.31399/asm.tb.ssde.9781627082860.

[2] Ahmadi, E.; Ebrahimi, A. R. Welding of 316L Austenitic Stainless Steel with Activated Tungsten Inert Gas Process. *J. Mater. Eng. Perform.*, **2014**, *24* (2), 1065–1071. https://doi.org/10.1007/s11665-014-1336-6.

[3] Modenesi, P. J.; Apolinário, E. R.; Pereira, I. M. TIG Welding with Single-Component Fluxes. *J. Mater. Process. Technol.*, **2000**, *99* (1), 260–265. https://doi.org/10.1016/S0924-0136(99)00435-5.

[4] usaweld.com/TIG-Pyrex-Cups-Kits-s/67.htm https://www.usaweld.com/TIG-Pyrex-Cups-Kits-s/67.htm (accessed May 1, 2017).

[5] Zhu, Z.; Zhang, G.; Wang, K.; Shi, Y.; Zhu, M. Joint Penetration Monitoring in Low-Frequency Pulsed GTA Root Pass Welding of Medium-Thick Steel Plates. *Weld. J.*, **2021**, *100* (09), 281–290. https://doi.org/10.29391/2021.100.025.

[6] Tseng, K. H.; Hsu, C. Y. Performance of Activated TIG Process in Austenitic Stainless Steel Welds. *J. Mater. Process. Technol.*, **2011**, *211* (3), 503–512. https://doi.org/10.1016/j.jmatprotec.2010.11.003.

[7] Heiple, C. R.; Roper, J. R. Mechanism for Minor Element Effect on Gta Fusion Zone Geometry. *Weld. J. (Miami, Fla)*, **1982**, *61* (4), 97s-102s.

[8] Tathgir, S.; Bhattacharya, A.; Bera, T. K. Influence of Current and Shielding Gas in TiO2 Flux Activated Tig Welding on Different Graded Steels. *Mater. Manuf. Process.*, **2015**, *30* (9), 1115–1123. https://doi.org/10.1080/10426914.2014.973591.

[9] Tathgir, S.; Bhattacharya, A. Activated-TIG Welding of Different Steels: Influence of Various Flux and Shielding Gas. *Mater. Manuf. Process.*, **2016**, *31* (3), 335–342. https://doi.org/10.1080/10426914.2015.1037914.

[10] Lowke, J. J.; Tanaka, M.; Ushio, M. Mechanisms Giving Increased Weld Depth Due to a Flux. *J. Phys. D. Appl. Phys.*, **2005**, *38* (18), 3438–3445. https://doi.org/10.1088/0022-3727/38/18/018.

[11] Sharma, P.; Dwivedi, D. K. A-TIG Welding of Dissimilar P92 Steel and 304H Austenitic Stainless Steel: Mechanisms, Microstructure and Mechanical Properties. *J. Manuf. Process.*, **2019**, *44*, 166–178. https://doi.org/10.1016/j.jmapro.2019.06.003.

[12] Kumar, H.; Ahmad, G. N.; Singh, N. K. Activated Flux TIG Welding of Inconel 718 Super Alloy in Presence of Tri-Component Flux. *Mater. Manuf. Process.*, **2019**, *34* (2),

216–223. https://doi.org/10.1080/10426914.2018.1532581.

[13] Bhattacharya, A. Revisiting Arc, Metal Flow Behavior in Flux Activated Tungsten Inert Gas Welding. *Mater. Manuf. Process.*, **2016**, *31* (3), 343–351. https://doi.org/10.1080/10426914.2015.1070421.

[14] Tseng, K. H.; Chen, P. Y. Effect of TiO2 Crystalline Phase on Performance of Flux Assisted GTA Welds. *Mater. Manuf. Process.*, **2016**, *31* (3), 359–365. https://doi.org/10.1080/10426914.2015.1058952.

[15] Tusek, J.; Suban, M. Experimental Research of the Effect of Hydrogen in Argon as a Shielding Gas in Arc Welding of High-Alloy Stainless Steel. *Int. J. Hydrogen Energy*, **2000**, *25* (25), 369–376.

[16] Wu, H.; Chang, Y.; Mei, Q.; Liu, D. Research Advances in High-Energy TIG Arc Welding. *Int. J. Adv. Manuf. Technol.*, **2019**, *104* (1–4), 391–410. https://doi.org/10.1007/s00170-019-03918-5.

[17] Sándor, T.; Mekler, C.; Dobránszky, J.; Kaptay, G. An Improved Theoretical Model for A-TIG Welding Based on Surface Phase Transition and Reversed Marangoni Flow. *Metall. Mater. Trans. A Phys. Metall. Mater. Sci.*, **2013**, *44* (1), 351–361. https://doi.org/10.1007/s11661-012-1367-2.

[18] Lu, S.; Fujii, H.; Nogi, K. Weld Shape Variation and Electrode Oxidation Behavior under Ar-(Ar-CO2) Double Shielded GTA Welding. *J. Mater. Sci. Technol.*, **2010**, *26* (2), 170–176. https://doi.org/10.1016/S1005-0302(10)60028-X.

[19] Kah, P.; Martikainen, J. Influence of Shielding Gases in the Welding of Metals. *Int. J. Adv. Manuf. Technol.*, **2013**, *64* (9–12), 1411–1421. https://doi.org/10.1007/s00170-012-4111-6.

[20] Tathgir, S.; Rathod, D. W.; Batish, A. A-TIG Welding Process for Enhanced-Penetration in Duplex Stainless-Steel: Effect of Activated Fluxes. *Mater. Manuf. Process.*, **2019**, *34* (15), 1659–1670. https://doi.org/10.1080/10426914.2019.1666990.

[21] Norrish, J. *Advanced Welding Processes Technologies and Process Control*, 2006th ed.; Woodhead Publishing Limited, Cambridge, England, 2006.

[22] Folkhard, E. *Welding Metallurgy of Stainless Steels*; Springer-Verlag: Wien New York, 1984.

[23] Acherjee, B. Hybrid Laser Arc Welding: State-of-Art Review. *Opt. Laser Technol.*, **2018**, *99*, 60–71. https://doi.org/10.1016/j.optlastec.2017.09.038.

[24] Reisgen, U.; Olschok, S.; Mavany, M.; Jakobs, S. Laser Beam Submerged Arc Hybrid Welding. *Phys. Procedia*, **2011**, *12* (PART 1), 179–187.

https://doi.org/10.1016/j.phpro.2011.03.023.

[25] Emmelmann, C.; Kirchhoff, M.; Petri, N. Development of Plasma-Laser-Hybrid Welding Process. *Phys. Procedia*, **2011**, *12* (PART 1), 194–200. https://doi.org/10.1016/j.phpro.2011.03.025.

[26] Ishide, T.; Tsubota, S.; Watanabe, M. Latest MIG, TIG Arc -. **2003**, *4831*, 347–352.

[27] Bîrdeanu, A. V.; Ciuc, C.; Puicea, A. Pulsed LASER-(Micro)TIG Hybrid Welding: Process Characteristics. *J. Mater. Process. Technol.*, **2012**, *212* (4), 890–902. https://doi.org/10.1016/j.jmatprotec.2011.11.014.

[28] Casalino, G.; Michele, D.; Perulli, P. FEM Model for TIG Hybrid Laser Butt Welding of 6 Mm Thick Austenitic to Martensitic Stainless Steels. *Procedia CIRP*, **2020**, *88*, 116–121. https://doi.org/10.1016/j.procir.2020.05.021.

[29] Ribic, B.; Palmer, T. A.; DebRoy, T. Problems and Issues in Laser-Arc Hybrid Welding. *Int. Mater. Rev.*, **2009**, *54* (4), 223–244. https://doi.org/10.1179/174328009X411163.

[30] Moteshakker, A.; Danaee, I. Microstructure and Corrosion Resistance of Dissimilar Weld-Joints between Duplex Stainless Steel 2205 and Austenitic Stainless Steel 316L. *J. Mater. Sci. Technol.*, **2016**, *32* (3), 282–290. https://doi.org/10.1016/j.jmst.2015.11.021.

[31] Kiran, D. V.; Na, S.-J. Experimental Studies on Submerged Arc Welding Process. *J. Weld. Join.*, **2014**, *32* (3), 1–10. https://doi.org/10.5781/jwj.2014.32.3.1.

[32] Kou, S. *Welding Metallurgy*, Second.; A John Wiley & Sons, Inc., Publication: New Jersey, 2003.

[33] Kotecki, Damian and Armao, F. Stainless Steels Properties – How To Weld Them Where To Use Them. *Lincoln Electr. Co.*, **2003**, 1–40.

[34] Lippold, J. C.; Kotecki, D. J. *Welding Metallurgy and Weldability of Stainless Steels*; A John Wiley & Sons, Inc., Publication: New Jersey, 2005.

[35] Outokumpu. *Handbook of Stainless Steel*; 2013.

[36] ASM. *ASM Handbook Vol 13 - Corrosion*; 1992.

[37] Arunkumar, V.; Vasudevan, M.; Maduraimuthu, V.; Muthupandi, V. Effect of Activated Flux on the Microstructure and Mechanical Properties of 9Cr-1Mo Steel Weld Joint. *Mater. Manuf. Process.*, **2012**, *27* (11), 1171–1177. https://doi.org/10.1080/10426914.2011.610212.

[38] Arivazhagan, B.; Vasudevan, M. Studies on A-TIG Welding of 2.25Cr-1Mo (P22) Steel. *J. Manuf. Process.*, **2015**, *18*, 55–59. https://doi.org/10.1016/j.jmapro.2014.12.003.

[39] Chern, T. S.; Tseng, K. H.; Tsai, H. L. Study of the Characteristics of Duplex Stainless

Steel Activated Tungsten Inert Gas Welds. *Mater. Des.*, **2011**, *32* (1), 255–263. https://doi.org/10.1016/j.matdes.2010.05.056.

[40] Hosseini, V. A.; Wessman, S.; Hurtig, K.; Karlsson, L. Nitrogen Loss and Effects on Microstructure in Multipass TIG Welding of a Super Duplex Stainless Steel. *Mater. Des.*, **2016**, *98*, 88–97. https://doi.org/10.1016/j.matdes.2016.03.011.

[41] Sakthivel, T.; Vasudevan, M.; Laha, K.; Parameswaran, P.; Chandravathi, K. S.; Mathew, M. D.; Bhaduri, A. K. Creep Rupture Strength of Activated-TIG Welded 316L(N) Stainless Steel. *J. Nucl. Mater.*, **2011**, *413* (1), 36–40. https://doi.org/10.1016/j.jnucmat.2011.03.047.

[42] Ruan, Y.; Qiu, X. M.; Gong, W. B.; Sun, D. Q.; Li, Y. P. Mechanical Properties and Microstructures of 6082-T6 Joint Welded by Twin Wire Metal Inert Gas Arc Welding with the SiO2 Flux. *Mater. Des.*, **2012**, *35*, 20–24. https://doi.org/10.1016/j.matdes.2011.09.002.

[43] Vasantharaja, P.; Vasudevan, M. Studies on A-TIG Welding of Low Activation Ferritic/Martensitic (LAFM) Steel. *J. Nucl. Mater.*, **2012**, *421* (1–3), 117–123. https://doi.org/10.1016/j.jnucmat.2011.11.062.

[44] Fu, J.; Yang, Y. Crystallography and Morphology of a Lathy Ferrite in Fe-Cr-Ni Alloys during Directional Solidification. *J. Mater. Res.*, **2013**, *28* (15), 2040–2046. https://doi.org/10.1557/jmr.2013.203.

[45] Xie, X.; Shen, J.; Cheng, L.; Li, Y.; Pu, Y. Effects of Nano-Particles Strengthening Activating Flux on the Microstructures and Mechanical Properties of TIG Welded AZ31 Magnesium Alloy Joints. *Mater. Des.*, **2015**, *81*, 31–38. https://doi.org/10.1016/j.matdes.2015.05.024.

[46] Sharma, P.; Dwivedi, D. K. A-TIG Welding of Dissimilar P92 Steel and 304H Austenitic Stainless Steel: Mechanisms, Microstructure and Mechanical Properties. *J. Manuf. Process.*, **2019**, *44* (June), 166–178. https://doi.org/10.1016/j.jmapro.2019.06.003.

[47] Sharma, P.; Dwivedi, D. K. Comparative Study of Activated Flux-GTAW and Multipass-GTAW Dissimilar P92 Steel-304H ASS Joints. *J. Manuf. Process.*, **2019**. https://doi.org/10.1080/10426914.2019.1605175.

[48] Vasantharaja, P.; Vasudevan, M.; Palanichamy, P. Effect of Welding Processes on the Residual Stress and Distortion in Type 316LN Stainless Steel Weld Joints. *J. Manuf. Process.*, **2015**, *19*, 187–193. https://doi.org/10.1016/j.jmapro.2014.09.004.

[49] Durgutlu, A. Experimental Investigation of the Effect of Hydrogen in Argon as a

Shielding Gas on TIG Welding of Austenitic Stainless Steel. *Mater. Des.*, **2004**, *25* (1), 19–23. https://doi.org/10.1016/j.matdes.2003.07.004.

[50] Gülenç, B.; Develi, K.; Kahraman, N.; Durgutlu, A. Experimental Study of the Effect of Hydrogen in Argon as a Shielding Gas in MIG Welding of Austenitic Stainless Steel. *Int. J. Hydrogen Energy*, **2005**, *30* (13–14), 1475–1481. https://doi.org/10.1016/j.ijhydene.2004.12.012.

[51] Michler, T. Toughness and Hydrogen Compatibility of Austenitic Stainless Steel Welds at Cryogenic Temperatures. *Int. J. Hydrogen Energy*, **2007**, *32* (16), 4081–4088. https://doi.org/10.1016/j.ijhydene.2007.03.009.

[52] Lu, S.; Li, D.; Fujii, H.; Nogi, K. Time Dependant Weld Shape in Ar-O2 Shielded Stationary GTA Welding. *J. Mater. Sci. Technol.*, **2007**, *23* (5), 650–654.

[53] Naumann, J.; Michler, T. Hydrogen Environment Embrittlement of Orbital Welded Austenitic Stainless Steels at -50 °C. *Int. J. Hydrogen Energy*, **2009**. https://doi.org/10.1016/j.ijhydene.2009.05.081.

[54] Lu, S.; Fujii, H.; Nogi, K. Weld Shape Variation and Electrode Oxidation Behavior under Ar-(Ar-CO2) Double Shielded GTA Welding. *J. Mater. Sci. Technol.*, **2010**, *26* (2), 170–176. https://doi.org/10.1016/S1005-0302(10)60028-X.

[55] Li, D.; Lu, S.; Dong, W.; Li, D.; Li, Y. Study of the Law between the Weld Pool Shape Variations with the Welding Parameters under Two TIG Processes. *J. Mater. Process. Technol.*, **2012**, *212* (1), 128–136. https://doi.org/10.1016/j.jmatprotec.2011.08.015.

[56] Niagaj, J. Effect of A-TIG Welding on Deformation of Austenitic Steel Components. *Weld. Int.*, **2013**, *27* (11), 853–856. https://doi.org/10.1080/09507116.2011.606145.

[57] Zou, Y.; Ueji, R.; Fujii, H. Effect of Oxygen on Weld Shape and Crystallographic Orientation of Duplex Stainless Steel Weld Using Advanced A-TIG (AA-TIG) Welding Method. *Mater. Charact.*, **2014**, *91*, 42–49. https://doi.org/10.1016/j.matchar.2014.02.006.

[58] Lothongkum, G.; Chaumbai, P.; Bhandhubanyong, P. TIG Pulse Welding of 304L Austenitic Stainless Steel in Flat, Vertical and Overhead Positions. *J. Mater. Process. Technol.*, **1999**, *89–90*, 410–414. https://doi.org/10.1016/S0924-0136(99)00046-1.

[59] Hosseini, V. A.; Hurtig, K.; Karlsson, L. Effect of Multipass TIG Welding on the Corrosion Resistance and Microstructure of a Super Duplex Stainless Steel. *Mater. Corros.*, **2017**, *68* (4), 405–415. https://doi.org/10.1002/maco.201609102.

[60] Sridhar, P. V. S. S.; Biswas, P.; Mahanta, P. Influence of Welding Current on Bead Profile and Mechanical Properties of Double Sided Submerged Arc Welding of AISI

304 Austenitic Stainless Steel. *Mater. Today Proc.*, **2019**, *19* (xxxx), 831–836. https://doi.org/10.1016/j.matpr.2019.08.140.

[61] Migiakis, K.; Daniolos, N.; Papadimitriou, G. D. Plasma Keyhole Welding of Uns S32760 Super Duplex Stainless Steel: Microstructure and Mechanical Properties. *Mater. Manuf. Process.*, **2010**, *25* (7), 598–605. https://doi.org/10.1080/10426910903179955.

[62] Dhandha, K. H.; Badheka, V. J. Effect of Activating Fluxes on Weld Bead Morphology of P91 Steel Bead-on-Plate Welds by Flux Assisted Tungsten Inert Gas Welding Process. *J. Manuf. Process.*, **2015**, *17*, 48–57. https://doi.org/10.1016/j.jmapro.2014.10.004.

[63] Rückert, G.; Huneau, B.; Marya, S. Optimizing the Design of Silica Coating for Productivity Gains during the TIG Welding of 304L Stainless Steel. *Mater. Des.*, **2007**, *28* (9), 2387–2393. https://doi.org/10.1016/j.matdes.2006.09.021.

[64] Lin, H. L.; Wu, T. M. Effects of Activating Flux on Weld Bead Geometry of Inconel 718 Alloy TIG Welds. *Mater. Manuf. Process.*, **2012**, *27* (12), 1457–1461. https://doi.org/10.1080/10426914.2012.677914.

[65] Sambherao, P. A. B. Use of Activated Flux For Increasing Penetration In Austenitic Stainless Steel While Performing GTAW. *Int. J. Emerg. Technol. Adv. Eng.*, **2013**, *3* (12), 520–524.

[66] Okano, S.; Mochizuki, M. Transient Distortion Behavior during TIG Welding of Thin Steel Plate. *J. Mater. Process. Technol.*, **2017**, *241*, 103–111. https://doi.org/10.1016/j.jmatprotec.2016.11.006.

[67] Zhang, G.; Xiong, J.; Gao, H.; Wu, L. Effect of Process Parameters on Temperature Distribution in Twin-Electrode TIG Coupling Arc. *J. Quant. Spectrosc. Radiat. Transf.*, **2012**, *113* (15), 1938–1945. https://doi.org/10.1016/j.jqsrt.2012.05.018.

[68] Ding, M.; Liu, S. S.; Zheng, Y.; Wang, Y. C.; Li, H.; Xing, W. Q.; Yu, X. Y.; Dong, P. TIG-MIG Hybrid Welding of Ferritic Stainless Steels and Magnesium Alloys with Cu Interlayer of Different Thickness. *Mater. Des.*, **2015**, *88*, 375–383. https://doi.org/10.1016/j.matdes.2015.09.022.

[69] Shenghai, Z.; Yifu, S.; Huijuan, Q. The Technology and Welding Joint Properties of Hybrid Laser-Tig Welding on Thick Plate. *Opt. Laser Technol.*, **2013**, *48*, 381–388. https://doi.org/10.1016/j.optlastec.2012.11.014.

[70] Modenesi, P. J.; Apolinário, E. R.; Pereira, I. M. TIG Welding with Single-Component Fluxes. *J. Mater. Process. Technol.*, **2000**, *99* (1), 260–265. https://doi.org/10.1016/S0924-0136(99)00435-5.

[71] Bhattacharya, A. Revisiting Arc , Metal Flow Behavior in Flux Activated Tungsten Inert Gas Welding Revisiting Arc , Metal Flow Behavior in Flux Activated Tungsten Inert Gas Welding. *LMMP*, **2016**, *31* (3), 343–351. https://doi.org/10.1080/10426914.2015.1070421.

[72] Vasantharaja, P.; Vasudevan, M.; Palanichamy, P. Effect of Welding Processes on the Residual Stress and Distortion in Type 316LN Stainless Steel Weld Joints. *J. Manuf. Process.*, **2015**, *19*, 187–193. https://doi.org/10.1016/j.jmapro.2014.09.004.

[73] Reisgen, U.; Olschok, S.; Mavany, M.; Jakobs, S. Laser Beam Submerged Arc Hybrid Welding. *Phys. Procedia*, **2011**, *12* (PART 1), 179–187. https://doi.org/10.1016/j.phpro.2011.03.023.

[74] Nakhaei, R.; Khodabandeh, A.; Najafi, H. Effect of Active Gas on Weld Shape and Microstructure of Advanced A-TIG-Welded Stainless Steel. *Acta Metall. Sin. (English Lett.*, **2016**, *29* (3), 295–300. https://doi.org/10.1007/s40195-016-0381-6.

[75] Shyu, S. W.; Huang, H. Y.; Tseng, K. H.; Chou, C. P. Study of the Performance of Stainless Steel A-TIG Welds. *J. Mater. Eng. Perform.*, **2008**, *17* (2), 193–201. https://doi.org/10.1007/s11665-007-9139-7.

[76] Elmesalamy, A.; Francis, J. A.; Li, L. A Comparison of Residual Stresses in Multi Pass Narrow Gap Laser Welds and Gas-Tungsten Arc Welds in AISI 316L Stainless Steel. *Int. J. Press. Vessel. Pip.*, **2014**, *113*, 49–59. https://doi.org/10.1016/j.ijpvp.2013.11.002.

[77] Verma, J.; Taiwade, R. V. Effect of Welding Processes and Conditions on the Microstructure, Mechanical Properties and Corrosion Resistance of Duplex Stainless Steel Weldments—A Review. *Journal of Manufacturing Processes*. The Society of Manufacturing Engineers 2017, pp 134–152. https://doi.org/10.1016/j.jmapro.2016.11.003.

[78] Reddy, G. M.; Rao, K. S.; Sekhar, T. Microstructure and Pitting Corrosion of Similar and Dissimilar Stainless Steel Welds. *Sci. Technol. Weld. Join.*, **2008**, *13* (4), 363–377. https://doi.org/10.1179/174329308X299968.

[79] Wang, Tian Fu Di, Xin Jie Li, Cheng Ning Wang, J. M.; Wang, D. P. Effect of δ Phase on Microstructure and Hardness of Heat-Affected Zone in TIG-Welded GH4169 Superalloy. *Acta Metall. Sin. (English Lett.*, **2018**, *10.1007/s4* (0123456789). https://doi.org/10.1007/s40195-018-0861-y.

[80] Michalska, J.; Soza, M. Qualitative and Quantitative Analysis of σ and χ Phases in 2205 Duplex Stainless Steel. *Mater. Charact.*, **2006**, *56*, 355–362.

https://doi.org/10.1016/j.matchar.2005.11.003.

[81] Paulraj, P.; Garg, R. Effect of Intermetallic Phases on Corrosion Behavior and Mechanical Properties of Duplex Stainless Steel and Super-Duplex Stainless Steel. *Adv. Sci. Technol. Res. J.*, **2015**, *9*, 87–105. https://doi.org/10.12913/22998624/59090.

[82] Blondeau, R. *Metallurgy and Mechanics of Welding: Processes and Industrial Applications*; A John Wiley & Sons, Inc., Publication: New Jersey, 2010. https://doi.org/10.1002/9780470611272.

[83] Lu, S.; Fujii, H.; Nogi, K. Weld Shape Variation and Electrode Oxidation Behavior under Ar- ( Ar-CO 2 ) Double Shielded GTA Welding. *J. Mater. Sci. Technol.*, **2010**, *26* (2), 170–176.

[84] Chen, J.; Zong, R.; Wu, C.; Padhy, G. K.; Hu, Q. Influence of Low Current Auxiliary TIG Arc on High Speed TIG-MIG Hybrid Welding. *J. Mater. Process. Technol.*, **2017**, *243*, 131–142. https://doi.org/10.1016/j.jmatprotec.2016.12.012.

[85] Zacharia, T.; David, S. A.; Vitek, J. M.; Debroy, T. Weld Pool Development during GTA and Laser Beam Welding of Type 304 Stainless Steel , Part II — Experimental Correlation. *Weld. J. Res. Suppl.*, **1989**, *68*, (12), 510s-520s.

[86] Zacharia, T.; David, S. A.; Vitek, J. M.; Debroy, T. Weld Pool Development during GTA and Laser Beam Welding of Type 304 Stainless Steel , Part I — Theoretical Analysis. *Weld. J. Res. Suppl.*, **1989**, *68* (12), 499s To 509s.

[87] Sandwik. Sandvik duplex stainless steels https://www.materials.sandvik/globalassets/global/downloads/products_downloads/tubular-products/s-120-eng_10.pdf.

[88] Saluja, R.; Moeed, K. M. The Emphasis of Phase Transformations and Alloying Constituents on Hot Cracking Susceptibility of Type 304L and 316L Stainless Steel Welds. *Int. J. Eng. Sci. Technol.*, **2012**, *4* (5), 2206–2216. https://doi.org/10.21829/abm118.

[89] Vora, J. J.; Badheka, V. J. Experimental Investigation on Mechanism and Weld Morphology of Activated TIG Welded Bead-on-Plate Weldments of Reduced Activation Ferritic/Martensitic Steel Using Oxide Fluxes. *J. Manuf. Process.*, **2015**, *20*, 224–233. https://doi.org/10.1016/j.jmapro.2015.07.006.

[90] Suban, M.; Tušek, J.; Uran, M. Use of Hydrogen in Welding Engineering in Former Times and Today. *J. Mater. Process. Technol.*, **2001**, *119* (1–3), 193–198. https://doi.org/10.1016/S0924-0136(01)00956-6.

[91] Singh, A. K.; Dey, V.; Rai, R. N. Techniques to Improveweld Penetration in TIG

Welding (A Review). *Mater. Today Proc.*, **2017**, *4* (2), 1252–1259. https://doi.org/10.1016/j.matpr.2017.01.145.

[92] Bhattacharya, A.; Kumar, R. Dissimilar Joining between Austenitic and Duplex Stainless Steel in Double-Shielded GMAW: A Comparative Study. *Mater. Manuf. Process.*, **2016**, *31* (3), 300–310. https://doi.org/10.1080/10426914.2015.1070414.

[93] Tathgir, S.; Rathod, D. W.; Batish, A. Process Enhancement Using Hydrogen-Induced Shielding: H2-Induced A-TIG Welding Process. *Mater. Manuf. Process.*, **2020**, *35* (10), 1084–1095. https://doi.org/10.1080/10426914.2020.1765251.

[94] Nelson, D. E.; Baeslack III, W. A.; Lippold, J. C. An Investigation of Weld Hot Cracking in Duplex Stainless Steels. *Weld. J. Res. Suppl.*, **1987**, *66*, 241s-250s.

[95] *Duplex Stainless Steels, Microstructure, Properties and Applications*; Gunn, R. N., Ed.; Abington Publishing: Cambridge England, 2003.

[96] Pramanik, A.; Littlefair, G.; Basak, A. K. Weldability of Duplex Stainless Steel. *Mater. Manuf. Process.*, **2015**, *30* (9), 1053–1068. https://doi.org/10.1080/10426914.2015.1019126.

[97] Gupta, I.; Mohanty, B. C. Eliminating Secondary Phases : Understanding Kesterite Phase Evolution of Cu 2 ZnSnS 4 Thin Fi Lms Grown from Ethanol Based Solutions with High Photosensitivity. *Sol. Energy*, **2019**, *181* (November 2018), 214–221. https://doi.org/10.1016/j.solener.2019.01.098.

[98] Rathod, D. W.; Pandey, S.; Singh, P. K.; Kumar, S. Microstructure-Dependent Fracture Toughness ( J IC ) Variations in Dissimilar Pipe Welds for Pressure Vessel System of Nuclear Plants. *J. Nucl. Mater.*, **2017**, *493*, 412–425. https://doi.org/10.1016/j.jnucmat.2017.06.038.

[99] Rathod, D.; Aravindan, S.; Singh, P. K.; Pandey, S. Metallurgical Characterization and Diffusion Studies of Successively Buttered Deposit of Ni-Fe Alloy and Inconel on SA508 Ferritic Steel. *ISIJ Int.*, **2014**, *54* (8), 1866–1875. https://doi.org/10.2355/isijinternational.54.1866.

[100] Muzaka, K.; Park, M. H.; Lee, J. P.; Jin, B. J.; Lee, B. R.; Kim, W. Y. I. S. A Study on Prediction of Welding Quality Using Mahalanobis Distance Method by Optimizing Welding Current for A Vertical-Position Welding. In *Procedia Engineering*; 2017. https://doi.org/10.1016/j.proeng.2017.01.143.

[101] De Lacerda, J. C.; Cândido, L. C.; Godefroid, L. B. Effect of Volume Fraction of Phases and Precipitates on the Mechanical Behavior of UNS S31803 Duplex Stainless Steel. *Int. J. Fatigue*, **2015**, *74*, 81–87. https://doi.org/10.1016/j.ijfatigue.2014.12.015.

[102] Çiçek, B.; Gündoğdu İş, E.; Gümüş, E.; Topuz, P. The Effect of Welding Positions on the Weldability of X20CrMoV11-1 Steels. *Hittite J. Sci. Eng.*, **2017**, *5* (1), 75–83. https://doi.org/10.17350/hjse19030000068.

[103] Figueirôa, D. W.; Pigozzo, I. O.; Silva, R. H. G. e.; Santos, T. F. de A.; Urtiga Filho, S. L. Influence of Welding Position and Parameters in Orbital Tig Welding Applied to Low-Carbon Steel Pipes. *Weld. Int.*, **2017**, *31* (8), 583–590. https://doi.org/10.1080/09507116.2016.1218615.

[104] Valiente Bermejo, M. A.; Karlsson, L.; Svensson, L. E.; Hurtig, K.; Rasmuson, H.; Frodigh, M.; Bengtsson, P. Effect of Welding Position on Properties of Duplex and Superduplex Stainless Steel Circumferential Welds. *Weld. World*, **2015**, *59* (5), 693–703. https://doi.org/10.1007/s40194-015-0245-0.

[105] Zhu, W.; Zhang, H.; Guo, C.; Liu, Y.; Ran, X. Wetting and Brazing Characteristic of High Nitrogen Austenitic Stainless Steel and 316L Austenitic Stainless Steel by Ag–Cu Filler. *Vacuum*, **2019**, *166* (2055), 97–106. https://doi.org/10.1016/j.vacuum.2019.04.064.

[106] Koç, M.; Mahabunphachai, S.; Billur, E. Forming Characteristics of Austenitic Stainless Steel Sheet Alloys under Warm Hydroforming Conditions. *Int. J. Adv. Manuf. Technol.*, **2011**, *56* (1–4), 97–113. https://doi.org/10.1007/s00170-011-3169-x.

[107] Olson, D. L. Prediction of Austenitic Weld Metal Microstructure and Properties With Advent of New Stainless Steels, a Wider Range of Alloys Must Be Considered in Predicting Ferrite. *Weld. Res. Supplemen*, **1984**, *64*, 281s-295s. https://doi.org/10.1017/CBO9781107415324.004.

[108] Gunaraj, V.; Murugan, N. Prediction and Optimization of Weld Bead Volume for the Submerged Arc Process - Part 2. *Weld. J. (Miami, Fla)*, **2000**, *79* (11), 331-s-338-s.

[109] Gunaraj, V.; Murugan, N. Prediction and Optimization of Weld Bead Volume for the Submerged Arc Process - Part 1. *Weld. J. (Miami, Fla)*, **2000**, *79* (10), 286s-294s.

[110] Kiran, D. V.; Cho, D. W.; Song, W. H.; Na, S. J. Arc Behavior in Two Wire Tandem Submerged Arc Welding. *J. Mater. Process. Technol.*, **2014**, *214* (8), 1546–1556. https://doi.org/10.1016/j.jmatprotec.2014.02.023.

[111] Ishigami, A.; Roy, M. J.; Walsh, J. N.; Withers, P. J. The Effect of the Weld Fusion Zone Shape on Residual Stress in Submerged Arc Welding. *Int. J. Adv. Manuf. Technol.*, **2017**, *90* (9–12), 3451–3464. https://doi.org/10.1007/s00170-016-9542-z.

[112] Dak, G.; Pandey, C. A Critical Review on Dissimilar Welds Joint between Martensitic and Austenitic Steel for Power Plant Application. *J. Manuf. Process.*, **2020**, *58* (May),

377–406. https://doi.org/10.1016/j.jmapro.2020.08.019.

[113] Jindal, S.; Chhibber, R.; Mehta, N. P. Investigation on Flux Design for Submerged Arc Welding of High-Strength Low-Alloy Steel. *Proc. Inst. Mech. Eng. Part B J. Eng. Manuf.*, **2013**, *227* (3), 383–395. https://doi.org/10.1177/0954405412468993.

[114] API5L-2019-Supplement. Supplementary Specification to API Specification 5L and ISO 3183 Line Pipe. **2019**, No. January.

[115] Kanjilal, P.; Pal, T. K.; Majumdar, S. K. Combined Effect of Flux and Welding Parameters on Chemical Composition and Mechanical Properties of Submerged Arc Weld Metal. *J. Mater. Process. Technol.*, **2006**, *171* (2), 223–231. https://doi.org/10.1016/j.jmatprotec.2005.06.083.

[116] Mitra, U.; Eagar, T. W. Slag Metal Reactions During Submerged Arc Welding of Alloy Steels. *Metall. Trans. A, Phys. Metall. Mater. Sci.*, **1984**, *15 A* (1), 217–227. https://doi.org/10.1007/BF02644404.

[117] Pandey, N. D.; Bharti, A.; Gupta, S. R. Effect of Submerged Arc Welding Parameters and Fluxes on Element Transfer Behaviour and Weld-Metal Chemistry. *J. Mater. Process. Tech.*, **1994**, *40* (1–2), 195–211. https://doi.org/10.1016/0924-0136(94)90486-3.

[118] Martorano, M. A.; Tavares, C. F.; Padilha, A. F. Predicting Delta Ferrite Content in Stainless Steel Castings. *ISIJ Int.*, **2012**, *52* (6), 1054–1065. https://doi.org/10.2355/isijinternational.52.1054.

[119] Kasana, S. S.; Pandey, O. P. Influence of Chemical Composition and Thermo-Mechanical Processing on the Formation of Delta Ferrite in 10.7CrMoVNbN Steel. *Trans. Indian Inst. Met.*, **2020**, *73* (10), 2491–2502. https://doi.org/10.1007/s12666-020-02052-1.

[120] Palani, P. K.; Murugan, N. Prediction of Delta Ferrite Content and Effect of Welding Process Parameters in Claddings by FCAW. *Mater. Manuf. Process.*, **2006**, *21* (5), 431–438. https://doi.org/10.1080/10426910500471409.

[121] Vicente, A. de A.; D'silva, P. A.; Santos, I. L. dos; Aguiar, R. R. de; Botelho Junior, A. B.; Santos, T. F. de A. The Effect of Shielding Gases in the Ferrite Number of Austenitic Stainless Steels Joints through GMAW. *Int. J. Adv. Eng. Res. Sci.*, **2020**, *7* (7), 332–341. https://doi.org/10.22161/ijaers.77.37.

[122] Bhattacharya, A.; Bera, T. K.; Suri, V. K. Influence of Heat Input in Automatic GMAW: Penetration Prediction and Microstructural Observation. *Mater. Manuf. Process.*, **2014**, *29* (10), 1210–1218. https://doi.org/10.1080/10426914.2014.930889.

[123] Tenni, B.; Brochu, M.; Godin, S.; Thibault, D. Shielding Gas and Inclusion Content Effects on Impact Toughness and Tensile Properties of 410NiMo Steel Welds. *Weld. J.*, **2021**, *100* (01), 52–62. https://doi.org/10.29391/2021.100.005.

[124] Rathod, D. W.; Pandey, S.; Singh, P. K.; Prasad, R. Experimental Analysis of Dissimilar Metal Weld Joint: Ferritic to Austenitic Stainless Steel. *Mater. Sci. Eng. A*, **2015**, *639*, 259–268. https://doi.org/10.1016/j.msea.2015.05.011.

[125] Svetlizky, D.; Das, M.; Zheng, B.; Vyatskikh, A. L.; Bose, S.; Bandyopadhyay, A.; Schoenung, J. M.; Lavernia, E. J.; Eliaz, N. Directed Energy Deposition (DED) Additive Manufacturing: Physical Characteristics, Defects, Challenges and Applications. *Mater. Today*, **2021**, *xxx* (xx). https://doi.org/10.1016/j.mattod.2021.03.020.

[126] Chatterjee, S.; van der Veldt, T. *Hybrid Welding Processes in Advanced High-Strength Steels (AHSS)*; Elsevier Ltd, 2015. https://doi.org/10.1016/B978-0-85709-436-0.00007-2.

[127] Sharma, S. K.; Maheshwari, S.; Kumar, R.; Singh, R. Effect of Heat-Input and Cooling-Time on Bead Characteristics in SAW. *Mater. Manuf. Process.*, **2019**, *34* (2), 208–215. https://doi.org/10.1080/10426914.2018.1532578.

[128] Arul Marcel Moshi, A.; Sundara Bharathi, S. R.; Rajeshkumar, R.; Kumar, R. Factors Influencing Submerged Arc Welding on Stainless Steel - a Review. *ARPN J. Eng. Appl. Sci.*, **2016**, *11* (2), 1237–1241.

[129] Rokhlin, S.; Guu, A. A Study of Arc Force, Pool Depression, and Weld Penetration during Gas Tungsten Arc Welding. *Weld. Journal(USA)*, **1993**, *72* (8), 381.

[130] David, S. A. Ferrite Morphology and Variations in Ferrite Content in Austenitic Stainless Steel Welds. *Weld. J. (Miami, Fla)*, **1981**, *60* (4), 63–71.

[131] Bhandari, D.; Chhibber, R.; Arora, N.; Mehta, R. Investigation of $TiO_2$-$SiO_2$-CaO-$CaF_2$ Based Electrode Coatings on Weld Metal Chemistry and Mechanical Behaviour of Bimetallic Welds. *J. Manuf. Process.*, **2016**, *23*, 61–74. https://doi.org/10.1016/j.jmapro.2016.05.013.